

# **Characterization of Machining-Induced Residual Stresses in Titanium-Based Alloys**

**Elias Abboud**

Department of Mechanical Engineering  
McGill University

Montreal, Quebec

August 2015

A thesis submitted to McGill University in partial fulfillment of the  
requirements of the degree of Doctor of Philosophy

Copyright © Elias Abboud 2015

All Rights Reserved

## ABSTRACT

Machining-induced residual stresses (RS) have a major impact on the fatigue life of critical aero-engine parts subjected to dynamic loads in harsh environments. Their state and magnitude can be controlled by careful selection of cutting conditions. Tensile RS are extremely harmful as they accelerate crack nucleation and propagation, diminishing the resistance to fatigue failures. It is crucial to identify cutting parameters that promote desirable compressive RS in critical parts without compromising other aspects of surface integrity. Limited information is available in the open literature on machining-induced RS in Ti-alloys.

In this research, an extensive experimental investigation is performed of the effect of cutting parameters on RS in two aerospace grade Ti-alloys, Ti-64 and Ti-6246, used for aero-engine fan and compressor parts. Cutting is performed at conditions relevant to industry. This is coupled with a comprehensive evaluation of surface integrity including RS, surface roughness, the near-surface microstructure, and hardness distribution. Based on x-ray diffraction measurements, empirical models are developed that offer fast and accurate predictions of surface RS. For the investigated finish turning regime, RS are compressive in nature. Due to a conflict between RS and surface finish, guidelines are established for the optimal selection of cutting parameters.

Empirical models are non-generic, cannot be extrapolated, and cannot offer a physical interpretation of the phenomena that govern the cutting process. Available FE models for Ti-alloys mostly focus on chip formation and force prediction, and rarely extend to RS. In this work, a 2D FE model is constructed using DEFORM™ for the prediction of machining-induced RS in Ti-alloys, and is optimized for accuracy and computational efficiency. This is preceded by a numerical study on the relative contribution of thermal loads, mechanical loads, and phase transformations to the resultant stress state in commercially available materials. The FE model is firstly validated against experimental machining forces, cutting temperatures, and RS. It is then used as a virtual machining medium to gain insight into the effect of cutting parameters, tool edge preparation, flank wear, and chip segmentation on residual stress formation. FE predictions for Ti-6246 show that RS are highly sensitive to flank wear, which can cause a severe shift from the compressive to the tensile state. For the investigated cutting regime, residual stress prediction errors for Ti-64 are limited to  $\pm 10\%$  provided that chip segmentation is modeled at relatively high cutting speeds.

## RÉSUMÉ

Les contraintes résiduelles (CR) induites par l'usinage ont un impact majeur sur la résistance à la fatigue des composantes soumises aux charges dynamiques dans les environnements sévères. Leur état peut être contrôlé par la sélection soignée des conditions de coupe. Les CR en tension réduisent la résistance à la défaillance par fatigue. Par conséquent, l'identification des paramètres de coupe qui promeuvent des CR compressives, en évitant l'endommagement de l'intégrité de la surface, est extrêmement importante. Les études sur les CR produites par l'usinage des alliages de titane sont très limitées.

Dans ce travail, une enquête approfondie est effectuée sur les effets des paramètres de coupe sur les CR générées dans deux alliages de titane, Ti-64 et Ti-6246, utilisées dans les moteurs d'avions. L'usinage est réalisé à des conditions pertinentes pour l'industrie. Cela est suivi par une évaluation de l'intégrité de la surface incluant les CR, la rugosité, la microstructure, et les profils de dureté. Basé sur des mesures des CR par diffraction des rayons X, des modèles empiriques rapides et précis sont développés. Pour les conditions de tournages de finition enquêtées, les CR sont compressives. Du à un conflit entre les CR et la rugosité, des lignes directrices sont développées pour la sélection des paramètres de coupe.

Les modèles empiriques qui sont non-génériques ne peuvent pas être extrapolés et ne peuvent pas offrir une interprétation des phénomènes physiques. Les modèles d'éléments finis disponibles pour les alliages de titane abordent rarement la formation des CR. Dans cette recherche, un modèle 2D d'éléments finis est développé à travers DEFORM<sup>TM</sup> pour la prédiction des CR générées par l'usinage. Le modèle est optimisé pour l'efficacité et la précision. Cela est précédé par une étude numérique sur la contribution relative des charges thermiques, charges mécaniques, et transformations de phases à l'état final des CR dans des nombreux matériaux. Le modèle est validé contre des mesures de forces, température, et CR produites par l'usinage. Par la suite, le modèle est utilisé comme un milieu d'usinage virtuel pour l'analyse des effets des paramètres de coupe, l'usure, et la segmentation des copeaux sur l'évolution des CR. Les études numériques liées au Ti-6246 démontrent que les CR sont très sensibles à l'usure qui peut promouvoir un changement d'état des CR de compression en tension. Pour les conditions de tournages de finition enquêtées, la marge d'erreur de prédiction des CR générées dans le Ti-64 est de  $\pm 10\%$  en condition que la segmentation des copeaux est modélisée à des vitesses de coupe relativement élevées.

## CLAIMS OF ORIGINALITY

This research addresses important gaps related to machining-induced residual stresses (RS) in Ti-alloys used in the manufacture of critical aero-engine parts subjected to dynamic loads in harsh environments. The knowledge gained through this work is highly significant to increasing the reliability, safety, and service life of aero-engines:

1. Prior numerical studies on the machining of Ti-alloys focused on chip formation and force prediction. Very limited attention was given to machining-induced residual stresses (RS) although they critically affect the fatigue resistance of machined components. Using the FE model developed in this work, an in-depth analysis of the effect of cutting parameters, tool edge radius, flank wear, and material properties on RS was performed that highlights important aspects that should be considered in order to generate compressive RS in Ti-alloys. Such an analysis for Ti-alloys is practically not available in the open literature and yields crucial information for the optimization of the machining process.
2. Analytical studies of the origins of RS are mainly focused on the grinding process. This research provided fundamental understanding of the significance and relative contributions of mechanical, thermal and metallurgical sources of RS generated during cutting. It allowed isolating the effect of these sources and gaining knowledge of how they are affected by material properties and process conditions. Without this information, emerging technologies such as laser-assisted machining (LAM) and cryogenic machining cannot be optimized to generate favorable residual stress distributions.
3. The effect of chip segmentation on machining-induced RS is not fully explored and in the case of Ti-alloys was only addressed for high speed machining. In this work, through FE analysis of state variable distributions, this effect was determined for conventional cutting speeds, and its impact on the accuracy of residual stress predictions was analyzed.
4. There is a lack of information on machining-induced RS in Ti-alloys, especially for the finish cutting regime. In this work, extensive experimental investigation was carried out to fill this gap for two aerospace grade  $\alpha/\beta$  Ti-alloys, Ti-64 and Ti-6246, used in the manufacture of aero-engine disks and blades. Guidelines were established for the optimal selection of cutting parameters that attain desired levels of compressive RS and surface quality.

## **ACKNOWLEDGMENTS**

I cannot sufficiently express my gratitude to my supervisors Prof. Helmi Attia and Prof. Vincent Thomson for their continued support and encouragement. I wish to extend my sincere appreciation to Prof. Attia for his guidance throughout this work, which allowed me to grow on a professional and personal level. I also wish to recognize the important contributions of Dr. Bin Shi and Dr. Ahmed Damir, and to thank Dr. Mouhab El Meshreki for his valuable help and advice.

The National Research Council Canada (NRC) is acknowledged for their support and for granting me access to their Structures, Materials, and Manufacturing (SMM) Laboratory in Montreal over the course of this research. I take this opportunity to thank all the Machining Group personnel including Research Officers and Laboratory Technicians for their cooperative spirit, and for making my presence at the NRC such an enriching experience. I would also like to thank my fellow graduate students and to wish them the best of luck in all their endeavors.

The Consortium for Research and Innovation in Aerospace in Quebec (CRIAQ), Le Ministère du Développement Économique, de l'Innovation, et de l'Éxportation (MDEIE), and Pratt & Whitney Canada are recognized for their financial support. I also wish to acknowledge Pratt & Whitney Canada for their valued contribution to this research and for their collaborative spirit throughout this work.

Finally, I wish to express my heartfelt thanks to my wife Julia for her emotional and moral support throughout this journey. I am also forever indebted to my parents, family, and friends. Words cannot express how lucky I am to have you.

# TABLE OF CONTENTS

|  |             |
|--|-------------|
| <b>Abstract</b>  | <b>i</b>    |
| <b>Claims of originality</b>   | <b>ii</b>   |
| <b>Acknowledgments</b>   | <b>iv</b>   |
| <b>Table of contents</b>   | <b>v</b>    |
| <b>Nomenclature</b>  | <b>viii</b> |
| <b>Chapter 1 Introduction</b>  | <b>1</b>    |
| 1.1 The significance and impact of residual stresses                 | 1           |
| 1.2 Research motivation and terminal objectives                      | 2           |
| 1.3 Thesis outline   | 3           |
| <b>Chapter 2 Critical literature review</b>                          | <b>6</b>    |
| 2.1 Nature and origins of residual stresses                          | 6           |
| 2.1.1 Residual stresses formation during machining                   | 8           |
| 2.2 The determination of machining-induced residual stresses         | 11          |
| 2.2.1 Experimental investigation                                     | 11          |
| 2.2.2 Modeling of the machining process                              | 15          |
| 2.3 Effect of process parameters and material properties             | 29          |
| 2.3.1 Effect of cutting parameters                                   | 29          |
| 2.3.2 Effect of tool geometry and edge preparation                   | 31          |
| 2.3.3 Effect of tool wear on residual stresses and surface integrity | 32          |
| 2.3.4 Effect of tool material and tool coatings                      | 32          |
| 2.3.5 Effect of workpiece material properties                        | 33          |
| 2.3.6 Effect of sequential cutting                                   | 34          |
| 2.4 Gap analysis   | 34          |
| 2.5 Research objectives  | 34          |
| 2.6 Research plan, methodology, and theoretical considerations       | 36          |
| <b>Chapter 3 Experimental setup</b>                                  | <b>40</b>   |
| 3.1 Introduction   | 40          |

|  |  |           |
|--|--|-----------|
| 3.2  | Three-dimensional oblique single point turning                   | 40        |
| 3.2.1  | Experimental setup   | 40        |
| 3.2.2  | Procedure for robust and stable cutting                          | 42        |
| 3.3  | Two-dimensional orthogonal cutting                               | 43        |
| 3.3.1  | Orthogonal cutting for FE model calibration and validation       | 43        |
| 3.3.2  | Orthogonal cutting for material identification                   | 44        |
| 3.4  | Experimental measurements  | 48        |
| 3.4.1  | Machining forces   | 48        |
| 3.4.2  | Cutting temperature  | 49        |
| 3.4.3  | Surface topography   | 50        |
| 3.4.4  | Microstructure evaluation  | 51        |
| 3.4.5  | Residual stresses  | 53        |
| 3.4.6  | Hardness distribution  | 54        |
| 3.4.7  | Tool wear  | 55        |
| <b>Chapter 4 Experimental results</b>  |  | <b>57</b> |
| 4.1  | Introduction   | 57        |
| 4.2  | Design of experiment   | 57        |
| 4.2.1  | Oblique single point turning                                     | 57        |
| 4.2.2  | Orthogonal cutting   | 58        |
| 4.3  | Results and discussion   | 59        |
| 4.3.1  | Normalization of experimental data                               | 59        |
| 4.3.2  | Assessment of experimental uncertainty                           | 60        |
| 4.3.3  | Orthogonal cutting results                                       | 61        |
| 4.3.4  | Oblique cutting results  | 66        |
| <b>Chapter 5 Fundamental aspects of residual stress formation during cutting</b> |  | <b>84</b> |
| 5.1  | Introduction   | 84        |
| 5.2  | The effect of thermal loading on residual stress formation       | 84        |
| 5.2.1  | FE model description   | 84        |
| 5.2.2  | Results of the thermal FE analysis                               | 86        |
| 5.3  | The effect of phase transformations on residual stress formation | 94        |

|  |   |            |
|--|---|------------|
| 5.3.1  | Transformation kinetics model   | 94         |
| 5.3.2  | Results of the coupling of phase transformation and thermal loads       | 97         |
| 5.4  | The contribution of thermal and mechanical loads to RS during machining | 101        |
| 5.4.1  | Description of the FE model   | 102        |
| 5.4.2  | Results of the numerical study  | 103        |
| <b>Chapter 6 FE Model development and results</b>                                |   | <b>112</b> |
| 6.1  | Introduction  | 112        |
| 6.2  | FE model development  | 112        |
| 6.2.1  | Model optimisation for accuracy and computational efficiency            | 114        |
| 6.2.2  | Model description   | 123        |
| 6.3  | FE model validation and analysis of results                             | 124        |
| 6.3.1  | Machining forces  | 124        |
| 6.3.2  | Cutting zone temperatures   | 126        |
| 6.3.3  | Residual stresses   | 129        |
| 6.3.4  | Interpretation of the dissimilar behavior of the Ti-alloys under study  | 140        |
| <b>Chapter 7 Chip segmentation in Ti-6Al-4V and its effect on FE predictions</b> |   | <b>143</b> |
| 7.1  | Introduction  | 143        |
| 7.2  | Characterization of chip segmentation for Ti-6Al-4V                     | 143        |
| 7.3  | FE modeling of segmental chip formation                                 | 150        |
| 7.3.1  | Implementation of the ductile fracture criterion                        | 153        |
| 7.4  | Effect of chip segmentation on FE predictions                           | 158        |
| 7.5  | Mechanism governing the effect of segmentation on RS predictions        | 160        |
| <b>Chapter 8 Conclusions and Recommendations</b>                                 |   | <b>165</b> |
| 8.1  | Experimental investigation  | 165        |
| 8.2  | FE modeling   | 166        |
| 8.3  | Recommendations for future work   | 169        |
| <b>References</b>  |   | <b>171</b> |
| <b>Appendix A</b>  |   | <b>180</b> |
| <b>Appendix B</b>  |   | <b>181</b> |

## LIST OF FIGURES

- Fig. 2.1: categorization of residual stress fields adapted from [6]. M and R represent the matrix and reinforcements, respectively, and  $\langle\sigma\rangle$  denotes the average stress value over the sampling volume. 6
- Fig. 2.2: idealized 2D model of the machining process. 8
- Fig. 2.3: residual stresses  $\sigma_R$  generated during (a) a predominantly tensile loading cycle with a high extent of burnishing following chip formation and (b) a predominantly compressive loading cycle. 9
- Fig. 2.4: (a) uniform inter-lattice spacing ( $d$ -spacing) in a stress free state, (b) varying  $d$ -spacing under tensile stress, and (c) schematic of the x-ray diffraction (XRD) measurement technique. Figures are adapted from Prevey [7] and Brinksmeier et al. [2]. 14
- Fig. 2.5: plane stress elastic model adopted in x-ray diffraction theory adapted from Prevey [7]. 14
- Fig. 2.6: plane strain idealization of the cutting process and discretization of the plastic zone. Figure adapted from Ulutan et al. and Lazoglu et al. [31, 32]. 20
- Fig. 2.7: the interrelationship between FEM modules. Figure adapted from [42, 43]. 22
- Fig. 2.8: systems approach to the characterization of machining-induced residual stresses in Ti-alloys. 39
- Fig. 3.1: experimental setup for oblique single point turning. 41
- Fig. 3.2: oblique turning: (a) process schematic and (b) representative tool geometry. 41
- Fig. 3.3: process flowchart for the 3D oblique cutting test procedure for Alloy 1. 42
- Fig. 3.4: experimental setup for dry orthogonal cutting for FE model calibration and validation. 43
- Fig. 3.5: orthogonal cutting: (a) process schematic and (b) representative tool geometry 44
- Fig. 3.6: orthogonal cutting with laser-assisted preheating for material identification. 45

- Fig. 3.7: images of tool/chip contact length ( $l_c$ ) obtained with a Winslow Engineering Model 560-Video tool analyser. 46
- Fig. 3.8: schematic diagram of the experimental setup for laser power and workpiece material emissivity calibration. 47
- Fig. 3.9: temperature evolution during laser preheating with power  $P = 350$  W and speed  $v = 80$  m/min: (a) Alloy 2: thermocouple measurements, (b) Alloy 1: comparison between thermocouple and infrared measurements for various emissivity ( $\epsilon$ ) values. 47
- Fig. 3.10: cutting force ( $F_c$ ) signals acquired for Alloy 1 at conditions ( $doc_i, v_2, f_i, R_3$ ), spanning: (a) the entire cutting path, and (b-g) 20 ms after the midpoint of the cutting path. 49
- Fig. 3.11: thermal images obtained during orthogonal cutting of Alloy 1 at condition ( $t_3, v_3$ ). The cutting zone is obscured by the continually winding chip. 50
- Fig. 3.12: surface of Alloy 1 specimens revealing no signs of chatter after oblique turning at relatively harsh conditions: (a) ( $doc_2, v_2, f_3, R_1$ ) and (b) ( $doc_2, v_2, f_3, R_3$ ). 51
- Fig. 3.13: surface roughness measurement setup for 3D machined specimens. 51
- Fig. 3.14: quarter cylinder coupons sectioned from a 3D turned bar. The NSM evaluation and RS measurements were performed on separate coupons (1 and 2) within the steady-state region. 52
- Fig. 3.15: images of chips produced in orthogonal cutting of Alloy 1 at condition ( $t_3, v_3$ ), showing the evaluation of: (a) chip geometry and (b) microstructural features. 53
- Fig. 3.16: Proto LXRD goniometer with: (a) 3D machined coupon, (b) orthogonally machined sample [113]. *Images courtesy of Proto Manufacturing Ltd.* 54
- Fig. 3.17: schematic diagram depicting the array of 60 micro-hardness indentations performed on polished surfaces perpendicular to the machined surface and parallel to the direction of axial feed. *All dimensions are in mm.* 54
- Fig. 3.18: modes of tool wear as per standard ISO 3685:1993 adapted from [114]. 55

- Fig. 4.1: chip morphology formed by room temperature (RT) orthogonal cutting at low speed, and with uncut chip thickness: (a)  $t = 0.25$  mm and (b)  $t = 0.1$  mm. 59
- Fig. 4.2: machining force signals acquired for Alloy 1 during oblique cutting at identical semi-finishing conditions ( $doc_2, v_1, f_2, R_2$ ). 61
- Fig. 4.3: effect of cutting parameters in dry orthogonal cutting of Alloy 1 on: (a) average steady-state machining forces, (b, c) cutting force signals, and (d, e) thrust force signals. 62
- Fig. 4.4: effect of cutting parameters on: (a, b) average steady-state machining forces for Alloy 2 as compared to Alloy 1, and (c, d) Alloy 2 machining force signals. 63
- Fig. 4.5: surface residual stresses measured by x-ray diffraction (XRD) for both Ti-alloys, as a result of dry orthogonal cutting. 64
- Fig. 4.6: flank wear (VB) produced in the carbide tools by (a) Alloy 1 and (b) Alloy 2 during dry orthogonal cutting at condition ( $t_3, v_3$ ). 65
- Fig. 4.7: average steady-state machining forces produced during oblique turning of Alloy 1, and for various cutting parameter combinations ( $doc_i, v_i, f_i, R_i$ ). 66
- Fig. 4.8: effect of cutting parameters and Ti-alloy type on average steady-state (a) cutting and (b) radial forces generated during oblique turning at conditions ( $doc_2, v_i, f_i, R_i$ ). 68
- Fig. 4.9: comparison between empirically predicted (Emp) and experimentally measured (Exp) cutting forces for Alloy 1 for the full range of investigated conditions ( $doc_i, v_i, f_i, R_i$ ). 70
- Fig. 4.10: (a) goodness of fit and (b) prediction error distribution for Alloy 1 oblique cutting force predictions over the full range of cutting conditions ( $doc_i, v_i, f_i, R_i$ ). 70
- Fig. 4.11: effect of speed and workpiece material on average flank wear at the tool corner radius,  $VB_C$ , for both Ti-alloys at conditions: (a) ( $doc_2, v_i, f_3, R_i$ ) and (b-e) SEM images ( $doc_2, v_i, f_3, R_1$ ). 71
- Fig. 4.12: Alloy 1: effect of oblique turning parameters on surface compressive RS in the cutting (hoop) direction at low depth of cut. 72

- Fig. 4.13: effect of cutting parameters on surface residual stresses induced in Alloy 2 during oblique turning for various cutting parameter combinations ( $doc_i, v_i, f_i, R_i$ ). 73
- Fig. 4.14: effect of cutting parameters on surface residual stresses generated in Alloy 2 at (a)  $doc_1$  and (b)  $doc_2$ , covering the full range of investigated cutting conditions. 74
- Fig. 4.15: effect of cutting parameters on surface RS generated in both Ti-alloys during oblique turning for various cutting parameter combinations ( $doc_2, v_i, f_i, R_i$ ). 75
- Fig. 4.16: Alloy 1: comparison between empirically predicted (Emp) and experimentally measured (Exp) surface RS in the cutting direction over the full range of cutting conditions ( $doc_i, v_i, f_i, R_i$ ). 76
- Fig. 4.17: (a) goodness of fit and (b) prediction error distribution for oblique cutting surface RS induced in Alloy 1, over the full range of cutting conditions ( $doc_i, v_i, f_i, R_i$ ). 77
- Fig. 4.18: surface topography of Alloy 1 specimens produced by longitudinal turning at the following conditions: (a) ( $doc_2, v_2, R_3, f_1$ ) and (b) ( $doc_2, v_2, R_3, f_3$ ). 78
- Fig. 4.19: effect of cutting parameters on surface roughness for both Ti-alloys at low depth of cut conditions ( $doc_1, v_i, f_i, R_i$ ). 78
- Fig. 4.20: effect of cutting parameters on surface roughness for both Ti-alloys at high depth of cut conditions ( $doc_2, v_i, f_i, R_i$ ). 79
- Fig. 4.21: effect of cutting parameters on surface roughness of Alloy 1 during oblique cutting over the full range of cutting conditions ( $doc_i, v_i, f_i, R_i$ ). 79
- Fig. 4.22: near-surface microstructure of specimens of (a) Ti-6Al-4V (Alloy 1) and (b) Ti-6Al-2Sn-4Zr-6Mo (Alloy 2) machined at ( $doc_2, v_2, f_3, R_3$ ). 80
- Fig. 4.23: hardness distribution below the machined surface of specimens machined at conditions: (a) ( $doc_1, v_2, f_i, R_i$ ) and (b) ( $doc_2, v_i, f_i, R_3$ ). 81

- Fig. 4.24: optimal cutting parameter selection guidelines; contrasting behavioral trends for RS and surface finish: (a, b) Alloy 1 and (c, d) Alloy 2. Condition ( $A_2$ , ( $doc_2$ ,  $v_2$ ,  $f_3$ ,  $R_1$ )) corresponding to the highest compressive RS, cutting force, and MRR is the reference case for normalization. 83
- Fig. 5.1: geometrical aspects and boundary conditions of the thermal analysis FE model. 85
- Fig. 5.2: temperature fields produced by the high intensity moving heat source and corresponding to a peak surface temperature of 850°C for Ti-64 SFTC. 86
- Fig. 5.3: the effect of peak surface temperature  $T_{\text{peak}}$  on stress evolution as a function of depth below the workpiece surface for Ti-64 SFTC: (a)  $T_{\text{peak}} = 950^\circ\text{C}$ , (b)  $T_{\text{peak}} = 850^\circ\text{C}$ , and (c)  $T_{\text{peak}} = 500^\circ\text{C}$ . Stresses are in the  $x$ -direction parallel to the heat source. 89
- Fig. 5.4: comparison of stress distributions along the surface of Ti-64 SFTC for peak temperatures of 500°C and 850°C: (a, b) during heating and (c, d) after cooling to ambient temperature (RS). Stresses are in the  $x$ -direction parallel to the movement of the heat source. 90
- Fig. 5.5: comparison of residual stresses generated by thermal loading with reference to the flow stress behavior under relevant conditions, with (a, b), (c, d), and (e, f) depicting the residual stress profiles and flow stress curves for 52100-53, 52100-62, and Ti64 SFTC, respectively. 92
- Fig. 5.6: ratio of effective to flow stress for 52100-53, 51200-62, and Ti-64 SFTC over the range of investigated peak surface temperatures. The flow stress of 52100 bearing steel accounts for the effect of phase transformation at high temperature. 93
- Fig. 5.7: comparison of (a) thermal expansion coefficient and (b) thermal conductivity and diffusivity for Ti-64 SFTC and bearing steel 52100. 93
- Fig. 5.8: effect of martensitic transformation on the residual stress distribution in 52100 (63 HRC) steel obtained under thermal loading at a peak surface temperature  $T_{\text{peak}} = 890^\circ\text{C}$ . 98

- Fig. 5.9: effect of phase transformation on stress distributions along the surface of 52100 (62 HRC) for  $T_{\text{peak}} = 890^{\circ}\text{C}$ : (a, b) during heating and (c, d) after cooling to ambient temperature (RS). Stresses are in the  $x$ -direction parallel to the movement of the heat source. 100
- Fig. 5.10: setup of the 2D FE model employed for mechanical and thermomechanically coupled simulations of the orthogonal cutting process. 102
- Fig. 5.11: predicted stress evolution at tool positions (a, b) 0.50 mm and (c, d) 1.00 mm during cutting of Ti-64 SFTC with parameters:  $t = 0.12$  mm,  $v = 60$  m/min, and  $r = 20$   $\mu\text{m}$ . The final residual stress distributions along and beneath the machined surface are shown in (e, f). 104
- Fig. 5.12: temperature distributions along the surface of Ti-64 SFTC obtained through thermomechanical analysis at various parameters combinations. 106
- Fig. 5.13: distribution along the surface of Ti-64 SFTC of (a) thermal, (b) mechanical, and (c) thermomechanical stresses. The inserts show the distribution of RS attained after relaxation. 108
- Fig. 5.14: predicted thermally, mechanically, and thermomechanically induced RS in Ti-64 SFTC during high speed machining with:  $t = 0.12$  mm,  $v = 300$  m/min,  $r = 20$   $\mu\text{m}$ ,  $\alpha = 0^{\circ}$ . 110
- Fig. 6.1: flow diagram of the FE simulation of orthogonal cutting for residual stress prediction. 113
- Fig. 6.2: systems approach to the generation of constitutive data and constitutive law identification. 116
- Fig. 6.3: (a) parallel-sided shear zone model [33] and (b) typical distributions of flow stress, strain, strain rate, and temperature from the Distributed Primary Zone Deformation (DPZD) model [90]. 116
- Fig. 6.4: flow stress behavior for both Ti-alloys at  $T = 500^{\circ}\text{C}$  as a function of effective strain and strain rate, as described by: (a) the JC model and (b) the V-JC model. 117

- Fig. 6.5: variation with temperature and effective plastic strain of (a) Alloy 1 flow stress, and (b) flow stress ratio of Alloy 2 to Alloy 1, as described by the Voce-Johnson-Cook (V-JC) model, and for a fixed strain rate of  $10^3 \text{ s}^{-1}$ . 118
- Fig. 6.6: Alloy 1: comparison of force prediction errors over the full range of conditions  $(t_i, v_i)$  obtained with: (a) Zorev's friction model ( $\mu = 0.55$ ) and (b) constant shear friction ( $m = 0.6$ ). 121
- Fig. 6.7: Alloy 1: comparison of RS prediction errors over the full range of conditions  $(t_i, v_i)$  obtained with Zorev's friction model ( $\mu = 0.55$ ) and constant shear friction ( $m = 0.6$ ). 121
- Fig. 6.8: FE model setup and boundary conditions. 123
- Fig. 6.9: comparison between FE predictions and experimentally acquired: (a, b) cutting force ( $F_c$ ) for Alloy 1 and Alloy 2, respectively, and (c, d) thrust force ( $F_t$ ). 125
- Fig. 6.10: percentage errors in FE predictions of (a, b) cutting force ( $F_c$ ) and (c, d) thrust force ( $F_t$ ). 126
- Fig. 6.11: Alloy 1: the dependence of the average predicted temperature at the tool/chip interface,  $T_{int}$ , on: (a) the cutting speed,  $v$ , and (b) the uncut chip thickness,  $t$ . 128
- Fig. 6.12: Alloy 1: effect of cutting speed on temperature predictions at high uncut chip thickness conditions  $(t_3, v_i)$ : (a) temperature distribution at the tool/chip interface and (b) temperature field in the tool, workpiece surface, and the chip. 128
- Fig. 6.13: Alloy 1: predicted temperature distribution in the workpiece surface after a simulated cutting length of 2.5 mm, and under the effect of: (a) uncut chip thickness,  $t$ , at conditions  $(t_i, v_3)$  and (b) cutting speed,  $v$ , at conditions  $(t_3, v_i)$ . 129
- Fig. 6.14: Alloy 1: (a) comparison between FE predictions and experimental measurements of RS and (b) effect of cutting parameters  $(t_i, v_i)$  on predicted residual stress profiles. 130

- Fig. 6.15: Alloy 1: FE residual stress prediction errors over the range of investigated cutting conditions ( $t_i$ ,  $v_i$ ) for dry orthogonal cutting. 130
- Fig. 6.16: Alloy 1: effect of (a) cutting speed,  $v$ , and (b) hone radius,  $r$ , on residual stresses, peak temperature, and the ratio of effective stress to flow stress in the machined surface. 132
- Fig. 6.17: Alloy 1: the effect of cutting speed ( $v$ ) and hone radius ( $r$ ) on the predicted (a, b) temperature distribution and (c, d) stress distribution along the machined surface at a tool position of 1.6 mm within the cutting path for conditions ( $A_1$ , ( $t_3$ ,  $v_i$ )) and ( $A_1$ , ( $t_3$ ,  $v_3$ ,  $r_i$ )). 133
- Fig. 6.18: Alloy 1: the influence of uncut chip thickness on the predicted effective stress field in the cutting zone and in the machined surface. 134
- Fig. 6.19: Alloy 1: effect of uncut chip thickness on the predicted stress distribution along the machined surface at a tool position of 1.6 mm within the cutting path for conditions ( $A_1$ , ( $v_1$ ,  $t_i$ )). 135
- Fig. 6.20: Alloy 2: (a) comparison between FE predictions and experimental measurements of RS and (b) effect of cutting parameters on predicted RS profiles, incorporating the effect of flank wear. 137
- Fig. 6.21: metallographic section of a carbide tool used in dry orthogonal cutting of Alloy 1 at condition ( $t_3$ ,  $v_3$ ): (a) prior to polishing and (b) in the polished state. 137
- Fig. 6.22: (a) sharp tool with edge radius  $r = 10 \mu\text{m}$  adopted in FE simulations for Alloy 1; (b) pre-worn tool with flank wear ( $VB$ ) used in FE simulations for Alloy 2 at high uncut chip thickness. 137
- Fig. 6.23: Alloy 2: effect of flank wear ( $VB$ ) on FE predictions of (a) surface RS and (b) residual stress distribution in the sub-surface layers at condition ( $t_3$ ,  $v_3$ ). 138
- Fig. 6.24: Alloy 2: effect of flank wear ( $VB$ ) at condition ( $t_3$ ,  $v_3$ ) on: (a) the temperature field in the cutting zone and (b) the temperature distribution beneath the machined surface. 139

- Fig. 6.25: comparison between Alloy 1 and Alloy 2 of predicted temperature and effective stress fields in the cutting zone for cutting conditions  $(t_1, v_1)$ . 141
- Fig. 6.26: comparison of FE predictions between Alloy 1 and Alloy 2 at cutting condition  $(t_1, v_1)$  of: (a) effective strain distribution and (b) temperature distribution below the machined surface. 141
- Fig. 7.1: (a, b) metallographically prepared chip of mill-annealed Ti-6Al-4V orthogonally machined with  $(t, v) = (0.15 \text{ mm/rev}, 350 \text{ m/min})$ , with (a) showing typical geometrical features of segmental chips; (c) chip specimen of bimodal Ti-6Al-4V (Alloy 1) obtained at conditions  $(t_3, v_3)$ . 144
- Fig. 7.2: metallographic chip sections produced during orthogonal cutting of bimodal Ti-6Al-4V (Alloy 1) over the full range of investigated cutting parameter combinations  $(t_i, v_i)$ . 146
- Fig. 7.3: variation in (a) peak thickness, (b) tooth pitch, and (c) chip load with cutting parameters during dry orthogonal cutting of Alloy 1. The bars represent variations about the average value. 146
- Fig. 7.4: Alloy 1: FE predictions of the effect of cutting speed on localized temperature distribution along the shear plane in close proximity to the tool tip at conditions (a)  $(t_2, v_i)$  and (b)  $(t_3, v_i)$ . The region of interest is delineated by a steep strain rate gradient and denoted by OA in (c). 148
- Fig. 7.5: Alloy 1; (a, b) flow stress-strain curves for 2 combinations of the C-JC model parameters, in comparison with JC and V-JC curves; the corresponding chip morphology and strain distribution is shown in (c, d) for condition  $(t_3, v_3)$  in contrast with the experimental result. 152
- Fig. 7.6: flow diagram of the FE simulation including the effect of chip morphology. 154
- Fig. 7.7: effect of the critical damage at failure  $C_f$  on the predicted cutting force  $F_c$ , thrust force  $F_t$  and residual stresses (RS), with (a) comparing predicted (FEM) and experimental (Exp) results, and (b) showing the influence of  $C_f$  on FE prediction errors. 156

- Fig. 7.8: Alloy 1: effect of the critical damage at failure  $C_f$  on (a) chip geometry prediction errors and (b) chip morphology and strain distribution, for the cutting condition  $(t_3, v_3)$ . 156
- Fig. 7.9: effect of chip segmentation on force predictions at high speed conditions  $(t_i, v_3)$ , contrasting trends and prediction errors for (a, b) the cutting force and (c, d) the thrust force. 158
- Fig. 7.10: effect of chip segmentation on RS predictions at high speed  $v_3$ , contrasting (a) trends and (b) prediction accuracy. The resulting error range for the investigated cutting regime is given in (c). 159
- Fig. 7.11: predicted (a) temperature and (b) residual stress distributions below the machined surface for Ti-6Al-4V (Alloy 1) at condition  $(t_3, v_3)$  for non-segmental and segmental chip morphologies. 160
- Fig. 7.12: predicted strain distribution (a) along the workpiece surface within the steady-state region and (b) below the machined surface for segmental and non-segmental chip morphology. 162
- Fig. 7.13: FE predictions of (a-d) stress evolution in the workpiece and (e-f) the corresponding crack initiation and propagation sequence at condition  $(t_3, v_3)$  for Ti-6Al-4V (Alloy 1). 162
- Fig. 7.14: predicted cutting ( $F_c$ ) and thrust ( $F_t$ ) force signals for Ti-6Al-4V (Alloy 1) at cutting condition  $(t_3, v_3)$ , and for a critical damage at failure  $C_f = 150$  MPa. 163
- Fig. B.1: near-surface microstructure of longitudinally turned Ti-6Al-4V (Alloy 1) at  $\times 500$  magnification etched with Kroll's reagent. Specimens are oriented parallel to the direction of feed, and were machined at the following cutting conditions: (a)  $(doc_1, f_1, v_2, R_3)$ ; (b)  $(doc_2, f_1, v_2, R_3)$ ; (c)  $(doc_1, f_3, v_2, R_3)$ ; (d)  $(doc_2, f_3, v_2, R_3)$ . 181

Fig. B.2: near-surface microstructure of longitudinally turned Ti-6Al-2Sn-4Zr-6Mo (Alloy 2) at  $\times 500$  magnification etched with Kroll's reagent. Specimens are oriented parallel to the direction of feed, and were machined at the following cutting conditions: (a) ( $doc_1, f_1, v_2, R_3$ ); (b) ( $doc_2, f_1, v_2, R_3$ ); (c) ( $doc_1, f_3, v_2, R_3$ ); (d) ( $doc_2, f_3, v_2, R_3$ ). 182

## LIST OF TABLES

|  |     |
|--|-----|
| Table 4-1: range of cutting parameters for oblique single point turning.   | 57  |
| Table 4-2: investigated range of parameters for orthogonal cutting.  | 58  |
| Table 4-3: effect on forces of increasing depth of cut ( $doc$ ) and feed rate ( $f$ ).  | 67  |
| Table 5-1: approximate predicted values of superficial tensile RS and tensile layer depths for various investigated materials and peak surface temperatures $T_{peak}$ during pure thermal loading.  | 91  |
| Table 5-2: parameter sets for Eq. 5.2 used to model the martensitic transformation from austenite to untempered martensite upon quenching.   | 96  |
| Table 5-3: matrix of the numerical investigation of the influence of process parameters on thermal and mechanical stresses during cutting.   | 101 |
| Table 6-1: Alloy 1: IR measurements for various emissivity values and FE predictions of the maximum temperature in the chip's free surface over the investigated cutting conditions.   | 127 |
| Table 7-1: chip geometry prediction error as a function of the critical damage at failure $C_f$ for Ti-6Al-4V (Alloy 1) and cutting condition ( $t_3, v_3$ ).  | 157 |
| Table A-1: cutting matrices for oblique turning of Ti-6Al-4V (Alloy 1) and Ti-6Al-2Sn-4Zr-6Mo (Alloy 2). Alloy 2 test conditions are shaded. The parameters $doc, v, f$ , and $R$ represent the depth of cut, cutting speed, feed rate and tool corner radius, respectively. | 180 |

# NOMENCLATURE

## Symbols

|             |   |
|-------------|---|
| $a$         | Half contact length   |
| Al          | Aluminum  |
| $A_s$       | Austenite start temperature for steels                      |
| $c$         | Kinematic hardening coefficient                             |
| $C_f$       | Critical damage at failure                                  |
| $C_t$       | Accumulated damage value at time t                          |
| Cl          | Clearance angle for orthogonal cutting tool                 |
| $d$         | Crystal lattice interplanar spacing                         |
| $d_0$       | Stress free interplanar spacing                             |
| $d_\psi$    | Inter-planar spacing for planes oriented at an angle $\psi$ |
| $doc$       | Depth of cut  |
| $e$         | Emissivity  |
| $E$         | Modulus of elasticity                                       |
| $E_p$       | Prediction error  |
| $E_{allow}$ | Allowable error   |
| $f$         | Feed rate   |
| $f_c$       | Segmentation frequency                                      |
| $f_m$       | Volume fraction of martensite                               |
| $f_{IJ}$    | Volume fraction of phase I transformed to phase J           |
| $F_c$       | Oblique cutting force component                             |
| $F_c$       | Orthogonal cutting force component                          |
| $F_f$       | Oblique feed force component                                |
| $F_r$       | Oblique radial force component                              |
| $F_t$       | Orthogonal thrust force component                           |
| $h$         | Isotropic hardening coefficient                             |
| $h_c$       | Heat transfer coefficient                                   |

|          |   |
|----------|---|
| $HNO_3$  | Nitric acid                             |
| $k_s$    | Local shear flow stress                 |
| $KT$     | Crater depth                            |
| $l_c$    | Tool/chip contact length                |
| $L$      | Oblique cutting length                  |
| $L$      | Orthogonal cutting length               |
| $L_0$    | Undeformed surface length               |
| $L_p$    | Chip segmentation pitch                 |
| $L_s$    | Distance of tooth glide or slip         |
| $L_{SB}$ | Distance between shear band centers     |
| $m$      | Shear friction coefficient              |
| $M_s$    | Martensite start temperature for steels |
| $n$      | Order of diffraction                    |
| $P$      | Laser power                             |
| $p(s)$   | Normal distributed load                 |
| $q(s)$   | Tangential distributed load             |
| $r$      | Tool edge radius (hone radius)          |
| $R$      | Tool corner radius                      |
| $Rsq$    | Coefficient of determination            |
| $R_T$    | Thermal constriction coefficient        |
| $s$      | Integration variable                    |
| $S_{kl}$ | Deviatoric stress tensor                |
| $SiC$    | Silicon carbide                         |
| $SiO_2$  | Colloidal silica                        |
| $Sn$     | Tin                                     |
| $t$      | Uncut chip thickness                    |
| $t_{on}$ | Laser "on" time                         |
| $t_p$    | Peak chip thickness                     |
| $t_v$    | Valley chip thickness                   |
| $T_{in}$ | Internal specimen temperature           |

|                        |  |
|------------------------|--|
| $T_{\text{int}}$       | Tool/chip interface temperature                                |
| $T_{\text{out}}$       | External specimen temperature                                  |
| $T_{\text{peak}}$      | Peak surface temperature                                       |
| $T_{\beta}$            | Beta transus for titanium alloys                               |
| <i>Ti-64</i>           | Ti-6Al-4V  |
| <i>Ti-6246</i>         | Ti-6Al-2Sn-4Zr-6Mo   |
| <i>TiC</i>             | Titanium carbide   |
| $T$                    | Instantaneous temperature                                      |
| $T_0$                  | Ambient temperature  |
| $T_{\text{melt}}, T_m$ | Melt temperature of the material                               |
| $T_r$                  | Room temperature   |
| $Ti$                   | Titanium   |
| $u_y$                  | Standard deviation   |
| $U$                    | Expanded uncertainty   |
| $v$                    | Oblique cutting speed  |
| $v$                    | Orthogonal cutting speed                                       |
| VB                     | Flank wear   |
| VB <sub>B</sub>        | Flank wear in the straight edge of the cutting tool            |
| VB <sub>C</sub>        | Flank wear within the corner radius region of the cutting tool |
| VB <sub>N</sub>        | Depth of cut notch wear  |
| $V$                    | Vanadium   |
| $w$                    | Width of cut   |
| <i>WC</i>              | Tungsten carbide   |
| $Y$                    | Measurand  |
| $y_m$                  | Measurement result   |
| $Zr$                   | Zirconium  |
| $\alpha_r$             | Rake angle for orthogonal cutting tools                        |
| $\alpha_{ij}$          | Back deviatoric stress tensor                                  |
| $\alpha_T$             | Coefficient of thermal expansion                               |

|                                |   |
|--------------------------------|---|
| $\delta_{kl}$                  | Kronecker delta                                       |
| $\bar{\varepsilon}$            | Effective plastic strain                              |
| $\dot{\bar{\varepsilon}}$      | Effective plastic strain rate                         |
| $\dot{\bar{\varepsilon}}_0$    | Effective reference plastic strain rate               |
| $\bar{\varepsilon}_f$          | Effective strain at failure                           |
| $\varepsilon_{ij}$             | Strain tensor   |
| $\varepsilon_\psi$             | Lattice strain for plains oriented at an angle $\psi$ |
| $\theta$                       | Diffraction angle                                     |
| $2\theta$                      | Bragg's angle   |
| $\bar{\theta}_T$               | Mean tool face temperature                            |
| $\theta_s$                     | Angle of segmented tooth slip                         |
| $\lambda$                      | Wavelength of beam of x-rays                          |
| $\mu$                          | Sliding friction coefficient                          |
| $\nu$                          | Possion's ratio                                       |
| $\bar{\sigma}$                 | Effective stress                                      |
| $\bar{\sigma}_0$               | Current material yield stress                         |
| $\sigma_f$                     | Flow stress   |
| $\sigma_n$                     | Normal stress on the tool rake face                   |
| $\sigma_{ij}$                  | Cauchy stress tensor                                  |
| $\sigma_{mm}$                  | Hydrostatic stress tensor                             |
| $\sigma_\phi$                  | Surface residual stress measured by XRD               |
| $\sigma_1, \sigma_2, \sigma_3$ | Principal stresses                                    |
| $\sigma^*$                     | Maximum principal stress in tension                   |
| $\tau_f$                       | Shear stress on the tool rake face                    |
| $\phi$                         | Orientation angle from principal axes during XRD      |
| $\psi$                         | Angle of tilt of XRD specimen                         |

## Abbreviations

|                      |   |
|----------------------|---|
| A1 or A <sub>1</sub> | Alloy 1   |
| A2 or A <sub>2</sub> | Alloy 2   |
| AISI                 | American Iron and Steel Institute                         |
| ASTM                 | American Society for Testing and Materials                |
| CBN                  | Cubic Boron Nitride                                       |
| C & L                | Cockroft & Latham   |
| CRIAQ                | Consortium of Research and Innovation in Aerospace Quebec |
| C-JC                 | Calamaz-Johnson-Cook                                      |
| DPZD                 | Distributed Primary Zone Deformation                      |
| DRX                  | Dynamic recrystallization                                 |
| EDM                  | Electric discharge machining                              |
| <i>F</i>             | Finishing   |
| FE                   | Finite element  |
| FEM                  | Finite element modeling                                   |
| Emp                  | Empirical results   |
| Exp                  | Experimental results                                      |
| IR                   | Infrared  |
| ISO                  | International Organization for Standardization            |
| JC                   | Johnson-Cook  |
| HRc                  | Hardness Rockwell   |
| HT                   | High temperature  |
| HV                   | Hardness Vickers  |
| LAM                  | Laser-assisted machining                                  |
| NDT                  | Non-destructive testing                                   |
| NIST                 | National Institute of Standards and Technology            |
| NRC                  | National Research Council Canada                          |
| NSM                  | Near-surface microstructure                               |
| PSZ                  | Primary shear zone  |
| RS                   | Residual stresses   |
| RSM                  | Residual stress measurement                               |

|      |   |
|------|---|
| RT   | Room temperature                            |
| SF   | Semi-finishing                              |
| SFTC | Scientific Forming Technologies Corporation |
| SHPB | Split Hopkinson Pressure Bar                |
| SMM  | Structures, Materials, and Manufacturing    |
| V-JC | Voce-Johnson-Cook                           |
| WL   | White layer                                 |
| XRD  | X-ray diffraction                           |

# CHAPTER 1 INTRODUCTION

## 1.1 The significance and impact of residual stresses

Residual stresses (RS) are stresses that remain in a stationary body at equilibrium after the external loads have been removed. They constitute a critical aspect of surface integrity. In general, surface integrity refers to the enhanced or unimpaired nature of a surface. It involves several superficial and sub-surface characteristics including surface roughness, plastic deformation, crack formation, residual stresses, and metallurgical changes. Surface integrity is one of the most important outputs of a machining operation and has a direct impact on the performance and durability of machined components [1].

The functional behavior of an engineering component is controlled by the properties of its near-surface layer. Sharp plastic deformation gradients that arise during the machining process lead to the formation of RS. This is primarily due to incompatibilities that develop between the near surface and the sub-surface material [2, 3]. In safety-critical industries such as the transportation, chemical, nuclear, and aerospace industries, RS are of great concern. Their presence can lead to the premature failure of parts and structures. However, if process conditions are intelligently controlled, RS can be exploited in the production of parts with improved damage resistance.

Residual stresses can alter the dynamic strength and chemical resistance of materials. They have a major influence on fatigue life and constitute a potential source of progressive failure that should not be ignored. Progressive failure can take place through several mechanisms including fatigue and stress-corrosion cracking [4, 5]. Tensile RS undermine fatigue and stress-corrosion cracking resistance. Their presence accelerates crack nucleation, crack propagation, and corrosion reactions, thereby shortening the fatigue life of dynamically stressed components operating in harsh environments. Furthermore, tensile RS can amplify the mean stress encountered over a fatigue cycle. At large mean stress levels, static fracture may even be triggered [6]. On the other hand, compressive RS are beneficial to fatigue life. Their presence enhances fatigue strength and increases the number of cycles to failure. As free surfaces constitute preferential sites for crack initiation, substantial gains can be achieved by introducing compressive RS in the near-surface layer of engineering components [2, 6].

## 1.2 Research motivation and terminal objectives

With increasing environmental concerns, the global drive for fuel efficiency and lower gas emissions is on the rise, especially in industries such as aerospace, automotive and transport. This requires less conservative designs that promote higher efficiency and weight reduction. Ever more stringent cost efficiency, reliability, and performance requirements necessitate the continual development and use of advanced lightweight materials that are increasingly more difficult-to-machine. Even with the advent of rapid manufacturing methods such as metal powder processing, it is most often through machining that the final geometrical size and tolerance of mechanical components are imparted.

Difficult-to-machine materials such as titanium alloys, nickel-based superalloys, stainless steels, and alloy steels used in the aerospace, automotive, chemical, and nuclear industries can be prone to tensile RS. Post-machining surface treatment procedures such as shot peening and induction hardening can be implemented to induce fatigue-inhibiting compressive RS in the surface of a part or to counterbalance existing tensile stresses. Nevertheless, such processes are difficult to integrate into the machining setup and often require customized equipment for a variety of part shapes and sizes. They constitute an independent processing stage requiring additional expense.

Consequently, accurate knowledge of residual stress distribution in machined specimens is of vital importance. Where stringent restrictions on surface roughness are in effect, as is the case for aero-engine parts, a finishing operation is often required. Therefore, residual stresses induced during the final finishing operation are of particular significance [1]. It is crucial to identify favorable machining parameters, tool geometry, and lubrication methods that promote compressive RS without compromising surface condition. Rough surfaces, machining artefacts, or material impurities are stress concentration sites. They promote crack nucleation at a significantly reduced number of cycles. They also constitute areas where residual stresses are extremely potent. Tensile RS developed in these areas can intensify applied loads and accelerate the onset of fracture [2].

As a result, residual stresses (RS), surface finish, and the near-surface microstructure (NSM) constitute critical acceptance criteria for aero-engine parts subjected to dynamic loads in harsh operating environments. These include fan and compressor disks and blades made from  $\alpha/\beta$  Ti-alloys.

Cutting experiments followed by in-depth profile measurements of RS are associated with long durations and high costs. This is compounded by the destructive nature of in-depth measurement methods. Models that provide accurate residual stress predictions would be of great benefit to safety-critical industries such as aerospace. Prior knowledge of machining-induced RS will enable the accurate prediction of fatigue life in the design stage, thereby greatly diminishing the need for cutting experiments while guaranteeing part longevity, structural integrity, and safety.

Limited information is available in the open literature on machining-induced RS in Ti-alloys, especially in the finish cutting regime. The terminal objectives of the research are: (1) to investigate the effect of cutting parameters and tool geometry on machining-induced RS in  $\alpha/\beta$  Ti-alloys at finish cutting conditions relevant to real production and to establish a correlation between RS and surface quality, (2) to study the role of the main contributors to residual stress formation during cutting, and (3) to develop FE and empirical models for RS prediction, where empirical models will allow frequent and accurate predictions during production, and where FE models will serve as a virtual investigative machining medium, wherein further insight into residual stress formation can be gained by analysing the evolution of state variables that are otherwise extremely difficult to measure.

This work is part of a comprehensive CRIAQ-funded research project driven by Pratt & Whitney Canada in partnership with McGill University and the National Research Council Canada (NRC).

### **1.3 Thesis outline**

To achieve the desired objectives, a methodology is adopted that combines experimental, FE modeling, and empirical modeling techniques. The research is focused on two aero-engine grade  $\alpha/\beta$  Ti-alloys, Ti-6Al-4V (Ti-64) and Ti-6Al-2Sn-4Zr-6Mo (Ti-6246). Material identification, together with FE model calibration and validation are based on orthogonal cutting tests. An extensive experimental investigation of residual stresses and surface integrity during finish turning is performed using the oblique single point turning process. An outline of the thesis is given below, together with a brief description of the areas addressed in each chapter:

❖ Chapter 1: Introduction

The significance of residual stresses (RS) and their impact on the fatigue resistance of engineering components and structures is introduced. The motivation behind the research is then elaborated, and its terminal objectives are presented.

❖ Chapter 2: Critical Literature Review

The outcomes of a critical literature review on machining-induced RS are discussed, followed by a gap analysis and a detailed description of the research objectives.

❖ Chapter 3: Experimental Setup

A detailed description is provided of the experimental setup used to achieve the research objectives. This includes orthogonal cutting (material identification, FE model calibration, and FE model validation) and oblique turning. The experimental procedure of the extensive oblique single point turning experiment is also elaborated. The techniques employed in the measurement and evaluation of key performance indicators and essential attributes of surface integrity are explained.

❖ Chapter 4: Experimental Results

The design of experiment adopted for orthogonal cutting and oblique single point turning tests is introduced, followed by a detailed discussion of the experimental results. The effect of cutting parameters and material properties on cutting performance indicators (machining forces and tool wear) and surface integrity attributes (residual stresses, surface roughness, hardness distribution, and near-surface microstructure) is discussed. Empirical models developed for cutting force and residual stress prediction during finish turning are evaluated. Guidelines are provided for the optimal selection of oblique turning parameters that promote desirable combinations of RS and surface finish.

❖ Chapter 5: Fundamental Aspects of Residual Stress Formation During Cutting

A numerical investigation is performed for standard non-proprietary grade 5 titanium alloy (Ti-64) and bearing steel AISI 52100. The significance and contribution of thermal and mechanical loads to RS is studied using FEM. The effect of phase transformations is addressed for the bearing steel at thermally dominant conditions.

The impact of material properties and cutting parameters on the imbalance between thermally and mechanically generated stresses during machining is discussed.

❖ Chapter 6: FE Model Development and Results

The development and optimization of a 2D FE model for the prediction of machining-induced RS is discussed in detail. Important aspects of model development are addressed including material identification, tool/chip interface interactions, as well as meshing and geometrical aspects. The model is then validated against experimental results. The effect of cutting parameters, tool wear, and material properties on RS is discussed thoroughly based on knowledge acquired from the FE model.

❖ Chapter 7: Chip Segmentation in Ti-6Al-4V and its Effect on FE Predictions

Chip segmentation in Ti-6Al-4V is characterized. The governing segmentation mechanism and the effect of cutting parameters on chip morphology are analysed based on experimental observations. A ductile fracture criterion is implemented to model chip segmentation at relatively high conventional speeds. This is followed by a detailed discussion of the mechanism by which chip segmentation influences FE predictions of RS, specifically at relatively high speeds within the conventional range.

❖ Chapter 8: Conclusions and Recommendations

The main findings of the research are summarized, and recommendations are made for future work based on the research findings, foreseeable trends, and the requirements of the aerospace industry.

# CHAPTER 2 CRITICAL LITERATURE REVIEW

## 2.1 Nature and origins of residual stresses

Residual stresses (RS) can be distinguished by the length scale  $l_0$  over which they stabilize or equilibrate. They can be classified into long range macrostresses and short range microstresses. Macrostresses are often referred to as type I stresses. These stresses stabilize over a length scale  $l_{0, I}$  that is large relative to the grain size of the material and represents a considerable fraction of the workpiece specimen (Fig. 2.1) [3, 6].

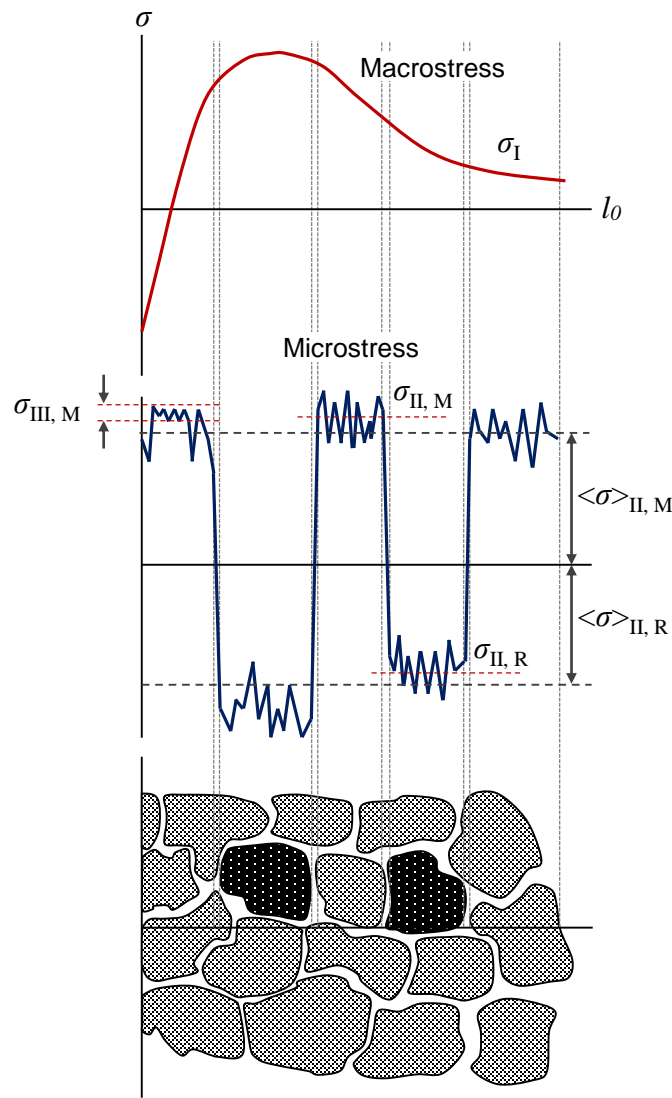


Fig. 2.1: categorization of residual stress fields adapted from [6]. M and R represent the matrix and reinforcements, respectively, and  $\langle \sigma \rangle$  denotes the average stress value over the sampling volume.

Macro stresses are tensor quantities whose magnitudes vary with direction at a single point within a body. They are produced by a vast array of metal forming, machining, joining and heat treatment processes and are of major interest to engineering design and failure analysis. Micro stresses arise due to imperfections in the crystal lattice [7]. As shown in Fig. 2.1, they can be further subdivided into stresses that vary over the grain scale (type II) or the atomic scale (type III). Type II stresses are intergranular. They stabilize over a distance equivalent to the size of several grains ( $l_{0, II} = 3-10 \times \text{grain size}$ ). Low level type II stresses are always present in polycrystalline materials due to varying elastic and thermal properties between differently oriented neighboring grains. Multiphase materials are susceptible to more significant type II stresses. Elevated mean phase stresses ( $\langle \sigma_{II} \rangle$ ) resulting from uneven partitioning of applied loads can significantly influence the performance of composite materials. Phase transformations also constitute a source of higher level type II stresses. Type III stresses exist over atomic dimensions and equilibrate within a grain ( $l_{0, III} < \text{grain size}$ ). Dislocations and point defects are typical sources of type III stresses.

The thesis is primarily concerned with characterizing the behavior of macro stresses resulting from the machining process. Consequently, the means by which macro stresses are generated will be discussed in further detail. In addition, any reference made to RS in what follows is exclusive to macro stresses. Macro stresses can be generated by interactions between misfitting components in an engineering assembly. In addition, they can arise due to the formation of mechanically, thermally, or chemically induced misfits between different regions within a single engineering component.

Varying residual stress distributions can be induced within a part by mechanical processing or cold working due to non-uniform plastic deformation. For instance, during drawing, high reductions in cross section promote the development of tensile RS in the near-surface layer, while subsequent drawing with very small reductions in area generate compressive RS. Similar results are obtained through roller burnishing or shot peening. These are mechanical methods adopted to improve the fatigue resistance of parts by the deliberate generation of compressive residual stresses [1, 2].

Thermally induced residual stresses can arise during routine operation, thermomechanical processing, and heat treatment. Engineering assemblies comprising various materials with different thermal properties and operating at varying temperatures

often experience stresses induced by thermal misfits. During processing and heat treatment, residual stress distributions depend mainly on the extent of heat localization and the associated thermal gradients. In addition, phase transformations can significantly alter the stress distribution. Welded joints are highly susceptible to RS and phase transformations due to severe thermal gradients during localized heating and cooling [2, 3].

Chemical treatments such as nitriding of steels are often employed to induce a beneficial compressive stress state in a component's near-surface layer. The process involves the diffusion of nitrogen into the base steel, producing a thin case (0.25 to 0.5 mm in depth) of high hardness with improved wear and corrosion resistance. The formation of nitrides in the surface is coupled with an increase in volume. Thus, the surface remains in a state of compressive RS due to chemically induced misfits [1-3].

### 2.1.1 Residual stresses formation during machining

Machining is a thermomechanical process during which a thin layer of material is removed from the surface of a part by plastic deformation in the form of a chip. Deformation takes place in three shear zones as shown in Fig. 2.2: (i) the primary shear zone, where the bulk of the plastic deformation occurs, (ii) the secondary shear zone at the tool/chip interface, and (iii) the tertiary shear zone at the tool/workpiece interface. During machining, plastic deformation is almost completely transformed into heat. The workpiece surface is deformed under the action of mechanical loads generated by chip formation, as well as thermal loads arising from plastic deformation and friction in the shear zones.

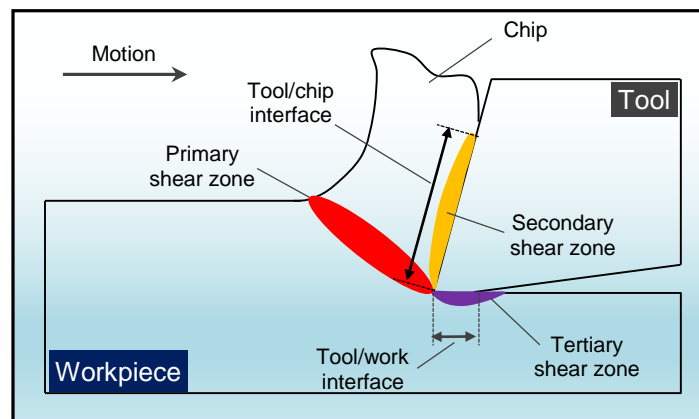


Fig. 2.2: idealized 2D model of the machining process.

The intensity of thermomechanical loading diminishes heavily with depth beneath the machined surface, resulting in severe plastic deformation gradients. When the tool is retracted, stress relaxation takes place as the workpiece cools down to ambient temperature in the absence of external loads. Residual stresses (RS) are generated due to severe incompatibilities that arise between the machined surface and the underlying layers.

Machining-induced RS is attributed to three main sources: (i) mechanical loads, (ii) thermal loads, and (iii) phase transformations. During machining, the mechanical and thermal sources are always in existence. Depending on the extent of deformation and temperature rise, phase transformations can occur that contribute to residual stress formation. Thus, there is a constant interaction between mechanical, thermal, and metallurgical impacts. It is, therefore, difficult to correlate residual stress formation to a single source. In general, plastic deformation that is predominantly thermal promotes tensile RS due to non-uniform thermal expansion, especially since heat generation is localized in a thin surface layer. In contrast, plastic deformation that is predominantly mechanical can lead to compressive RS depending on the extent of material burnishing following chip formation [2].

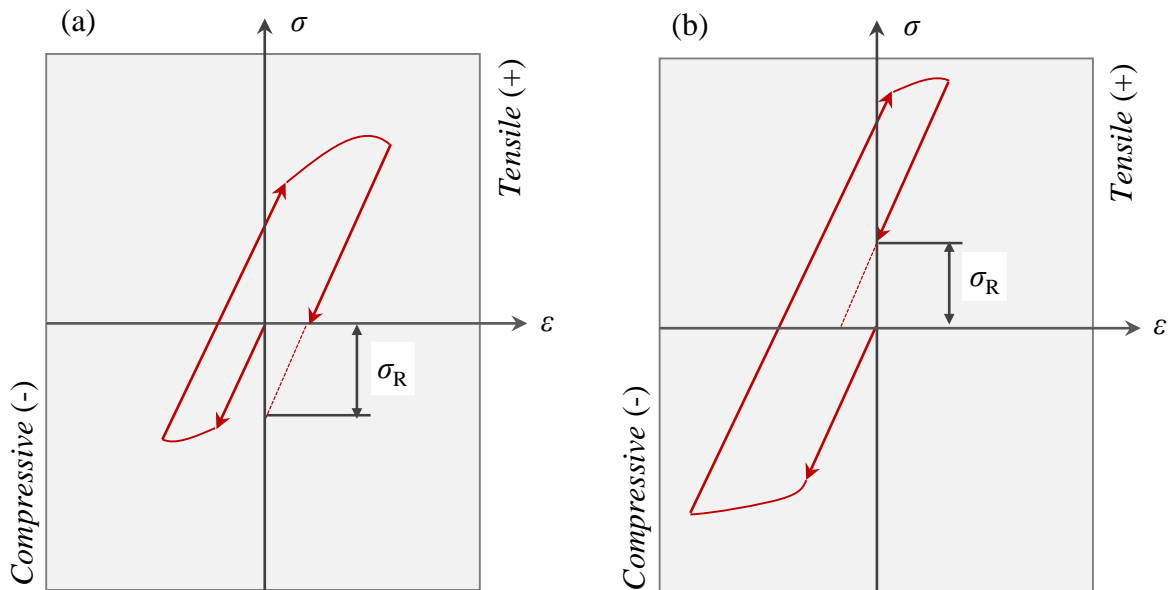


Fig. 2.3: residual stresses  $\sigma_R$  generated during (a) a predominantly tensile loading cycle with a high extent of burnishing following chip formation and (b) a predominantly compressive loading cycle.

During cutting, material in the vicinity of the tool tip is firstly deformed in compression when ahead of the cutting edge. It is then partially ploughed beneath the tool and plastically deformed in tension (burnished) as the tool moves further away. The extent of burnishing determines whether the deformation is mostly compressive or tensile. A predominantly tensile loading cycle leads to compressive RS (Fig. 2.3a), whereas tensile RS are generated by a predominantly compressive cycle (Fig. 2.3b) [2, 8].

Analytical studies of the origins of residual stresses during machining and the relative contributions of thermal and mechanical loads are mainly focused on the grinding process [9-17]. During grinding, the workpiece surface can be prone to large magnitudes of tensile RS due to the high intensity of heat generated by the process. The energy required to remove a unit volume of metal is much higher than other chip formation processes such as turning and milling as grinding produces chips that are considerably smaller in size [11]. Mahdi et al. [12] found that the contributions of thermal and mechanical loads to plastic deformation vary depending on the ratio of the peak normal load to the material's yield stress ( $P_a/Y$ ). At ratios below 0.5, thermally induced plastic deformation was dominant. Under such conditions, increasing the mechanical load had a small effect on the onset of plastic deformation. At ratios exceeding 2, mechanically induced deformation was dominant. Under such conditions, the increase in heat flux intensity had very little effect on the onset of plastic deformation. Furthermore, RS were influenced by the surface traction profile. To generate compressive RS, a down-grinding operation was recommended with a small depth of cut and sufficiently large ratios of horizontal to normal loads.

Conflicting views exist over the relative contribution of mechanical and thermal loads to RS during cutting. Lin et al. [18] concluded that RS are mainly the result of mechanical loading, which is in agreement with the findings by Liu and Barash [19-21]. However, Okushima and Kakino [22] found that thermal loading is more dominant at cutting speeds exceeding 50 m/min.

It is concluded from the above that thermal loads can be harmful as they promote highly undesirable tensile RS. The vulnerability of a material to thermally generated plastic deformation, however, is largely determined by its physical and thermal properties. The state and magnitude of machining-induced RS is essentially controlled by the conflicting effects of strain hardening and thermal softening of the workpiece material during cutting. This

behavior is dictated by the cutting parameters, cutting edge condition, and lubrication methods. Cutting parameters can influence both thermal and mechanical aspects of residual stress formation. For example, blunt cutting tools with honed edges can have a mixed influence on RS. Increased friction due to a larger area of contact with the workpiece can elevate the temperatures in the cutting zone, promoting tensile RS. On the other hand, a larger extent of plastic deformation in tension behind the cutting edge due to intensified burnishing can increase compressive RS. A deeper understanding is, therefore, required of the effect of cutting parameters and material properties on the mechanical, thermal, and metallurgical contributions to RS during cutting.

## **2.2 The determination of machining-induced residual stresses**

Several approaches exist to the determination of machining-induced RS. These are discussed below together with the advantages and disadvantages of each. A complete characterization of residual stress behavior for a particular workpiece/tool material combination often requires a hybrid approach that comprises more than one method.

### **2.2.1 Experimental investigation**

Experimental investigations have been extremely valuable in identifying the dominant factors and mechanisms influencing machining-induced RS. The experimental approach allows the correlation of RS to process parameters, cutting performance indicators, and other aspects of surface integrity. However, it is associated with high equipment and material costs, destructive residual stress measurement (RSM) methods, and long durations.

#### *2.2.1.1 Residual stress measurement methods*

Several techniques are available for residual stress measurement (RSM) with varying penetration depths and spatial resolution. These can be classified into mechanical, diffraction, ultrasonic, and electromagnetic techniques. A comprehensive review is given in [6].

Mechanical methods such as curvature, deflection, compliance, and hole drilling are inevitably destructive. The equilibrium is disturbed by the removal of material, and RS are estimated from the resulting deformation in the remaining part. Deformation is measured as a function of depth with strain gages, mechanical inductive sensors, or interferential methods. Mechanical methods are suitable for the determination of macrostresses (type I) over large depths. They are, however, restricted to simple geometries and are limited by assumptions

regarding the nature of the residual stress field. In addition, further RS can be introduced during material removal that can lead to measurement errors.

Electromagnetic methods measure stress dependent changes in electrical conductivity and magnetic properties. They are, however, limited to ferromagnetic materials. Ultrasonic methods capture stress related changes in the propagation of ultrasound. Although they can determine type I, II and III stresses in very short times, both techniques have restricted applications. Test results are influenced by microstructure, composition, texture, grain size, density, temperature, as well as electrical and magnetic properties. In addition, these techniques require stress free samples that are otherwise identical to the specimen under investigation. At their current state of development, they are generally not suitable for routine residual stress measurements.

The x-ray diffraction technique (XRD) is the most commonly applied method for residual stress measurement due to its high state of development and its superior spatial and depth resolution [7]. Unlike mechanical methods that measure deformation on a macroscopic scale, XRD measures strains in the crystal lattice at the atomic level. Bragg's Law forms the fundamental basis of x-ray diffraction theory and is given by [7, 23, 24]:

$$n\lambda = 2d \sin \theta \quad (2.1)$$

where  $\lambda$  is the wavelength of a beam of x-rays impinging at an angle  $\theta$  on a crystal with inter-planar spacing  $d$ . The order of diffraction is denoted by the integer  $n$ . Bragg's law describes the conditions that lead to constructive interference resulting in a peak in diffraction intensity. The diffraction angle  $2\theta$  at which this occurs is called the Bragg angle.

In XRD, the inter-planar spacing often termed the  $d$ -spacing is used as a strain gage. The lattice strain for planes oriented at an angle  $\psi$  to the surface is defined as:

$$\varepsilon_{\psi} = \frac{\Delta d}{d_0} = \frac{d_{\psi} - d_0}{d_0} \quad (2.2)$$

where  $d_0$  is the stress free inter-planar spacing. In a stress free state, no change in inter-planar spacing is observed in grains of various orientations (Fig. 2.4a). Under the action of stress, crystallographic planes oriented at various angles  $\psi$  to the surface will undergo varying changes in  $d$ -spacing, producing differing shifts in the diffraction angle  $2\theta$ . If for instance the stress is tensile (Fig. 2.4b), planes oriented at  $\psi = 90^\circ$  experience an increase in  $d$ -spacing

leading to a negative shift in the diffraction angle. However, planes oriented at  $\psi = 0^\circ$  undergo a decrease in  $d$ -spacing due to Poisson contractions, causing a positive shift in the diffraction angle.

In XRD, a monochromatic beam of x-rays is impinged on the surface of a polycrystalline specimen (Fig. 2.4c). The specimen is tilted at several angles  $\psi$ , and the shift in diffraction peaks is measured for grains at various orientations to the surface. The corresponding values of inter-lattice spacing  $d_\psi$  are then calculated from Eq. 2.1. Although they are caused by non-uniform plastic deformation, residual macrostresses remaining after deformation are elastic in nature. A condition of plane stress is assumed in the exposed surface of the measured specimen (Fig. 2.5). The stress state consists of in-plane principal stresses  $\sigma_1$  and  $\sigma_2$ , with the normal principal stress  $\sigma_3 = 0$ . The normal strain component  $\varepsilon_3$  does not vanish due to Poisson contractions imposed by the in-plane stresses. The elastic strain  $\varepsilon_{\phi\psi}$  in a direction defined by the orientation angles  $\phi$  and  $\psi$  is given by:

$$\varepsilon_{\phi\psi} = \left[ \left( \frac{1+\nu}{E} \right) \sigma_\phi \sin^2 \psi \right] - \left[ \left( \frac{\nu}{E} \right) (\sigma_1 + \sigma_2) \right], \quad (2.3)$$

where  $E$  and  $\nu$  are the modulus of elasticity and Poisson's ratio of the material, respectively. By substituting Eq. 2.2 into Eq. 2.3, the fundamental relationship between the inter-planar spacing  $d_{\phi\psi}$  and the bi-axial stresses in the surface of the specimen is obtained:

$$d_{\phi\psi} = \left[ \left( \frac{1+\nu}{E} \right) \sigma_\phi d_0 \sin^2 \psi \right] - \left[ \left( \frac{\nu}{E} \right) d_0 (\sigma_1 + \sigma_2) + d_0 \right] \quad (2.4)$$

It is evident from Eq. 2.4 that the inter-planar spacing  $d_{\phi\psi}$  is a linear function of  $\sin^2 \psi$ . Following experimental measurements of the inter-planar spacing at several tilt angles  $\psi$ , a line is fitted into the results using linear regression. The slope of the line is then estimated, and the surface residual stress  $\sigma_\phi$  is obtained as follows:

$$\sigma_\phi = \left( \frac{E}{1+\nu} \right) \left( \frac{1}{d_0} \right) \left( \frac{\delta d_{\phi\psi}}{\delta \sin^2 \psi} \right) \quad (2.5)$$

This approach is called the  $\sin^2 \psi$  method. Through multiple exposures at more than 2 values of  $\psi$ , the linear dependence of the  $d$ -spacing on  $\sin^2 \psi$  can be verified, and the suitability of

the XRD method for the specimen under evaluation can be confirmed. The quantity  $E/(1+\nu)$  is termed the x-ray elastic constant of the material. It is determined empirically by measuring deflections produced by known loads in four-point bending tests.

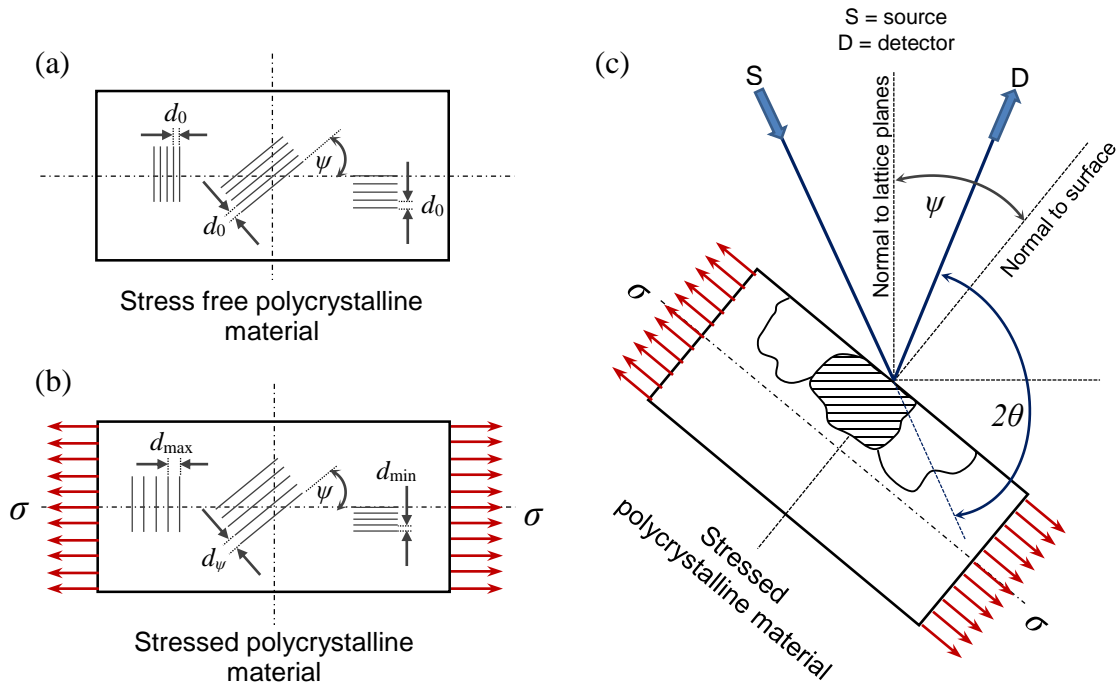


Fig. 2.4: (a) uniform inter-lattice spacing ( $d$ -spacing) in a stress free state, (b) varying  $d$ -spacing under tensile stress, and (c) schematic of the x-ray diffraction (XRD) measurement technique.

Figures are adapted from Prevey [7] and Brinksmeier et al. [2].

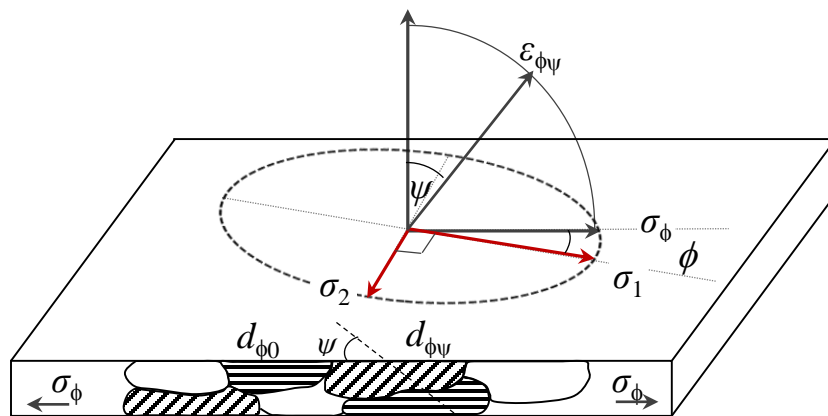


Fig. 2.5: plane stress elastic model adopted in x-ray diffraction theory adapted from Prevey [7].

Due to the shallow penetration depth of x-rays (5-20  $\mu\text{m}$ ), macrostresses (type I) and microstresses (type II and III) can be measured as a function of depth with a resolution orders of magnitude higher than that achievable by other techniques. Consequently, XRD is a suitable method to determine stress distributions with severe gradients.

A disadvantage of the x-ray diffraction technique is that it is limited to fine grained polycrystalline materials that are not severely textured. Non-destructive testing is only possible for a shallow surface layer not exceeding 25  $\mu\text{m}$ . Measurement of in-depth stress distributions requires material removal by electro-polishing and is inherently destructive.

## **2.2.2 Modeling of the machining process**

### *2.2.2.1 Empirical modeling*

Although empirical methods do not offer physical scientific insight into the formation of residual stresses, it is often argued that they are more accurate than analytical and numerical approaches, mainly due to the shortcomings of plasticity theory and to the lack of a complete solution that takes all contributing factors to machining-induced RS into account. Furthermore, analytical and numerical approaches require the knowledge of certain material properties that are not readily available, and which have to be determined experimentally [25]. Empirical models are therefore useful for frequent use in product and process development, especially that they are much faster to compute and require a significantly lower level of expertise in comparison to FE models.

On the other hand, empirical models are heavily reliant on cutting experiments and residual stress measurements, and are thus associated with an extreme cost disadvantage. Moreover, they are non-generic, cannot be extrapolated, and are only accurate over the investigated parameter range.

Experimental designs based on response surface methodology have been used in the development of empirical models for RS generated during milling [26, 27]. A range of commercially available alloys including steel, brass, and aluminium were addressed. Empirical models were also developed for the milling of Ti-alloy IMI 834 of nominal composition Ti-5.8Al-4.5Sn-4Zr-0.7Nb-0.5Mo-0.40Si-0.06C based on factorial analysis [28]. Deterministic functions have been employed to express RS in terms of cutting parameters and their mutual interactions. Two main approaches to empirical modeling of RS were identified in the open literature.

### *Empirical prediction of the peak magnitude of RS*

The first approach [26-28] is concerned with determining the peak magnitude of RS in the near-surface layer of the material. In a factorial design [28], the peak residual stress is expressed as a linear polynomial in terms of cutting parameters and their mutual interactions. Response surface methodology [26, 27] postulates that the peak residual stress can be expressed as a second degree polynomial in terms of process variables and their mutual interactions:

$$\sigma = b_0 + \sum_{i=1}^n b_i x_i + \sum_{j=1}^n b_{jj} x_j^2 + \sum_{i<j} b_{ij} x_i x_j, \quad (2.6)$$

where  $x_i$ ,  $x_j^2$ , and  $x_i x_j$  represent the process variables, their quadratic effects, and the linear interactions between them, respectively; and  $b_0$ ,  $b_i$ ,  $b_{jj}$ , and  $b_{ij}$  are the polynomial coefficients. The coefficients of the quadratic polynomial are determined using curve fitting techniques based on experimentally measured residual stress profiles.

### *Empirical prediction of the residual stress profile*

The second approach [25, 29] aims at predicting the residual stress distribution as a function of depth beneath the machined surface. It postulates that RS can be expressed as a polynomial function of the depth  $z$  beneath the surface whose coefficients are a function of process variables and mutual interactions between them:

$$\sigma_i = c_{0i} + c_{1i}z + c_{2i}z^2 + c_{3i}z^3 + \dots + c_{ni}z^n, \text{ where } i = 1, 2, 3, \text{ and} \quad (2.7)$$

$$c_{li} = b_{0li} + \sum_{j=1}^m b_{jli} x_j + \sum_{j=1}^m \sum_{k=1}^m b_{jkli} x_j x_k, \text{ where } l = 0 \dots n \text{ and } j < k \quad (2.8)$$

where  $c_l$  represents the stress polynomial coefficients;  $x_j$  and  $x_j x_k$  are the process variables and linear interactions between them, respectively, and  $b_0$ ,  $b_j$ , and  $b_{jk}$  are the coefficients of  $c_l$ . It was shown that a fifth order polynomial is required for an accurate representation of the residual stress distribution [25, 29]. Mittal and Liu [25] adopted a refined expression for RS by substituting the depth beneath the surface in Eq. 2.7 with its natural logarithm.

#### 2.2.2.2 Analytical modeling

Analytical models of machining-induced residual stresses are a useful alternative to computationally heavy numerical models as they are more practical to run and much faster to compute, and hence, can be potentially integrated into process optimization tools that are significantly important from an industrial perspective. Their main disadvantage is that they cannot model the full scope of mechanisms contributing to RS during machining. Although they do offer physical insight to the formation of RS, their closed mathematical form imposes limits in terms of in-depth scientific analysis of the causes and effects. They are, however, useful in providing a primary indication of dominant parameters and trends. Analytical models for residual stress prediction have been developed for several commercially available alloy steels (AISI 4340, AISI 316L, and AISI 52100) [30, 31] and Ni-based superalloy Waspaloy [32].

Analytical models have mainly been used to investigate the effects of tool geometry and cutting parameters on RS. Ulutan et al. [31] investigated the effects of nose radius and depth of cut for AISI 52100 bearing steel. Experiments revealed a clear shift of surface RS towards the tensile region with increasing nose radius. In contrast, predicted residual stress profiles exhibited an opposite trend. Moreover, the magnitude of surface RS was largely overestimated. Although measured RS were compressive, predicted values were mostly tensile. Liang and Sue [30] investigated the effects of tool edge radius and feed rate for AISI 316 and AISI 4340 steel. The model seemed to accurately capture trends in residual stress behavior. However, errors in the magnitude of surface and sub-surface RS nearing 300 MPa were identified. Residual stress profiles predicted by Lazoglu et al [32] for Waspaloy could not accurately reflect the stress state at the material surface. Although measured RS were always tensile, simulations predicted both compressive and tensile stresses.

Prediction errors associated with analytical modeling can be attributed to several factors: (i) the omission of the effects of temperature, strain, and strain rate on material flow stress evolution, (ii) the exclusion of the temperature dependency of material properties due to the modeling complexity arising from interactions of several mechanisms, and (iii) the idealized approximation in the estimation of the contact length between the tool and the workpiece during stress field calculations. In their current state, analytical models of machining-induced RS are useful to predict the shape of the residual stress profile as a

function of depth below the machined surface. They can also provide an initial indication of the influence of cutting parameters. Due to prediction errors and conflicting trends, current analytical models cannot be adopted as a single design or optimization tool.

Due to the complexity of the cutting process, analytical models are usually based on a two dimensional adaptation of machining such as orthogonal cutting that assumes plane strain conditions. In general, the workpiece is modelled as a semi-infinite, homogenous, isotropic, elasto-plastic material with a von Mises yield surface. Analytical models are comprised of three constituent sub-models: force, temperature, and deformation. The main task of the force and temperature models is to estimate the mechanical loads sustained by the workpiece and its temperature distribution at specific cutting conditions. These are then fed into the thermomechanical deformation model to estimate the resulting stress distribution.

#### *Prediction of machining forces*

Two approaches to force prediction have been used in analytical models of machining-induced RS. The first approach adopts slip line models that estimate machining forces based on process parameters and material properties. Liang and Su [30] used Oxley's predictive machining theory [33] and Waldorf's slip line model [34] to predict cutting and plowing forces, respectively. The second approach [31, 32] is based on discretizing the chip-load in the tool/workpiece engagement domain. This technique is fully elaborated in [35]. Calibration is required for both methods through the use of orthogonal cutting tests. Thus, force modeling combines analytical and mechanistic components.

#### *Prediction of temperature rise*

Numerous analytical models have been developed to estimate temperature rise during cutting with varying heat sources, movement direction, and boundary conditions. The workpiece surface is commonly considered as an adiabatic boundary, and heat transfer to the surroundings by convection is generally neglected. Extensions of Jaeger's solution to moving heat sources during sliding contact [36] are widely used to estimate temperature fields generated by the moving thermal loads during cutting. A review of thermal prediction models implemented in machining is given in Komanduri and Hou [37]. With the objective of predicting RS, Liang and Su implemented the techniques developed by Komanduri and Hou [37, 38] to estimate the temperature rise during cutting. The primary and tertiary shear zones where considered as the main heat sources. In some cases, numerical methods of temperature

prediction were integrated into the analytical approach. Ulutan et al. [31] used the finite difference method to predict the temperature field in the workpiece. The primary and secondary shear zones were considered as heat sources. A similar approach was adopted by Lazoglu et al. [32]. A detailed description of the finite difference model is provided in Lazoglu and Altintas [39].

### *Prediction of thermomechanically induced deformation*

Analytical models of machining-induced RS have exploited the similarity between thermomechanical loading during cutting and that produced in rolling contact problems. Elasto-plastic rolling contact algorithms are commonly adopted to quantify stress and strain fields due to moving mechanical and thermal loads. This approach assumes that points at the same depth from the passing tool experience the same loading history. A plane strain idealization of the cutting process is shown in Fig. 2.6, together with the stresses acting at a point of interest  $m$  located at a depth  $z$  below the machined surface [31, 32]. The origin of coordinates  $O$  coincides with the tool tip and advances in the  $x$ -direction with the cutting tool. In the thermomechanical modeling of stresses, the elastic loading, plastic loading, and elastic unloading regimes are treated separately. In Fig. 2.6, elastic loading is assumed to occur before point  $A$  when the tool tip is still sufficiently far from the point of interest  $m$ . During elastic loading, mechanical stresses are determined by integrating the solution for a moving point load over the contact length for an assumed load distribution:

$$\begin{aligned}\sigma_{xx}^{mechanical} &= -\frac{2z}{\pi} \int_{-a}^a \left( \frac{p(s)(x-s)^2 + q(s)(x-s)^3}{((x-s)^2 + z^2)^2} \right) ds \\ \sigma_{zz}^{mechanical} &= -\frac{2z^3}{\pi} \int_{-a}^a \left( \frac{p(s) + q(s)(x-s)}{((x-s)^2 + z^2)^2} \right) ds \\ \sigma_{xz}^{mechanical} &= -\frac{2z^2}{\pi} \int_{-a}^a \left( \frac{p(s)(x-s) + q(s)(x-s)^2}{((x-s)^2 + z^2)^2} \right) ds,\end{aligned}\tag{2.9}$$

where  $a$  is the half contact length with  $-a \leq x \leq a$ ; the normal and tangential distributed loads in the feed and speed directions are given by  $p(s)$  and  $q(s)$ , respectively, and  $s$  is the

integration variable. Varying load distributions have been used by several authors. Liang and Su [30] adopted a uniform force distribution in the shear zone and a two-dimensional Hertzian profile at the contact between the cutting tool and the machined surface. Ulutan et al. [31] used uniformly distribute forces, while Lazoglu et al. [32] implemented triangular force distributions.

To quantify the thermal stress field during elastic loading, Liang and Su [30] applied the rolling/sliding contact algorithm developed by McDowell [40]. The superposition of stresses due to (i) body forces, (ii) tensile surface traction, and (iii) hydrostatic pressure has also been used to predict the thermal stress distribution in the cutting zone [31, 32]. Finally, the thermomechanical stress field during elastic loading under plane strain conditions is obtained by superposing the mechanically and thermally generated stresses as follows:

$$\sigma_{ij}^{elastic} = \sigma_{ij}^{mechanical} + \sigma_{ij}^{thermal} \quad (2.10)$$

$$\sigma_{yy}^{elastic} = \nu \left( \sigma_{xx}^{elastic} + \sigma_{zz}^{elastic} \right) - \alpha_T ET, \quad (2.11)$$

where  $\sigma_{ij}$  represents the in-plane stress components  $\sigma_{xx}$ ,  $\sigma_{zz}$ , and  $\sigma_{xz}$ ; the out-of-plane stress component is given by  $\sigma_{yy}$ ;  $\nu$ ,  $\alpha_T$ , and  $E$  are Poisson's ratio, the thermal expansion coefficient, and the modulus of elasticity, respectively, and  $T$  is the instantaneous temperature.

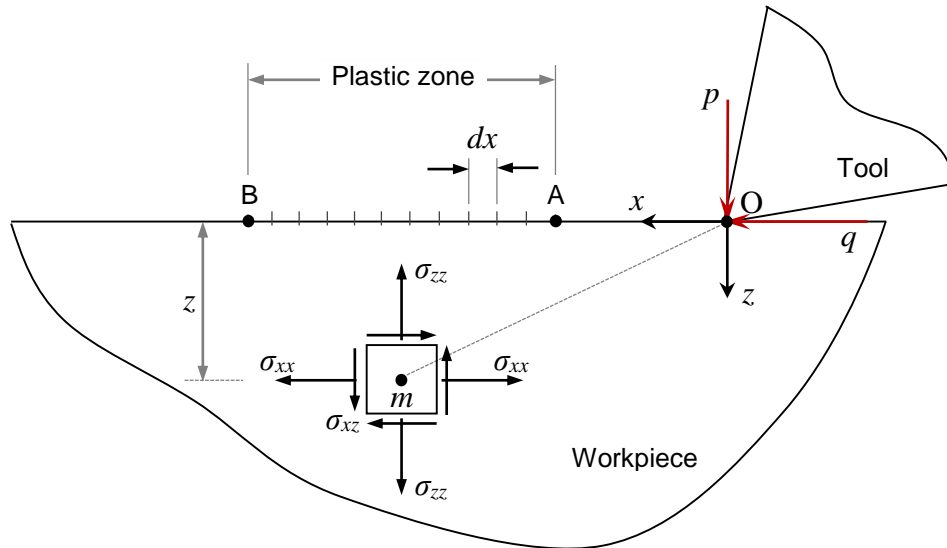


Fig. 2.6: plane strain idealization of the cutting process and discretization of the plastic zone. Figure adapted from Ulutan et al. and Lazoglu et al. [31, 32].

As the tool becomes sufficiently close the point of interest, the thermomechanical load is high enough to cause the material to yield. In Fig. 2.6, plastic loading is assumed to occur in the region AB where the motion of the cutting tool is discretized. The von Mises yield criterion is widely used to determine the onset of plastic deformation. The stress invariant assumption and subsequent relaxation procedure adopted in contact problems is commonly utilized. This approach is based on incremental plasticity. The in-plane stresses during plastic loading are assumed to be equal to their elastic counterparts, and thus:

$$\sigma_{ij} = \sigma_{ij}^{elastic} \quad (2.12)$$

The out-of-plane stress component  $\sigma_{yy}$  is calculated based on the plane strain assumption. The resulting incremental plastic strains are estimated through a plasticity flow rule which describes the variation of strain as a function of stress and material properties. The associated flow rule of plasticity is most commonly used. The form adopted by Lazoglu et al. [32] incorporates the effect of isotropic and kinematic hardening as shown:

$$d\varepsilon_{ij}^{plastic} = \left( \frac{1}{h+c} \right) \left( \frac{3}{2\bar{\sigma}_0^2} \right) (S_{kl} - \alpha_{kl}) d\sigma_{kl}, \quad (2.13)$$

$$S_{kl} = \sigma_{kl} - \frac{1}{3} \sigma_{mm} \delta_{kl} \quad (2.14)$$

where  $h$  and  $c$  are the isotropic and kinematic hardening coefficients, respectively;  $S_{kl}$  and  $\alpha_{kl}$  are the deviatoric and back deviatoric stress components, respectively, and  $\bar{\sigma}_0$  is the current yield stress of the workpiece material.

As the tool moves further away from the point of interest (beyond point B in Fig. 2.6), the thermomechanical load diminishes. Eventually, the workpiece cools down to room temperature. Due to the stress invariant assumption, however, an incremental relaxation procedure is performed in order to satisfy plain strain, equilibrium and surface planarity conditions. The following stress and strain components are reduced in  $M$  steps until their values converge to zero while monitoring the stress increments  $d\sigma_{xx}$  and  $d\sigma_{yy}$ :

$$d\sigma_{zz} = -\frac{\sigma_{zz}}{M}, \quad d\sigma_{xz} = -\frac{\sigma_{xz}}{M}, \quad d\varepsilon_{xx} = -\frac{\varepsilon_{xx}}{M} \quad (2.15)$$

At that point, the values obtained for  $\sigma_{xx}$  and  $\sigma_{yy}$  correspond to the RS in the cutting and the transverse direction, respectively.

### 2.2.2.3 Finite element modeling (FEM)

In the last three decades, FEM has played an important role in strengthening the understanding of the underlying mechanisms and dominant parameters promoting residual stress formation during machining. Numerical studies have constituted the bulk of residual stress research as they allow a more detailed interpretation of the effects of various parameters than closed-form analytical models [41].

The effects of cutting parameters [42-50], tool edge preparation [42, 46, 48-53], tool wear [54], tool coatings [52, 55], interface friction [42-44, 53, 56], chip morphology [54], heat transfer [44, 56], workpiece material properties [47, 57, 58], sequential cutting [45, 48, 52, 59], and plowing [43, 44] were investigated for a range of conventional cutting processes and commercially available alloys including bearing steels, stainless steels, die steels, nickel-based superalloys, and aluminum alloys. Very few numerical studies have addressed machining-induced RS in titanium alloys, especially at finish turning conditions.

In FE simulations, two-way coupling between thermal, mechanical, and metallurgical aspects can be achieved, and mutual interactions can be integrated into the process. The interrelationship between the different modules of the FE package DEFORM™ is shown in Fig. 2.7. The diagram is adapted from [60, 61] and illustrates that through FEM, the full scope of the physical phenomena that occur during the machining process can be considered when predicting RS.

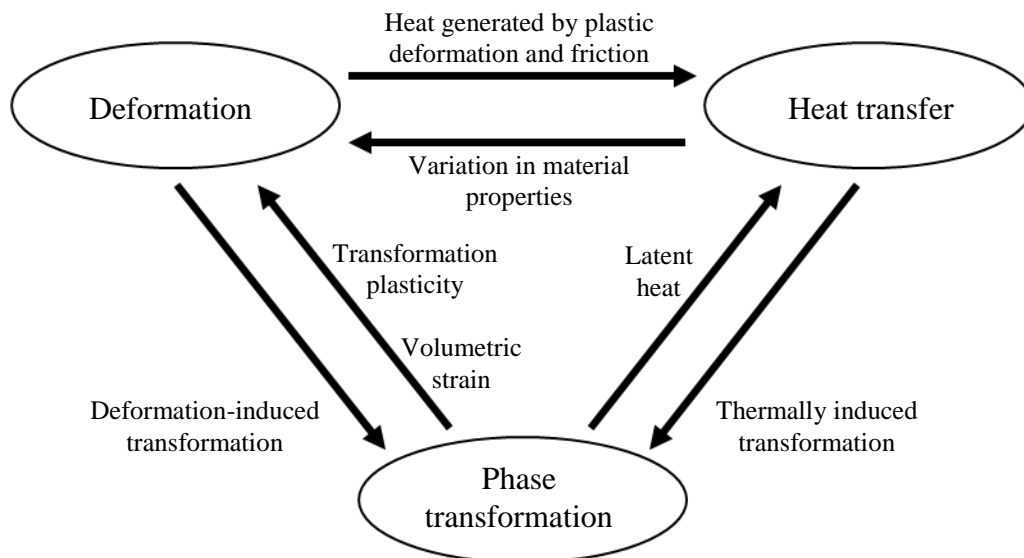


Fig. 2.7: the interrelationship between FEM modules. Figure adapted from [60, 61].

One of the advantages of FEM over analytical models is its ability to integrate the effect of thermal softening, strain hardening, and strain rate hardening on material flow stress through the use of constitutive data or constitutive laws [62]. Furthermore, a more detailed representation of the tribological interactions at the tool/chip interface can be implemented [63-66] through FEM that narrows the gap between modeling assumptions and process physics. More elaborate modeling of tool edge preparation and cutting edge condition is also possible. In addition to honed cutting edges [46, 48, 51, 52, 67, 68], the effect of chamfered edges [46, 47, 67], double chamfered edges [47], chamfered and honed edges [69], and flank wear [54] on machining-induced RS have been investigated using FEM. Furthermore, the influence of chip segmentation on the cutting process can be considered, which is not possible in analytical models that adopt contact mechanics algorithms. Research in this direction has, however, been focused on the prediction of chip morphology and the associated machining forces for different materials including steels [62, 70] and titanium alloys [68, 71-82]. Chip segmentation has also been implemented in the prediction of metallurgical alterations in the surface material during hard turning of steels [83-86]. Few studies have incorporated chip segmentation into FE models for residual stress prediction [47, 52, 54, 87]. However, the effect of chip segmentation on residual stress evolution is not fully explored.

Through in-depth progressive analysis of state variable evolution beyond the capabilities of analytical models, FEM can be used as a virtual machining medium to gain insight into residual stress formation. This can be extended to hybrid manufacturing processes such as laser-assisted machining (LAM) where the effect of process parameters on RS remains relatively unknown.

#### *FE modeling developments in relation to residual stress prediction*

The modeling of flow stress behavior has a major bearing on the accuracy of FE predictions. The Johnson-Cook (JC) model is the most commonly used flow stress model in numerical simulations of metal cutting, including FE predictions of RS [42, 46, 48, 51, 52, 54, 55, 57-59, 88]. The model is comprised of three functions representing the effect of strain, strain rate, and temperature on material flow stress as shown below:

$$\sigma_f = f(\bar{\epsilon}) \cdot g(\dot{\bar{\epsilon}}) \cdot h(T), \quad (2.16)$$

$$\sigma_f = (A + B\bar{\varepsilon}^n) \left( 1 + C \ln \left( \frac{\dot{\varepsilon}}{\dot{\varepsilon}_0} \right) \right) \left( 1 - \left( \frac{T - T_0}{T_{melt} - T_0} \right)^m \right) \quad (2.17)$$

where  $\sigma_f$ ,  $\bar{\varepsilon}$ ,  $\dot{\varepsilon}$ , and  $\dot{\varepsilon}_0$ , are the material flow stress, effective plastic strain, effective plastic strain rate, and reference strain rate, respectively;  $T$ ,  $T_0$ , and  $T_{melt}$  are the instantaneous, ambient (reference), and melt temperature of the workpiece material, respectively; and  $A$ ,  $B$ ,  $C$ ,  $n$ , and  $m$  are material constants.

Umbrello et al. [58] investigated the effect of Johnson-Cook (JC) model parameters identified by several authors on RS generated during orthogonal cutting of AISI 316L steel. Residual stresses were found to be highly sensitive to JC material constants. The most accurate predictions were obtained for parameters that were determined based on cutting tests. Parameters determined by Split Hopkinson Pressure Bar (SHPB) tests resulted in lower accuracy. This was attributed to the limited ranges of temperature, strain, and strain rate achievable by this method.

To address this problem, a methodology was developed by Shi et al. [89-91] at the National Research Council Canada (NRC) for material characterization, which consists of the identification and calibration of constitutive laws. Their approach combines orthogonal cutting and analytical modeling. Based on experimental measurements of chip thickness, contact length, and machining forces for a limited number of orthogonal cutting tests, the Distributed Primary Zone Deformation (DPZD) model generates a vast amount of constitutive data sets  $(\bar{\sigma}, \bar{\varepsilon}, \dot{\varepsilon}, T)$ . Orthogonal cutting tests with laser-assisted preheating are performed to extend the temperature range towards the higher levels attained at the tool/chip interface, thereby eliminating extrapolation errors. Regression methods are then used to fit the constitutive data to several flow stress models applicable to the machining process. Quasi-static impact tests at very low strain rates are carried out to identify some equation parameters and to improve convergence. Using evaluation criteria for constitutive law formulation, the suitability of the calibrated constitutive laws for a particular workpiece material/tool combination is assessed. The evaluation criteria include statistical measures and the accuracy of preliminary FE predictions. A detailed description of the methodology is given in section 6.2.1.1, and a systems approach to the generation of constitutive data and constitutive law identification is illustrated in Fig. 6.2. This methodology for material characterization was

adopted by Bejjani et al. [92] in the prediction of chip morphology and machining forces for titanium metal matrix composites (TiMMC) and by Abboud et al. [93] in the prediction of machining-induced RS in Ti-6Al-4V.

Umbrello et al. [85] used the Johnson-Cook (JC) approach as a basis to develop a hardness-based constitutive model adapted for the hard turning process. The model reflects the sensitivity of flow stress to the material's initial hardness in addition to strain, strain rate, and temperature. The flow stress according to the hardness-based model is given by:

$$\sigma(\bar{\varepsilon}, \dot{\bar{\varepsilon}}, T, HRc) = B(T)(C\bar{\varepsilon}^n + F + G\bar{\varepsilon}) \left[ 1 + \left( \ln(\dot{\bar{\varepsilon}})^m - A \right) \right] \quad (2.18)$$

$$B(T) = \exp(aT^5 + bT^4 + cT^3 + dT^2 + eT + f) \quad (2.19)$$

$$F(HRc) = 27.4HRc - 1700.2 \quad (2.20)$$

$$G(HRc) = 4.48HRc - 279.9 \quad (2.21)$$

where  $HRc$  represents the initial hardness of the workpiece material;  $B(T)$  is an exponential function of temperature that reduces to one at  $T_0 = 20^\circ\text{C}$ , and  $a$  to  $f$  are material constants;  $C$  and  $n$  are the strength multiplier and the strain hardening coefficient, respectively;  $F(HRc)$  and  $G(HRc)$  are linear functions of initial hardness;  $m$  is the strain rate sensitivity factor; and  $A$  is a material parameter. The linear functions of hardness  $F(HRc)$  and  $G(HRc)$  modify the initial yield strength and the strain hardening curve of the material, respectively. These are given in Eq. 2.19 and Eq. 2.20 for bearing steel AISI 52100.

The hardness-based flow stress model was implemented in the prediction of microstructural alterations and RS during the hard turning of bearing steel AISI 52100 [47, 84, 86, 87]. Microstructural changes consisted of white layers (WL) due to quenching of the surface material and dark layers (DL) due to tempering of the sub-surface layers. The estimation of the thickness of WL and DL was based on the incremental changes in material hardness during quenching and tempering, respectively. This was implemented through the use of simple empirical equations. A closer agreement between the predicted and measured residual stress distributions was observed when microstructural alterations were included in the FE model [87].

Ramesh et al. [94] modeled white layer formation in the surface of AISI 52100 steel during orthogonal cutting. Their approach was based on the coupling of phase transformation

kinematics with the thermomechanical model. The Koistinen-Marburger [95] equation was used to model the martensitic phase transformation upon quenching. The effect of stress on phase equilibria was incorporated in the model. It was also concluded in this study that more accurate residual stress predictions can be obtained by capturing the phase transformation effects. White layer formation was found to have a significant impact on the magnitude of surface RS and on the depth of the peak compressive RS.

The Johnson-Cook (JC) flow stress model (Eq. 2.16-2.17) has been criticised for having certain deficiencies that can be summarized as follows [74, 81]: (i) it is not universally applicable to all materials, (ii) it fails to capture the effect of strain softening exhibited by some materials such as Ti-alloys and the resulting adiabatic shear banding that leads to segmental chip formation, and (iii) it excludes the coupling between the effects of strain, strain rate and temperature, which in reference to Eq. 2.16 can be written as  $g_1(\bar{\epsilon}, \dot{\bar{\epsilon}})$  or  $h_1(\bar{\epsilon}, T)$ . As a result, modifications to the JC model have been suggested by several authors.

Strain softening is defined as the phenomenon that gives rise to diminishing stress with increasing strain. This occurs beyond a critical level of strain. Below this value, the material undergoes strain rate hardening [81]. This type of behavior was observed for Ti-6Al-4V. It was related to one of several phenomena including microstructural softening by dynamic recrystallization (DRX), which takes place at high levels of strain and strain rate. Calamaz et al [81] modified the JC model to capture the effect of strain softening as follows:

$$\sigma = f_1(\bar{\epsilon}) \cdot g(\dot{\bar{\epsilon}}) \cdot h_1(\bar{\epsilon}, T) \quad (2.22)$$

$$\sigma = \left( A + \frac{B\bar{\epsilon}^n}{\exp(\bar{\epsilon}^a)} \right) \left( 1 + C \ln \left( \frac{\dot{\bar{\epsilon}}}{\dot{\bar{\epsilon}}_0} \right) \right) \times \left( 1 - \left( \frac{T - T_0}{T_{melt} - T_0} \right)^m \right) \left( D + (1 - D) \tanh \left( \frac{1}{(\bar{\epsilon} + S)^c} \right) \right) \quad (2.23)$$

$$D = 1 - \left( \frac{T}{T_{melt}} \right)^d \quad \text{and} \quad S = \left( \frac{T}{T_{melt}} \right)^b \quad (2.24)$$

The strain hardening function  $f(\bar{\epsilon})$  of the JC model was modified to include the effect of diminishing flow stress at higher levels of strain. This was achieved through the division of

the strain hardening term by an exponential function of strain. The thermal softening function  $h(T)$  was modified to capture the gradually increasing influence of strain softening at higher temperatures. This was attained by the introduction of a hyperbolic tangent (tanh) function. For the purposes of the discussion, the constitutive law developed by Calamaz et al. is referred to as the C-JC model. In addition to the JC parameters ( $A$ ,  $B$ ,  $C$ ,  $n$  and  $m$ ), the C-JC law requires the determination of four additional constants ( $a$ ,  $b$ ,  $c$ , and  $d$ ). Sima et al. [74] introduced an additional exponent to the tanh function to further control the interaction between strain softening and temperature. This large number of model parameters casts an important doubt over the applicability of current experimental and analytical procedures for material characterization, and the possibility of convergence to a single solution for the complete set of equation parameters. The current approach for parameter selection is based on arbitrary manipulation of the additional equation parameters to achieve accurate FE predictions of chip geometry and cutting forces, with the only reference being the initial JC flow curves up to a low strain value of around 0.3.

The strain softening approach was mainly used for chip morphology and machining force predictions. It has seen limited applications in the FE prediction of machining-induced RS [68]. Sima et al. [74] concluded that by incorporating the influence of strain softening on flow stress behavior for Ti-6Al-4V, segmental chip formation can be modeled without the implementation of a ductile fracture criterion. Calamaz et al. [81] found that the highest accuracy of chip geometry predictions is obtained by combining ductile fracture with the strain softening approach. The Cockcroft and Latham criterion was implemented for Ti-6Al-4V as per [73, 79] in combination with the C-JC model given in Eq. 2.22-2.24. Both works highlighted the fundamental importance of the material constitutive law to accurate predictions of chip morphology, machining forces, and cutting temperatures. It is argued that the adiabatic shear theory on its own is not sufficient to model chip segmentation [79]. It was established by Shaw that a combination of thermal and fracture analyses are required to address all the aspects of segmental chip formation [1].

It has been common practice to model metal cutting as a two dimensional process, thereby reducing the complexity of simulations and leading to shorter running times. A few studies have adopted 3D models [68, 96] for residual stress prediction in order to achieve higher fidelity modeling of the cutting process. A major disadvantage of numerical modeling

using FE analysis, however, is the time required to run simulations. Depending on the complexity of the process and the variables considered, a simulation could consume several days. Several research efforts have attempted to address this problem.

Nasr et al. [88] used the commercial software ABAQUS™ to develop a time-efficient method to predict RS during orthogonal machining. The main focus was on reducing the simulation time during stress relaxation. Steady-state values ( $\leq 10\%$  variation) of the state variables were imported from the cutting simulation into a separate model and uniformly applied prior to relaxation. The new model consisted of a reduced length workpiece. Furthermore, sites of minute elements comprising the tool, the chip and the uncut workpiece were eliminated from the relaxation step. In addition, an implicit solver was used with the aim of increasing the simulation time increment. Valiorgue et al. [56] eliminated chip formation completely from the cutting process simulation. Instead, the thermomechanical load was quantified analytically, and FEM was used to simulate its application and movement along the workpiece surface. Analytical force and temperature predictions were based on orthogonal cutting experiments. This method was extended to 3D modeling of the cutting process [96]. Anurag and Guo [44] assumed that chip formation would have little contribution to the formation of RS during hard turning, and that plowing forces would be their major determinant. After a simulation of plowing that excludes chip formation, the thermomechanical stress state was imported into the implicit solver for stress relaxation in a similar approach to Nasr et al. [88].

#### *Accuracy and sources of error in FEM in relation to residual stress prediction*

Numerical models using FE analysis are extremely useful to metal cutting research as they provide insight and knowledge while reducing the dependency on experiments. FE models were found to be more reliable than analytical models in predicting behavioral trends for residual stress distribution, albeit with sizeable errors in magnitude estimated as  $\geq 50\%$  for peak RS in the cutting direction. Errors in metal cutting simulations have been largely attributed to the following aspects [51, 59]:

1. Meshing aspects including mesh density and distortion.
2. Material modeling: Flow stress models calibrated with data generated from Split Hopkinson Pressure Bar (SHPB) tests provide inaccurate results due to limitations in strain, strain rate and temperature levels achievable during the tests [58].

3. Numerical integration and interpolation.
4. Tribological aspects at the tool/chip interface: Hybrid friction models produce more accurate predictions than simple shear or sliding friction models that adopt a fixed coefficient of friction along the entire tool/chip interface [63, 65].
5. Exclusion of progressive tool wear from simulations: At harsh cutting conditions involving high cutting speeds, tool wear has a significant impact on the temperature rise in the machined surface and an important influence on RS [54].
6. Omission of microstructural alterations in the near-surface layer: In the event of phase transformation at conditions promoting elevated temperatures, latent heat and transformation strains alter the residual stress distribution [87, 94].
7. Chip separation criteria: Failure criteria for chip separation are a common source of error as they require the estimation of a damage value for the workpiece and a parting line for the chip.

Nevertheless, FE models are probably the only tools capable of capturing the effect of all the relevant variables in metal cutting on RS.

## **2.3 Effect of process parameters and material properties**

Together with the physical properties of the tool and workpiece materials, cutting parameters (feed, speed and depth of cut), tool geometry (rake angle and nose radius), tool edge preparation (honed and chamfered edges), tool wear, and the method of lubrication play an important role in defining the state, magnitude, and distribution of RS. The above aspects also influence other attributes of surface integrity including microstructural alteration, plastic deformation, hardness variation and surface finish. Experimental and numerical investigations have identified conditions that can diminish tensile RS and promote compressive RS.

### **2.3.1 Effect of cutting parameters**

When investigating Inconel 718, Arunachalam et al. [97] found that increasing the depth of cut diminished compressive RS, and increasing the cutting speed shifted RS from compressive to tensile. On the other hand, lubrication helped reduce tensile RS. High speed face turning under wet conditions with small depths of cut ( $\approx 0.05$  mm) and relatively low speed ( $\approx 150$  m/min) was recommended for reduced tensile RS. In contrast, Pawade et al.

[98] found that increasing the depth of cut enhanced compressive RS, whereas increasing the feed rate had an adverse effect. Furthermore, above 300 m/min the trend for cutting speed was reversed, and tensile RS were reduced. High speed milling with moderate depth of cut, low feed rate, and relatively high speed was recommended for enhanced compressive RS. Sharman et al. [99] found that increasing the cutting speed from 80-120 m/min diminished tensile RS, which is in contradiction with the above findings. Salio et al. [45] found that increasing the depth of cut had opposite effects on tensile RS in the surface and peak compressive RS in the sub-surface of the material. Superficial tensile RS were diminished, which is in agreement with the findings reported in Pawade et al. [98], while peak compressive RS in the sub-surface of the material were increased. Darwish [64] identified feed rate as the dominant parameter on surface roughness. Surface finish deteriorated heavily with increasing feed rate.

Sridhar et al. [28] found that tensile RS in IMI-834 Ti-alloy diminished with increasing speed and intensified with increasing feed rate, especially at high cutting speed. In contrast, Mantle and Aspinwall [100] found that for Ti-45-2-2-0.8, compressive RS diminished with increasing speed. An increase in the hardness of the machined surface of up to 40% above the bulk material was also observed [100, 101]. Moreover, cutting speed was found to have a dominant effect on surface roughness for Ti-64 and Ti-6246 [102, 103]. Surface finish deteriorated near the end of tool life with increasing speed, and work hardening at the surface was amplified. A significant deterioration in surface finish was exhibited by Ti-6242S with increasing feed rate [104].

When investigating the hard turning of bearing steel AISI 52100, Dahlman et al. [105] found that compressive RS diminished with increasing depth of cut. Furthermore, Hua et al. [69], Dahlman et al [105], and Javidi et al [106] confirmed the importance of feed rate and found compressive RS to increase significantly at higher feed rate levels. In contrast, when investigating the turning of AISI 316L, Outeiro et al. [107] found feed rate to have an adverse effect on RS. An increase in feed rate produced a significant increase in superficial tensile RS as well as an increase in the thickness of the tensile layer. Cutting speed and depth of cut were found to promote an opposite trend to feed rate. In addition, Outeiro et al. [52] identified uncut chip thickness as the parameter having the largest influence on RS during orthogonal

cutting of AISI 316L. When turning several grades of steel Capello [108] identified feed rate as the key determinant of RS, with depth of cut having negligible influence.

### **2.3.2 Effect of tool geometry and edge preparation**

When investigating the high speed milling of Inconel 718, Arunachalam et al. [97] found that round CBN inserts promoted predominantly tensile RS, whereas square inserts induced compressive RS. On the other hand, Pawade et al. [98] emphasized that coupled with the favorable cutting parameters, a honed cutting edge can promote compressive RS. Chamfered tools with a honed edge were found to produce larger compressive RS than those with a sharp edge. During face turning of Inconel 718, Arunachalam et al. [97] found that honed edges improved surface finish by preventing chipping. Larger nose radii, positive rake angles, and lubrication were found to have a positive effect on surface finish.

When hard turning AISI 52100 bearing steel, Hua et al. [47] recommended the use of chamfered tools at high feed rates to achieve more deeply penetrating compressive RS. This effect was more pronounced at higher hardness levels. Moreover, Hua et al. [69] emphasized that the use of chamfered tools with medium sized hone radii can promote deeply penetrating compressive RS in hardened steels, while keeping cutting forces and tool temperatures at sustainable levels. They found that increasing the tool edge radius from 20 to 50  $\mu\text{m}$  enhanced sub-surface compressive RS. Dahlman et al. [105] found the rake angle to have the strongest influence on RS in face turned bearing steel, with greater negative rake angles producing larger and more deeply penetrating compressive stresses. Furthermore, Li et al. [109] found that residual stress profiles and affected depths produced by rhombic and square inserts were largely different. When investigating the hard turning of AISI H13 die steel with PCBN tools, Chen et al. [46] found that compared to honed tools, chamfered tools generated smaller surface compressive stresses, together with larger and more deeply penetrating sub-surface compressive stresses. This was attributed to a larger extent of stagnation leading to higher temperatures and increased plastic strain.

When investigating the orthogonal cutting of stainless steel grade AISI 316L, Nasr et al. [51] found that increasing the edge radius from 20 to 100  $\mu\text{m}$  intensified tensile RS. This was attributed to additional heat generation due to increased contact with the tool. Work by Capello [108], Javidi et al. [106], and Liu et al. [110] identified tool nose radius as a key

parameter for turned steels. Larger nose radii were found to shift superficial stresses towards the tensile range.

### **2.3.3 Effect of tool wear on residual stresses and surface integrity**

Tool edge deterioration is an integral phenomenon of the machining process that is heavily accelerated by difficult-to-machine materials. Investigations by Sharman et al. [99] and Li et al. [109] on the surface integrity of Ni-based superalloys determined that tool wear had the largest effect on RS. Turning with a worn tool produced peak tensile RS of up to 1000 MPa in the material's surface.

When investigating the orthogonal cutting of Ti-6Al-4V, Chen et al. [54] found that worn tools produced a very thin tensile surface layer ( $< 5 \mu\text{m}$ ) in the machined surface. Larger flank wear was found to generate higher machining forces leading to more deeply penetrating RS. At the same time, the increased rubbing between the tool and the workpiece surface produced more elevated temperatures, intensifying superficial tensile RS. Similar behavior was observed by Liu et al. [110] when hard turning bearing steels. Tool wear was found to significantly increase superficial tensile RS, as well as sub-surface compressive RS.

Che-Haron and Jawaid [102] detected a very thin plastically deformed layer in the immediate sub-surface of Ti-6Al-4V whose thickness was found to increase with progressive tool wear. Similar behavior was observed for Ti-6246 [103] that exhibited a very thin white layer ( $< 10 \mu\text{m}$ ) due to plastic deformation upon prolonged machining. Furthermore, progressive tool wear beyond the half-life of the tool produced a marked increase in surface roughness for both types of Ti-alloys. Ginting and Nouari [104] found that for Ti-6242S, worn tools ( $VB = 0.3$ ) intensified plastic deformation. Material hardness dropped below the bulk at a depth of  $50 \mu\text{m}$ , but exceeded the bulk at  $200 \mu\text{m}$  below the surface. The largest divergence from bulk hardness was obtained at the harshest machining conditions.

### **2.3.4 Effect of tool material and tool coatings**

While tool coatings reduce premature tool failure and promote higher productivity, their effect on RS in materials with low thermal conductivity can be detrimental. This was confirmed by Sharman et al. [99] and Arunachalam et al. [97] in their investigations on Inconel 718. The former found that coated tools generated higher tensile RS, whereas uncoated tools promoted deep compressive RS beneath a reduced tensile layer. The latter found ceramic cutting tools to generate tensile RS of much higher magnitudes than CBN

tools. It was emphasised that the lower thermal conductivity of coated and ceramic tools prevented heat from dissipating into the bulk material of the tool, thereby causing a rise in workpiece surface temperature, which in turn promoted tensile RS. The use of lubrication was highly recommended for heat evacuation from the cutting zone and was found to significantly reduce tensile RS.

Outeiro et al. [55] investigated the effect of coated tools on RS generated when dry turning Inconel 718 and AISI 316L. They concluded that higher superficial tensile RS were generated with uncoated tools, which increased the magnitude and penetration depth of peak compressive RS. This contradicts the findings reported by Sharman et al. [99]. Work by Outeiro et al. [52] on the orthogonal cutting of AISI 316L showed that coated tools intensified tensile RS in the machined surface, thus contradicting the findings by Outeiro et al. [55].

### **2.3.5 Effect of workpiece material properties**

Capello [111] emphasised that enhanced mechanical properties increase the level of machining-induced RS in a manner that is additive to the effect of process parameters. Furthermore, material hardness was identified as a mechanical characteristic closely related to residual stresses. Hua et al. [69] found that for the same cutting parameters, higher workpiece material hardness promoted larger compressive RS, confirming findings by Wu and Matsumoto [8] that attributed the increase in compressive RS to a higher inclination of the primary shear zone. It was explained that the larger shear angles associated with materials of increased hardness distanced the compressive stress lobe from the material ahead of the cutting tool, altering the balance of the deformation cycle in favor of more compressive RS.

Nasr et al. [57] used the JC equation (Eq. 2.17) to investigate the effects of strain hardening and initial yield strength on RS induced when orthogonal cutting a range of commercial steels. This was achieved by varying the initial yield strength  $A$ , the strain hardening coefficient  $B$ , and the strain hardening exponent  $n$ . It was concluded that materials with lower initial yield strength  $A$  and higher strain hardening sensitivity (higher  $B$  and  $n$ ) required a larger amount of plastic deformation energy. Therefore, such materials experienced larger magnitudes of thermally induced tensile RS.

### **2.3.6 Effect of sequential cutting**

Salio et al. [45] investigated the effect of depth of cut when turning Inconel 718 jet engine turbine disks using an orthogonal model of dry machining with 2 sequential cuts. A first pass with low depth of cut followed by a second pass with high depth of cut was found to radically increase tensile RS, the thickness of the affected layer, and the penetration of the peak compressive stress. Li et al. [59] modelled the effect of continuous feed during high speed end milling of steel SKD 11 hardened to 60-62 HRc and concluded that RS tended to increase after the second cutting process.

## **2.4 Gap analysis**

Based on the critical literature review, important gaps related to machining-induced residual stresses (RS) in Ti-alloys were identified:

1. Limited experimental data was found in the open literature on machining-induced RS in Ti-alloys, especially for the finish cutting regime. Finish cutting conditions that can promote a desirable compressive residual stress state in the machined surface without compromising surface quality have not been determined. A correlation between RS, surface finish, and the near-surface microstructure (NSM) for Ti-alloys is practically non-existent.
2. Prior numerical studies on machining-induced RS in Ti-alloys focused mainly on chip formation and force prediction, and very limited attention was given to RS. Huge benefits can be gained through FEM of residual stress formation in Ti-alloys during cutting. In addition to offering valuable predictive capability for RS, FEM can serve as a valuable investigative medium, especially that the experimental approach is associated with large costs and destructive methods of residual stress profile measurement, and that analytical models cannot integrate the full range of mechanisms leading to residual stress formation during cutting.
3. Analytical studies of the origins of RS are mainly focused on the grinding process. Conflicting views exist over the relative contribution of mechanical and thermal loads to RS during cutting. Fundamental understanding is required of the significance and relative contributions of mechanical, thermal and metallurgical sources of RS generated during the machining process.

4. Chip segmentation is an important aspect of Ti-alloy machining. The effect of chip segmentation on machining-induced RS is not fully explored. In the case of Ti-alloys, this effect was only addressed for high speed machining. The mechanism by which chip segmentation influences residual stress formation at conventional production speeds is not known.

It was concluded from the literature review that a full characterization of machining-induced RS can only be obtained through a hybrid approach combining experimental investigation techniques and FE analysis.

## **2.5 Research objectives**

The research objectives were defined in-line with industrial needs and the available scope for research in the field of machining-induced residual stresses (RS). They are summarized as follows:

1. The investigation with the aid of FEM of the effects of thermal loading and phase transformations on RS in difficult-to-machine materials, and the study of the influence of material properties, cutting parameters, and tool geometry on the relative contributions of thermal stresses and mechanical loading to machining-induced RS.
2. The development of a FE model to predict machining-induced RS in Ti-alloys optimized for accuracy and computational efficiency, and taking the following aspects into consideration:
  - a. The contact pressure dependency of friction at the tool chip/interface
  - b. Phase transformations in the near-surface of the material.
  - c. Effects of tool edge preparation and flank wear.
  - d. Adaptive remeshing to eliminate errors due to chip separation criteria.

Material characterization will be performed using the cutting process to accurately capture the behavior of material flow stress and eliminate extrapolation errors. The FE model will be validated by x-ray diffraction measurements of RS.

3. Characterization of chip formation in Ti-6Al-4V during orthogonal cutting, and the use of FEM to study the influence of chip segmentation on residual stress generation at higher cutting speeds within the conventional range ( $\leq 90$  m/min).

4. Experimental investigation of the effects of cutting parameters, tool geometry, and material properties on RS generated during turning for two aero-engine grade Ti-alloys, Ti-6Al-4V and Ti-6Al-2Sn-4Zr-6Mo, including the measurement and evaluation of:
  - a. Performance indicators: Machining forces and tool wear.
  - b. Surface integrity: Residual stresses (RS), surface roughness, and the near-surface microstructure (NSM).
5. Development of an empirical model to predict RS for practical applications, based on the results of 2 and 4. Residual stresses will be predicted for both Ti-alloys as a function of cutting parameters and their mutual interactions.

The specific objectives listed above satisfy the terminal objectives of the research previously outlined in Chapter 1 in terms of experimental investigation and modeling of RS. An in-depth study of the main contributors to residual stress formation during cutting as elaborated in item 1 will serve as a foundation for the development of the FE model and its use as an investigative medium (items 2 and 3). Process parameters of major importance to RS and surface quality will be identified through an extensive experimental investigation, which will provide a vast data population for empirical model development (items 4 and 5).

## **2.6 Research plan, methodology, and theoretical considerations**

A research plan was developed as shown in Fig. 2.8 in systems approach form. In order to characterize the machining-induced RS in Ti-alloys, a methodology will be adopted that combines experimental investigation, FE modeling, and empirical modeling.

Two types of cutting experiments will be carried out. Orthogonal cutting tests will serve to characterize the flow stress behavior of the material at conditions of strain, strain rate, and temperature encountered during cutting. The procedure developed by Shi et al. [89-91] at the National Research Council Canada (NRC) for the identification and calibration of material constitutive laws will be implemented in this research to eliminate the uncertainties associated with plastic flow properties. The orthogonal cutting tests will also serve to validate the FE model. Orthogonal cutting will be performed in dry conditions without the use of lubricant, and will involve the measurement of machining forces by dynamometry and temperature history in the cutting zone by infrared imagery. Following the cutting tests, chip

morphology will be evaluated using metallographic preparation and optical microscopy. The measured cutting and thrust force components will provide an initial estimate of the sliding friction coefficient at the tool/chip interface. Surface RS will be measured using the x-ray diffraction method for all test conditions. Residual stress measurement (RSM) will be sub-contracted to a specialist Canadian firm. The near-surface microstructure (NSM) will be evaluated for specimens machined under relatively harsh conditions. The cutting tools employed in orthogonal cutting will be inspected for wear. In addition to orthogonal machining, 3D oblique cutting will be performed. Longitudinal single point turning tests will serve to investigate the effect of cutting parameters and tool geometry on RS. Oblique cutting tests will be performed in wet conditions with forced lubrication. Forces sustained during cutting and the resulting tool wear will be measured and assessed. The surface integrity will be evaluated for all machined specimens. This includes, surface RS, surface roughness, the near-surface microstructure (NSM) and hardness distribution. The effects of cutting parameters and tool geometry on RS and surface integrity will be evaluated, and guidelines will be established for optimal parameter selection. Experimental measurements of machining forces and RS will serve to validate the empirical models.

The FE model of the machining process will be developed using the FE software package DEFORM<sup>TM</sup> developed by Scientific Forming Technologies Corporation (SFTC). It employs Lagrangian formulation with implicit integration and adaptive remeshing. The constitutive model that constitutes the central nervous system of the FE model will be identified and calibrated based on orthogonal cutting tests as previously explained. In modeling the interactions at the tool/chip interface, the effect of friction models on machining force and residual stress predictions will be evaluated with the view of implementing a hybrid friction model that captures contact pressure variations. During the cutting simulation, plastic deformation in the three shear zones will be considered to quantify the stress field in the near-surface of the workpiece. The effect of chip segmentation on the predicted machining forces, cutting temperatures, and RS will be studied. The experimental study of chip morphology will provide guidelines for the selection of a suitable approach to integrate chip segmentation into the FE model. If phase transformations in the near-surface material should occur at the investigated cutting conditions, phase transformation kinetics will be coupled with the thermomechanical simulation of the cutting process. As a first step, the effect of phase

transformation will be incorporated into the model for AISI 52100 bearing steel, since it is known to be susceptible to phase changes during machining. The model will then be modified for Ti-6Al-4V if needed, based on phase transformation kinetics models available in the open literature.

The permissible error value defined by the project's industrial partner is  $\pm 70$  MPa for FE and empirical predictions. In the case of FEM, if the error involved is larger than the allowable value, further development will be undertaken in several areas including friction, chip segmentation, and flow stress behavior.

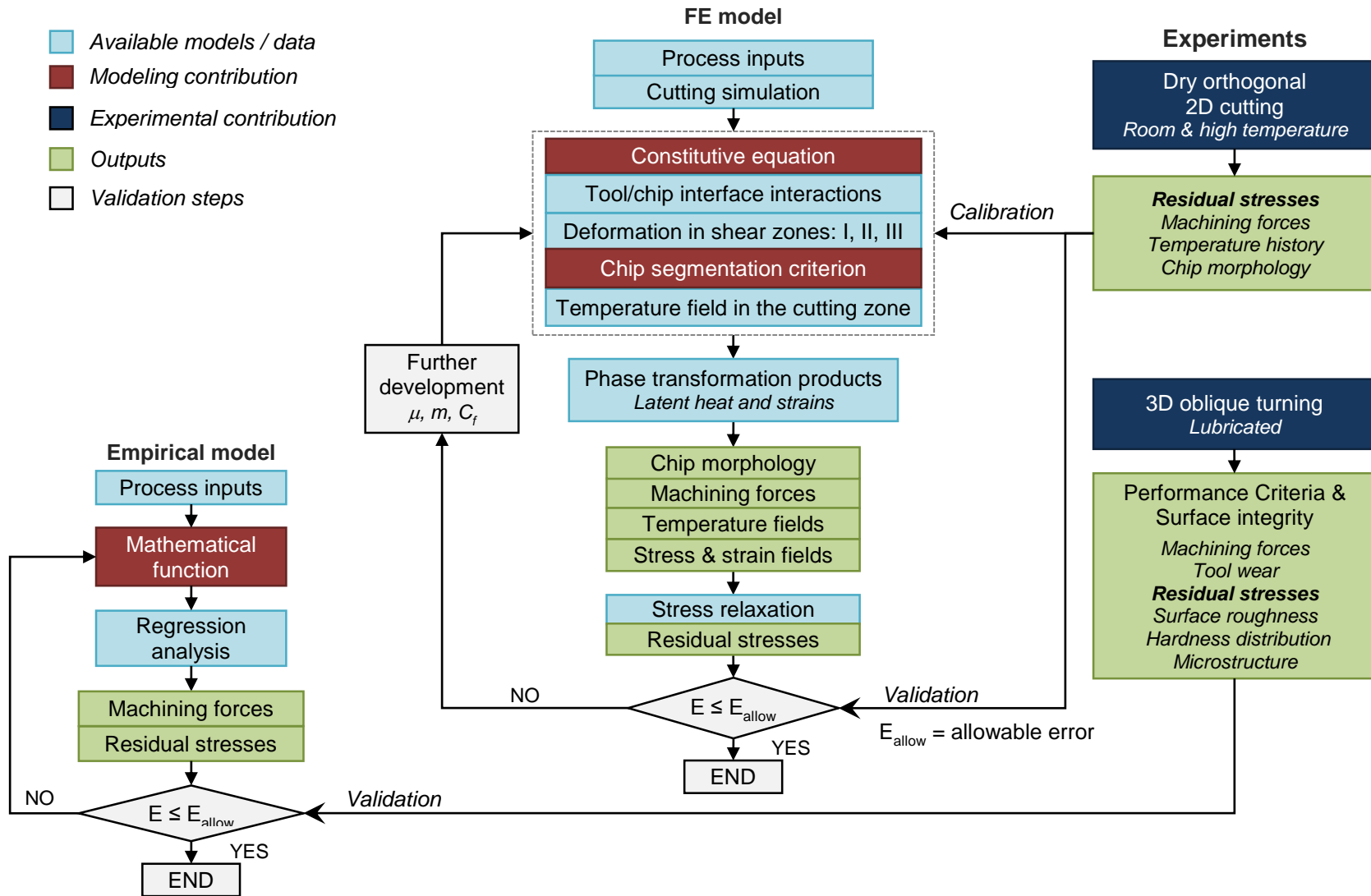


Fig. 2.8: systems approach to the characterization of machining-induced residual stresses in Ti-alloys.

## CHAPTER 3 EXPERIMENTAL SETUP

### 3.1 Introduction

To fulfil the objectives of this research, two categories of cutting tests were performed: (i) oblique single point turning and (ii) orthogonal cutting. In addition, two aerospace grade titanium alloys, Ti-6Al-4V and Ti-6Al-2Sn-4Zr-6Mo were investigated. These are referred to as Alloy 1 and Alloy 2, respectively, in the text and as A1 and A2 in the figures. This chapter describes the experimental setup used to achieve the research objectives, and the techniques employed in the measurement and evaluation of key performance indicators and essential attributes of workpiece surface quality.

All the machining tests were carried out at the Structures, Materials, and Manufacturing (SMM) laboratory of the National Research Council (NRC) in Montreal on a Boehringer NG 200 turning center, equipped with a Kistler 9121 piezoelectric dynamometer for force measurement. Cutting was performed with uncoated tungsten carbide tools (Kennametal grade K68) with sharp cutting edges (hone radius  $< 20 \mu\text{m}$ ), specially manufactured to the specifications of the industrial partner. Throughout the thesis, notations and symbols referring to oblique cutting are presented in italic form, whereas those pertaining to orthogonal cutting are not italicized.

### 3.2 Three-dimensional oblique single point turning

To characterize the behavior of machining-induced residual stresses (RS) in Ti-alloys, an extensive experimental investigation was conducted in the finish turning regime at conditions that closely replicate those encountered in a real manufacturing environment. Machining forces and tool wear were examined as performance indicators over a wide range of cutting conditions. Residual stresses, surface roughness, hardness distribution and the near-surface microstructure (NSM) were evaluated as part of a comprehensive analysis of workpiece surface integrity.

#### 3.2.1 Experimental setup

The experimental setup is shown in Fig. 3.1. Workpiece samples consisted of solid cylindrical bars of titanium alloy with a nominal diameter of 50 mm, pre-cut to lengths of 120 and 100 mm for Alloy 1 and Alloy 2, respectively. The cutting length ( $L$ ) during the tests

ranged from 50 to 80 mm. Tests were performed under flood lubrication conditions. An industrial grade soluble-oil coolant concentrate (TRIM® VHP® E210) was employed.

A process schematic of oblique machining is shown in Fig. 3.2a. In oblique cutting, the cutting edge is inclined with respect to the direction of cutting speed,  $v$ . Furthermore, the tool tip is under the action of three mutually perpendicular force components as follows: (i) the cutting force ( $F_c$ ), tangential to the workpiece circumference, (ii) the feed force ( $F_f$ ), parallel to the axial feed direction, and (iii) the radial force ( $F_r$ ), perpendicular to the feed direction. The representative tool geometry of the process is depicted in Fig. 3.2b.

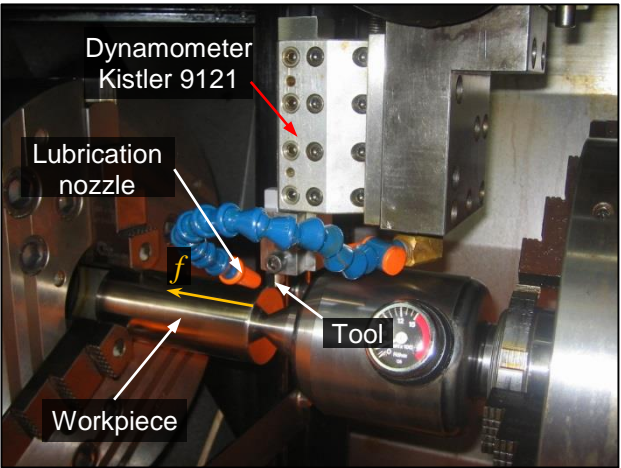


Fig. 3.1: experimental setup for oblique single point turning.

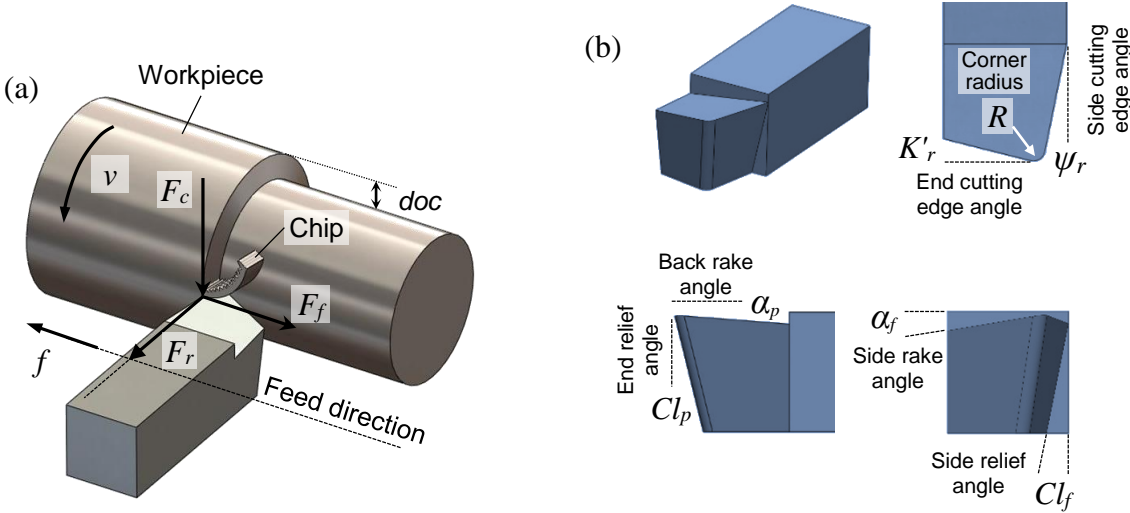


Fig. 3.2: oblique turning: (a) process schematic and (b) representative tool geometry.

### 3.2.2 Procedure for robust and stable cutting

A procedure for the cutting tests was developed in collaboration with the project's industrial partner to ensure a stable and robust cutting process. Each test comprised a series of three passes performed in sequence. The first pass, the initial cut, served to eliminate geometrical variations in the workpiece such as out-of-straightness and radial run-out. The second pass, the semi-finishing (*SF*) cut, served to induce an identical initial stress state among all workpiece samples. Initial and *SF* cuts were performed with fixed cutting parameters. The third pass, the finishing (*F*) cut, was carried out at conditions that conformed to the design of experiment. The workpiece diameter was measured prior to and following each cut. Positional errors of the cutting tool were therefore adjusted, and errors between the set and actual *doc* were maintained within a 3% tolerance. The majority of the tests were within  $\pm 2\%$  error. A process flowchart of the cutting test procedure is shown in Fig. 3.3.

Machined surfaces were examined to ensure that they had no signs of chatter. To ensure consistency of the results and to minimize the effect of tool wear, a fresh cutting edge was used for each pass.

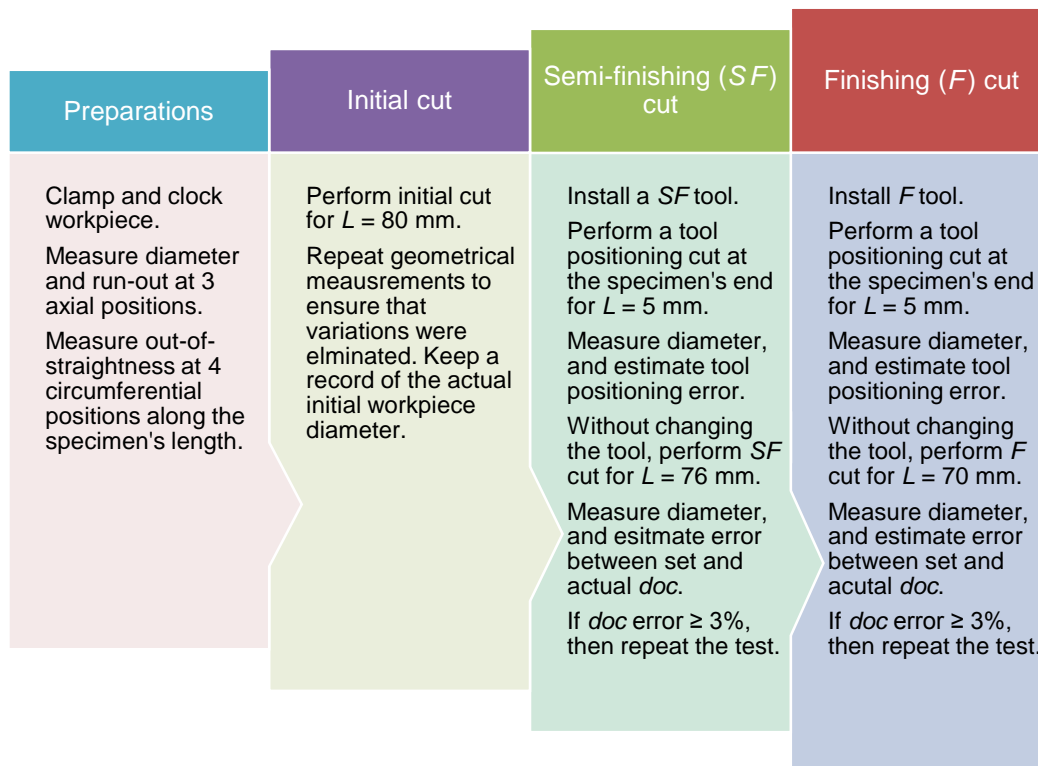


Fig. 3.3: process flowchart for the 3D oblique cutting test procedure for Alloy 1.

Oblique cutting conditions are described throughout by the cutting parameter combination  $(doc_i, v_i, f_i, R_i)$ , where  $doc$ ,  $v$ ,  $f$ , and  $R$  are the depth of cut, cutting speed, feed rate and tool corner radius, respectively.

### 3.3 Two-dimensional orthogonal cutting

#### 3.3.1 Orthogonal cutting for FE model calibration and validation

To calibrate and validate the FE model for residual stress prediction, a set of orthogonal cutting experiments was carried out. The experimental setup is shown in Fig. 3.4. Machining tests were performed in a dry environment without lubrication to eliminate its effect on the tribological interactions between the workpiece and the tool, specifically the friction and heat transfer at the tool/chip interface. Based on preliminary tests for Alloy 1, a length of cut  $L = 5$  mm was adopted to achieve steady-state machining with negligible tool wear. As no flood lubrication was used in these tests, temperature measurement by infrared imaging was possible. For this purpose, a FLIR SYSTEMS ThermoVision A20M infrared camera was installed. During cutting, the camera follows the motion of the tool in the feed direction and continually captures the temperature distribution in the workpiece surface, the cutting tool, and the forming chip in the vicinity of the cutting zone.

Specimen preparation was necessary for orthogonal cutting. The cylindrical bars of Ti-alloy were firstly sectioned into 2 parts of identical length. A groove was then end milled at one end of each part to produce a 25 mm deep tube. The selected tube thickness satisfied plane strain conditions by minimizing side flow. Finally, workpiece specimens were stress relieved prior to cutting to diminish initial stresses induced during preparation.

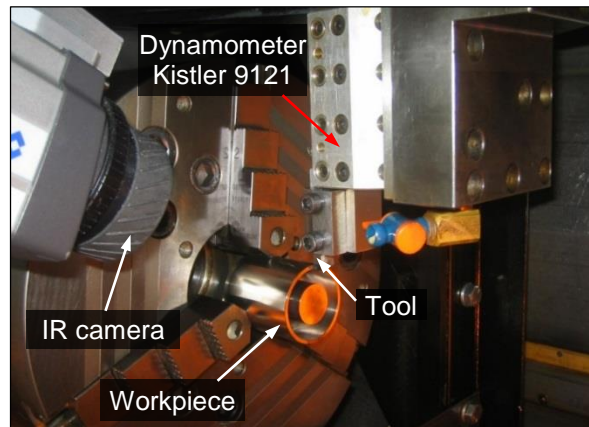


Fig. 3.4: experimental setup for dry orthogonal cutting for FE model calibration and validation.

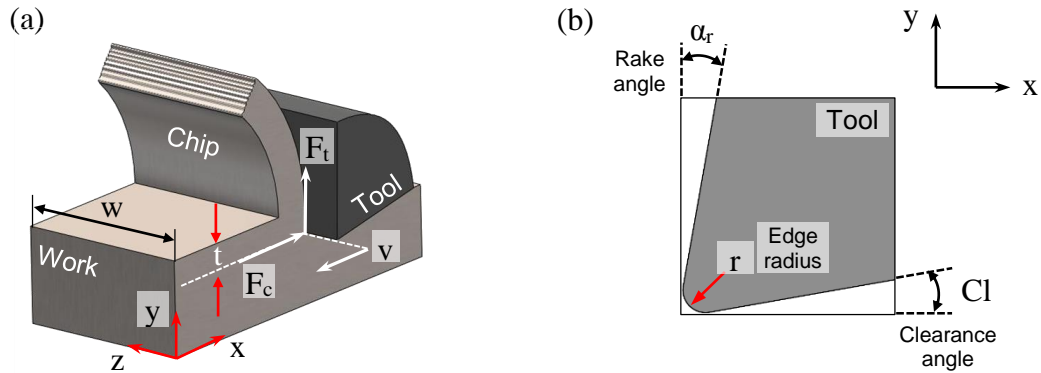


Fig. 3.5: orthogonal cutting: (a) process schematic and (b) representative tool geometry

Orthogonal cutting is an idealized two dimensional form of the cutting process mainly used for research purposes, where the cutting edge is maintained perpendicular to the cutting speed direction. The process schematic is shown in Fig. 3.5a. Two force components act on the tool tip as follows: (i) the cutting force ( $F_c$ ), parallel to the cutting speed, and (ii) the thrust force ( $F_t$ ), perpendicular to the cutting speed direction. The characteristic tool geometry is depicted in Fig. 3.5b. Orthogonal cutting conditions are represented throughout by the parameter combination ( $t$ ,  $v$ ), where  $t$  (mm) and  $v$  (m/min) are the uncut chip thickness and the cutting speed, respectively. Machining forces, temperature maps and residual stresses were acquired for a range of cutting conditions. In addition, chip specimens were metallographically prepared for chip morphology analysis.

### 3.3.2 Orthogonal cutting for material identification

To identify the constitutive law that describes the flow stress behavior of the workpiece material, dry orthogonal cutting tests were performed. A high intensity laser source with a fiber optic delivery system was incorporated into the setup for orthogonal cutting. In addition, a slip ring assembly was introduced that permits the measurement of workpiece surface temperature with the use of thermocouples. The experimental setup is shown in Fig. 3.6. The dynamometer and slip ring outputs were connected to data amplifiers, which were in turn connected to a data acquisition system (DAS) for machining force and temperature measurement. Specimens used for material identification had a similar geometry to those employed for FE model validation. They were, however, maintained at their original length (100-120 mm) to facilitate laser beam impingement and connection to the slip ring assembly.

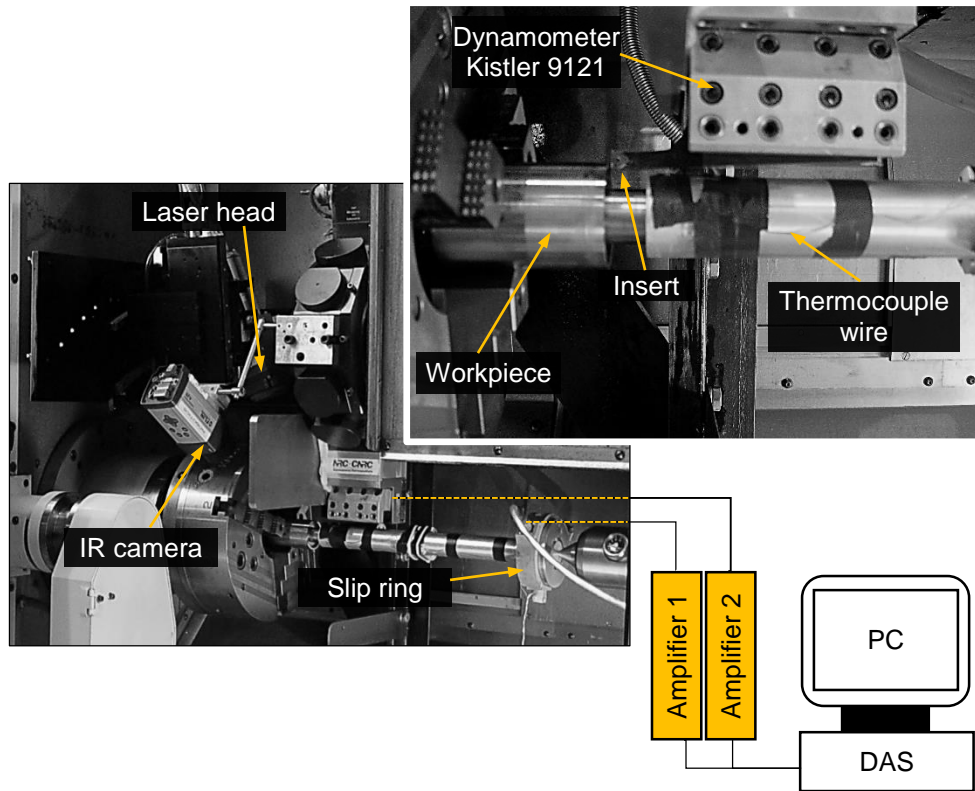


Fig. 3.6: orthogonal cutting with laser-assisted preheating for material identification.

Two types of material identification tests were carried out as follows: (i) room temperature (RT) tests, where the workpiece was maintained at ambient temperature prior to cutting, and (ii) high temperature (HT) tests, where the workpiece was preheated with a laser beam prior to cutting, thereby extending the temperature range of the constitutive data. The tests were designed to satisfy plain strain conditions and non-segmental chip formation through careful selection of cutting parameters. Machining was performed with standard uncoated carbide inserts, Sandvik TCMW 110204 grade H13A, suitable for non-ferrous heat resistant alloys. The inserts have the following geometrical properties: rake angle  $\alpha = 0^\circ$ , clearance angle  $Cl = 7^\circ$ , and cutting edge radius  $r = 0.02\text{-}0.04$  mm. The representative tool geometry of the orthogonal cutting process is depicted in Fig. 3.5b.

Machining forces, chip thickness, and the tool/chip contact length were acquired for a range of cutting conditions. In addition, chip morphology was inspected to ensure that chip segmentation was minimized since the adopted methodology was based on continuous non-segmental chip formation.

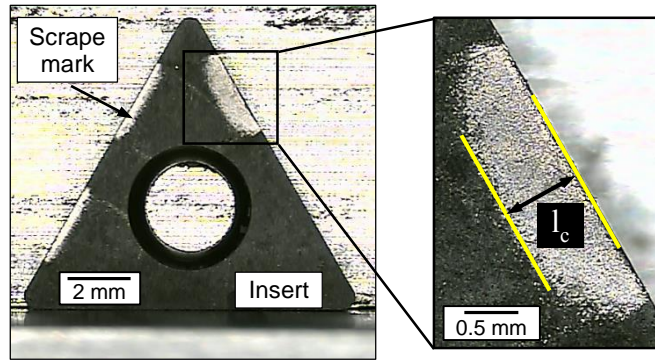


Fig. 3.7: images of tool/chip contact length ( $l_c$ ) obtained with a Winslow Engineering Model 560-Video tool analyser.

The chip thickness was measured at 5 different positions with a digital caliper. The contact length ( $l_c$ ) was determined with a tool analyzer (Winslow Engineering Model 560-Video) by measuring the scrape mark left by the chip on the rake face of the insert as shown in Fig. 3.7.

### 3.3.2.1 Calibration of laser power and workpiece material emissivity

To select a suitable power and “on” time for the laser that would preheat the workpiece surface to the desired temperature prior to cutting, preliminary laser heating tests were performed at several cutting speeds within the investigated range of parameters. These tests did not involve any machining. To avoid undesirable metallurgical changes in the workpiece surface, a preheating temperature of 450°C was chosen for the material identification tests at high temperature (HT). Two K-type (chromel-alumel) thermocouples were spot-welded onto the outer and inner surfaces of the workpiece within the targeted area of impingement of the laser beam. Connecting the thermocouple wires to the slip-ring allowed them to rotate freely with the workpiece specimen. A laser spot diameter of 4.3 mm was used to ensure preheating of sufficient material prior to HT orthogonal cutting.

A schematic diagram of the calibration setup is shown in Fig. 3.8. Two types of temperature measurements were made within the pre-heated region as follows: (i) measurements by thermocouple of the external surface temperature ( $T_{out}$ ) and the internal surface temperature ( $T_{in}$ ) of the workpiece specimen, providing an accurate indication of surface temperature prior to tool engagement, and (ii) infrared radiation measurements with the IR camera. This facilitated the calibration of material emissivity, which was essential for the correct interpretation of infrared thermal images.

As a result, a laser power  $P = 350 \text{ W}$ , a rotation speed  $v = 80 \text{ m/min}$ , and a laser “on” time  $t_{\text{on}} = 60 \text{ s}$ , were selected to attain a preheating temperature of  $450^\circ\text{C}$ . The temperature evolution at the above conditions, as measured by thermocouples is depicted in Fig. 3.9a.

To calibrate the emissivity of the cylindrical Ti-alloy specimens, the temperature evolution captured by the IR camera was compared to that measured with the thermocouples. The material’s emissivity was then adjusted in the infrared image capturing software to yield the best match between the thermal histories measured by both methods. Consequently, the correct value of emissivity was acquired. This value was then utilized in the interpretation of the thermal images captured by the IR camera during the orthogonal cutting tests.

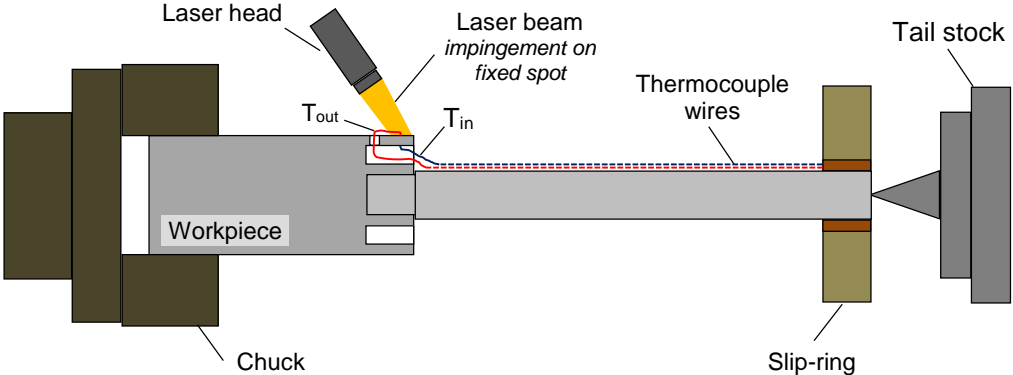


Fig. 3.8: schematic diagram of the experimental setup for laser power and workpiece material emissivity calibration.

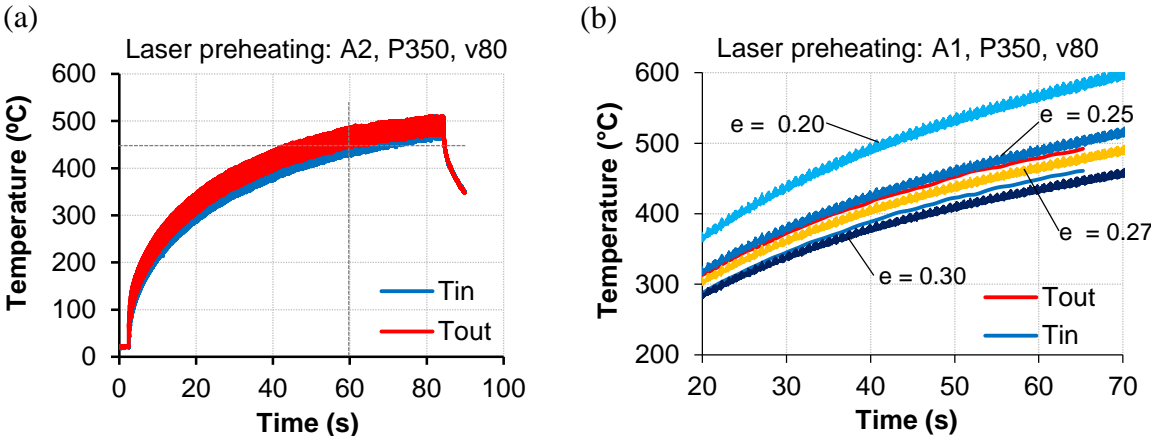


Fig. 3.9: temperature evolution during laser preheating with power  $P = 350 \text{ W}$  and speed  $v = 80 \text{ m/min}$ : (a) Alloy 2: thermocouple measurements, (b) Alloy 1: comparison between thermocouple and infrared measurements for various emissivity ( $e$ ) values.

Within the investigated range of cutting speeds ( $v = 20\text{-}90$  m/min), the emissivity of Alloy 1 was found to change from 0.25 to 0.27 with increasing speed. A comparison between the thermal histories extracted from the infrared images for various emissivity ( $e$ ) values and those measured by thermocouples is shown in Fig. 3.9b. It is evident that for a speed  $v = 80$  m/min, the emissivity  $e = 0.27$  results in good agreement with the external ( $T_{\text{out}}$ ) and internal ( $T_{\text{in}}$ ) surface temperatures of the tube shaped specimen.

## 3.4 Experimental measurements

### 3.4.1 Machining forces

A system comprised of a Kistler 9121 tool holder dynamometer, three Kistler 5010 charge amplifiers, and a data acquisition system (DAS) was used to measure force signals during cutting. The amplifiers convert the dynamometer's charge signals into voltage outputs proportional to the forces sustained during cutting. The combined error rating of the dynamometer and charge amplifiers is  $\pm 2\%$ , arising from linearity, hysteresis, and crosstalk. The frequency response range of the system is from 0 to 200 kHz. Based on the current work and on previous tests for several materials including Ti-alloys, the uncertainty in force measurement at a confidence level of approximately 95% is within  $\pm 10\%$  of the nominal steady-state value. The uncertainty arises from dynamometer errors, machine tool imprecision, and microstructural inhomogeneity (see section 4.3.2).

During oblique turning of Alloy 1, force data were sampled at a rate of 20 kHz to capture cyclic forces arising from chip segmentation. Typical signals acquired for the cutting force component,  $F_c$ , are depicted in Fig. 3.10 for various test conditions. Results are normalized as explained in section 4.3.1. For each cutting condition, a steady-state average value was estimated for each force component, neglecting tool run-in and disengagement regions. Throughout the analysis of results, machining forces for a specific cutting condition were represented by their steady-state average values. In addition, a steady-state machining region of around 25 mm common to all specimens was identified at the center of the cutting path where the variation in cutting force was within  $\pm 10\%$  from the steady-state average. Consequently, residual stress measurement (RSM) and near-surface microstructure (NSM) evaluation were performed within this region. The same approach was adopted for Alloy 2.

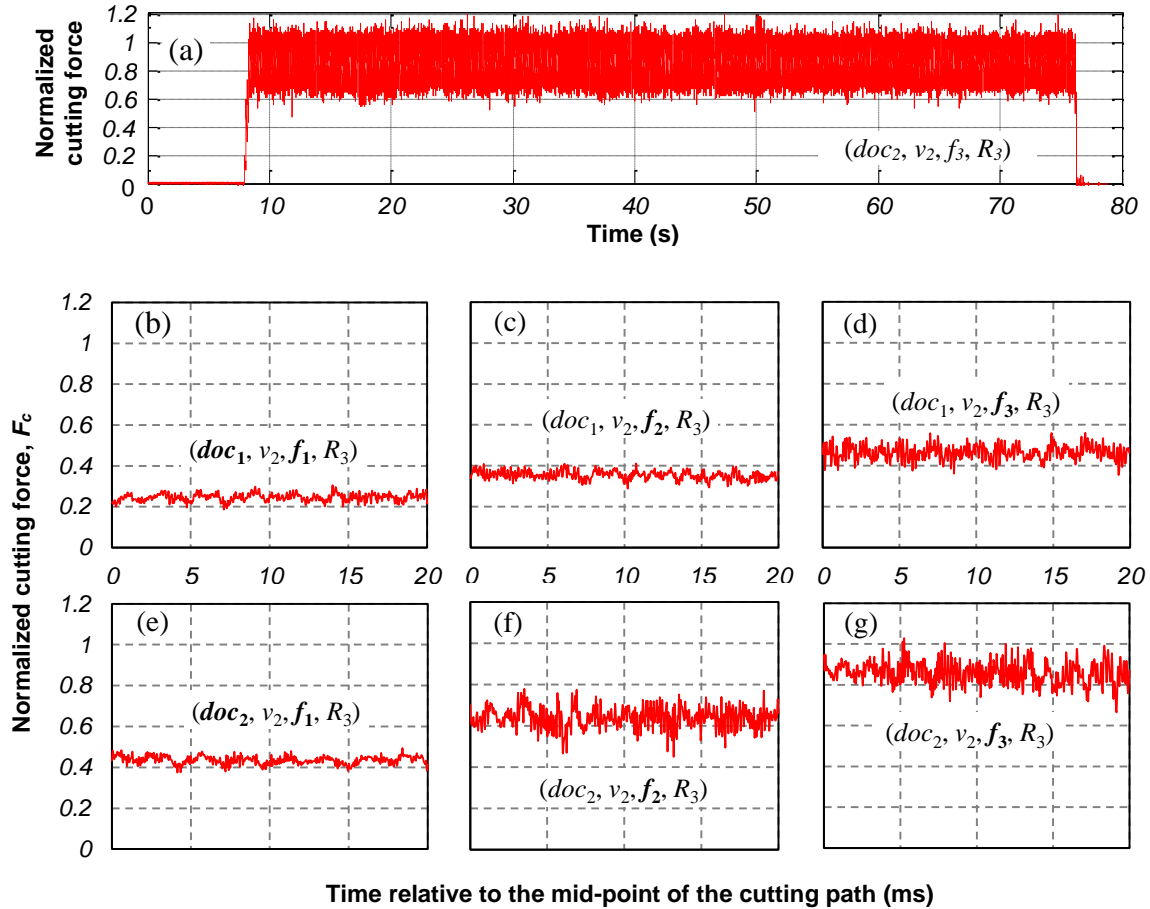


Fig. 3.10: cutting force ( $F_c$ ) signals acquired for Alloy 1 at conditions  $(doc_i, v_2, f_i, R_3)$ , spanning: (a) the entire cutting path, and (b-g) 20 ms after the midpoint of the cutting path.

### 3.4.2 Cutting temperature

During dry orthogonal cutting tests, non-contact temperature measurement was made with a FLIR Systems ThermoVision A20M infrared imaging camera. The camera features micro-bolometer focal plane array (FPA) detector technology that allows it to capture small temperature variations as low as  $0.12^\circ\text{C}$ . Furthermore, the camera's rated accuracy is  $\pm 2\%$  in the temperature range of  $120$  to  $900^\circ\text{C}$ . Thermal images were acquired with a sampling frequency of  $60$  Hz with the use of image acquisition software ThermoCAM Researcher Pro developed by FLIR Systems Inc. For the investigated range of cutting parameters, the chip produced during orthogonal cutting of both Ti-alloys had a continuously winding and non-fragmented nature. Consequently, the cutting zone was largely obscured by the forming chip, as evidenced in Fig. 3.11. As a result, the temperature at the free surface of the nascent chip at several instances during cutting was used in the analysis.

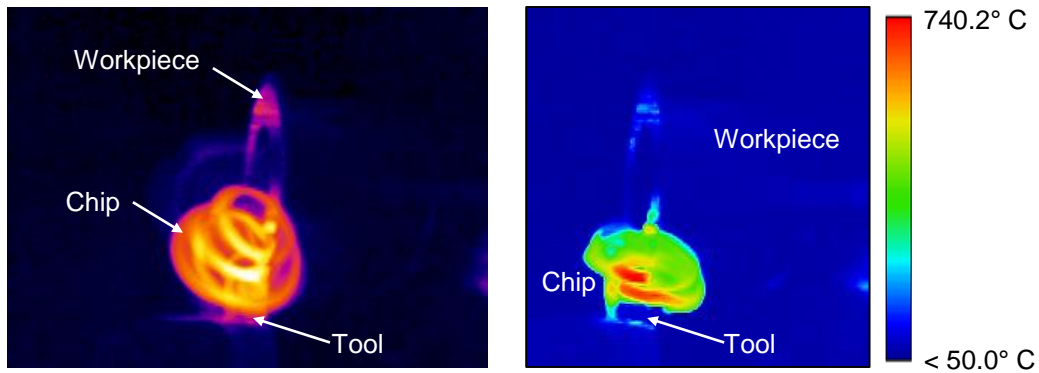


Fig. 3.11: thermal images obtained during orthogonal cutting of Alloy 1 at condition  $(t_3, v_3)$ . The cutting zone is obscured by the continuously winding chip.

### 3.4.3 Surface topography

#### 3.4.3.1 Visual inspection of the machined surface after 3D oblique turning

To confirm the stability of the process, the machined surface was examined at low magnification for evidence of chatter marks. Fig. 3.12 shows the surface of two specimens of Alloy 1 machined at relatively harsh conditions  $(doc_2, v_2, f_3, R_i)$ , but with varying corner radius  $R$ . The machined surfaces revealed no signs of chatter, which was confirmed by the absence of high amplitude low-frequency cyclic forces in the cutting force signals (Fig. 3.10) and by the lack of severe attrition wear and chipping in the cutting tools.

#### 3.4.3.2 Surface roughness measurements for 3D machined specimens

Surface roughness measurements were performed with a Taylor Hobson Form Talysurf Series 2 profilometer as per the setup depicted in Fig. 3.13. The machined sample was placed in a magnetic V-block, and roughness was measured along the specimen axis in the feed direction (Fig. 3.13a). Two-dimensional linear scans were performed spanning the entire finish turned surface (40-60 mm) to examine the evolution of roughness throughout the passage of the tool. Four scans were carried out for each specimen at four circumferential positions separated by  $90^\circ$  as shown in Fig. 3.13b, and an average  $R_a$  value was calculated for each test condition. In addition,  $R_a$  values were extracted for the steady-state machining region located at the center of the tool path, and spanning 25 mm. Upon comparison of the results, little variation was observed between the  $R_a$  values for the full span and steady-state regions. Moreover, several specimens machined at selected cutting conditions were subjected to three-dimensional surface topography scans within the steady-state region.

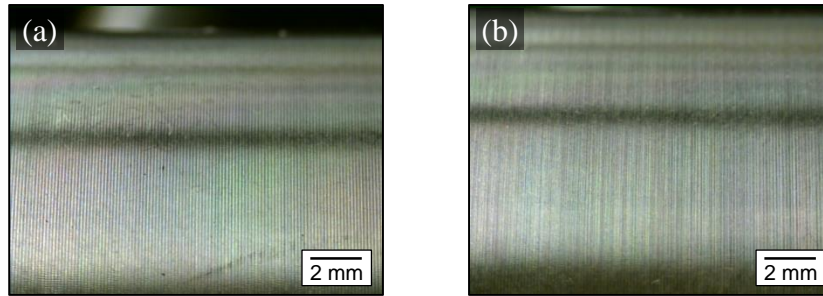


Fig. 3.12: surface of Alloy 1 specimens revealing no signs of chatter after oblique turning at relatively harsh conditions: (a) ( $doc_2, v_2, f_3, R_1$ ) and (b) ( $doc_2, v_2, f_3, R_3$ ).

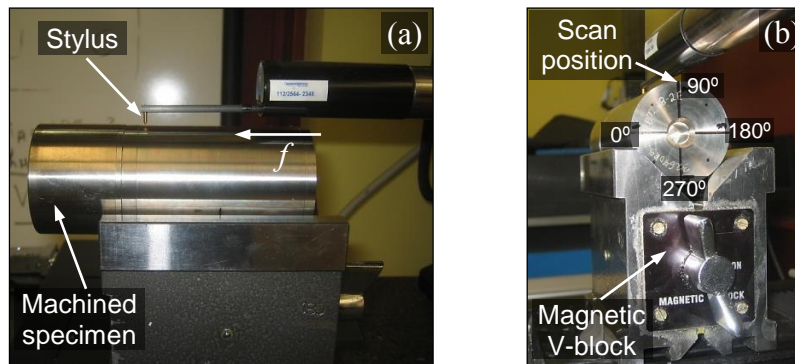


Fig. 3.13: surface roughness measurement setup for 3D machined specimens.

### 3.4.4 Microstructure evaluation

#### 3.4.4.1 Metallographic preparation of machined specimens

Cylindrical specimens having undergone oblique cutting were firstly sectioned with an electrical band saw into four identical coupons shaped like quarter cylinders and spanning the entire cutting path as shown in Fig. 3.14. To avoid thermal damage and metallurgical alterations of sections, low feed rate and cutting speed were employed along with flood lubrication. This approach allowed the near-surface microstructure (NSM) evaluation and residual stress measurement (RSM) to be performed on different coupons, but at the same axial location within the steady-state machining region as indicated in Fig. 3.14.

Next, two NSM samples of suitable size were extracted from a representative coupon for selected test conditions. To prevent thermal damage of the sectioned surfaces, a SiC abrasive disk was used at low feed rates (0.02-0.05 mm/s) with the assistance of flood lubrication. The coupons were secured in a V-block that was in turn clamped in a hydraulic vice to ensure a sufficiently stiff fixture during sectioning.

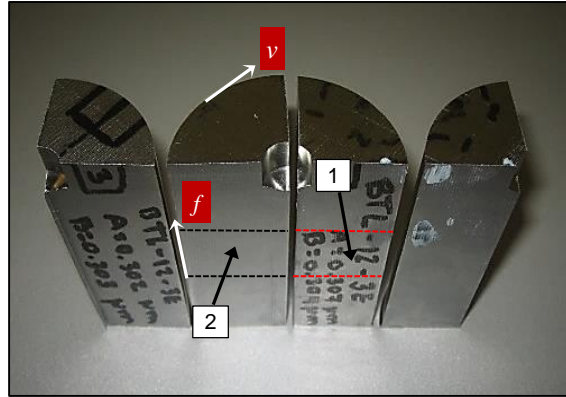


Fig. 3.14: quarter cylinder coupons sectioned from a 3D turned bar. The NSM evaluation and RS measurements were performed on separate coupons (1 and 2) within the steady-state region.

Following their extraction, the NSM samples were hot-mounted in Struers PolyFast carbon filled Bakelite resin, providing good edge retention and high conductivity. Sections were mounted in two different orientations, parallel to the feed and to the cutting speed. Samples were then polished by means of a 3-step procedure especially devised for Ti-alloys as follows: (i) fine grinding with P500 grit SiC paper, (ii) polishing with 9  $\mu\text{m}$  diamond slurry, and (iii) fine chemical-mechanical polishing with a colloidal silica ( $\text{SiO}_2$ ) suspension. Finally, the NSM samples were etched using Kroll's reagent that is composed of 100 ml of  $\text{H}_2\text{O}$ , 5 ml HF, and 2 ml  $\text{HNO}_3$ .

The metallographic preparation for 3D longitudinal turning comprised 40 Alloy 1 and 24 Alloy 2 NSM specimens, representing 20 and 12 carefully selected cutting conditions, respectively. To assess the effect of cutting parameters on chip morphology and the relevance of chip segmentation to the prediction of residual stresses, metallographic specimens of chips obtained during orthogonal cutting of Alloy 1 were prepared with the same procedure.

#### 3.4.4.1 NSM evaluation of machined specimens

Longitudinally turned NSM specimens having undergone metallographic preparation were examined under an Olympus GX-71 inverted optical microscope at high magnification. Firstly, the machined surface was inspected for machining artefacts including cracks, tears, gouges, and protrusions. Then, the near surface layer was examined for metallurgical alterations, including grain distortion and white layer formation. Several photomicrographs scanning various areas of the machined surface were obtained for each NSM specimen.

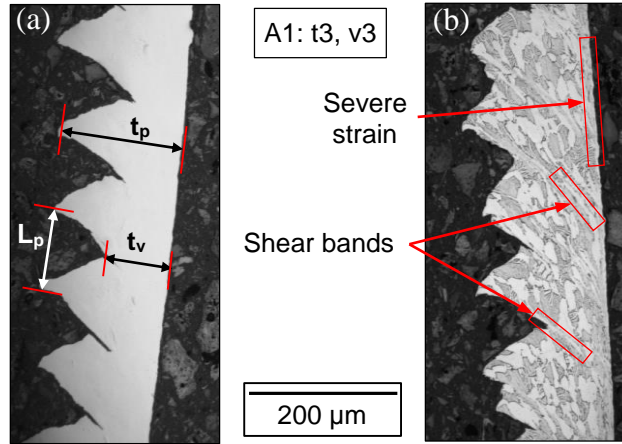


Fig. 3.15: images of chips produced in orthogonal cutting of Alloy 1 at condition ( $t_3$ ,  $v_3$ ), showing the evaluation of: (a) chip geometry and (b) microstructural features.

The morphology and microstructure of Alloy 1 chips obtained during orthogonal cutting were evaluated using the same setup. The peak thickness ( $t_p$ ), valley thickness ( $t_v$ ), and segmentation pitch ( $L_p$ ) were measured at high magnification as depicted in Fig. 3.15. The chips were also examined for strain localization or shear banding.

### 3.4.5 Residual stresses

Residual stress measurement (RSM) was outsourced to Proto Manufacturing Ltd., which specializes in automated non-destructive testing (NDT). Surface residual stresses in the cutting (hoop) direction of the specimen were measured using the x-ray diffraction (XRD) method. All measurements were performed with the Proto LXRD stress analyzer as shown in Fig. 3.16. A Cu target was used to generate  $K\alpha$  radiation with a wavelength  $\lambda = 1.542 \text{ \AA}$ . Diffraction measurements were collected using the multiple exposure technique (MET) in conjunction with the  $\sin^2 \psi$  method [112]. A minimum of 22 tilt angles  $\psi$  were used for each measurement as per standard SAE HS784. A Gaussian function was applied to fit the diffraction peaks. Instrument alignment was verified according to standard ASTM E 915. Calibration was carried out using stress free Ti powder. Measurements for 3D longitudinal turning were performed on quarter cylinder shaped coupons as shown in Fig. 3.16a. The orthogonal cutting workpiece specimen was not altered as a precaution against errors arising from damage and/or deflection of thin sections during specimen preparation (Fig. 3.16b). In both cases, no further surface preparations were necessary prior to RSM.

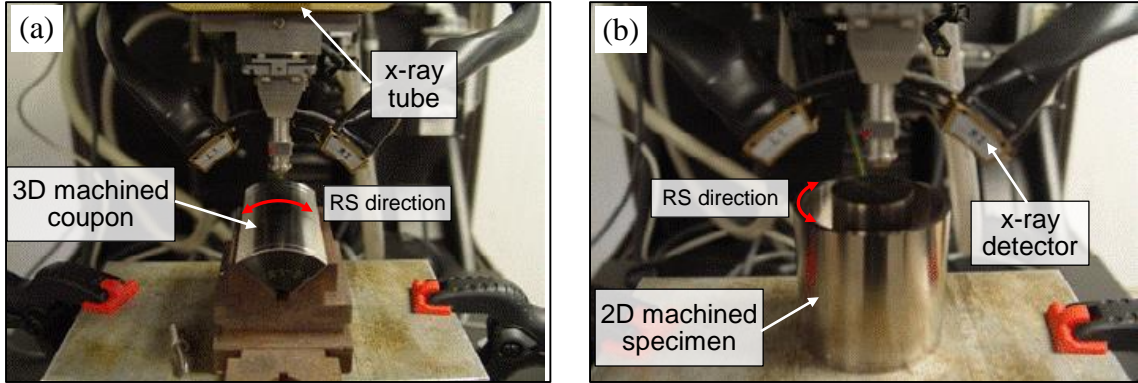


Fig. 3.16: Proto LXR D goniometer with: (a) 3D machined coupon, (b) orthogonally machined sample [112]. *Images courtesy of Proto Manufacturing Ltd.*

### 3.4.6 Hardness distribution

Micro-indentation tests were performed with a Struers Duramin A-300 hardness tester using a Vickers indenter and an indentation force of 100 g. The tests were performed on metallographic samples previously prepared for NSM evaluation in the polished state. To quantify the hardness distribution in the near-surface layer and in the material bulk, an array of indentations was applied in a plane perpendicular to the machined surface and parallel to the direction of axial feed as shown in Fig. 3.17.

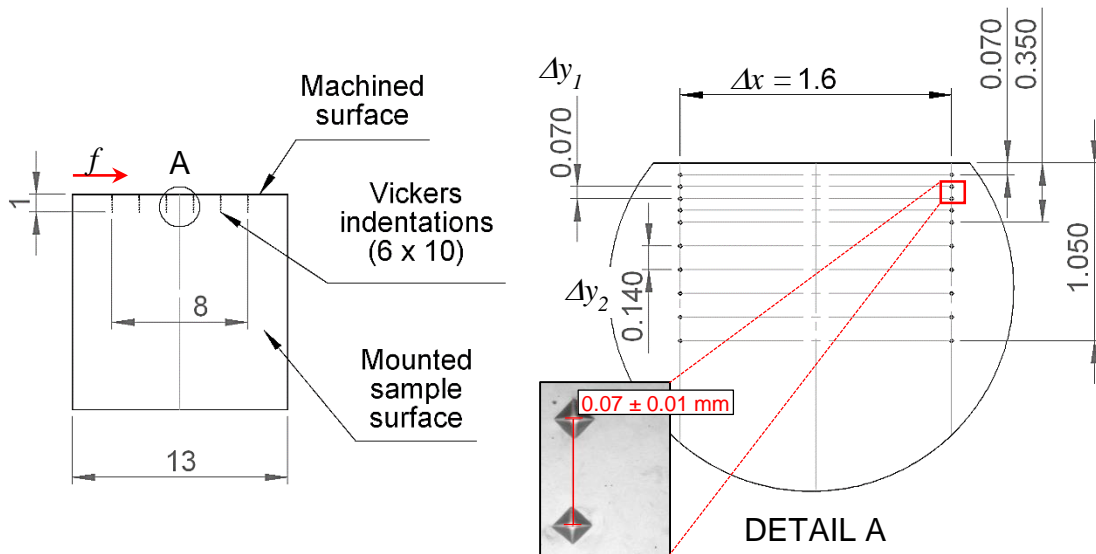


Fig. 3.17: schematic diagram depicting the array of 60 micro-hardness indentations performed on polished surfaces perpendicular to the machined surface and parallel to the direction of axial feed.

*All dimensions are in mm.*



Flank wear is most widely used for the monitoring of tool condition. According to ISO 3685, cemented carbide tools should be rejected when one of the following criteria is satisfied: (i) average flank wear  $VB_B = 0.3$  mm, (ii) in case of irregular flank wear, maximum flank wear  $VB_B \text{ max.} = 0.6$  mm, or (iii) when crater wear is the dominant, crater depth  $KT = 0.06 + 0.3 f$ , where  $f$  is the feed rate.

Using the above as guidelines, a Winslow Engineering Model 560-Video tool analyzer was used for the inspection of cutting tools and inserts for flank and crater wear. Other common forms of wear, including plastic deformation, mechanical fatigue cracking, chipping, and built-up edge were also examined. The system was calibrated with an ocular scale to ensure the accuracy of measurements.

# CHAPTER 4 EXPERIMENTAL RESULTS

## 4.1 Introduction

In this chapter, the design of experiments adopted for oblique and orthogonal cutting is introduced, followed by a detailed discussion of the experimental results. The Ti-alloys, Ti-6Al-4V and Ti-6Al-2Sn-4Zr-6Mo, under study are referred to as Alloy 1 and Alloy 2, respectively in the text and as A1 and A2 in the figures. Notations and symbols referring to oblique cutting are presented in italic form, whereas those pertaining to orthogonal cutting are not italicized. Results are presented in normalized form due a confidentiality agreement with the industrial partner.

## 4.2 Design of experiments

### 4.2.1 Oblique single point turning

In the absence of detailed publications on machining-induced residual stresses in Ti-alloys, the investigated parameters were selected based on published findings for various difficult-to-machine materials, including nickel-based superalloys, stainless steels, and bearing steels, and on the requirements of the industrial partner. These parameters are depth of cut ( $doc$ ), cutting speed ( $v$ ), feed rate ( $f$ ), and the tool corner radius ( $R$ ). Except for the corner radius, all geometrical features of the tool were maintained at fixed levels throughout the tests. Schematic diagrams of the process and its characteristic tool geometry are shown in Fig. 3.2. A full factorial experiment with 36 parameter combinations was performed for Alloy 1. The levels assigned to each parameter, and the range covered during the oblique cutting tests are listed in Table 4-1.

Table 4-1: range of cutting parameters for oblique single point turning.

| Parameter     | Symbol | Range       |        | Parameter levels           |
|---------------|--------|-------------|--------|----------------------------|
| Depth of cut  | $doc$  | 0.1 – 0.3   | mm     | 2, where $doc_2 > doc_1$   |
| Cutting speed | $v$    | 20 – 90     | m/min  | 2, where $v_2 > v_1$       |
| Feed rate     | $f$    | 0.05 – 0.25 | mm/rev | 3, where $f_3 > f_2 > f_1$ |
| Corner radius | $R$    | 0.2– 1.6    | mm     | 3, where $R_3 > R_2 > R_1$ |

The test matrix for Alloy 2 was reduced to 24 cutting conditions through the following changes: (i) exclusion of intermediary corner radius level  $R_2$  at low depth of cut conditions and (ii) elimination of intermediary feed rate level  $f_2$  at high depth of cut conditions. The oblique turning test matrices for both alloys are presented Table A-1, Appendix A. Due to the limited availability of specially prepared workpiece material and cutting tools, and the time consuming nature of the tests (section 3.2.2), only some tests were repeated.

## 4.2.2 Orthogonal cutting

### 4.2.2.1 Orthogonal cutting for FE model calibration and validation

A full factorial design of experiments was implemented with one repetition per cutting condition for both Ti-alloys under study. Two cutting parameters were investigated as follows: the uncut chip thickness ( $t$ ) and the cutting speed ( $v$ ). A schematic diagram of the process and its representative tool geometry are shown in Fig. 3.5. The levels assigned to each parameter and the range covered during orthogonal cutting are given in Table 4-2. The range of cutting parameters is identical to that of oblique cutting. While 9 parameter combinations were investigated for Alloy 1, the test matrix for Alloy 2 was reduced to 4 conditions. This was achieved by eliminating the intermediary uncut chip thickness and cutting speed levels,  $t_2$  and  $v_2$ , respectively. The cutting width ( $w$ ), rake angle ( $\alpha_r$ ), and clearance angle ( $Cl$ ) were maintained at fixed levels throughout the tests.

A preliminary orthogonal cutting experiment was performed to determine a suitable cutting length ( $L$ ) that achieved steady-state cutting with negligible tool wear. Cutting tests were carried out with various combinations of uncut chip thickness and cutting speed ( $t_i, v_i$ ). For each condition, two tests were performed with varying cutting lengths:  $L_1 = 0.6$  mm and  $L_2 = 5.75$  mm. Tool wear was found to be minimal for both cutting lengths, and observations using optical microscopy were supported by surface profilometry scans. Consequently, a cutting length  $L = 5$  mm was selected for these tests.

Table 4-2: investigated range of parameters for orthogonal cutting.

| Parameter            | Symbol | Range       |       | Parameter levels           |
|----------------------|--------|-------------|-------|----------------------------|
| Cutting speed        | $v$    | 20 – 90     | m/min | 3, where $v_3 > v_2 > v_1$ |
| Uncut chip thickness | $t$    | 0.05 – 0.25 | mm    | 3, where $t_3 > t_2 > t_1$ |

#### 4.2.2.2 Orthogonal cutting for material identification

The test matrix for material identification was designed around the range of parameters given in Table 4-2 . At an uncut chip thickness  $t = 0.25$  mm, however, a heavily segmented chip was formed in comparison with  $t = 0.1$  mm, as shown in Fig. 4.1. Since the Distributed Primary Zone Deformation (DPZD) model used for material identification [89, 90] estimated state variable distributions for continuous non-cyclic chip formation as elaborated in section 5.2.1, the uncut chip thickness was varied within the range of 0.05 to 0.1 mm to avoid severe segmental chip formation. Material identification was performed for both alloys under study. The constitutive data generated by the identification process covered the following state variable ranges approximately:

- Effective strain:  $\bar{\epsilon} = 0.002 \sim 1.5$ .
- Effective strain rate:  $\dot{\epsilon} = 0.001 \sim 2.8 \times 10^4 \text{ s}^{-1}$ .
- Temperature:  $T = 20 \sim 720^\circ\text{C}$ .

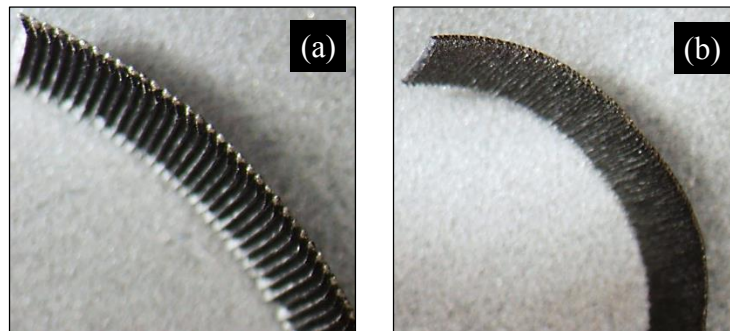


Fig. 4.1: chip morphology formed by room temperature (RT) orthogonal cutting at low speed, and with uncut chip thickness: (a)  $t = 0.25$  mm and (b)  $t = 0.1$  mm.

### 4.3 Results and discussion

#### 4.3.1 Normalization of experimental data

Due to a confidentiality agreement with the project's industrial partner, experimental results are presented in normalized form. An approach is adopted that accurately reflects behavioral trends and clearly contrasts the behavior of the two Ti-alloys. Experimental results were normalized with respect to the cutting condition at which the largest compressive RS were obtained within the investigated cutting regime. Different reference conditions were adopted for oblique and orthogonal cutting.

Oblique cutting results for machining forces, tool wear, RS, and surface roughness were normalized with respect to condition ( $A_2, (doc_2, v_2, f_3, R_1)$ ) associated with the Ti-6Al-2Sn-4Zr-6Mo alloy of higher strength. This condition corresponds to the highest material removal rate, cutting force, and flank wear, as well as the largest compressive RS. Vickers micro-indentation hardness values (HV, 0.1) were normalized against the bulk hardness of Alloy 2. As regards orthogonal cutting, RS and machining forces were normalized against condition ( $A_1, (t_3, v_1)$ ) associated with the Ti-6Al-4V alloy of relatively lower strength.

#### 4.3.2 Assessment of experimental uncertainty

To obtain a measure of experimental uncertainty, the expanded uncertainty approach recommended by the National Institute of Standards and Technology (NIST) US [114] was adopted in this work. An interval about the measurement result  $y_m$ , within which the measurand  $Y$  is confidently believed to lie, is defined by the expanded uncertainty  $U = k \cdot u_y$ , where  $k$  and  $u_y$  are the coverage factor and the standard deviation, respectively. Therefore, it is believed that  $y_m - U \leq Y \leq y_m + U$  with a certain level of confidence determined by the coverage factor  $k$ . Measurement results are commonly reported in the form of  $Y = y_m \pm U$ . By convention the value  $k = 2$  corresponding to a confidence level of 95% is used at NIST and was adopted in this work.

For machining force measurement, the interval corresponding to 95% confidence was found to be within  $\pm 10\%$  of the acquired nominal steady-state value for the three machining force components. In other words  $F = F_m \pm 10\%$ , where  $F$  designates the actual force component and  $F_m$  its measured value. This uncertainty is attributed to several factors including dynamometer errors, machine tool imprecision, microstructural variations in the workpiece material, and inconsistencies in tool edge preparation. As explained in section 3.2.2, a semi-finishing (SF) pass was performed for every workpiece specimen during oblique cutting prior to the final finishing cut. For Alloy 1, a total of 36 SF cuts were performed with fresh cutting tools of identical geometry, and with fixed cutting parameters. Identical flood lubrication conditions were also maintained. The force data acquired during the SF tests was used to assess the experimental uncertainty. An example of the force signals acquired for 2 tests at identical SF conditions is given in Fig. 4.2. Moreover, previous orthogonal cutting tests performed with standard cutting tools for several aerospace and automotive alloys, including Ti-alloys, produced a similar result.

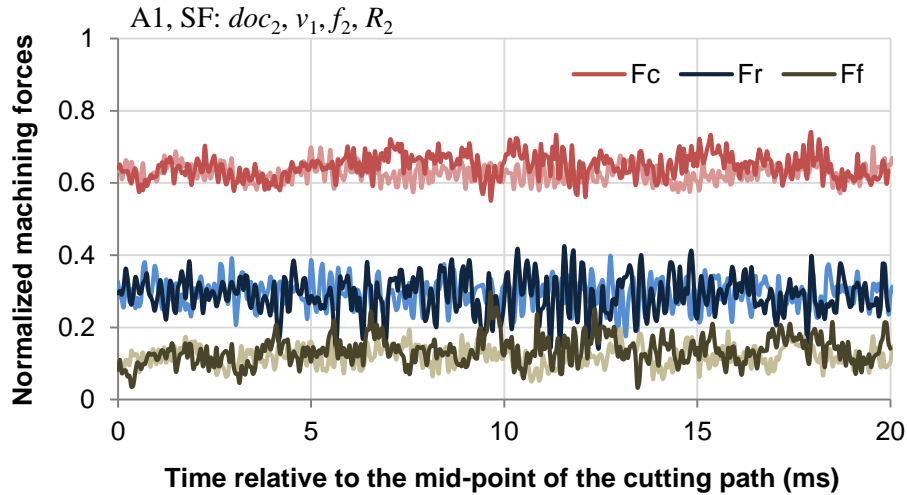


Fig. 4.2: machining force signals acquired for Alloy 1 during oblique cutting at identical semi-finishing conditions ( $doc_2, v_1, f_2, R_2$ ).

Due to the large number of cutting tests performed and associated cost implications, a similar treatment of residual stress measurements by XRD was not practical. An indication of RS measurement errors was supplied by Proto Manufacturing Ltd., however, for every inspected specimen.

### 4.3.3 Orthogonal cutting results

#### 4.3.3.1 Machining forces

The effect of cutting parameters on average steady-state machining forces and on the measured force signals for Alloy 1 is depicted in Fig. 4.3. The experimental uncertainty in force measurement is within  $\pm 10\%$  of the nominal value (section 4.3.2). It is represented by error bars in Fig. 4.3a. Within the investigated range of parameters, the uncut chip thickness,  $t$ , has a significant positive effect on machining forces. Increasing the uncut chip thickness by 150% ( $t_1$  to  $t_3$ ) produced an average increase in the cutting force ( $F_c$ ) and the thrust force ( $F_t$ ) of around 140% and 55%, respectively. This is due to the larger volume of material being removed and the subsequent need for higher cutting energy. Cutting speed has a smaller effect on forces. It appears that at low and intermediary uncut chip thickness levels, the material has undergone strain rate hardening. Increasing the speed by 150% ( $v_1$  to  $v_3$ ) increases  $F_c$  by approx. 35% at  $t_1$  and  $t_2$ , but little change is observed at  $t_3$ . The effect of cutting speed on  $F_t$  is, however, negligible. The force signals reflect the above trends.

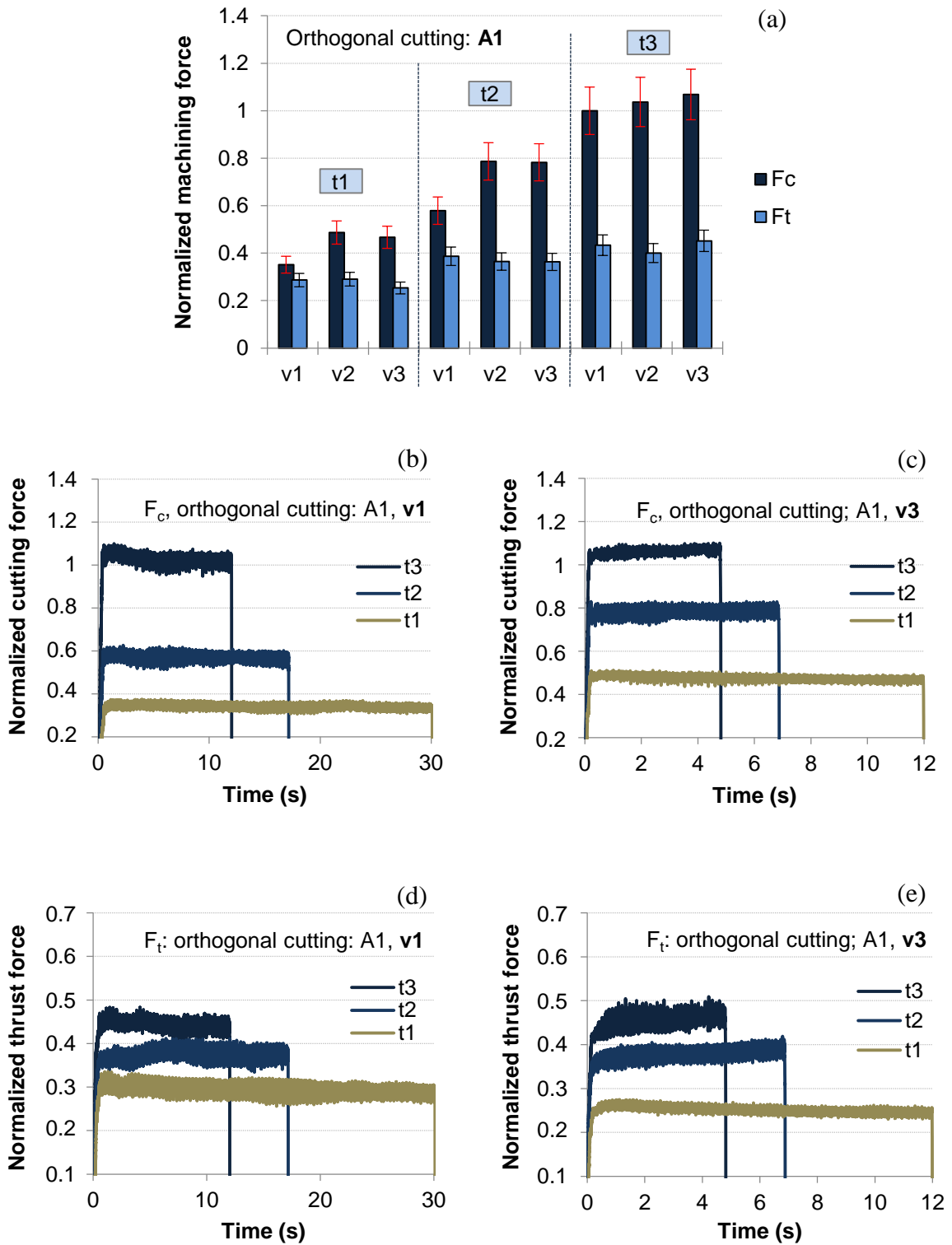


Fig. 4.3: effect of cutting parameters during dry orthogonal cutting of Alloy 1 on: (a) average steady-state machining forces, (b, c) cutting force signals, and (d, e) thrust force signals.

A comparison between the average steady-state force components for both Ti-alloys is presented in Fig. 4.4(a, b). The higher bulk hardness of Alloy 2 (section 4.3.4.8) and its lower sensitivity to thermal softening (discussed in Chapter 5) promoted machining forces of higher magnitude. Fig. 4.4a reveals that at low uncut chip thickness  $t_1$ , Alloy 2 sustained a larger cutting force ( $F_c$ ) by around 30% on average. Fig. 4.4b shows that at high cutting speed  $v_3$ , the thrust force ( $F_t$ ) exceeded Alloy 1 by about 45%.

Similar to Alloy 1, increasing the uncut chip thickness by 150% ( $t_1$  to  $t_3$ ) increased  $F_c$  and  $F_t$  by around 110% and 55%, respectively. Furthermore, the material underwent strain rate hardening with increasing speed. Although a minimal increase in  $F_c$  was observed, the effect of cutting speed on  $F_t$  was large. Unlike Alloy 1, increasing the cutting speed by 150% ( $v_1$  to  $v_3$ ) produced an average increase in  $F_t$  of around 40%. The force signals acquired during orthogonal cutting of Alloy 2 are depicted in Fig. 4.4(c, d) and reflect the above behavior.

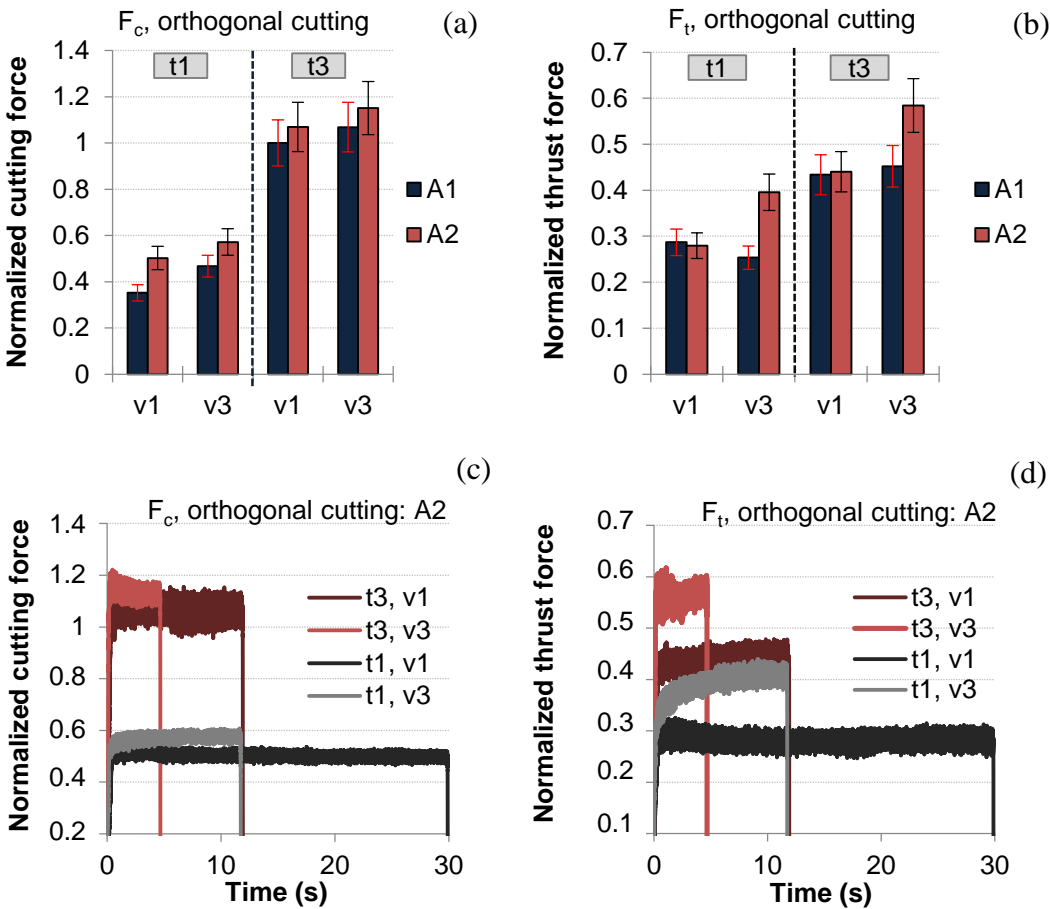


Fig. 4.4: effect of cutting parameters on: (a, b) average steady-state machining forces for Alloy 2 as compared to Alloy 1, and (c, d) Alloy 2 machining force signals.

#### 4.3.3.2 Residual stresses

Within the investigated range of parameters, residual stresses (RS) were found to be compressive in nature for both Ti-alloys, as shown in Fig. 4.5. The error in x-ray diffraction (XRD) measurements is within  $\pm 2\%$  and  $\pm 2.5\%$  for Alloy 1 and Alloy 2, respectively [112]. In the presence of good surface quality and suitable specimen geometry, the above error is mainly due to slight misalignment of the diffraction apparatus [7]. The experimental errors are represented by error bars.

For Alloy 1, residual stresses became more compressive with increasing uncut chip thickness,  $t$ . Increasing the uncut chip thickness by 150% ( $t_1$  to  $t_3$ ) produced an average increase (downwards shift) in compressive RS of around 25%. This suggests that at these conditions, the mechanical contribution to plastic deformation further outweighed its thermal counterpart, thereby promoting more compressive RS. Cutting speed, however, had the opposite effect. Increasing the cutting speed by 150% ( $v_1$  to  $v_3$ ) caused a small reduction (upwards shift) in compressive RS of about 10%. This is usually the result of a rise in temperature in the cutting zone and in the machined surface with increasing speed, thereby intensifying the thermal contribution to plastic deformation. An unexpected drop in compressive RS was observed at the intermediary uncut chip thickness and cutting speed condition ( $A_1$ , ( $t_2$ ,  $v_2$ )). This could be due to the changes in chip morphology associated with strain rate hardening of the workpiece material as elaborated in Chapter 6. The FE model revealed that variations in chip morphology can alter the loading conditions of the machined surface behind the tool tip, thereby affecting the magnitude of RS.

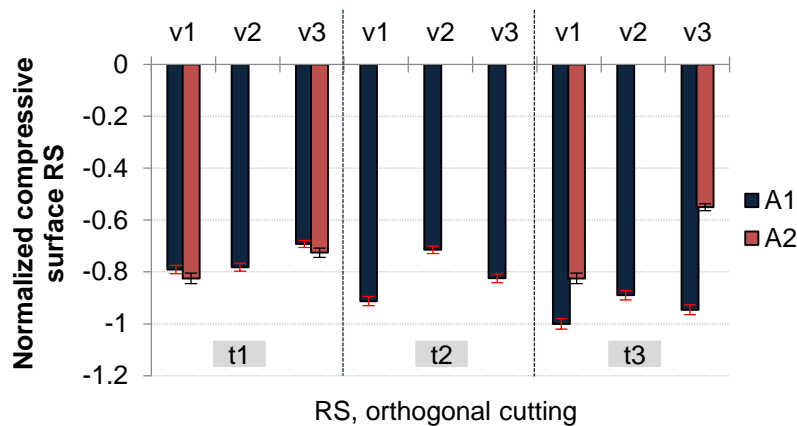


Fig. 4.5: surface residual stresses measured by x-ray diffraction (XRD) for both Ti-alloys, as a result of dry orthogonal cutting.

Compressive RS in Alloy 2 exhibited dissimilar behavior to Alloy 1 with increasing uncut chip thickness ( $t_1$  to  $t_3$ ). Although minimal change in RS occurred at low speed  $v_1$ , compressive RS diminished by around 25% at high speed  $v_3$ . As for the effect of cutting speed on RS, similar behavior to Alloy 1 was observed at low uncut chip thickness  $t_1$ , where increasing the speed from  $v_1$  to  $v_3$  reduced compressive RS by around 12%. At high uncut chip thickness  $t_3$ , however, compressive RS were reduced by about 33% with increasing speed, surpassing the residual stress reduction in Alloy 1 by around 3 times.

Firstly, in order to explain the dissimilar behavior of the Ti-alloys, a comparison was made of the temperatures measured by the infrared camera. It was revealed that at high uncut chip thickness  $t_3$ , the peak temperatures in the forming chip were higher by around 120°C on average for Alloy 2. This indicates more elevated temperatures at the tool/chip interface and at the machined surface, thereby promoting a reduction in compressive residual stresses. Next, a comparison was made of the flank wear (VB) at identical cutting conditions. Although similar flank wear was observed for both Ti-alloys at low uncut chip thickness  $t_1$ , the flank wear caused by Alloy 2 at high uncut chip thickness  $t_3$  was almost 1.5 times larger than that produced by Alloy 1 (Fig. 4.6).

It was concluded that the behavior of compressive RS exhibited by Alloy 2 consisting of: (i) minimal change at low speed and a reduction at high speed with increasing uncut chip thickness, and (ii) a larger drop with increasing speed at high uncut chip thickness relative to Alloy 1, is largely due to the thermal effect exacerbated by increased flank wear. At the same time flank wear could also have contributed to the small rise in machining forces beyond Alloy 1 shown in Fig. 4.4(a, b). The above conclusion for the effect of wear on temperature distribution and on RS is supported by the FE predictions. The results of a wide-ranging sensitivity analysis of the effect of flank wear on RS are presented in Chapter 5.

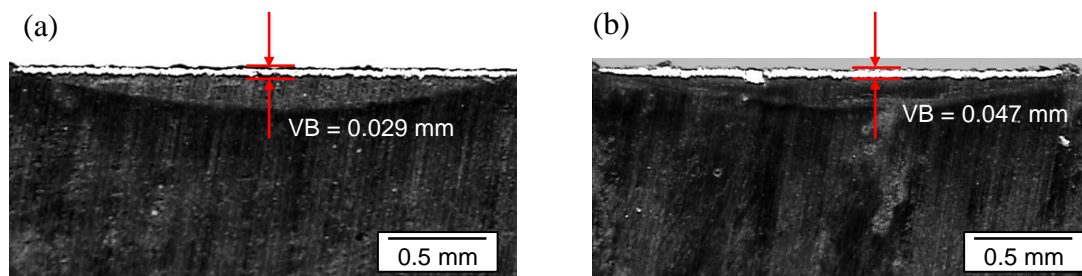


Fig. 4.6: flank wear (VB) produced in the carbide tools by (a) Alloy 1 and (b) Alloy 2 during dry orthogonal cutting at condition ( $t_3$ ,  $v_3$ ).

### 4.3.4 Oblique cutting results

In this section, a thorough analysis and discussion of the results obtained for oblique turning is presented, which encompasses: (i) process performance indicators, including machining forces and tool wear, and (ii) surface integrity, comprising surface roughness, residual stresses (RS), the near-surface microstructure (NSM), and hardness distribution. The comprehensive interpretation of the results for oblique cutting was supported by statistical analysis. Analysis of variance (ANOVA) was implemented to determine cutting parameters and their mutual interactions that have a statistically significant effect on machining forces and residual stresses. This also served in the development of empirical models for fast and accurate force and RS prediction.

#### 4.3.4.1 Machining forces

The effect of cutting parameters on the average steady-state machining forces for Alloy 1 is shown in Fig. 4.7 for various cutting parameter combinations ( $doc_i$ ,  $v_i$ ,  $f_i$ ,  $R_i$ ). Due to the inherent measurement errors (section 4.3.2), the experimental uncertainty in force measurement is within  $\pm 10\%$  of the nominal value. It is represented by error bars. It was determined that for both Ti-alloys, the feed force was much lower than the other force components, and a relationship between forces was established as follows:  $F_f \approx 0.2 \times F_c$  and  $F_r \approx 0.5 \times F_c$ , where  $F_c$ ,  $F_r$ , and  $F_f$  represent the cutting, radial and feed forces, respectively. Consequently, the discussion focuses on the cutting and radial force components.

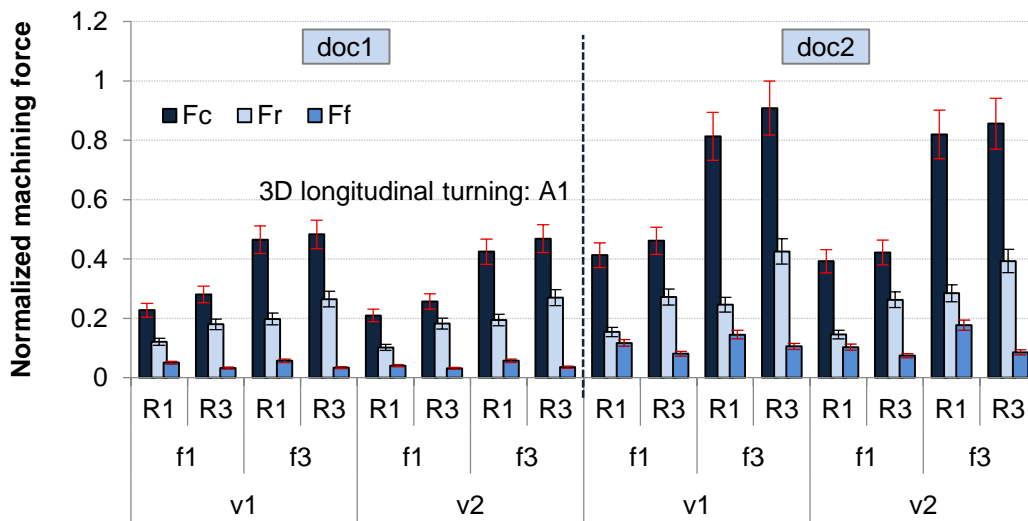


Fig. 4.7: average steady-state machining forces produced during oblique turning of Alloy 1 for various cutting parameter combinations ( $doc_i$ ,  $v_i$ ,  $f_i$ ,  $R_i$ ).

Within the investigated range of cutting parameters, depth of cut and feed rate have more significant effects on forces. The effect of increasing the depth of cut by 100% ( $doc_1$  to  $doc_2$ ) and increasing the feed rate by 150% ( $f_1$  to  $f_3$ ) is depicted in Fig. 4.7 for Alloy 1, and is summarized in Table 4-3 for both Ti-alloys. It is evident that due to the larger volume of material being removed and the subsequent need for higher cutting energy, both forces increased substantially. This is clearly reflected in the upwards shift of the cutting force signals with increasing depth of cut and feed rate as shown in Fig. 3.10. Although Alloy 2 exhibited similar behavior to Alloy 1, it sustained a larger increase in forces. This can be attributed to its higher sensitivity to strain hardening at the strain levels encountered in the shear zones, as discussed in Chapter 6.

Cutting speed had a small influence on forces in general. Increasing the speed by 150% ( $v_1$  to  $v_2$ ) reduced both cutting and radial forces by less than 10% for Alloy 1, which could be associated with a marginal increment in thermal softening with increasing speed. No such trend was identifiable for Alloy 2. However, as shown in Fig. 4.8, at high depth of cut and feed rate conditions ( $doc_2$ ,  $v_{1-2}$ ,  $f_3$ ,  $R_i$ ), Alloy 2 sustained an average increase with speed of around 10% and 40% in  $F_c$  and  $F_r$ , respectively, approaching 20% and 100% at small corner radius,  $R_1$ . This suggests that the workpiece material underwent strain rate hardening at these conditions. Although corner radius had a small effect on cutting force, its effect on radial force was significant. Increasing the corner radius by 200% ( $R_1$  to  $R_3$ ), increased  $F_c$  by around 10% for Alloy 1, whereas no clear trend was identifiable for Alloy 2. However,  $F_r$  was increased by more than 50% for both Ti-alloys.

In general, machining of Alloy 2 generated higher forces than Alloy 1, especially at conditions involving high depth of cut, cutting speed, and feed rate levels ( $doc_2$ ,  $v_2$ ,  $f_3$ ,  $R_i$ ). At these conditions, the cutting force  $F_c$  sustained by Alloy 2 exceeded Alloy 1 by around 15% on average (Fig. 4.8a).

Table 4-3: effect on forces of increasing depth of cut ( $doc$ ) and feed rate ( $f$ ).

| Percentage increase in cutting parameter | Mean percentage increase in force |           |           |           |
|--|-----------------------------------|-----------|-----------|-----------|
|  | Alloy 1                           |           | Alloy 2   |           |
|  | $F_c$ (%)                         | $F_r$ (%) | $F_c$ (%) | $F_r$ (%) |
| 100% increase in $doc$                   | 80                                | 40        | 86        | 56        |
| 150% increase in $f$                     | 99                                | 60        | 114       | 83        |

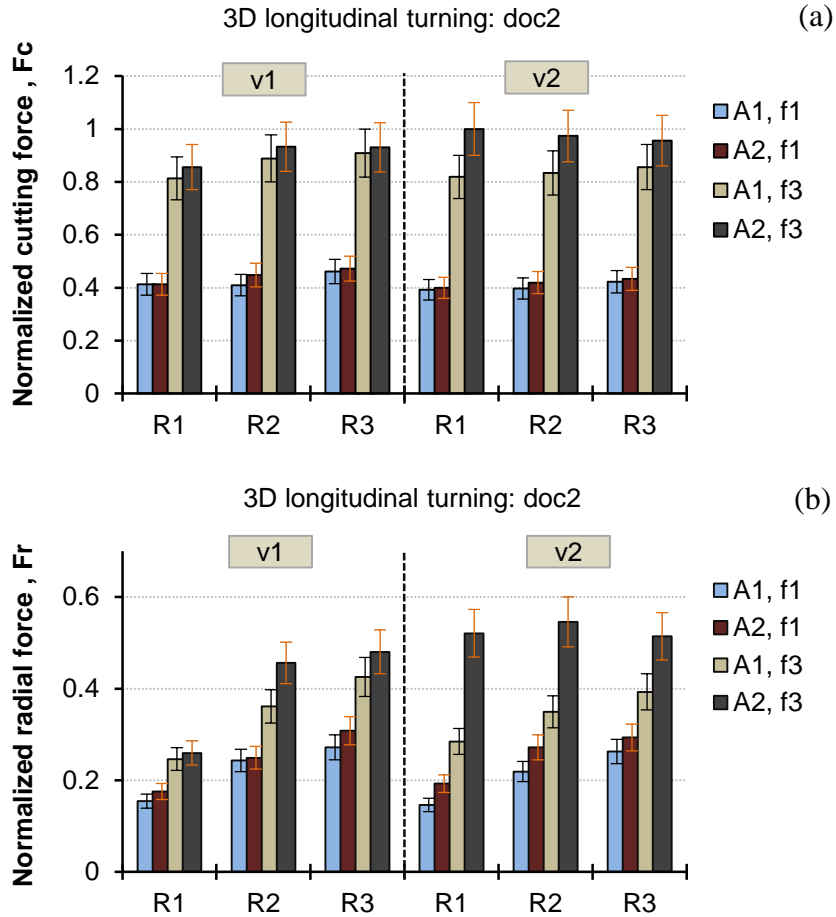


Fig. 4.8: effect of cutting parameters and Ti-alloy type on average steady-state (a) cutting and (b) radial forces generated during oblique turning at conditions ( $doc_2, v_i, f_i, R_i$ ).

The radial force  $F_r$  sustained by Alloy 2 surpassed Alloy 1 by around 20% on average over the entire range of conditions (Fig. 4.8b). The largest increase in  $F_r$  beyond Alloy 1, however, occurred at high levels of depth of cut, cutting speed, and feed, amounting to 55% on average and attaining around 80% at ( $doc_2, v_2, f_3, R_1$ ). The higher bulk hardness of Alloy 2 (section 4.3.4.8) and its lower sensitivity to thermal softening, as elaborated in Chapter 6, can contribute towards the generation of machining forces of higher magnitude at similar cutting conditions.

#### 4.3.4.2 Empirical models for machining force prediction

Empirical models for the prediction of the average steady-state machining forces were developed for both Ti-alloys based on the experimental force measurements for 3D cutting. The least squares approach and response surface methodology were adopted to generate mathematical equations expressing the 3 machining force components in terms of

the investigated cutting parameters and their mutual interactions. Model development was based on statistical analysis of variance (ANOVA). For both Ti-alloys, cutting force and radial force prediction errors were within  $\pm 10\%$ , while feed force prediction errors were within  $\pm 20\%$ . It should be noted, however, that the feed force is much smaller than the other force components, with  $F_f \approx 0.2 \times F_c$ , which explains the larger inaccuracies in feed force prediction. The empirical models for the prediction of average steady-state machining forces generated by Alloy 1 are given by:

$$F_c = a_0 + a_1 \left( \frac{doc - \alpha_1}{\alpha_2} \right) + a_2 \left( \frac{v - \beta_1}{\beta_2} \right) + a_3 f + a_4 R + a_5 \left( \frac{doc - \alpha_1}{\alpha_2} \right) (f - \gamma) \quad (4.1)$$

$$F_r = b_0 + b_1 \left( \frac{doc - \alpha_1}{\alpha_2} \right) + b_2 f + b_3 R + b_4 \left( \frac{doc - \alpha_1}{\alpha_2} \right) (f - \gamma) + b_5 \left( \frac{doc - \alpha_1}{\alpha_2} \right) (R - \delta) + b_6 (f - \gamma)^2 + b_7 (R - \delta)^2 \quad (4.2)$$

$$F_f = c_0 + c_1 \left( \frac{doc - \alpha_1}{\alpha_2} \right) + c_2 f + c_3 R + c_4 \left( \frac{doc - \alpha_1}{\alpha_2} \right) (f - \gamma) + c_5 \left( \frac{doc - \alpha_1}{\alpha_2} \right) (R - \delta) + c_6 (f - \gamma)^2 + c_7 (f - \gamma)(R - \delta) \quad (4.3)$$

where,  $F_c$ ,  $F_r$ , and  $F_f$  are the cutting, radial, and feed force components, respectively;  $doc$ ,  $v$ ,  $f$ , and  $R$  are the cutting parameters;  $a_0 - a_5$ ,  $b_0 - b_7$ , and  $c_0 - c_7$  are constants, and:

$$\alpha_1 = \frac{doc_1 + doc_2}{2} \quad \text{and} \quad \alpha_2 = \frac{doc_2 - doc_1}{2}, \quad (4.4)$$

$$\beta_1 = \frac{v_1 + v_2}{2} \quad \text{and} \quad \beta_2 = \frac{v_2 - v_1}{2}, \quad (4.5)$$

$$\gamma = \frac{f_1 + f_3}{2} \quad \text{and} \quad \delta = \frac{R_1 + R_3}{2} \quad (4.6)$$

A graphical comparison between empirically predicted (Emp) and experimentally measured (Exp) cutting forces generated by Alloy 1 for the full range of cutting conditions ( $doc_i$ ,  $v_i$ ,  $f_i$ ,  $R_i$ ) is given in Fig. 4.9. The significant increase in cutting force with depth of cut and feed rate is clearly reflected by both empirical and experimental data sets.

The accuracy of the models was assessed by plotting the force predictions against their experimental counterparts and the distribution of prediction errors over the range of investigated cutting conditions. An example of the above is shown in Fig. 4.10 for the cutting force sustained by Alloy 1. The model's high goodness of fit is evidenced in Fig. 4.10a. The coefficient of determination  $R_{sq} = 0.996$  indicates a good correlation between the cutting force  $F_c$  and the cutting parameters. The prediction error for the majority of conditions lies within  $\pm 5\%$  as shown in Fig. 4.10b.

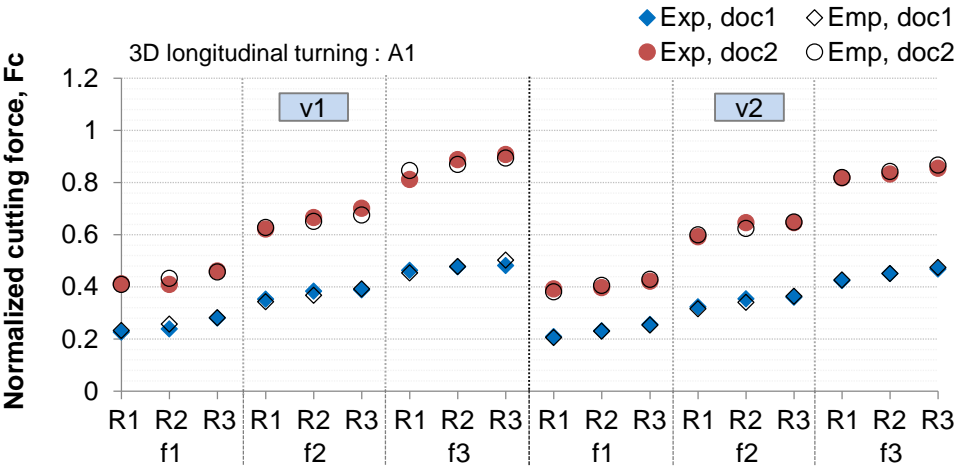


Fig. 4.9: comparison between empirically predicted (Emp) and experimentally measured (Exp) cutting forces for Alloy 1 for the full range of investigated conditions ( $doc_i, v_i, f_i, R_i$ ).

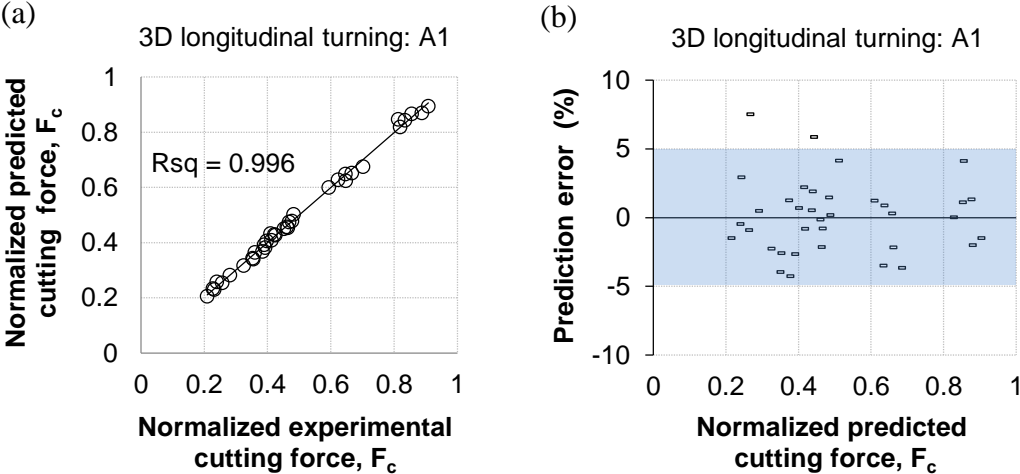


Fig. 4.10: (a) goodness of fit and (b) prediction error distribution for Alloy 1 oblique cutting force predictions over the full range of cutting conditions ( $doc_i, v_i, f_i, R_i$ ).

#### 4.3.4.3 Tool wear

The inspection of tool wear for finish turning was performed according to standard ISO 3685:1993 (section 3.4.7). No severe flank wear was observed in any of the tools, and cutting edges were free from chipping and plastic deformation. Cutting tools revealed no sign of built-up edge, cratering, or depth of cut notch wear. Light flank wear was observed, which was confined to the corner radius of the tool. The average flank wear land within the corner radius,  $VB_C$ , did not exceed 0.03 mm, and was around one order of magnitude below the rejection criterion for tungsten carbide tools recommended by the ISO standard.

Cutting speed is known to have a profound effect on tool wear when cutting Ti-alloys due to their low thermal conductivity and high reactivity with tool materials. The effect of cutting speed on tool wear was analyzed at relatively harsh cutting conditions within the investigated range of parameters, involving high depth of cut and feed rate ( $doc_2, v_i, f_3, R_i$ ). The effect of cutting speed on flank wear for both Ti-alloys is shown in Fig. 4.11.

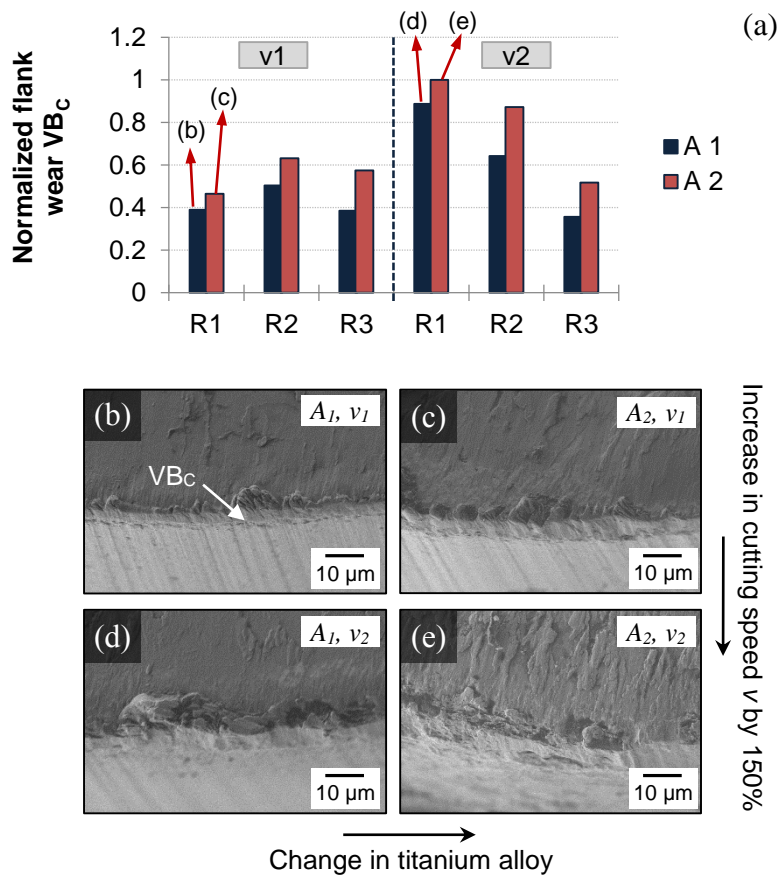


Fig. 4.11: effect of speed and workpiece material on average flank wear at the tool corner radius,  $VB_C$ , for both Ti-alloys at conditions: (a) ( $doc_2, v_i, f_3, R_i$ ) and (b-e) SEM images ( $doc_2, v_i, f_3, R_i$ ).

As expected, cutting speed was found to have a substantial effect on flank wear. Increasing the speed by 150% ( $v_1$  to  $v_2$ ) led to an average growth in  $VB_C$  of around 120% and 30% at low and intermediate corner radii  $R_1$  and  $R_2$ , respectively. Little change was observed, however, at large corner radius level  $R_3$ . In addition, flank wear at high cutting speed  $v_2$  seemed to grow with decreasing corner radius for both Ti-alloys.

Flank wear exhibited by the carbide tools when machining Alloy 2 was around 30% higher on average as compared to Alloy 1 (Fig. 4.11a). At conditions involving high depth of cut, speed, and feed ( $doc_2$ ,  $v_2$ ,  $f_3$ ,  $R_i$ ), Alloy 2 sustained an average increase beyond Alloy 1 of around 15% and 55% in the cutting and radial forces, respectively, reaching 20% and 80% at small corner radius  $R_1$ . Coupled with increasing speed, an upsurge in load can contribute towards a higher wear volume. The wear increment generated by Alloy 2 and by increasing the cutting speed is shown in Fig. 4.11(b-e) for small corner radius level  $R_1$ .

4.3.4.4 Residual stresses

Surface residual stresses (RS) were compressive in nature for both Ti-alloys. The effect of cutting parameters on compressive RS generated in Alloy 1 in the cutting (hoop) direction is shown in Fig. 4.12. The experimental errors in residual stress measurement by x-ray diffraction (XRD) fell within  $\pm 2.5\%$  and  $\pm 5.5\%$  for Alloy 1 and Alloy 2, respectively [112], and are represented by error bars.

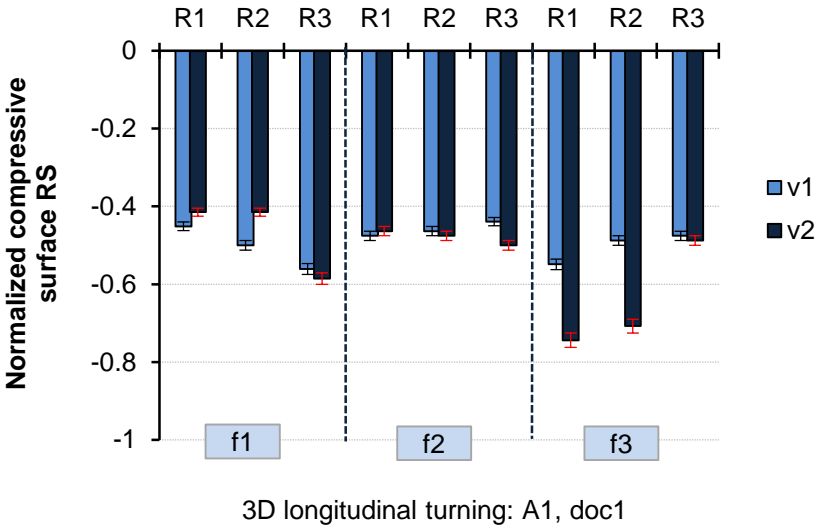


Fig. 4.12: Alloy 1: effect of oblique turning parameters on surface compressive RS in the cutting (hoop) direction at low depth of cut.

As regards Alloy 1, cutting speed, feed rate, and corner radius have significant effects on RS. Larger compressive RS were induced at conditions  $(doc_i, v_2, f_3, R_1)$  involving high speed, high feed, and small corner radius. The effect of  $doc$  was small ( $< 5\%$ ) at these conditions. The largest compressive RS were obtained at the condition  $(doc_2, v_2, f_3, R_1)$ . In general, the effect of  $doc$  was unclear and was not found to be statistically significant. Feed rate and corner radius exhibited an opposite behavioral pattern. As shown in Fig. 4.12, increasing the corner radius by 200% ( $R_1$  to  $R_3$ ) at low feed rate  $f_1$  enhanced compressive RS by around 25% on average. At high feed rate  $f_3$ , this trend was reversed, and compressive RS were reduced by around 20% on average for the same increment in corner radius, reaching 30% at high speed  $v_2$ . Cutting speed has a more significant influence on RS at high feed rate. Increasing the cutting speed at high feed rate  $f_3$  enhanced compressive RS substantially by around 30% on average, and by up to 50% at small corner radius  $R_1$ . The above observations suggest the presence of interactions between cutting speed, feed rate, and corner radius, which were confirmed by statistical analysis. For Alloy 1, opposing levels of feed rate and corner radius,  $(f_1, R_3)$  or  $(f_3, R_1)$ , promote relatively larger compressive RS.

The effect of cutting parameters on surface residual stresses induced in Alloy 2 is shown in Fig. 4.13. Similar to Alloy 1, cutting speed, feed rate, and corner radius significantly affect the magnitude of RS. Larger compressive RS were obtained at parameter combinations involving high feed rate and small corner radius  $(doc_i, v_i, f_3, R_1)$ . The uttermost compressive RS were induced at the condition  $(doc_2, v_2, f_3, R_1)$ .

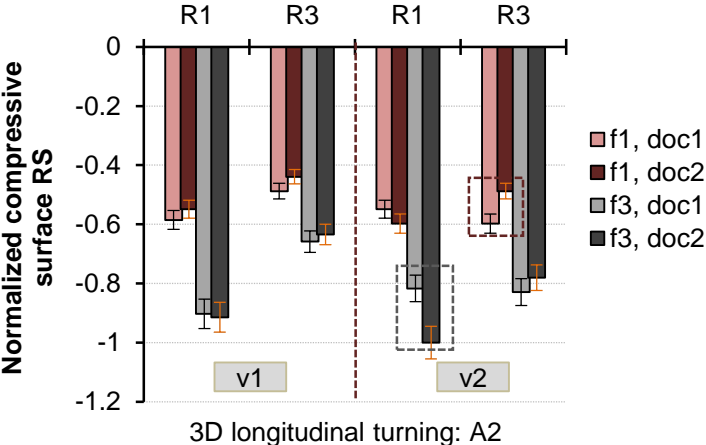


Fig. 4.13: effect of cutting parameters on surface residual stresses induced in Alloy 2 during oblique turning for various cutting parameter combinations  $(doc_i, v_i, f_i, R_i)$ .

For Alloy 2, the effect of *doc* is generally small ( $\leq 10\%$ ) except at cutting conditions  $(v_2, f_3, R_1)$  and  $(v_2, f_1, R_3)$  where it is around 20%. As in the case of Alloy 1, however, the effect of *doc* is not statistically significant. Feed rate has the largest effect on RS induced in Alloy 2. As shown in Fig. 4.13, increasing the feed rate by 150% ( $f_1$  to  $f_3$ ) enhanced compressive RS by around 50% on average. Increasing the corner radius by 200% ( $R_1$  to  $R_3$ ), however, diminished compressive residual stresses by about 20% on average, except at conditions of low depth of cut and high speed where little change was observed.

The effect of cutting speed on surface RS induced in Alloy 2 is dependent on the depth of cut and the corner radius. At low depth of cut and small corner radius conditions  $(doc_1, R_1)$  as shown in Fig. 4.14a, increasing the speed by 150% ( $v_1$  to  $v_2$ ) diminished compressive RS by 15% on average, reaching 25% at intermediate feed rate  $f_2$ . At large corner radius  $R_3$ , the trend was reversed, and compressive RS were enhanced by about 25% on average. Therefore, relatively larger compressive RS are attainable at conforming speed and corner radius levels,  $(v_1, R_1)$  or  $(v_2, R_3)$ . At high depth of cut (Fig. 4.14b), a similar increase in speed enhanced compressive RS by around 15% on average, except for condition  $(doc_2, v_2, f_3, R_2)$ , where RS diminished by about 30%. It was therefore concluded that at high depth of cut, conditions involving high speed promote more compressive RS. Similar to Alloy 1, the above suggests that interactions between the cutting parameters control the behavior of residual stresses.

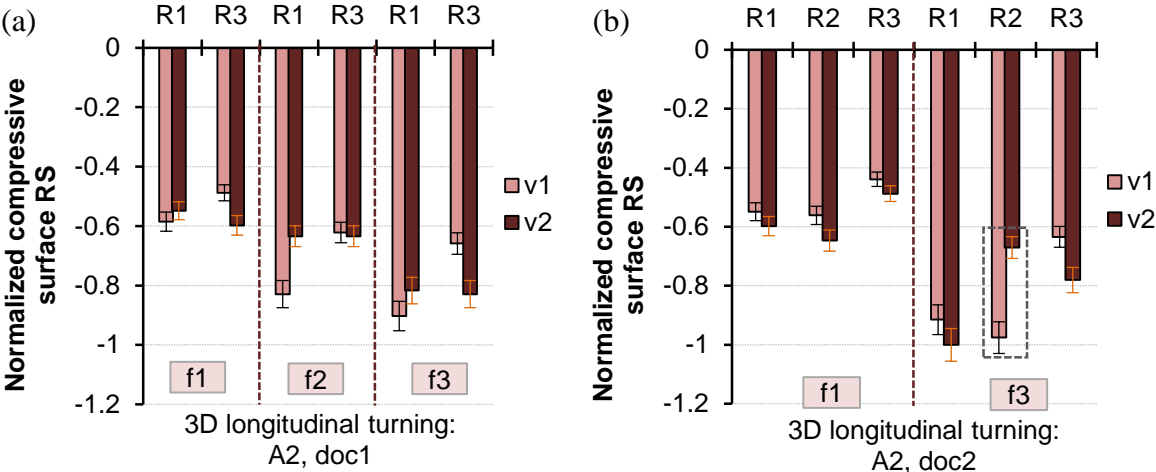


Fig. 4.14: effect of cutting parameters on surface residual stresses generated in Alloy 2 at (a)  $doc_1$  and (b)  $doc_2$ , covering the full range of investigated cutting conditions.

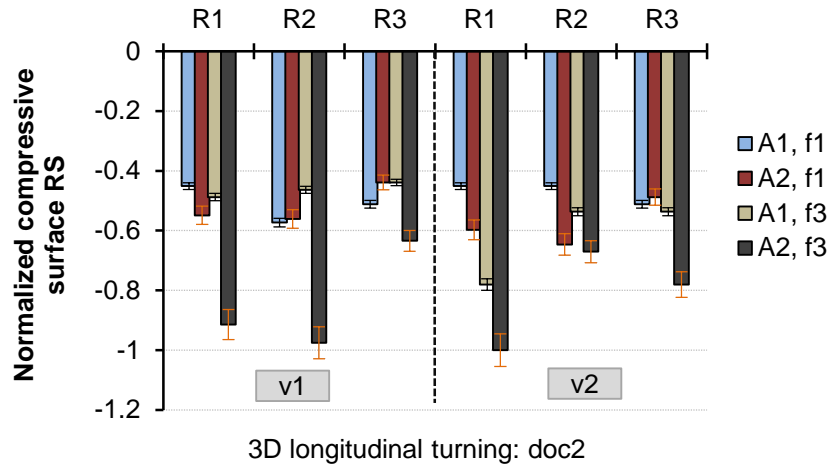


Fig. 4.15: effect of cutting parameters on surface RS generated in both Ti-alloys during oblique turning for various cutting parameter combinations ( $doc_2$ ,  $v_i$ ,  $f_i$ ,  $R_i$ ).

As shown in Fig. 4.15, compressive RS induced in Alloy 2 are generally higher than Alloy 1 by around 45% on average, and especially at high feed conditions ( $doc_i$ ,  $v_i$ ,  $f_3$ ,  $R_i$ ). The highest average increase beyond Alloy 1 of about 65% occurred for combinations of low cutting speed and high feed rate ( $v_1$ ,  $f_3$ ), reaching around 80% at high depth of cut conditions ( $doc_2$ ,  $v_1$ ,  $f_3$ ,  $R_i$ ).

In the absence of phase transformations in the near-surface layer of the material (section 4.3.4.7), residual stresses are a result of sharp plastic deformation gradients in the machined surface induced by thermomechanical deformation. As elaborated in section 4.3.4.1, machining forces sustained by Alloy 2 exceed Alloy 1 levels, especially at conditions involving high depth of cut, cutting speed, and feed rate. The characteristic flow stress behavior discussed in Chapter 6 indicates that Alloy 2 is much less sensitive to thermal softening than Alloy 1. Consequently, sharper plastic deformation gradients could be formed in the machined surface, leading to compressive residual stresses of higher magnitude. This was confirmed through the comparison of plastic strain profiles extracted from the FE simulations for both Ti-alloys at identical cutting conditions (section 6.3.4).

#### 4.3.4.5 Empirical models for residual stress prediction

Empirical models for the prediction of surface residual stresses (RS) were developed for both Ti-alloys, based on the experimental x-ray diffraction measurements for 3D cutting. The least squares approach and response surface methodology were adopted to generate

mathematical equations expressing surface residual stress in the cutting (hoop) direction in terms of the investigated cutting parameters and their mutual interactions. Model development was based on statistical analysis of variance (ANOVA).

Depth of cut was found not to have a statistically significant effect on RS. Its effect on predicted results was tested and found to be negligible. It was therefore excluded from the empirical models. The prediction error for both Ti-alloys is within  $\pm 20\%$  or  $\pm 70$  MPa, which is in accordance with the industrial partner's acceptable error margin. The empirical model for Alloy 1 is given by:

$$\sigma_c = r_0 + r_1 \left( \frac{v - \beta_1}{\beta_2} \right) + r_2 f + r_3 R + r_4 \left( \frac{v - \beta_1}{\beta_2} \right) (f - \gamma) + r_5 \left( \frac{v - \beta_1}{\beta_2} \right) (R - \delta) + r_6 (f - \gamma)^2 + r_7 (f - \gamma)(R - \delta) + r_8 (R - \delta)^2 \quad (4.7)$$

where  $\sigma_c$  is the surface residual stress in the cutting direction;  $v$ ,  $f$ , and  $R$  are the cutting parameters;  $r_0 - r_8$  are constants, and where  $\beta_1$ ,  $\beta_2$ ,  $\gamma$ , and  $\delta$  are given by Eq. 4.5 and 4.6.

A graphical comparison between empirically predicted (Emp) and experimentally measured (Exp) surface residual stresses in the cutting direction is given in Fig. 4.16 for Alloy 1, covering the full range of cutting conditions ( $doc_i$ ,  $v_i$ ,  $f_i$ ,  $R_i$ ). The empirical predictions reflect the increase in compressive RS with rising speed at high feed rate. The interaction between feed rate and corner radius and their opposing effects on surface RS are also captured by the model.

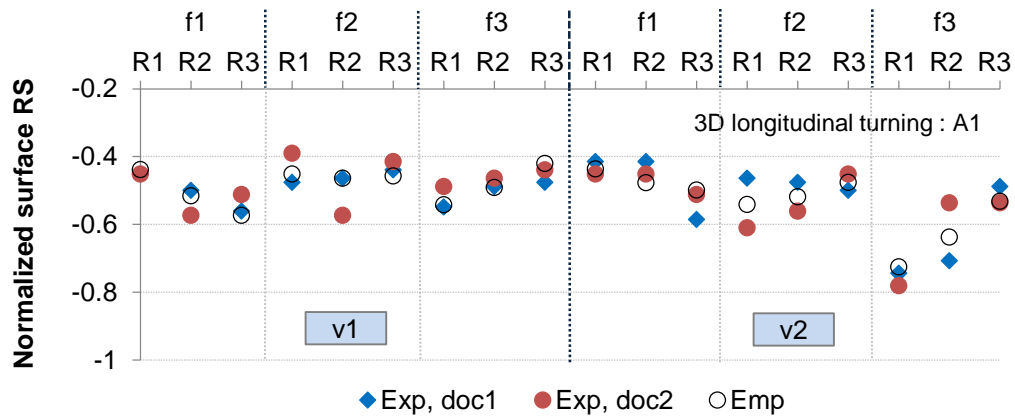


Fig. 4.16: Alloy 1: comparison between empirically predicted (Emp) and experimentally measured (Exp) surface RS in the cutting direction over the full range of cutting conditions ( $doc_i$ ,  $v_i$ ,  $f_i$ ,  $R_i$ ).

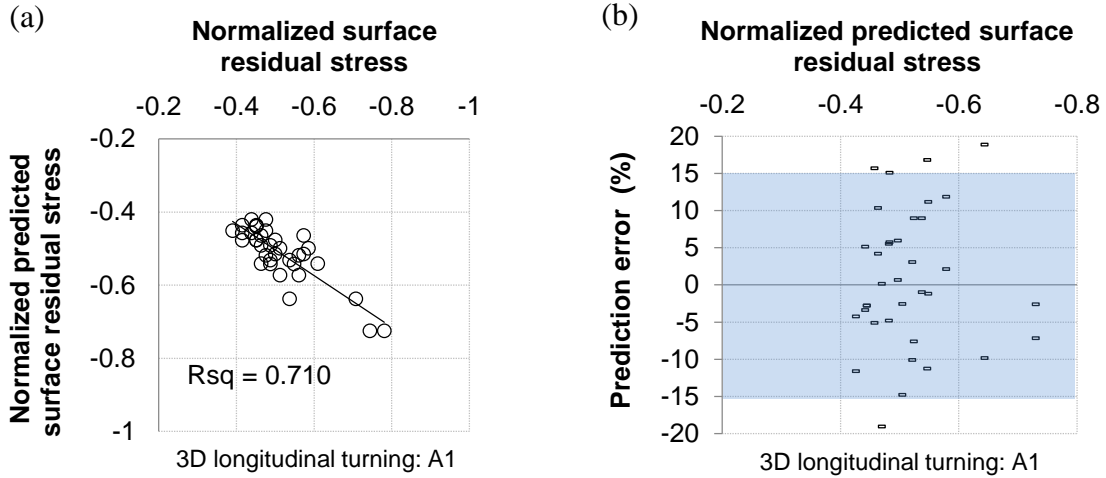


Fig. 4.17: (a) goodness of fit and (b) prediction error distribution for oblique cutting surface RS induced in Alloy 1, over the full range of cutting conditions ( $doc_i, v_i, f_i, R_i$ ).

To assess the overall accuracy of the models, the RS predictions were plotted against the experimental values measured by XRD together with the prediction error distribution over the range of investigated cutting conditions. An example of is shown in Fig. 4.17 for Alloy 1. The model's goodness of fit is evidenced in Fig. 4.17a. The coefficient of determination  $Rsq = 0.710$  indicates a reasonable correlation between surface RS and the cutting parameters. The prediction error for the majority of conditions lies within  $\pm 15\%$ , as shown in Fig. 4.17b.

#### 4.3.4.6 Surface roughness

For various materials, the  $Ra$  value during steady-state cutting is known to be directly proportional to the square of the feed rate and inversely proportional to the corner radius of the cutting tool as follows [108, 115]:

$$Ra = k_R \cdot \frac{f^2}{R}, \quad (4.8)$$

where  $k_R$  is a material constant. Fig. 4.18 compares two surface topographies obtained for Alloy 1 at low and high feed rate levels,  $f_1$  and  $f_3$ , respectively, during steady-state cutting. For the investigated range of cutting parameters, feed rate was found to have the most significant effect on surface roughness. Increasing the feed rate by 150% ( $f_1$  to  $f_3$ ) increased the  $Ra$  value by around 100% for both Ti-alloys (Fig. 4.19 and Fig. 4.20).

As expected, depth of cut was not found to have a statistically significant effect on surface roughness. As regards Alloy 1, no clear trend for the effect of corner radius on surface roughness was identifiable. However, as shown in Fig. 4.19, substantial reduction in Ra of around 40% was obtained by increasing the corner radius at low cutting speed and high feed rate conditions ( $v_1, f_3$ ). Alloy 2 conformed to the expected trend of decreasing roughness with increasing corner radius. A reduction in Ra of around 30% on average (Fig. 4.19) was attained by increasing the corner radius by 200% ( $R_1$  to  $R_3$ ). This effect was greatly diminished (Fig. 4.20) at conditions of high depth of cut and cutting speed ( $doc_2, v_2$ ).

Finer machined surfaces were obtained in general for Alloy 2 as a result of machining with particular cutting parameters. At large corner radius  $R_3$  (Fig. 4.19), Alloy 2 exhibited around 30% lower roughness as compared to Alloy 1. Moreover, about 20% lower roughness was achieved at high depth of cut conditions (Fig. 4.20).

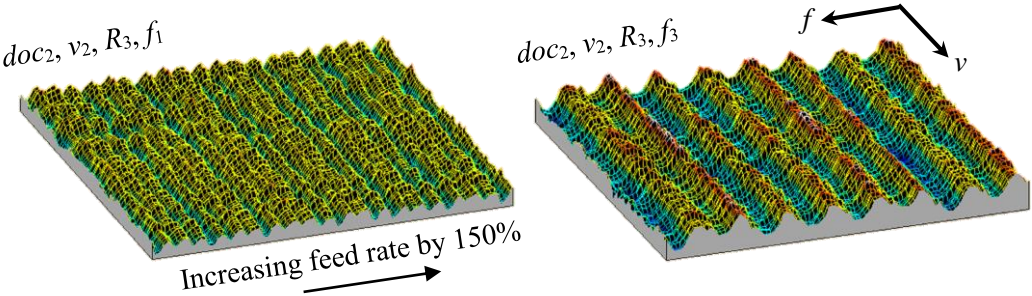


Fig. 4.18: surface topography of Alloy 1 specimens produced by longitudinal turning at the following conditions: (a) ( $doc_2, v_2, R_3, f_1$ ) and (b) ( $doc_2, v_2, R_3, f_3$ ).

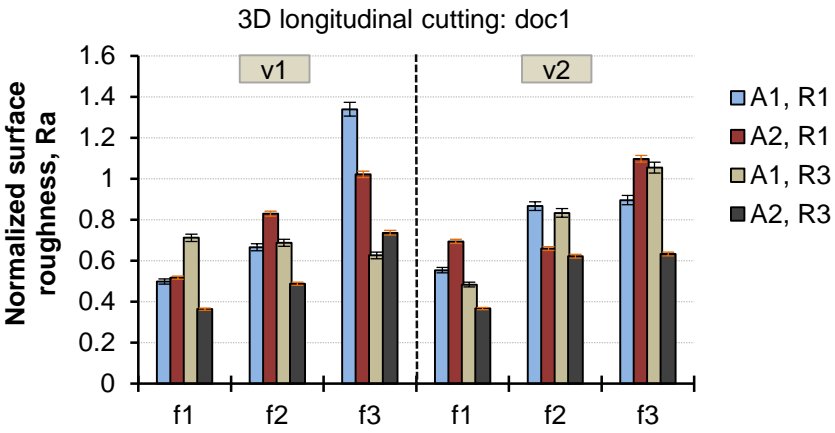


Fig. 4.19: effect of cutting parameters on surface roughness for both Ti-alloys at low depth of cut conditions ( $doc_1, v_i, f_i, R_i$ ).

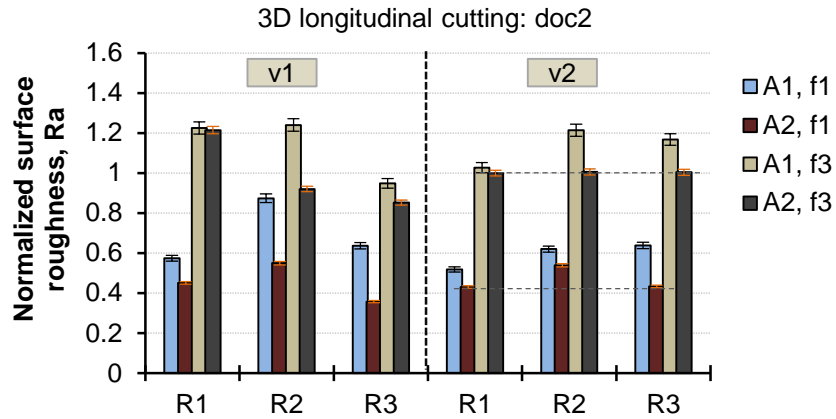


Fig. 4.20: effect of cutting parameters on surface roughness for both Ti-alloys at high depth of cut conditions ( $doc_2$ ,  $v_i$ ,  $f_i$ ,  $R_i$ ).

As depicted in Fig. 4.21, the effect of cutting speed on surface roughness of Alloy 1 is dependent on the feed rate and corner radius. This effect is more pronounced at high feed rate  $f_3$ . Increasing the cutting speed by 150% ( $v_1$  to  $v_2$ ) produced varied effects for each feed rate level. At low feed rate conditions ( $doc_i$ ,  $v_{1-2}$ ,  $f_1$ ,  $R_i$ ), no clear trend was identified. A reduction in Ra by around 30%, however, was attained at ( $doc_1$ ,  $v_{1-2}$ ,  $f_1$ ,  $R_3$ ). At intermediary feed rate conditions ( $doc_i$ ,  $v_{1-2}$ ,  $f_2$ ,  $R_i$ ), an average increase in roughness of about 40% was achieved except at ( $doc_2$ ,  $v_{1-2}$ ,  $f_2$ ,  $R_1$ ) where the change in Ra was minimal.

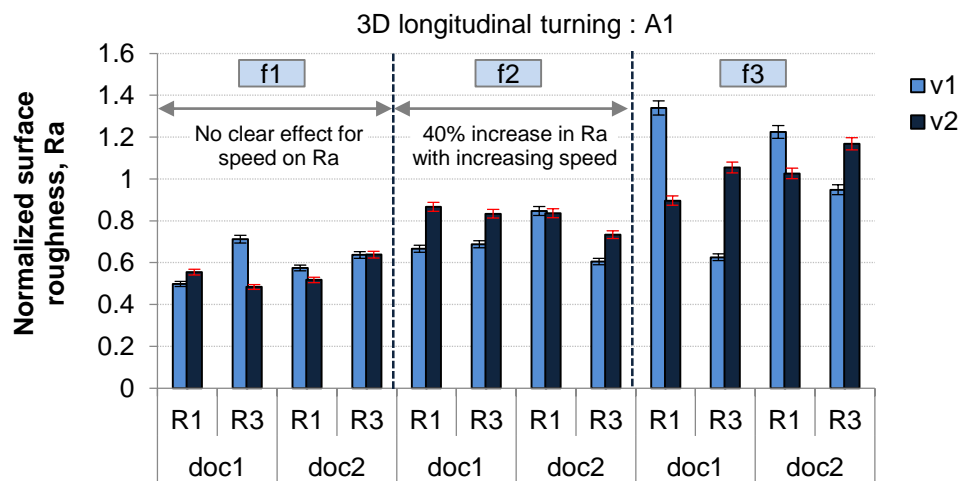


Fig. 4.21: effect of cutting parameters on surface roughness of Alloy 1 during oblique cutting over the full range of cutting conditions ( $doc_i$ ,  $v_i$ ,  $f_i$ ,  $R_i$ ).

At high feed rate levels ( $doc_i, v_{1-2}, f_3, R_i$ ), cutting speed and corner radius exhibited an opposite behavioral pattern. At small radius  $R_1$ , increasing the speed reduced Ra by around 25% on average, nearing 35% at ( $doc_1, v_{1-2}, f_3, R_1$ ). In contrast, Ra increased by about 45% at large corner radius  $R_3$ , approaching 70% at ( $doc_1, v_{1-2}, f_3, R_3$ ). Thus, at high feed rate, combinations of low speed and large corner radius ( $v_1, R_3$ ), as well as high speed and small corner radius ( $v_2, R_1$ ) offer an improvement in surface finish. Alloy 2 exhibited similar behavior to Alloy 1 at high feed rate, but to a lesser extent.

#### 4.3.4.7 Near-surface microstructure

The microstructure of the two Ti-alloys under study is contrasted in Fig. 4.22 for the harshest cutting condition within the investigated range of parameters ( $doc_2, v_2, f_3, R_3$ ). The Ti-6Al-4V alloy (Fig. 4.22a) has a bimodal microstructure comprising equiaxed primary alpha grains in a lamellar alpha/beta matrix. The Ti-6Al-2Sn-4Zr-6Mo alloy (Fig. 4.22b) exhibits a structure comprised of acicular alpha (light) in a beta matrix (dark). Within the investigated range of cutting conditions, machining parameters were found to have no discernible effect on microstructure. Furthermore, machined surfaces were free from artefacts such as cracks, tears, gouges, laps, folds, protrusions, and redeposited materials. In addition, no smearing, grain distortion or white layer formation was observed. The absence of white layers indicates that the temperatures in the machined surface did not exceed the phase transformation temperature (beta transus) of Ti-6Al-4V ( $970 \pm 50^\circ\text{C}$ ) and Ti-6Al-2Sn-4Zr-6Mo ( $935^\circ\text{C}$ ) during cutting [116-118]. The near-surface microstructure of workpiece specimens machined at various cutting conditions is contrasted in Fig. B.1 and Fig. B.2, Appendix B, for both Ti-alloys.

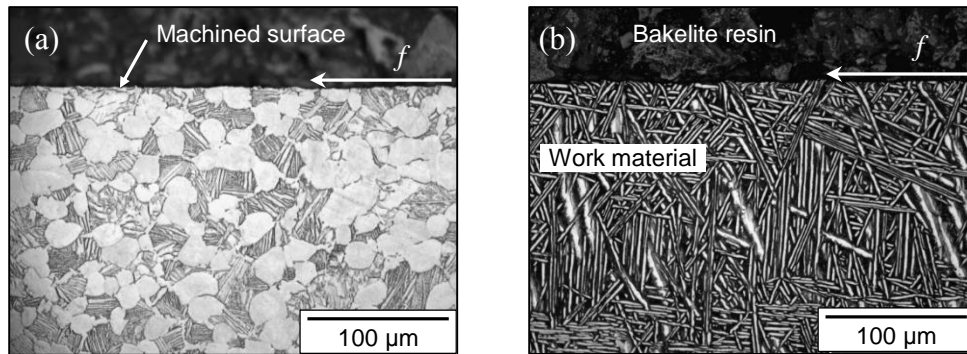


Fig. 4.22: near-surface microstructure of specimens of (a) Ti-6Al-4V (Alloy 1) and (b) Ti-6Al-2Sn-4Zr-6Mo (Alloy 2) machined at ( $doc_2, v_2, f_3, R_3$ ).

#### 4.3.4.8 Micro-hardness distribution

The hardness distribution below the machined surface for various cutting conditions ( $doc_i, v_i, f_i, R_i$ ) is depicted in Fig. 4.23 for both Ti-alloys. Hardness values acquired by micro-indentation with a Vickers indenter and a 100 g force were normalized against the bulk hardness of Alloy 2, which was around 20% higher than that of Alloy 1. The average hardness exhibited by each Ti-alloy over the range of investigated cutting conditions was estimated and used to analyze hardness fluctuation. Furthermore, hardness distributions were compared with that obtained for an unmachined sample of Alloy 1.

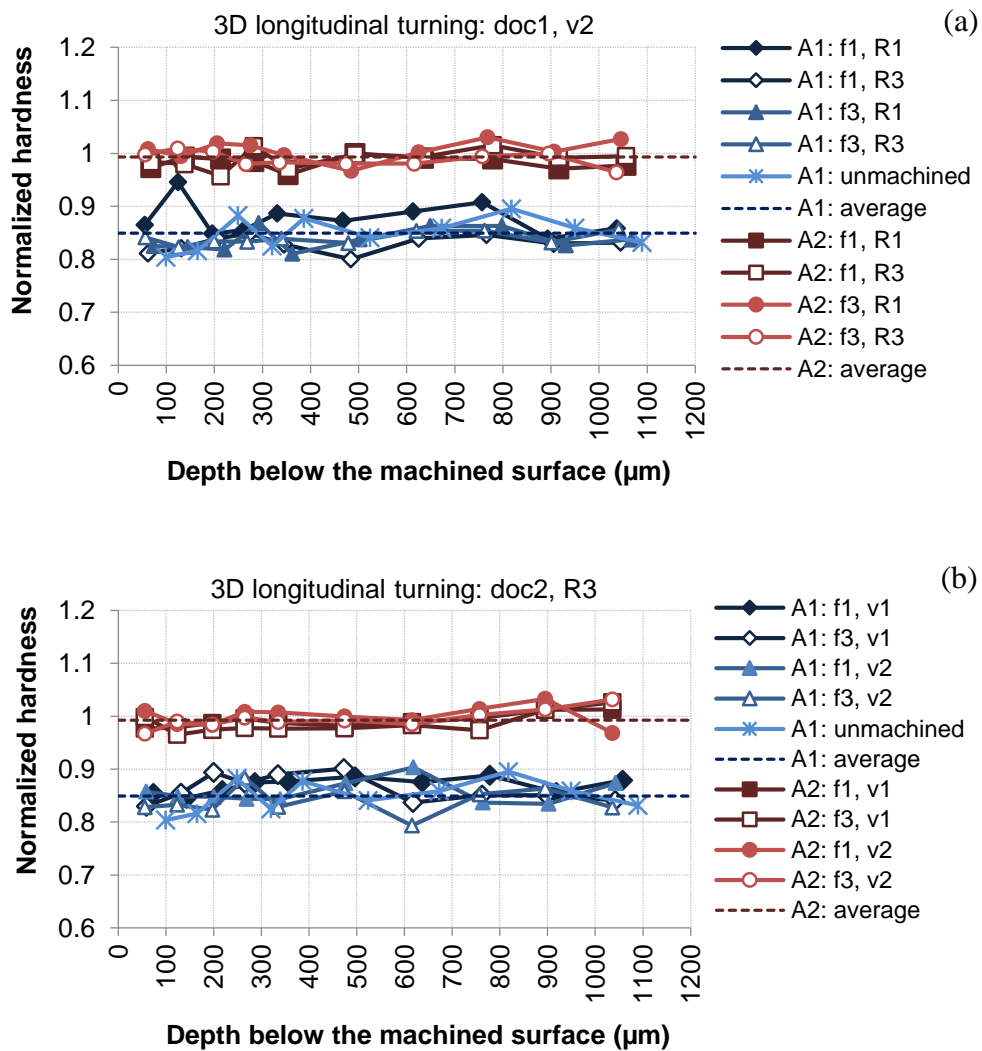


Fig. 4.23: hardness distribution below the machined surface of specimens machined at conditions: (a) ( $doc_1, v_2, f_i, R_i$ ) and (b) ( $doc_2, v_i, f_i, R_3$ ).

It was observed that machining parameters did not have a significant effect on the hardness distribution in the near surface layer of the longitudinally turned specimens. This is in agreement with the findings of the near-surface microstructure evaluation that did not reveal any grain distortion or white layer in the machined surface.

It is concluded that the measured hardness profile is due to variations in microstructure within the inspected specimens. The variation in hardness at every position below the machined surface was within  $\pm 20\%$  and  $\pm 12\%$  of the average value for Alloy 1 and Alloy 2, respectively. The higher variation in hardness exhibited by Alloy 1, as seen in Fig. 4.23, reflects the bimodal nature of its microstructure (Fig. 4.22).

#### 4.3.4.9 Optimal selection of cutting parameters

The surface roughness obtained for both Ti-alloys over the investigated finish turning regime is within the allowable range for aero-engine compressor parts. Nevertheless, a conflict exists between residual stresses and surface roughness in that the enhanced compressive RS attained at high feed rate levels are at the expense of surface finish.

Both residual stresses and surface roughness constitute critical acceptance criteria for aero-engine parts subjected to dynamic loads. Guidelines were therefore established for the optimal selection of cutting parameters to achieve the desired levels of RS and surface finish, depending on the application. These are presented in Fig. 4.24 in the form of behavioral trends for compressive RS and surface roughness ( $R_a$ ).

It is evident for Alloy 1 (Fig. 4.24a) that conditions ( $doc_i, v_2, f_3, R_1$ ) promote relatively high compressive RS. The high feed rate at these conditions, however, has a detrimental effect on surface finish (Fig. 4.24b). Similarly for Alloy 2 (Fig. 4.24c), machining at conditions ( $doc_i, v_i, f_3, R_1$ ) attains higher compressive RS. The  $R_a$  value at these conditions, however, is significantly increased (Fig. 4.24d).

For applications where surface finish is highly critical, it is recommended to machine at conditions ( $doc_i, v_i, f_1, R_3$ ) and ( $doc_i, v_i, f_1, R_1$ ) for Alloy 1 and Alloy 2, respectively. Due to the lower level of feed, these parameter combinations generate compressive RS of average magnitude with a largely improved surface finish. As a result, both criteria are satisfied by the finishing operation.

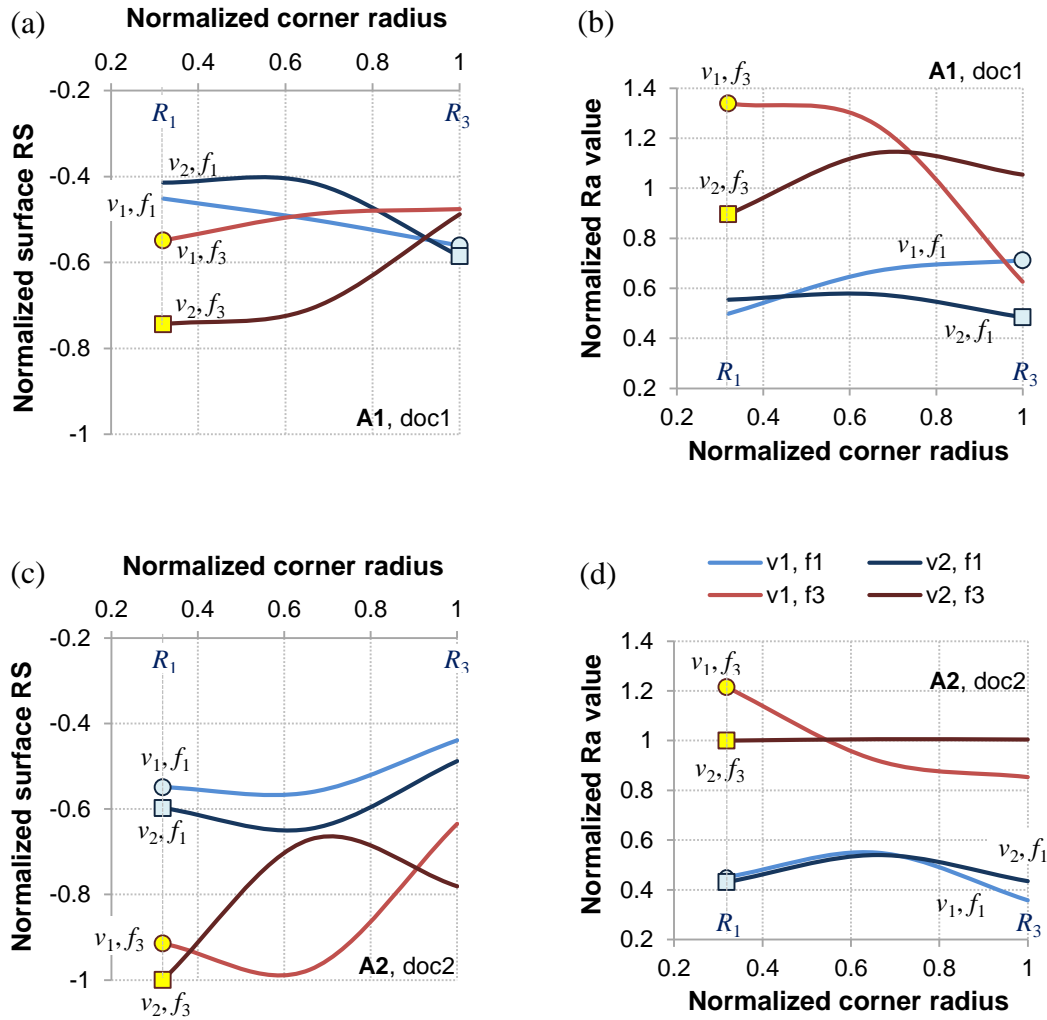


Fig. 4.24: optimal cutting parameter selection guidelines; contrasting behavioral trends for RS and surface finish: (a, b) Alloy 1 and (c, d) Alloy 2. Condition ( $A_2, (doc_2, v_2, f_3, R_1)$ ) corresponding to the highest compressive RS, cutting force, and MRR is the reference case for normalization.

# **CHAPTER 5    FUNDAMENTAL ASPECTS OF RESIDUAL STRESS FORMATION DURING CUTTING**

## **5.1 Introduction**

Due to its advantages over other methods of investigation, finite element modeling (FEM) was used to perform an in-depth analysis of the fundamental aspects of residual stress formation during metal cutting. The central objective is to determine the significance and the relative influence of the main contributors to residual stresses (RS) on their resultant state and magnitude. The isolated and coupled effects of thermal loads and mechanical loads were studied using DEFORM™ 2D V 10.0 for several commercially available materials with different physical properties comprising: grade 5 Ti-alloy Ti-6Al-4V and high chromium content bearing steel AISI 52100 with 2 levels of initial hardness, 53 and 62 HRC. In addition, the effect of phase transformations on residual stress formation was addressed in the case of the bearing steel at thermally dominant conditions.

The temperature dependent physical properties of the materials provided by Scientific Forming Technologies Corporation (SFTC) as part of DEFORM's material database were employed in the FE simulations. In the following discussion, the alloys under study are referred to as Ti-64 SFTC, 52100-53, and 52100-62. The suffix used in the description of the steel indicates its initial hardness level. The flow stress properties available in DEFORM™ and based on the work of several authors were used to model the plastic deformation behavior of Ti-64 SFTC and 52100-53. The flow stress evolution for 52100-62 was modeled using the Johnson-Cook equation parameters provided in [94]. As no proprietary material grades were used in this analysis, results are presented in their absolute form.

## **5.2 The effect of thermal loading on residual stress formation**

### **5.2.1 FE model description**

A plane-strain thermal analysis was performed in order to isolate the contribution of thermal loads to residual stress development. The evolution of stresses in an elasto-plastic workpiece was monitored under the action of a uniformly distributed moving heat source of predetermined high intensity. The heat source was modeled by the use of an environment window of set width. In the majority of cases, the width was fixed to 0.1 mm to simulate

conditions analogous to a moving strip load on a semi-infinite half-plane. The model's geometry and boundary conditions are shown in Fig. 5.1. To capture the sharp temperature and deformation gradients that develop in the near-surface layer, a densely meshed region was produced with an element size of  $4\ \mu\text{m}$  and extending to around  $40\ \mu\text{m}$  in depth below the workpiece surface. The elements furthest away from the heat affected zone were retained at ambient temperature. Velocities  $v_x = v_y = 0$  were imparted to the bottom edge of the workpiece to fix it in space.

During the simulation, the environment window moves in the negative  $x$ -direction at a set speed. A fixed speed of  $60\ \text{m/min}$  common to metal cutting practices for various materials was used in the analysis. By varying the intensity of the heat source, several peak temperatures,  $T_{\text{peak}}$ , were attained at the workpiece surface resulting in varying thermal stress fields. The onset of plastic deformation was modeled using the von Mises yield criterion. Plastic flow occurs when the effective von Mises stress is equal to or higher than the flow stress of the material. The flow stress behavior of the workpiece material is modeled as a function of temperature, strain, and strain rate.

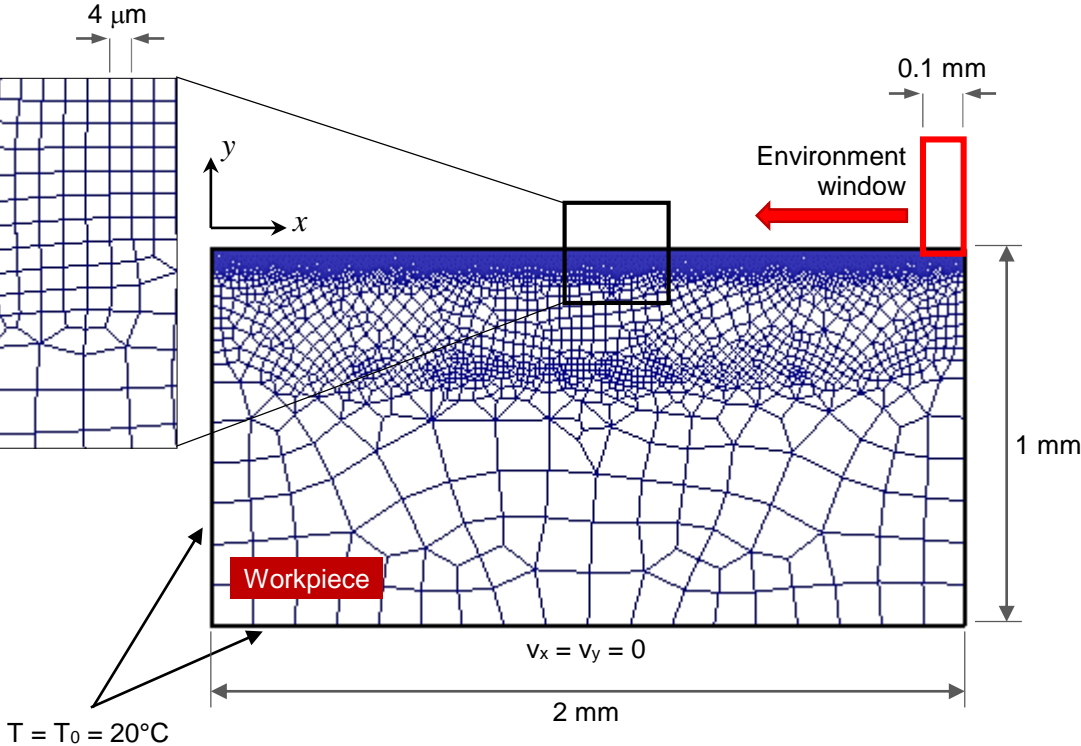


Fig. 5.1: geometrical aspects and boundary conditions of the thermal analysis FE model.

### 5.2.2 Results of the thermal FE analysis

The evolution of stress as a function of depth beneath the surface was monitored at a fixed position in the workpiece. The stress distribution  $\sigma_x$  parallel to the heat source was captured at several simulation steps corresponding to varying positions of the thermal load during its progressive displacement along the workpiece surface. The temperature fields corresponding to a peak surface temperature  $T_{\text{peak}} = 850^\circ\text{C}$  are shown in Fig. 5.2 for Ti-64 SFTC. At step 15, the monitored position A is located at the apex of the temperature field. As the load moves further away, the material in the near-surface layer in the vicinity of position A begins to cool down progressively. At step 60, the load has completely traversed the workpiece, which is now cooling down to ambient temperature. The effect of peak temperature (heat flux intensity) on the evolution of residual stress distribution at position A is shown in Fig. 5.3 for Ti-64 SFTC. At step 150, the workpiece is at ambient temperature, and the resulting stresses represent the RS remaining in the material after relaxation.

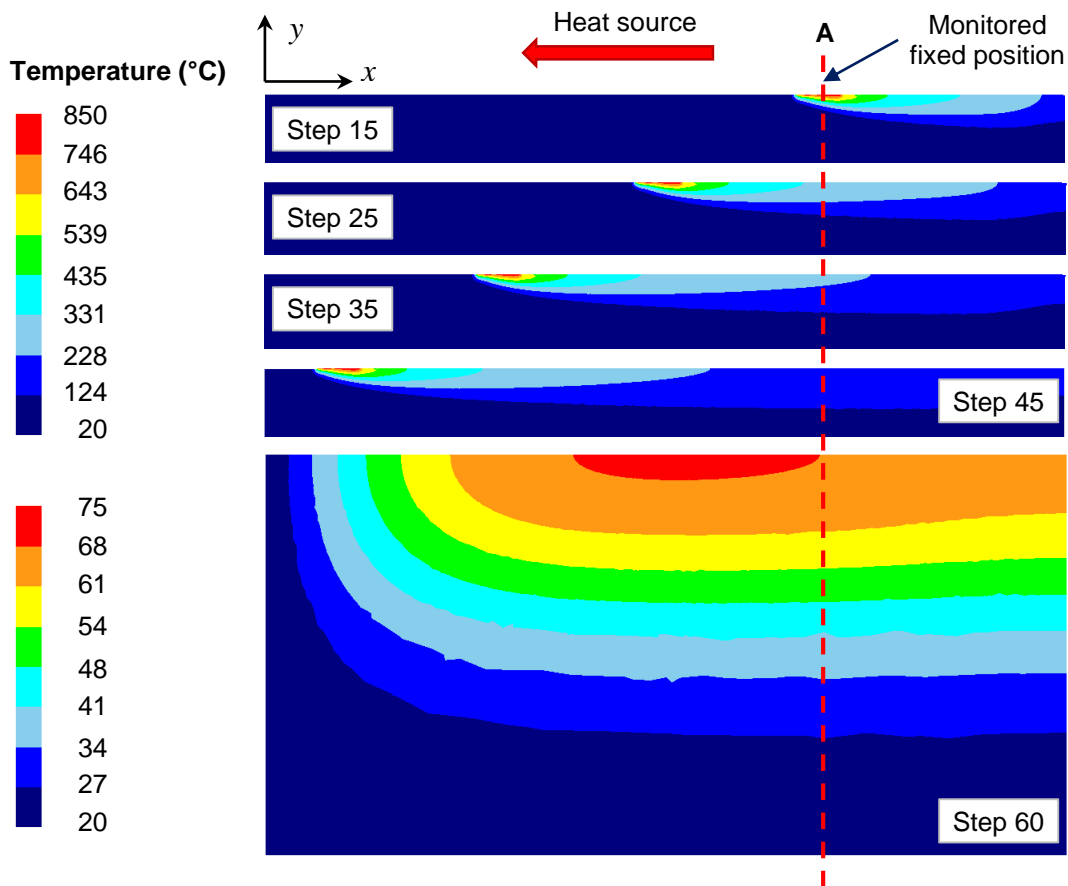


Fig. 5.2: temperature fields produced by the high intensity moving heat source and corresponding to a peak surface temperature of  $850^\circ\text{C}$  for Ti-64 SFTC.

In Fig. 5.3, the effect of load intensity on stress evolution in the Ti-alloy is analyzed by order of decreasing peak temperature. Immediately under the thermal load at the position corresponding to step 15, stresses  $\sigma_x$  in the near-surface layer are compressive (-) in nature for all peak temperatures: 950°C (Fig. 5.3a), 850°C (Fig. 5.3b), and 500°C (Fig. 5.3c). Due to the sharp temperature gradients that arise in the near-surface region during heating, the surface material undergoes a larger extent of thermal expansion and is restrained by the underlying layers. Consequently, a highly compressive stress state arises in the near-surface region together with relatively smaller tensile stresses in the sub-surface material.

For peak temperatures of 950°C (Fig. 5.3a) and 850°C (Fig. 5.3b), as the load advances (step 25), surface stresses abruptly change to tensile. At this stage, the temperature of the monitored position has dropped sufficiently (Fig. 5.2) causing incompatibilities to arise between the surface and the sub-surface material. During heating, the surface material experiences a severe reduction in flow stress due to thermal softening. If the compressive stresses arising from non-uniform thermal expansion (step 15) exceed the flow stress of the surface material, it is plastically deformed in compression. As the heated surface becomes more distant from the heating zone, its temperature drops at a high rate. As a result, the surface material undergoes a larger extent of contraction due to two factors: (i) higher cooling rate and (ii) previously occurring permanent deformation in compression. Thus, a tensile stress state is generated in a thin surface layer due to restraints by the underlying material, which is in turn subjected to compressive stress. With further movement of the load and subsequent cooling of the monitored region, the incompatibilities between the surface and sub-surface materials are intensified. The stress profile gradually shifts upwards indicating an increase in superficial tensile stresses and a decrease in peak sub-surface compressive stresses (step 25 to 45). As the load completely traverses the surface, and the workpiece enters the relaxation phase (step 60), a sudden upward shift in the stress profile takes place. The superficial and sub-surface stresses stabilize at their residual level when ambient temperature is attained (step 150).

For peak temperatures of 950°C and 850°C, tensile RS are generated by the thermal load as expected. Furthermore, the magnitude of tensile RS is highly sensitive to load intensity. Increasing  $T_{\text{peak}}$  from 850°C to 950°C by around 12% increased superficial tensile RS by almost two fold. In addition, the penetration depth of tensile RS was almost doubled.

For a lower peak temperature of 500°C (Fig. 5.3c), different behavior was observed. Compressive stresses generated by the thermal load diminished gradually and nearly vanished as the workpiece returned to ambient temperature. This indicates that very little or no plastic deformation has occurred at this condition. Fig. 5.4 compares the stress distributions along the surface of the Ti-alloy in the  $x$ -direction (parallel the heat source) for peak temperatures of 500°C and 850°C during heating (Fig. 5.4(a, b)) and at ambient temperature (Fig. 5.4(c, d)) after a complete passage of the thermal load. In the heating phase, the comparison is made at identical positions of the thermal load. Temperature distributions are also included for reference. The peak temperature and compressive stress developed during the heating phase indicate the position of the load.

It is evident by comparing Fig. 5.4a and Fig. 5.4b that the intensity of the thermal load considerably affects the peak compressive stress developed in the heating zone, as well as the stress state behind the load. Peak surface temperature  $T_{\text{peak}} = 850^{\circ}\text{C}$  produced a compressive stress of around -620 MPa in the heating zone, while stresses behind the thermal load shifted to tensile due to the sharp plastic deformation gradient in the near-surface region as explained previously. In comparison, a lower compressive stress of around -400 MPa was generated in the heating zone at  $T_{\text{peak}} = 500^{\circ}\text{C}$ , while stresses behind the thermal load remained in the compressive state.

As shown in Fig. 5.4c and Fig. 5.4d, following a complete passage of the thermal load, and upon cooling to ambient temperature, different residual stress states were developed. While stresses almost vanished for  $T_{\text{peak}} = 500^{\circ}\text{C}$ , tensile RS of around 450 MPa were generated for  $T_{\text{peak}} = 800^{\circ}\text{C}$ . This indicates that the lower compressive stresses sustained during heating at 500°C did not reach the flow stress of the material at this temperature. This suggests that in the absence of cutting loads, heating the Ti-alloy to below 500°C does not produce harmful tensile RS.

The observed behavior of the Ti-alloy is largely dictated by its temperature dependent physical and thermal properties, including flow stress, thermal expansion coefficient, thermal conductivity, and specific heat capacity. The physical and thermal properties of materials exert a large influence on their susceptibility to tensile RS under the action of thermal loads. This is brought into evidence through the following comparison of the behavior of the Ti-alloy and bearing steels under study.

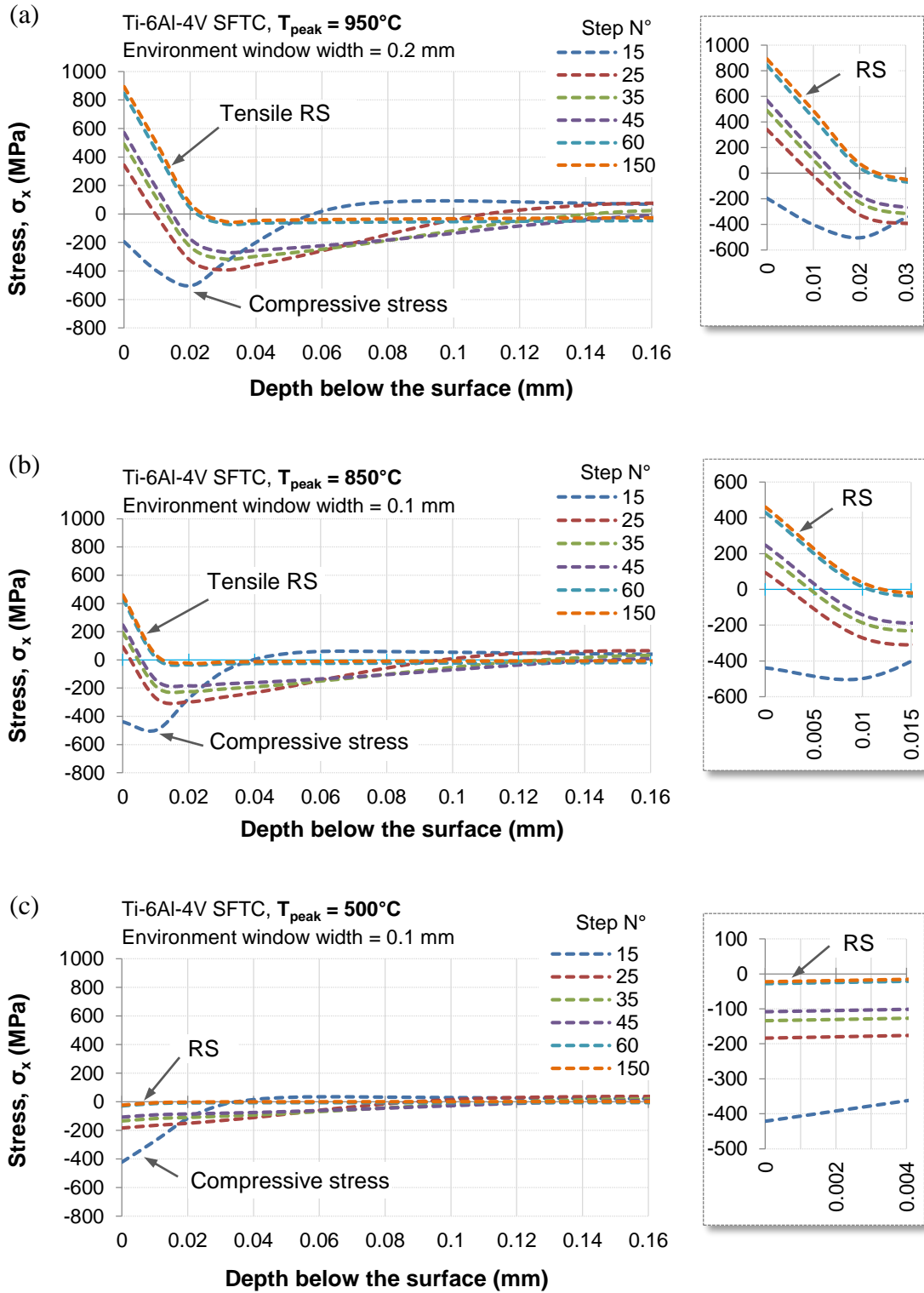


Fig. 5.3: the effect of peak surface temperature  $T_{\text{peak}}$  on stress evolution as a function of depth below the workpiece surface for Ti-64 SFTC at position 'A': (a)  $T_{\text{peak}} = 950^{\circ}\text{C}$ , (b)  $T_{\text{peak}} = 850^{\circ}\text{C}$ , and (c)  $T_{\text{peak}} = 500^{\circ}\text{C}$ . Stresses are in the  $x$ -direction parallel to the heat source.

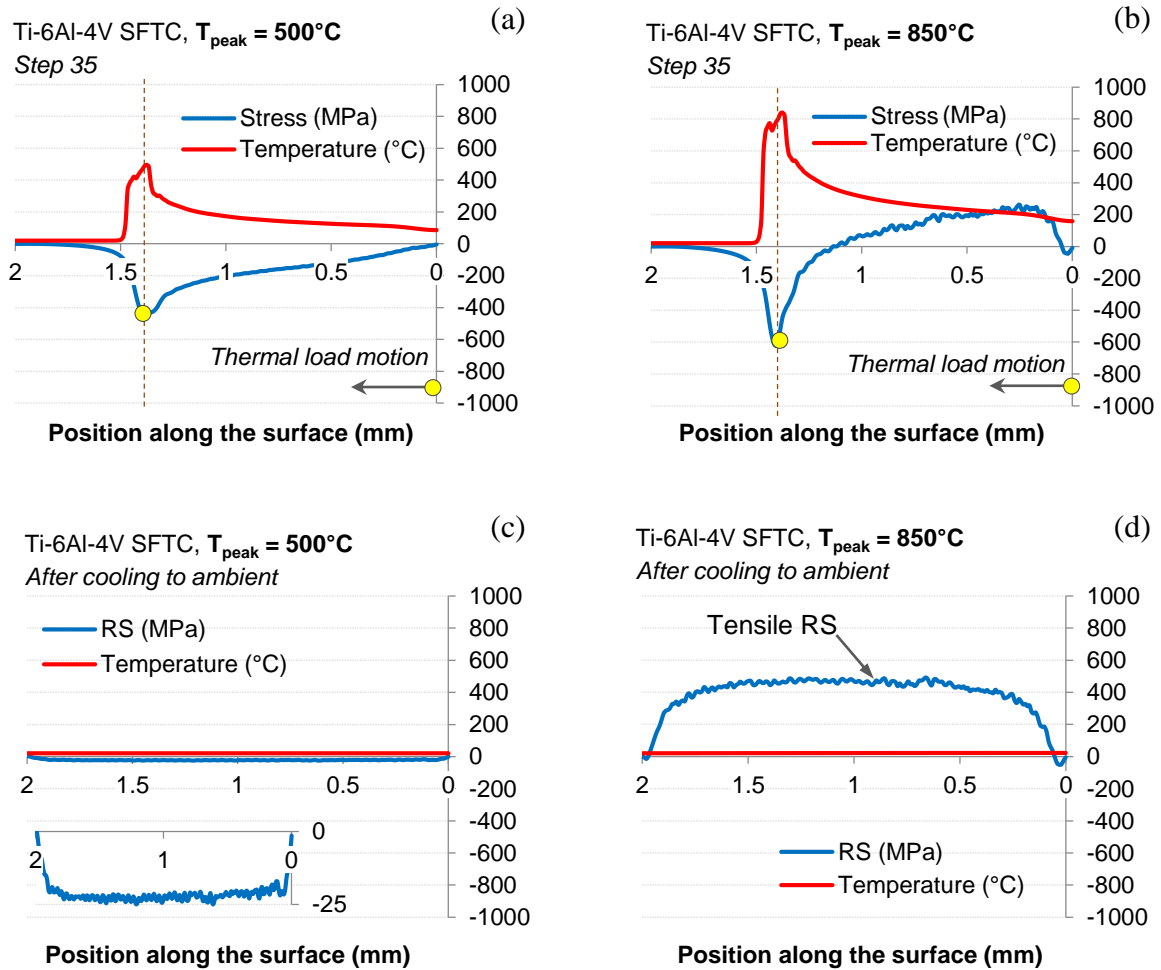


Fig. 5.4: comparison of stress distributions along the surface of Ti-64 SFTC for peak temperatures of 500°C and 850°C: (a, b) during heating and (c, d) after cooling to ambient temperature (RS). Stresses are in the  $x$ -direction parallel to the movement of the heat source.

### 5.2.2.1 Effect of material properties on RS generated by purely thermal loading

The residual stress distributions at various peak temperatures are compared in Fig. 5.5 for the materials under study. The comparison is made with reference to their flow stress behavior at the temperatures and strain levels encountered during the heating process. Over the investigated range of peak temperatures, effective strains and strain rates up to 0.03 and  $100 \text{ s}^{-1}$ , respectively, were attained. In general, the Ti-alloy and the low hardness steel are much more sensitive to thermal softening than the high hardness steel. The evolution of the ratio of effective to flow stress over the range of investigated peak temperatures is contrasted in Fig. 5.6. This ratio is based on the instantaneous magnitudes of the effective and flow stress corresponding to the peak compressive stress generated during heating. Due to its

lower susceptibility to thermal softening, the ratio for 52100-63 varies in a very narrow range and is very close to 1 as shown in the inset of Fig. 5.6. A comparison of the temperature dependent elastic and thermal properties of the Ti-alloy and the bearing steels is presented in Fig. 5.7.

Fig. 5.5a shows that tensile RS are always produced in the surface of the softer bearing steel 52100-53, even at temperatures as low as 270°C. This is largely due to the lower flow stress at moderate temperatures of this material as compared to the harder bearing steel and the Ti-alloy. Its flow stress is always exceeded by the compressive stresses generated during heating, and plastic deformation always occurs. Therefore, the ratio of effective to flow stress for this material is always greater than 1 as shown in Fig. 5.6. The FEM results suggest that the critical temperature for the onset of plastic deformation is in the range of 350 to 400°C and 550 to 600°C for 52100-62 and Ti-64 SFTC, respectively.

The approximate values of superficial RS and tensile layer depths predicted by the FE model for the materials under study are presented in Table 5-1 for various peak temperatures. It should be noted that the peak tensile residual stress is located at the surface in all cases. With reference to Fig. 5.5 and Table 5-1, it is observed that Ti-64 SFTC exhibits lower tensile RS at  $T_{\text{peak}} = 715^\circ\text{C}$  than both bearing steels at 520°C. This is due to the Ti-alloy's lower coefficient of thermal expansion (Fig. 5.7a), which leads to the generation of lower compressive stresses in the heating zone. Moreover, a much thinner tensile layer is produced in Ti than in the steels. As the Ti-alloy exhibits much lower thermal conductivity and diffusivity than the bearing steels at these temperatures (Fig. 5.7b), the heat generated by the high intensity heat source is trapped in a thinner surface layer. Since the harder steel is considerably less sensitive to thermal softening, sharper deformation gradients can arise in the surface region that increase the magnitude of the tensile RS and diminish their penetration depth as compared to the softer steel.

Table 5-1: approximate predicted values of superficial tensile RS and tensile layer depths for various investigated materials and peak surface temperatures  $T_{\text{peak}}$  during pure thermal loading.

| <b>Material</b> | <b><math>T_{\text{peak}}</math> (°C)</b> | <b>Surface RS (MPa)</b> | <b>Tensile layer depth (<math>\mu\text{m}</math>)</b> |
|-----------------|--|-------------------------|---|
| Ti-64 SFTC      | 715                                      | 100                     | 10  |
| 52100-62 HRc    | 520                                      | 500                     | 30  |
| 52100-53 HRc    | 520                                      | 350                     | 60  |

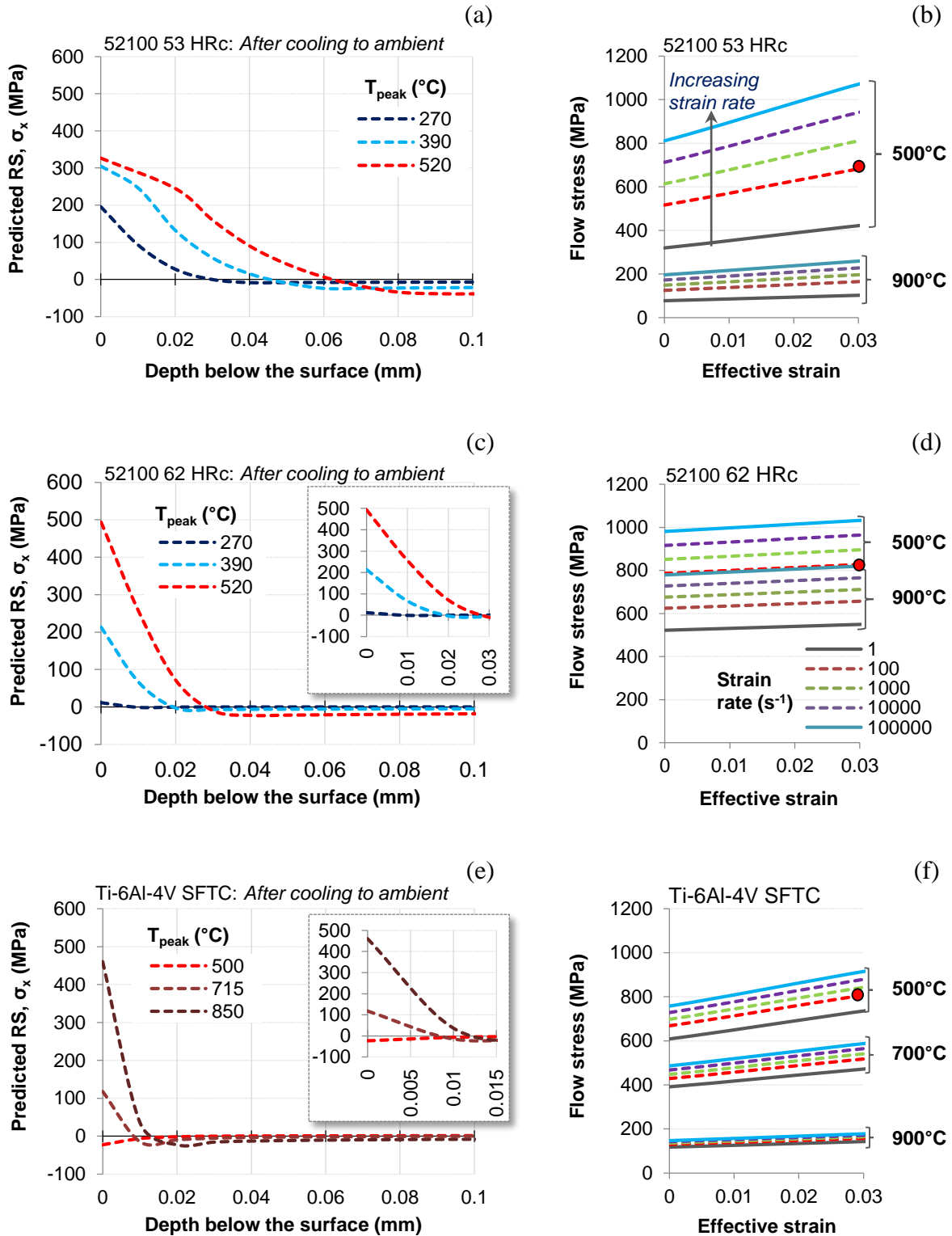


Fig. 5.5: comparison of residual stresses generated by thermal loading with reference to the flow stress behavior under relevant conditions, with (a, b), (c, d), and (e, f) depicting the residual stress profiles and flow stress curves for 52100-53, 52100-62, and Ti64 SFTC, respectively.

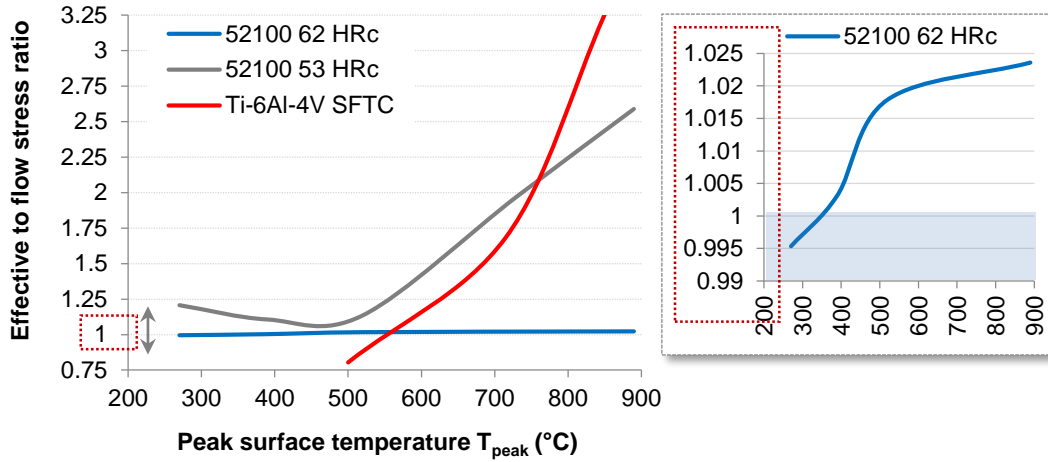


Fig. 5.6: ratio of effective to flow stress for 52100-53, 51200-62, and Ti-64 SFTC over the range of investigated peak surface temperatures. The flow stress of 52100 bearing steel accounts for the effect of phase transformation at high temperature.

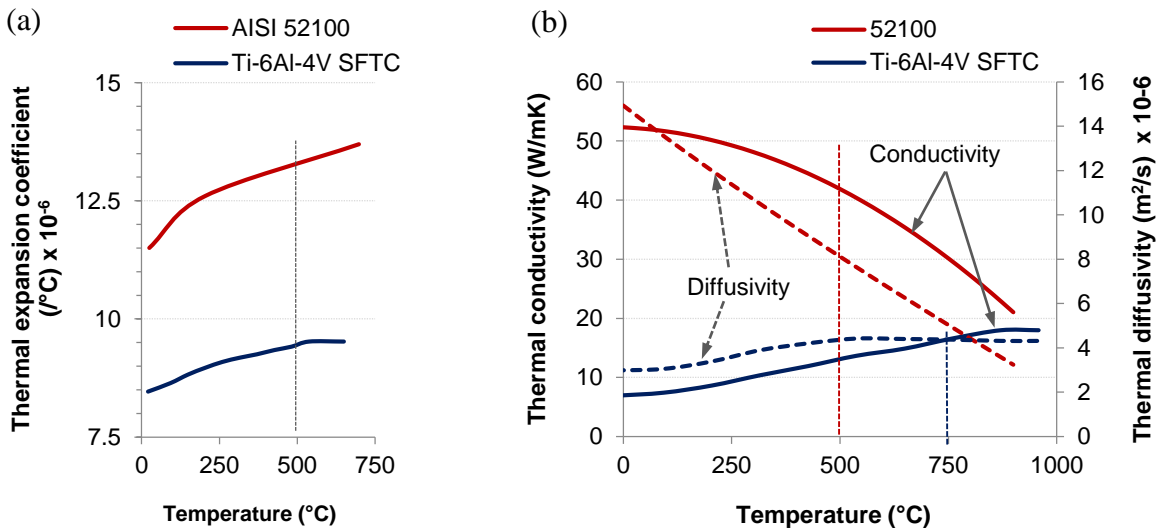


Fig. 5.7: comparison of (a) thermal expansion coefficient and (b) thermal conductivity and diffusivity for Ti-64 SFTC and bearing steel 52100.

In conclusion, residual stresses induced by purely thermal loads are tensile in nature and are highly sensitive to the intensity of the heat flux. For certain materials, optimal heating conditions can be identified that eliminate undesirable tensile RS. This is highly relevant to hybrid machining processes such as laser-assisted machining (LAM) that seek to soften the

workpiece material by preheating it prior to cutting. In this manner, the gains of thermal softening that include machining force reduction, surface roughness improvement, and tool life extension are not obtained at the expense of surface integrity. As evident in Fig. 5.6, Ti-alloys are good candidates for such processes due to their relatively high critical temperature at which the onset of plastic deformation occurs.

### **5.3 The effect of phase transformations on residual stress formation**

Difficult-to-machine materials can be prone to phase transformations at certain cutting conditions. The combination of high cutting speed and progressive flank wear can elevate surface temperatures to levels exceeding the phase transformation temperature of the material. In hybrid machining processes such as laser-assisted machining (LAM), a high intensity heat source locally preheats the material prior to cutting. This can raise the surface temperature even further, thus promoting an earlier onset of phase transformation. Under such conditions, phase transformations are integral to machining, and their contribution to surface integrity and RS in particular is highly significant. Bearing steels are prone to martensitic transformations that lead to the formation of brittle white etching layers (WL) on the machined surface. Residual stresses are generated in the workpiece surface due to the metallurgical changes. The nominal austenitization start temperature,  $A_s = 722^\circ\text{C}$ , of bearing steel AISI 52100 is lower than the beta transus,  $T_\beta = 970 \pm 50^\circ\text{C}$  [117], of Ti-64. Thus, under similar machining conditions, bearing steels are more prone to phase transformations in the machined surface than Ti-alloys.

To study the contribution of phase transformations to RS, a transformation kinetics model was coupled with the thermal model described in section 5.2.1 for martensitic bearing steel 52100 of high hardness (63 HRC). The analysis was performed for high temperature conditions that heated the surface to the austenitic region.

#### **5.3.1 Transformation kinetics model**

The material was modelled as a mixture of phases. The initial microstructure was assumed to be comprised of a volume fraction of 0.95 tempered martensite and 0.05 retained austenite. Different mechanical and thermal properties available in DEFORM's material database were adopted for the constituent phases. The flow stress behavior was modeled

identically for all phases present. It was described by the Johnson-Cook (JC) constitutive law and the model parameters reported in [94] as follows:

$$\sigma_f = \left(688 + 151\bar{\varepsilon}^{0.336}\right) \left[1 + 0.0428 \ln\left(\frac{\dot{\varepsilon}}{\dot{\varepsilon}_0}\right)\right] \left[1 - \left(\frac{T - T_0}{T_{melt} - T_0}\right)^{2.779}\right] \quad (5.1)$$

where,  $\sigma_f$  (MPa),  $\bar{\varepsilon}$ , and  $\dot{\varepsilon}$  ( $s^{-1}$ ) are the flow stress, effective strain, and effective strain rate, respectively;  $\dot{\varepsilon}_0 = 1 s^{-1}$  is the reference strain rate; and  $T$  ( $^{\circ}C$ ),  $T_0 = 20^{\circ}C$ , and  $T_{melt} = 1487^{\circ}C$  are the instantaneous, ambient, and melt temperatures, respectively.

During rapid movement (60 m/min) of the high intensity thermal load, extremely high heating and cooling rates ( $> 1000^{\circ}Cs^{-1}$ ) are encountered by the surface material as shown by the FE analysis. Sharp temperature gradients in the near-surface region lead to the formation of very thin austenitized layers ( $\leq 20 \mu m$ ). Thus, having exceeded the austenitization start temperature  $A_s$  during heating, transformation to austenite is assumed to be almost immediate.

During quenching, diffusion controlled phase transformations are most likely to be suppressed at the abovementioned cooling rates. Diffusion transformation kinetics where, however, not excluded from the model. Three transformations were considered during quenching: (i) diffusion transformation from austenite to bainite, (ii) diffusion transformation from austenite to pearlite, and (iii) diffusionless transformation from austenite to untempered martensite. Diffusion transformations were modeled using the isothermal time-temperature-transformation (TTT) diagrams for 52100 steel available in DEFORM's material database. These are provided as transformation start and end curves, denoting volume fractions of 0.05 and 0.95, respectively, of the forming phases. The kinetics of the martensitic transformation were modeled based on the Koistinen-Marburger equation [95] modified for the effect of stress on the martensite start temperature  $M_s$  as follows:

$$f_m = 1 - \exp\left[-k_m (M_s - T) - k_m (A\sigma_{mm} + B\bar{\sigma})\right], \text{ with} \quad (5.2)$$

$$\Delta M_s = A\sigma_{mm} + B\bar{\sigma}, \quad (5.3)$$

where  $f_m$ ,  $T$  ( $^{\circ}C$ ),  $\sigma_{mm}$  (MPa), and  $\bar{\sigma}$  (MPa) are the volume fraction of untempered martensite, instantaneous temperature, hydrostatic stress, and effective stress, respectively, and  $k_m$  ( $^{\circ}C^{-1}$ ),  $A$  ( $^{\circ}C/MPa$ ), and  $B$  ( $^{\circ}C/MPa$ ) are the equation parameters.

Table 5-2: parameter sets for Eq. 5.2 used to model the martensitic transformation from austenite to untempered martensite upon quenching.

| <i>Parameter set</i> | $A_s$<br>(°C) | $M_s$<br>(°C) | $k_m$<br>(°C <sup>-1</sup> ) | <b>A</b><br>(°C/MPa) | <b>B</b><br>(°C/MPa) |
|----------------------|---------------|---------------|------------------------------|----------------------|----------------------|
| MT1                  | 722           | 324           | 0.016                        | 0.08                 | 0.06                 |
| MT2                  | 560           | 324           | 0.016                        | 0.08                 | 0.06                 |

Two sets of parameters were adopted for Eq. 5.2 to model the martensitic transformation from austenite to untempered martensite (Table 5-2). The aim is to examine the effect of transformation kinetics on RS. The first set of parameters MT1 is based on standard values for AISI 52100 steel available in DEFORM's material database. The second set MT2 is identical to MT1, except that the  $A_s$  temperature was diminished to fully reflect the effect of thermal stresses on phase equilibria [84], including both  $A_s$  and  $M_s$  temperatures.

Upon quenching, latent heat generated during phase transformation acts as an internal heat source. Latent heat of transformation was accounted for as enthalpy change, and values of 595.36 and 661.51 MJ/m<sup>3</sup> were assigned for diffusion controlled and martensitic phase transformations, respectively. Volumetric expansion due to changes in the lattice structure of the steel was modeled as a function of temperature. At ambient temperature, the volumetric strain ( $\Delta V/V$ ) is around 1.7% and 2.5% for diffusion and martensitic transformations, respectively. Mechanical interactions between stresses and phase transformations cause transformation plasticity. Materials undergoing transformation under applied loads exhibit plastic deformation below the yield stress of the parent phase [60]. Transformation plasticity effects are only considered for the martensitic transformation. The additional components of strain arising from volumetric changes and transformation plasticity are modeled according to the following [60, 61, 119]:

$$d\varepsilon_{ij}^{df} = \frac{1}{3} \frac{\Delta V}{V} df_{ij} \delta_{ij} \quad (5.4)$$

$$d\varepsilon_{ij}^{fp} = \frac{3}{2} K_m g(f_m) df_m S_{ij}, \text{ where} \quad (5.5)$$

$$g(f_m) = 2(1 - f_m), \quad (5.6)$$

and where  $d\varepsilon_{ij}^{vf}$  and  $d\varepsilon_{ij}^{tp}$  are the volumetric and transformation plasticity strain increments, respectively,  $f_{IJ}$  is the volume fraction of phase I transformed to phase J,  $K_m = 5.08 \times 10^{-5}$  MPa<sup>-1</sup> is the martensitic transformation plasticity coefficient, and  $S_{ij}$  is the deviatoric stress tensor.

### 5.3.2 Results of the coupling of phase transformation and thermal loads

As expected, due to the extremely high cooling rates, no diffusion transformation products were obtained. Under the action of the thermal load, martensitic transformation took place in a very thin superficial layer. The resulting residual stress distributions for both kinematic conditions (Table 5-2) were examined in conjunction with the predicted thickness of white layer (WL) on the surface of the specimens (Fig. 5.8). The residual stress profiles extracted from the center of the workpiece at a peak temperature of 890°C are presented in Fig. 5.8a. When phase transformations were excluded from the FE model, the peak tensile residual stress occurred at the surface of the material. As a result of the martensitic transformation, superficial stresses shifted from tensile to compressive. In addition, the peak tensile stress diminished in magnitude and moved into the sub-surface. Decreasing the austenitization start temperature  $A_s$  from 722 °C to 560°C had little effect on the magnitude of superficial compressive stress. The earlier onset of transformation, however, resulted in a deeper compressive layer and a lower magnitude of sub-surface tensile stresses.

The residual stress distributions in the bearing steel up to a depth of 10 μm are shown in Fig. 5.8b and Fig. 5.8c for  $A_s = 722^\circ\text{C}$  and  $560^\circ\text{C}$ , respectively, together with the variation in the volume fraction of untempered martensite  $f_m$ . The predicted WL thickness is also displayed on the workpiece mesh. The WL thickness was estimated based on a volume fraction  $f_m = 0.8$ , indicating a concentration of 80% of untempered martensite. This figure constitutes an average value for white layers produced in AISI 52100 steel under thermally dominant conditions, including high speed machining and electric discharge machining (EDM) [120]. As shown in Fig. 5.8(b, c), at the point where  $f_m$  attains a level of 0.8, stresses shift from compressive to tensile. This indicates that the depth of penetration of the compressive layer is directly related to the thickness of the WL. The white layer and hence compressive layer obtained for  $A_s = 560^\circ\text{C}$  (slightly above 7 μm) is much larger than that obtained for  $A_s = 722^\circ\text{C}$  (just under 1 μm).

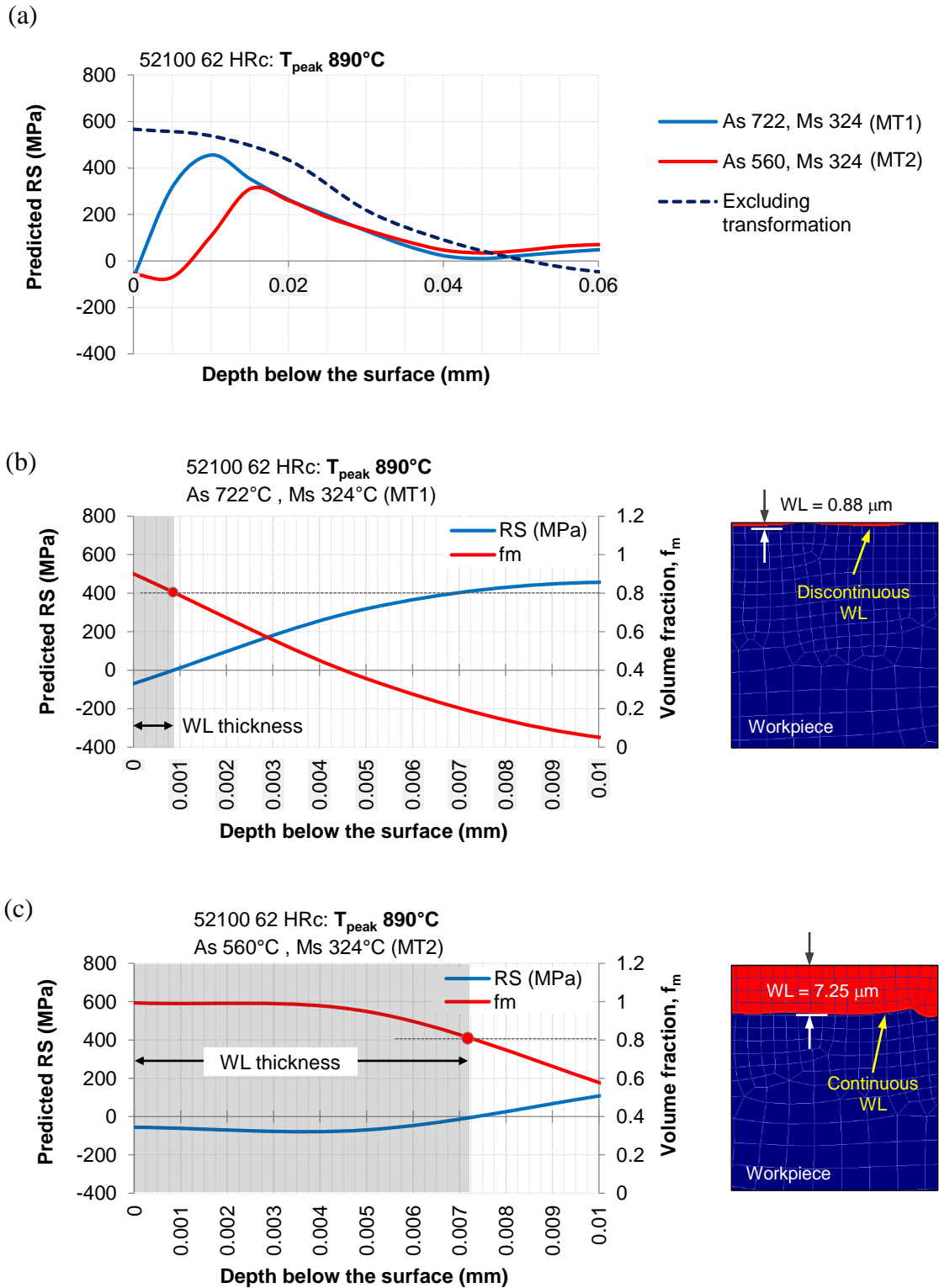


Fig. 5.8: effect of martensitic transformation on the residual stress distribution in 52100 (63 HRC) steel obtained under thermal loading at a peak surface temperature  $T_{\text{peak}} = 890^{\circ}\text{C}$ .

To analyse the effect of phase transformation on stress evolution, the stress distribution along the workpiece surface for  $T_{\text{peak}} = 890^{\circ}\text{C}$  is examined at two simulation instances: (i) during the motion of the thermal load at step 45 (Fig. 5.9 (a, b)) and (ii) upon cooling to ambient temperature after a complete traverse of the load (Fig. 5.9 (c, d)). A comparison is made between the case that excludes phase transformation and coupled condition with  $A_s = 560^{\circ}\text{C}$  (Table 5-2). In Fig. 5.9d, the prediction results for  $A_s = 722^{\circ}\text{C}$  are also included for analysis.

In the absence of phase transformation (Fig. 5.9a), the workpiece is subjected to compressive stresses in the heating zone that shift to tensile behind the load as the surface temperature drops rapidly. As explained previously, this is due to plastic deformation in compression of the surface material. During martensitic transformation, the ferrite lattice is distorted due to a supersaturated solution of carbon, which leads to a localized permanent volumetric expansion in the transforming material [121]. As the volume fraction of martensite increases (Fig. 5.9b), plastic unloading occurs that diminishes the extent of plastic deformation in compression and shifts it to tension. As this occurs, stresses behind the load shift from the tensile to the compressive state. Eventually, when the workpiece cools down to ambient temperature, the remaining RS are compressive in nature. With the exclusion of phase transformation, tensile RS of around 600 MPa are predicted by the FE model as shown in Fig. 5.9c. When martensitic transformation is accounted for, compressive RS averaging around -60 MPa are induced by the thermal load (Fig. 5.9d).

As shown in Fig. 5.9d, the superficial volume fraction of untempered martensite  $f_m$  obtained for  $A_s = 560^{\circ}\text{C}$  exhibits very little fluctuation. This is associated with a continuous and relatively thick WL and more deeply penetrating compressive RS. With  $A_s = 722^{\circ}\text{C}$ , the level of  $f_m$  fluctuates heavily. This indicates the presence of a discontinuous thin WL and shallow compressive RS. The correlation between  $A_s$ , WL thickness, WL continuity, and compressive layer depth is evidenced by the comparison of Fig. 5.8b and Fig. 5.8c.

Since they are extremely brittle and may contain microcracks, white layers are generally undesirable for industrial parts that are prone to fatigue failures. It is common industrial practice to remove white layers generated during the production of components from 52100 bearing steel [87]. Automotive transmission parts are a good example. Intelligent control of process parameters is required to ensure that compressive RS generated by in-

process heat treatment due to phase transformations are not obtained at the expense of other aspects of surface integrity. With in-depth knowledge of the interactions between thermomechanical loads and phase transformations under various modes of cooling, investigative tools such as FEM can be used to optimize process conditions. This is an issue of high importance to hybrid production processes such as laser-assisted machining (LAM).

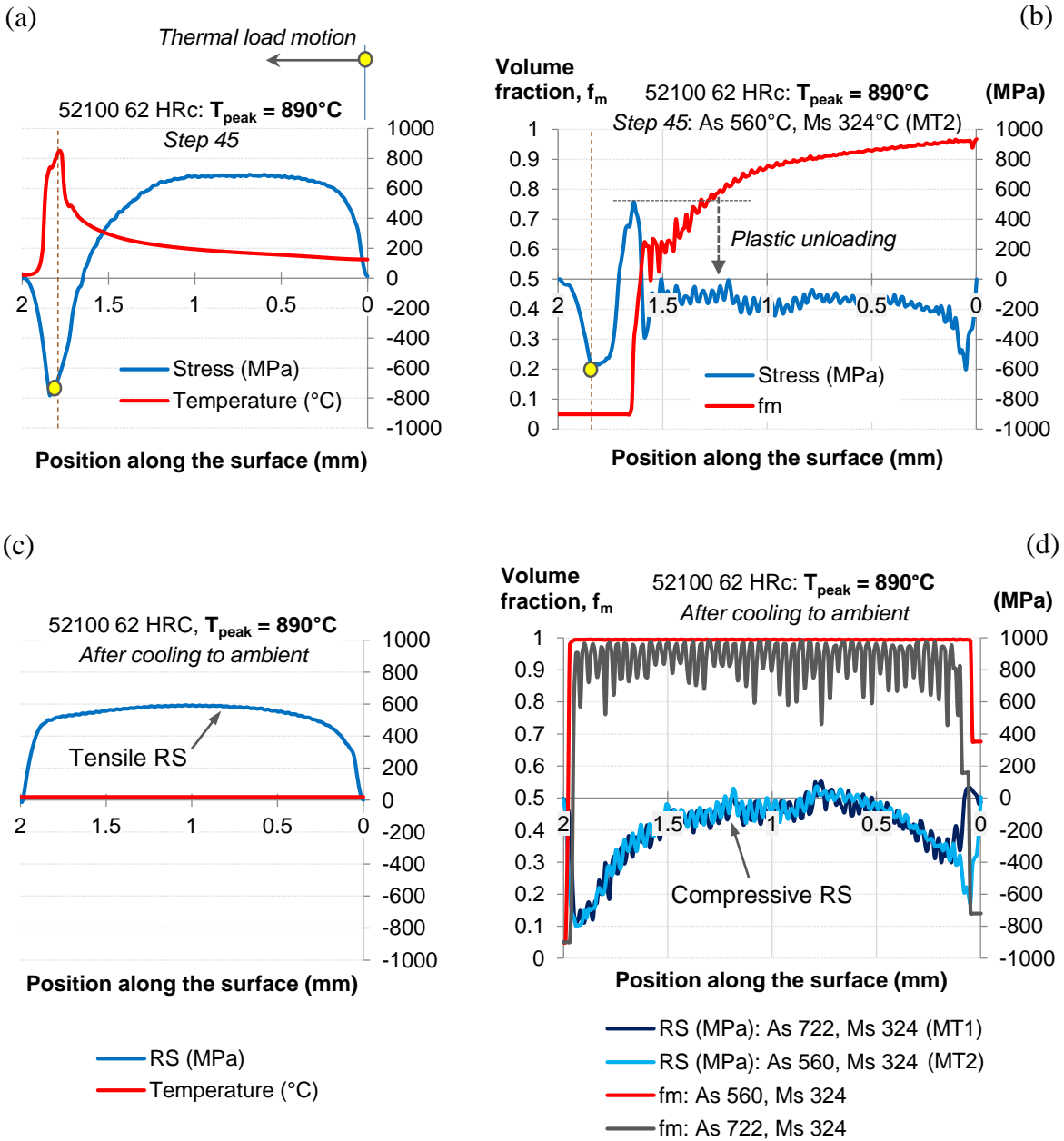


Fig. 5.9: effect of phase transformation on stress distributions along the surface of 52100 (62 HRC) for  $T_{\text{peak}} = 890^{\circ}\text{C}$ : (a, b) during heating and (c, d) after cooling to ambient temperature (RS). Stresses are in the  $x$ -direction parallel to the movement of the heat source.

## 5.4 The contribution of thermal and mechanical loads to RS during machining

A two-dimensional plane strain model of the orthogonal cutting process was constructed using DEFORM 2D V10.0 to analyse the significance of thermal and mechanical loads to residual stress formation during cutting. The following discussion will focus on the Ti-alloy Ti-64 SFTC. The influence of several process parameters on thermally generated and mechanically induced stresses was investigated including: cutting speed ( $v$ ), tool hone radius ( $r$ ) and rake angle ( $\alpha_r$ ). The cutting matrix adopted in this numerical investigation is given in Table 5-3.

For each case, simulations were performed in three modes: (i) coupled thermomechanical FE analysis followed by (ii) uncoupled mechanical analysis, and (iii) uncoupled thermal analysis. This was done to study the relative contribution of isolated mechanical and thermal loads in comparison with the coupled thermomechanical loads. For pure thermal loading, the moving heat source model described previously in section 5.2.1 was used with conditions that produce a similar peak temperature in the workpiece surface to that obtained during the thermomechanical cutting simulation. It is acknowledged that the narrow moving heat source adopted in this work is not fully representative of cutting. During machining, both the inclined shear zone and the tool/chip interface can influence the temperature distribution in the workpiece surface. It is maintained, however, that the method adopted is suitable for the purpose of the present analysis, which is to identify existing effects and trends. The development of an optimized FE model for the accurate prediction of machining-induced RS is later described in detail in Chapter 6.

Table 5-3: matrix of the numerical investigation of the influence of process parameters on thermal and mechanical stresses during cutting.

| Case # | $t$ (mm) | $v$ (m/min) | $r$ ( $\mu\text{m}$ ) | $\alpha_r$ ( $^\circ$ ) |
|--------|----------|-------------|-----------------------|-------------------------|
| 1      | 0.12     | 60          | 20                    | 0                       |
| 2      | 0.12     | 60          | 20                    | -20                     |
| 3      | 0.12     | 60          | 100                   | 0                       |
| 4      | 0.12     | 300         | 20                    | 0                       |

### 5.4.1 Description of the FE model

The construction of the cutting model was similar to the thermal model described previously in section 5.2.1 in terms of geometry, mesh size and boundary conditions. An element size of  $4\ \mu\text{m}$  was maintained in the workpiece surface. A fine mesh was also used in the contact region involving high temperature, strain, and strain rate gradients. The model setup is depicted in Fig. 5.10. During the simulation, the tool moves relative to the fixed workpiece in the negative  $x$ -direction at the desired uncut chip thickness ( $t$ ) and with a cutting speed ( $v$ ). The bottom edge of the workpiece is fixed in space by assigning a zero velocity to its nodes. During thermomechanically coupled simulations, the edges of the workpiece and the cutting tool furthest away from the cutting zone are maintained at ambient temperature  $T_0 = 20^\circ\text{C}$ . Tool and workpiece boundaries in close proximity to the cutting zone undergo heat transfer between themselves and with the surrounding atmosphere.

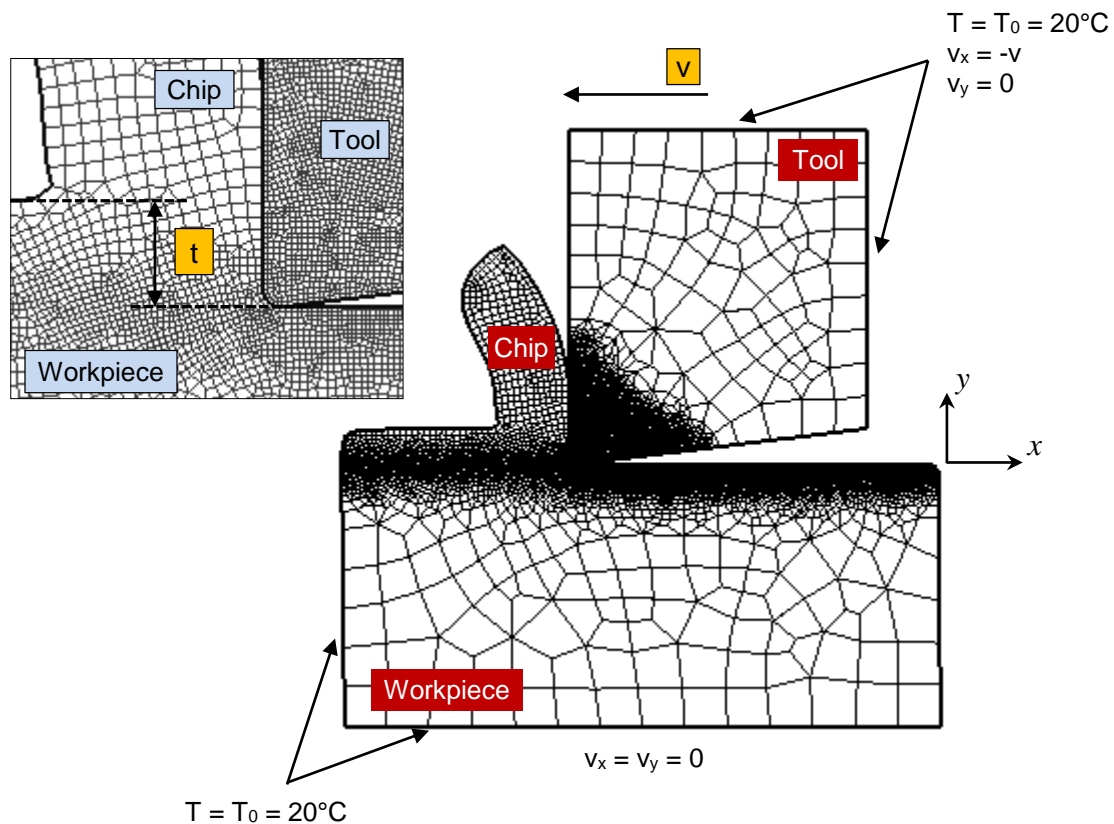


Fig. 5.10: setup of the 2D FE model employed for mechanical and thermomechanically coupled simulations of the orthogonal cutting process.

Perfect contact was assumed at the tool chip interface. Zorev's sticking-sliding friction model [122] was adopted, together with a constant heat transfer coefficient  $h_c = 10^5$  KW/m<sup>2</sup>°C. The selection of friction and heat transfer criteria is based on previous work performed at the National Research Council Canada (NRC) for titanium and nickel-based alloys [66, 123]. Identical values were used for all simulation cases. During cutting simulations, a tool stroke of 1.25 mm was adopted. When the cutting phase was complete, stress relaxation was carried out. The tool was retracted from the workpiece to release the loads. This was performed for both mechanical and thermomechanical analyses. At the end of the stress relaxation phase, residual stresses were extracted from the FE model.

#### **5.4.2 Results of the numerical study**

For case 1 (Table 5-3), which constitutes the reference case, surface compressive RS averaging around -450 MPa were predicted by the thermomechanical model. The negative sign adopted indicates the compressive nature of the stress. An experimental value of -600 MPa was reported in [124] for Ti-64 as a result of orthogonal cutting at identical parameters. The 25% difference between the results could be due to several factors. Although a tool hone radius of 20  $\mu$ m was adopted in this work, no mention of this parameter was made in [124]. Cutting edge preparation can have an important influence on the magnitude and state of RS. Furthermore, difference in microstructure between the alloys can result in varying magnitudes of RS. As further explained in Chapter 6, material identification is required to capture the accurate behavior of flow stress during plastic deformation at temperature, strain, and strain rate levels encountered during the cutting process. Although both alloys are of the same nominal composition, variations in processing could lead to dissimilar levels of RS. At this stage, the 25% difference is considered sufficiently accurate for the purpose of this analysis, which is to study the contribution of thermal and mechanical loads to residual stresses for various cutting parameter combinations.

##### *5.4.2.1 Analysis of stress evolution during cutting*

The stress evolution at several instances during cutting is shown in Fig. 5.11 for simulation case 1. Each instance corresponds to a more advanced position of the tool along its path. A comparison is made of the superficial and in-depth distribution of stresses generated by thermal, mechanical, and thermomechanical loads. The comparison culminates with the analysis of RS obtained after the stress relaxation phase.

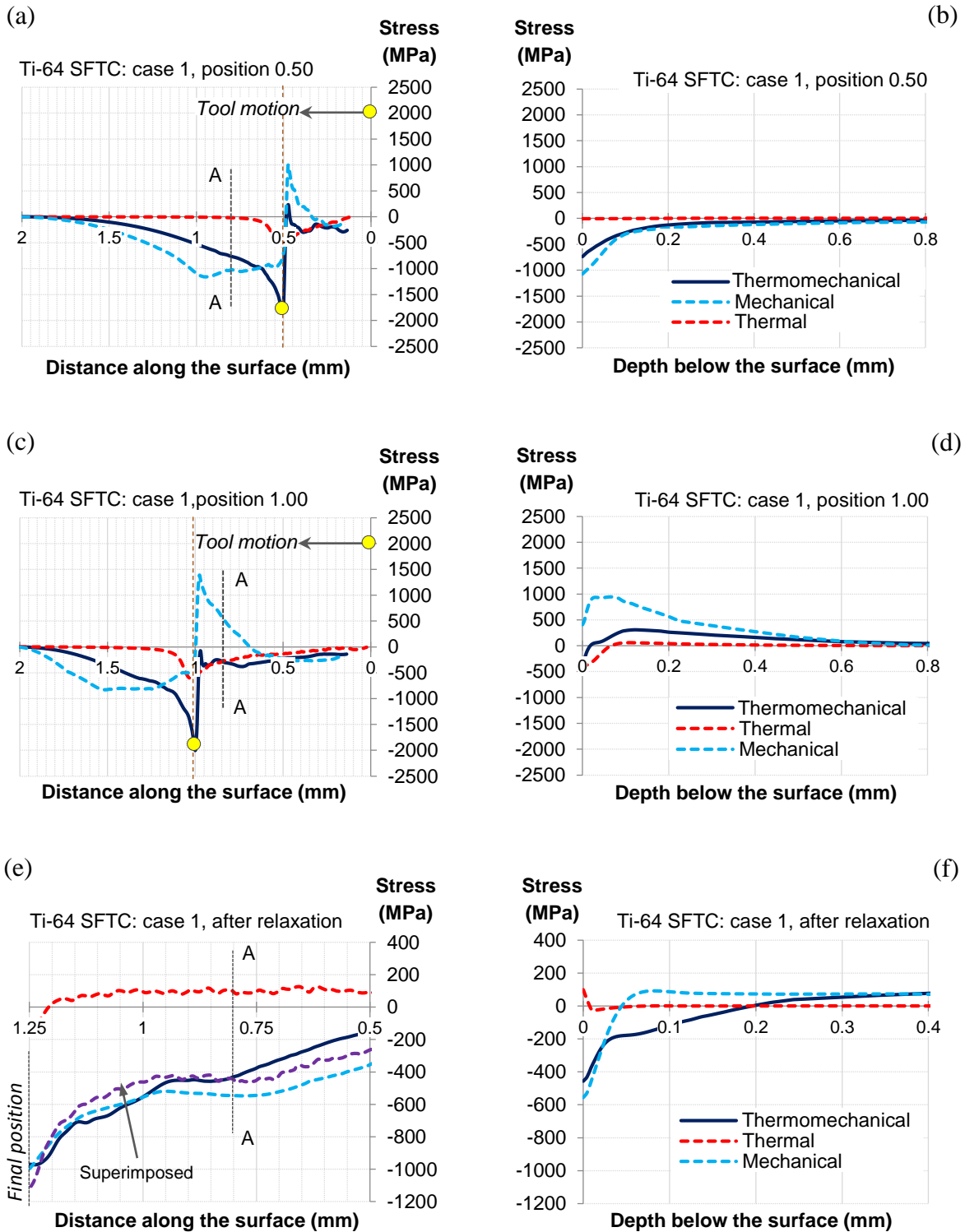


Fig. 5.11: predicted stress evolution at tool positions (a, b) 0.50 mm and (c, d) 1.00 mm during cutting of Ti-64 SFTC with parameters:  $t = 0.12$  mm,  $v = 60$  m/min, and  $r = 20$   $\mu$ m. The final residual stress distributions along and beneath the machined surface are shown in (e, f).

Stress distributions along and beneath the machined surface are shown in Fig. 5.11a and Fig. 5.11b, respectively, when the tool is at 0.5 mm of its cutting path. The region behind the cutting tool reveals the current stresses in the machined surface. The region in front of the tool depicts the stresses encountered by the surface material prior to contact. The current contact point is indicated by a position locator and coincides with peaks in the stress profiles. A similar illustration is provided in Fig. 5.11(c, d) for an advanced tool position of 1.0 mm. The residual stress distributions obtained at the end of the relaxation phase are presented in Fig. 5.11 (e, f). Residual stresses produced by purely thermal and purely mechanical loads were linearly superimposed. The resulting distribution is shown in Fig. 5.11e for analysis. Residual stresses are evaluated in a region sufficiently far from the tool tip where convergence is achieved. At a tool position of 0.8 mm within the stable region, the stress distribution as a function of depth beneath the surface (along A-A) is assessed in parallel to the superficial stresses at the same instances. The following observations were made.

During cutting, thermal compressive stresses ahead of the cutting tool are much smaller than the mechanical stresses, but their coupling is highly non-linear. The combination of thermal and mechanical loads produces a large increase in the magnitude of compressive stress, which becomes far more localized at the tool tip. Localized deformation due to high temperature gradients contributes to sharper stress peaks, whereas mechanical stresses alone are distributed over a greater surface region. Consequently, during plastic unloading in tension behind the tip, thermomechanical loads most often remain in the compressive region, whereas mechanical loads shift into the tensile region. The extent of deformation during the tensile half of the mechanical loading cycle determines the state of residual stresses. If the stretching or burnishing of the machined surface exceeds its deformation in compression as is the case here (Fig. 5.11c), the resulting residual stress state is compressive [2].

Although the material furthest from the cutting tool has already initiated the cooling process, thermal stresses do not cross over into the tensile region until the stress relaxation process is complete. This is due to the higher heat flux intensity required to generate large tensile stresses during heating for this material as shown in section 5.2.2. This slow formation of tensile stresses behind the tool could indicate that the mechanical load is dominant for this cutting condition (case 1, Table 5-3).

After stress relaxation (Fig. 5.11e), the superimposed stress profile and the resultant thermomechanical stress profile are very close. Thermal RS are slightly tensile ( $\approx 100$  MPa), while the mechanical RS are moderately compressive ( $\approx -540$  MPa). Thermomechanical RS are also moderately compressive with a magnitude of around  $-450$  MPa, which is very close in magnitude to the linear superposition of the isolated thermal and mechanical results. The dominance of the mechanical contribution is evident in this case.

By examining the residual stress profiles as a function of depth beneath the machined surface, it is observed that thermomechanical stress in the near-surface region always lies between the thermal and the mechanical stresses. Ahead of the cutting tool (Fig. 5.11b), the thermal stress is minimal. Compressive stresses generated by the thermomechanical load are lower than those introduced by the mechanical load due to thermal softening. Thermal stresses delineate the upper boundary (tensile), while the mechanical stresses define the lower boundary (compressive). Behind the tool, due to the persistent effect of the mechanical load and the delayed relaxation with respect to the thermal load, the mechanical stresses are in tension and constitute the upper boundary. After the relaxation process (Fig. 5.11f), thermal RS shift to slightly tensile and are re-established as the upper limit, while mechanical RS shift to moderately compressive and reconstitute the lower limit. The thermomechanically induced RS are closer to the mechanically generated RS. Coupling of thermal and mechanical stresses in the sub-surface of the material is highly more complex due to the varying penetration and distribution of the mechanical and thermal stress fields.

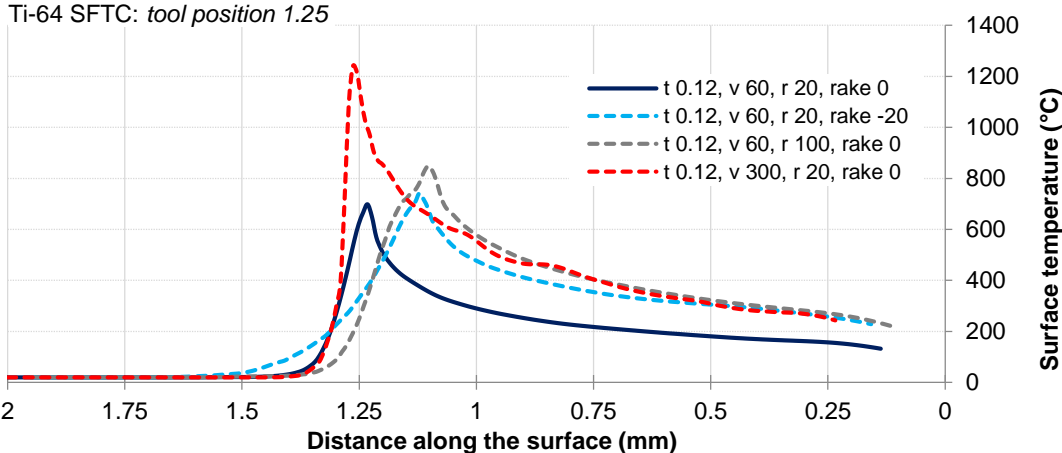


Fig. 5.12: temperature distributions along the surface of Ti-64 SFTC obtained through thermomechanical analysis at various parameter combinations.

#### 5.4.2.2 Influence of process parameters on thermal and mechanical loading

The surface temperature distributions obtained during thermomechanically coupled analysis for various parameter combinations (Table 5-3) are shown in Fig. 5.12 at the end of the tool stroke (1.25 mm). As previously discussed, the peak temperature attained at the surface is a strong indicator of the expected level of tensile RS induced by pure thermal loading. The lowest temperature was obtained for the reference condition (case 1). Cutting with a negative rake angle produced a relatively small increase in temperature ( $< 50^{\circ}\text{C}$ ). This can be attributed to the increased contact length and contact pressure at the tool/chip interface, as well as the possible occurrence of a stagnation zone in front of the tool tip that leads to additional shearing of the surface material and the generation of additional heat. Increasing the hone radius (0.02 to 0.10 mm) or the cutting speed (60 to 300 m/min) by 5 fold produced a greater elevation in surface temperature. In the case of hone radius, a temperature rise of around  $150^{\circ}\text{C}$  was observed due to the additional frictional heat arising from the increase in contact area between the workpiece surface and the tool. Surface temperature was mostly sensitive to cutting speed. At 300 m/min, a temperature rise of around  $550^{\circ}\text{C}$  was obtained that reflects the significant addition of frictional heat at the tool/chip and the tool/workpiece interfaces.

Fig. 5.13 shows the distribution along the surface of thermal (Fig. 5.13a), mechanical (Fig. 5.13b) and thermomechanical (Fig. 5.13c) stresses at a position of 1.25 mm of the load within its path. For the mechanical and thermomechanical analyses, this refers to the final position of the cutting tool. Stresses are evaluated parallel to the movement of the thermal load (Fig. 5.13a) for the thermal analysis and in the cutting direction (Fig. 5.13(b, c)) for the mechanical and thermomechanical analyses. An insert is provided for each case that shows the distribution of superficial RS after stress relaxation in a surface region sufficiently far from the tool tip and the leading edge of the workpiece. A higher degree of convergence of RS is obtained in this region.

The rise in surface temperature with varying cutting conditions (Fig. 5.12) is reflected in the increasing magnitude of thermally generated tensile RS. Moderately tensile ( $\approx 460$  MPa) and highly tensile ( $\approx 865$  MPa) thermal RS are obtained for the cases involving large hone radius ( $r = 100\ \mu\text{m}$ ) and high speed ( $v = 300$  m/min).

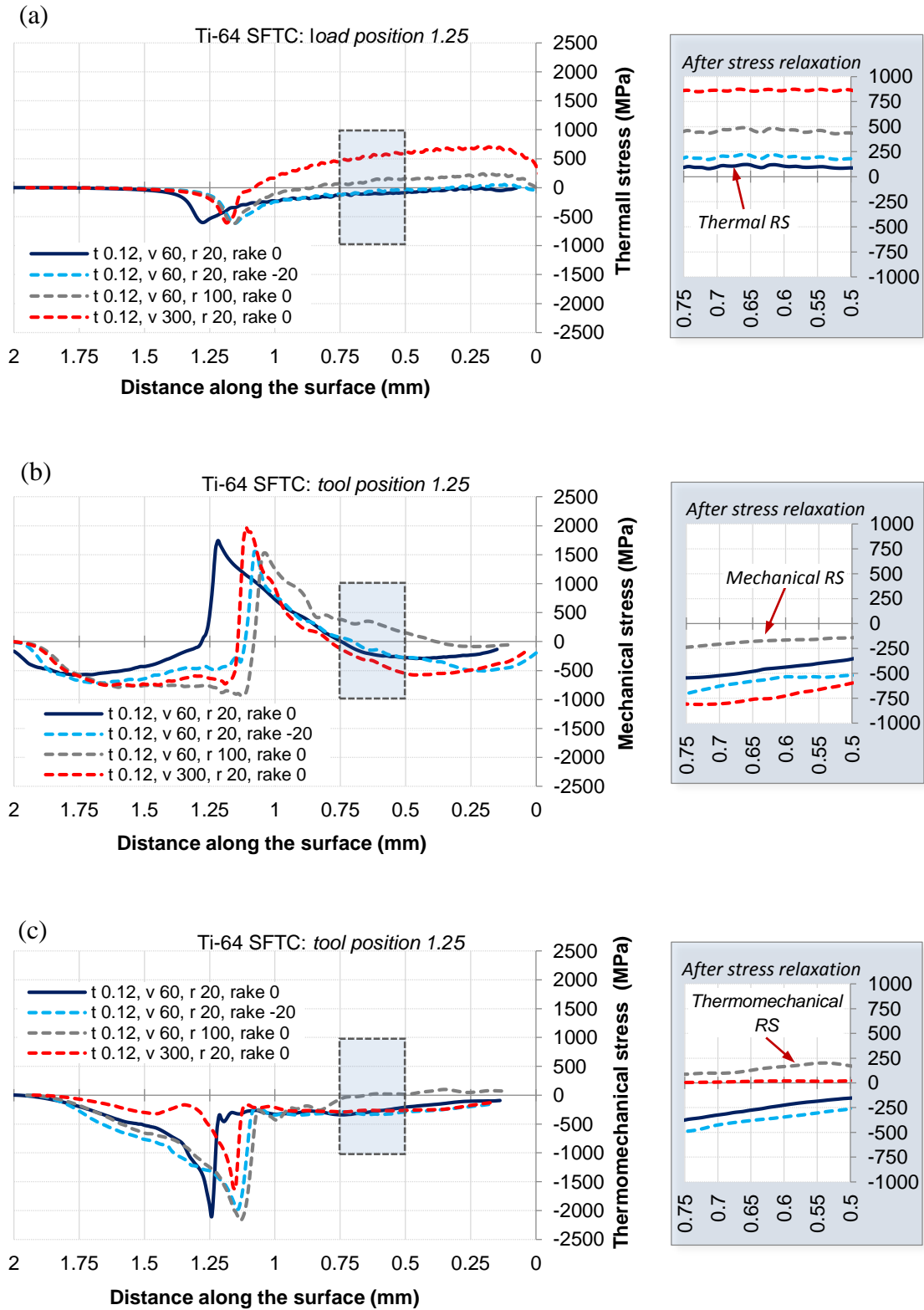


Fig. 5.13: distribution along the surface of Ti-64 SFTC of (a) thermal, (b) mechanical, and (c) thermomechanical stresses. The inserts show the distribution of RS attained after relaxation.

The resultant mechanically generated RS depend on the relative amount of plastic deformation in compression and in tension of the surface material during the loading cycle [8]. Mechanical RS are compressive for all the investigated parameter combinations. This reflects the dominance of the tensile phase of the loading cycle over the compressive phase for the investigated finish turning conditions. The largest compressive stresses were predicted for high speed machining at  $v = 300$  m/min (Fig. 5.13b). In the absence of thermal softening in a purely mechanical analysis, the material undergoes an important amount of strain rate hardening with increasing speed. Consequently, large compressive stresses are generated ahead of the cutting tool. This is coupled with a higher amount of plastic unloading in tension. As a result, a highly compressive residual stress state is obtained. The most compressive mechanically induced RS are obtained at this condition. A large hone radius  $r = 100$   $\mu\text{m}$  intensifies the compressive load ahead of the cutting tool. This could be the result of a dead metal zone beneath the curved cutting edge [51, 125]. The dominance of the tensile loading phase is diminished, and stresses induced in the machined surface are less compressive. The least compressive mechanically generated residual stress state is obtained at this condition. The negative rake angle  $\alpha_r = -20^\circ$  generates a more compressive load in the contact region compared to the reference condition. This could be due to stagnant material build up as in the case of the large hone radius. More compressive RS were obtained, however, than the reference case. When cutting with a negative rake angle, the resultant force acting on the tool tip is inclined further away from the machined surface and deeper into the sub-surface. Thus, the compressive load is distributed in a deeper elasto-plastic deformation zone. The contribution of plowing is increased leading to larger compressive RS [44].

It is inferred from the above analysis that a deeper understanding of the evolution of RS can be obtained by separating the thermally and mechanically induced residual stress components. While surface RS generated by thermal loads are always tensile, those generated by mechanical loads at the investigated finish turning conditions are always compressive in nature. The resulting thermomechanically induced stress state is, therefore, dependent on the imbalance between the thermal and mechanical components, which is highly influenced by the cutting parameters. As previously elaborated, cutting parameters have a significant influence on both thermally and mechanically generated RS. By comparing the RS generated by isolated thermal and mechanical loads shown in Fig. 5.13(a, b) with the resultant

thermomechanical stress state (Fig. 5.13c), it is observed that cutting with moderate speeds and sharp tools shifts the imbalance towards mechanically generated stresses (compressive), while high speeds and large edge radii shift the imbalance towards thermally induced stresses (tensile).

For the Ti-64 SFTC alloy under study, it appears that high speed machining can generate largely compressive mechanical RS and largely tensile thermal RS of nearly equal magnitudes (Fig. 5.14). The overall result is a slightly tensile residual stress state, as the imbalance is in slight favor of the thermally generated stresses. This indicates that if efficient cooling can be applied, higher speeds could potentially lead to compressive RS, depending on the speed range and the mode of lubrication. It was shown in Chapter 4 (section 4.3.4.4) that when machining aerospace grade bimodal Ti-6Al-4V alloy with conventional speeds and flood lubrication, compressive RS were enhanced by increasing the speed at certain cutting conditions. Compressive RS were reported for Ti-64 when orthogonal cutting with  $t = 0.1$  mm and  $v = 320$  m/min even in a dry cutting environment [54]. This could be driven by the lower sensitivity to thermal softening and hence to thermally induced tensile RS of the material. It was also shown that larger feed rate (section 4.3.4.4) and uncut chip thickness (section 4.3.3.2) levels lead to more compressive RS. This indicates that feed rate (uncut chip thickness) favors mechanically induced stresses during finish turning.

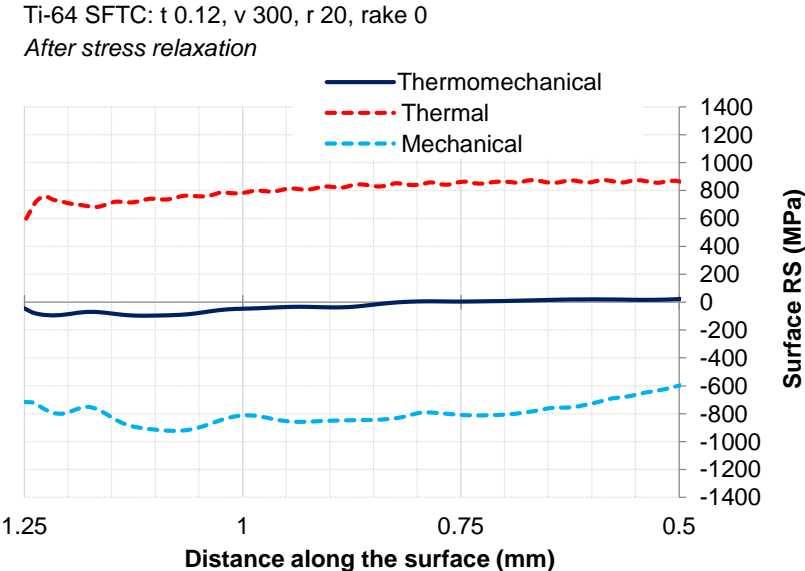


Fig. 5.14: predicted thermally, mechanically, and thermomechanically induced RS in Ti-64 SFTC during high speed machining with:  $t = 0.12$  mm,  $v = 300$  m/min,  $r = 20$   $\mu$ m,  $\alpha_r = 0^\circ$ .

Following the numerical study of the effect of cutting parameters on the evolution of RS during finish turning, and based on the results of the extensive experimental investigation for Ti-alloys, it is concluded that more compressive RS can be obtained by limiting the contribution of thermal stresses during cutting. The sensitivity of the material to thermal softening considerably influences the onset of plastic deformation due to thermal loading and the resulting magnitude of tensile RS. If machining is performed with minimal tool wear, sufficiently small hone radii, and moderate speeds, compressive RS can be generated in the near-surface layer. Increasing the feed rate (uncut chip thickness) within the finish turning range can further enhance compressive RS. It is possible to generate larger compressive RS at high speeds, but this requires the use of appropriate modes of cooling depending on the selected range of speeds.

## CHAPTER 6 FE MODEL DEVELOPMENT AND RESULTS

### 6.1 Introduction

A thermomechanically coupled finite element model of the orthogonal cutting process was developed using DEFORM™ 2D V 10.0 to predict machining forces, temperatures, and residual stresses (RS) for aerospace grade Ti-alloys Ti-6Al-4V and Ti-6Al-2Sn-4Zr-6Mo machined with sharp uncoated carbide tools. The DEFORM™ software is based on an updated Lagrangian formulation utilizing implicit integration. The model was optimized for accuracy and computational efficiency. Material identification was carried out to characterize the plastic deformation behavior of the Ti-alloys under investigation. Cutting simulations were performed for several combinations of uncut chip thickness and cutting speed ( $t_i$ ,  $v_i$ ) in the finish turning regime. Chip morphology was assumed to be continuous and non-segmental for the investigated cutting conditions. The final outcome consists of an accurate predictive numerical tool that can be used as a virtual machining medium for predicting the effect of machining parameters on residual stress formation.

### 6.2 FE model development

A flow diagram of the FE simulation of orthogonal cutting is shown in Fig. 6.1 that describes the methodology adopted in this research. In addition, the interaction between the modeling and experimental components of the research are emphasized. As elaborated previously in section 4.2.2, two sets of orthogonal cutting tests were carried out with the following purpose: (i) material identification, or more explicitly the identification of the constitutive law that accurately describes the deformation behavior of the workpiece material during cutting and (ii) validation of the FE model against experimental results of cutting forces, temperatures, and residual stresses.

In reference to Fig. 6.1, the inputs of the FE model are the cutting parameters, tool geometry, and the physical properties of the workpiece and tool material. Plastic deformation of the workpiece is largely governed by the constitutive law, which is calibrated by cutting experiments. As a result of the relative motion between the workpiece and the tool, normal and shear loads are generated on the rake face of the tool. These are influenced by the cutting parameters, tool geometry, and friction at the tool/chip interface.

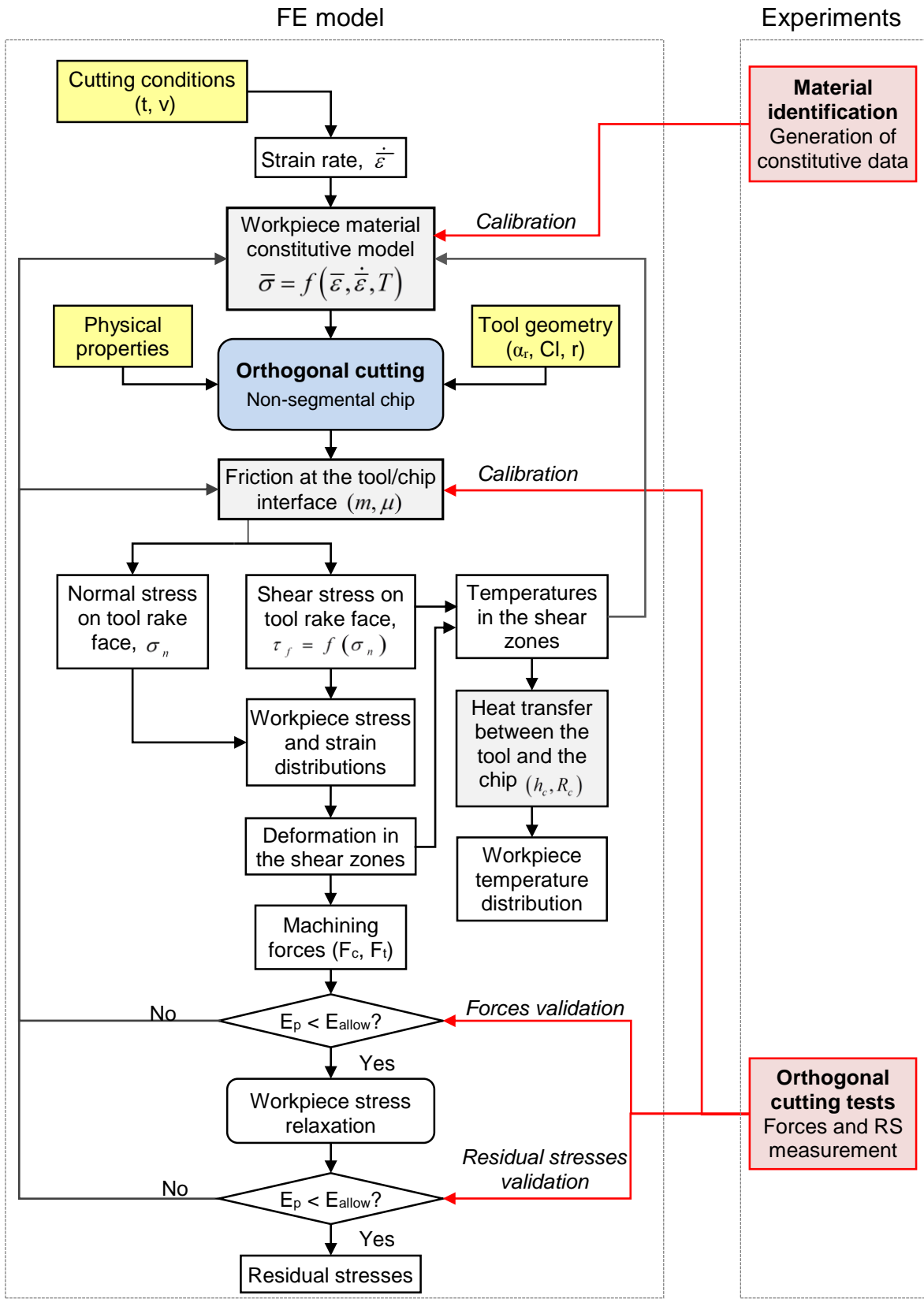


Fig. 6.1: flow diagram of the FE simulation of orthogonal cutting for residual stress prediction.

Plastic deformation in the shear zones is largely converted into heat. The temperature distribution in the tool, the chip, and the workpiece surface is determined by the thermal properties of the workpiece and the tool, and by the contact conditions at the tool/chip interface. The flow stress in the near-surface material is altered by the deformation and temperature rise in this region. This in turn affects the magnitude of machining forces. When the desired cutting length is attained, the tool is retracted. The workpiece is then allowed to cool down to ambient temperature. At this point, stress relaxation is complete, and the RS can be extracted from the model. The evolution of thermally and mechanically generated stresses with the advancement of the cutting tool determine the state and magnitude of RS. The objective is to develop a model that can predict machining forces and residual stresses with good accuracy. Consequently, they are both considered in the validation process.

### **6.2.1 Model optimisation for accuracy and computational efficiency**

It is widely established that material flow stress characteristics and tribological interactions at the tool/chip interface govern the accuracy of FE element predictions [58, 63, 65]. Several steps were taken to build a suitable model that balances accuracy and computational intensity. Firstly, material identification was carried out. A thorough analysis was then performed of the effect of several FEM parameters on the prediction accuracy including the material constitutive law, tool/chip interface friction, geometrical aspects, and workpiece mesh distribution.

#### *6.2.1.1 Material identification*

To model the plastic deformation behavior of the workpiece under the combined effect of very high strain, strain rate, and temperature, proprietary methodology for material identification developed at the National Research Council Canada (NRC) was implemented. The Distributed Primary Zone Deformation (DPZD) analytical model was used to generate broad ranges of constitutive data for the Ti-alloys based on orthogonal cutting tests [89-91]. Consequently, the data was generated at strain, strain rate, and temperature levels encountered during the cutting process, thereby overcoming the limitations of Split Hopkinson Pressure Bar (SHPB) based methods. The experimental setup and procedure are elaborated in section 3.3.2. Laser-assisted preheating was employed during the cutting tests to attain the higher temperatures encountered in the secondary shear zone. Quasi-static (QS) tests were performed at very low strains and strain rates to identify some coefficients and to

improve the convergence to a unique solution of the constitutive law. The constitutive data generated by the DPZD model was then fitted using regression analysis to several prevailing material constitutive laws applicable to the cutting process, including the Johnson-Cook (JC) and the Voce-Johnson-Cook (V-JC) models described in Eq. 6.1 and Eq. 6.2, respectively:

$$\sigma_f = (A + B\bar{\varepsilon}^n) \left( 1 + C_1 \ln \frac{\dot{\varepsilon}}{\dot{\varepsilon}_0} \right) \left[ 1 - \left( \frac{T - T_0}{T_{melt} - T_0} \right)^{m_1} \right] \quad (6.1)$$

$$\sigma_f = (a - b \exp(-c\bar{\varepsilon})) \left( 1 + C_2 \ln \frac{\dot{\varepsilon}}{\dot{\varepsilon}_0} \right) \left[ 1 - \left( \frac{T - T_0}{T_{melt} - T_0} \right)^{m_2} \right], \quad (6.2)$$

where  $\sigma_f$ ,  $\bar{\varepsilon}$ , and  $\dot{\varepsilon}$  are the flow stress, effective strain, and effective strain rate, respectively;  $\dot{\varepsilon}_0$  is the reference strain rate;  $T$ ,  $T_0$ , and  $T_{melt}$  are the instantaneous, ambient, and material melt temperatures, respectively;  $A$ ,  $B$ ,  $n$ ,  $C_1$ , and  $m_1$  are material constants for the JC law; and  $a$ ,  $b$ ,  $c$ ,  $C_2$ , and  $m_2$  are material constants for the V-JC law. Both the JC and V-JC equations constitute the product of three terms describing the material's sensitivity to strain hardening, strain rate hardening and thermal softening, respectively.

A systems approach to the generation of the constitutive data and identification of the constitutive law adapted from Shi et al. [89] is given in Fig. 6.2. The inputs into the DPZD model comprise: (i) the physical properties and initial temperature  $T_0$  of the workpiece material, (ii) the cutting parameters, and (iii) the average steady-state cutting force ( $F_c$ ), thrust force ( $F_t$ ), and chip thickness ( $t_c$ ) acquired from orthogonal cutting tests.

Based on the above information, the DPZD model generates hundreds of constitutive data sets for each cutting condition. A representative description of the primary shear zone using Oxley's parallel-sided shear zone model [33, 91], together with typical distributions of flow stress, strain, strain rate, and temperature obtained from the DPZD model are shown in Fig. 6.3. Each constitutive data set  $(\bar{\sigma}, \bar{\varepsilon}, \dot{\varepsilon}, T)$  represents one point along  $x$  at the center of the primary shear zone. The DPZD model is based on several assumptions including plane strain conditions, a sharp cutting edge, and continuous non-segmental chip morphology. The orthogonal cutting tests for material identification were carefully designed to fulfil the above idealizations to the greatest degree possible by selecting suitable workpiece and tool geometry, and by using appropriate cutting conditions.

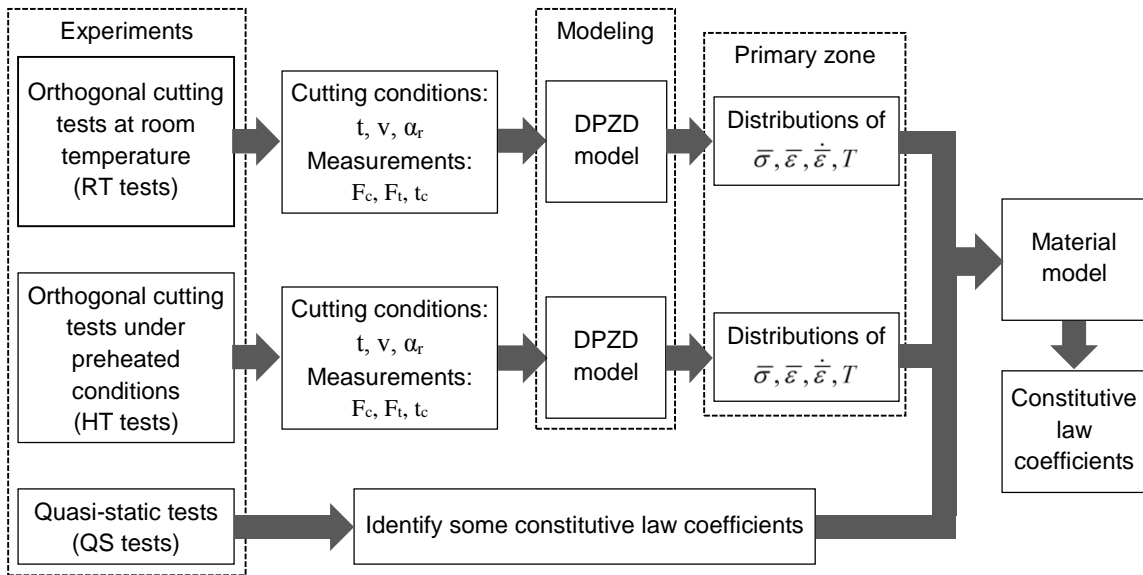


Fig. 6.2: systems approach to the generation of constitutive data and constitutive law identification.

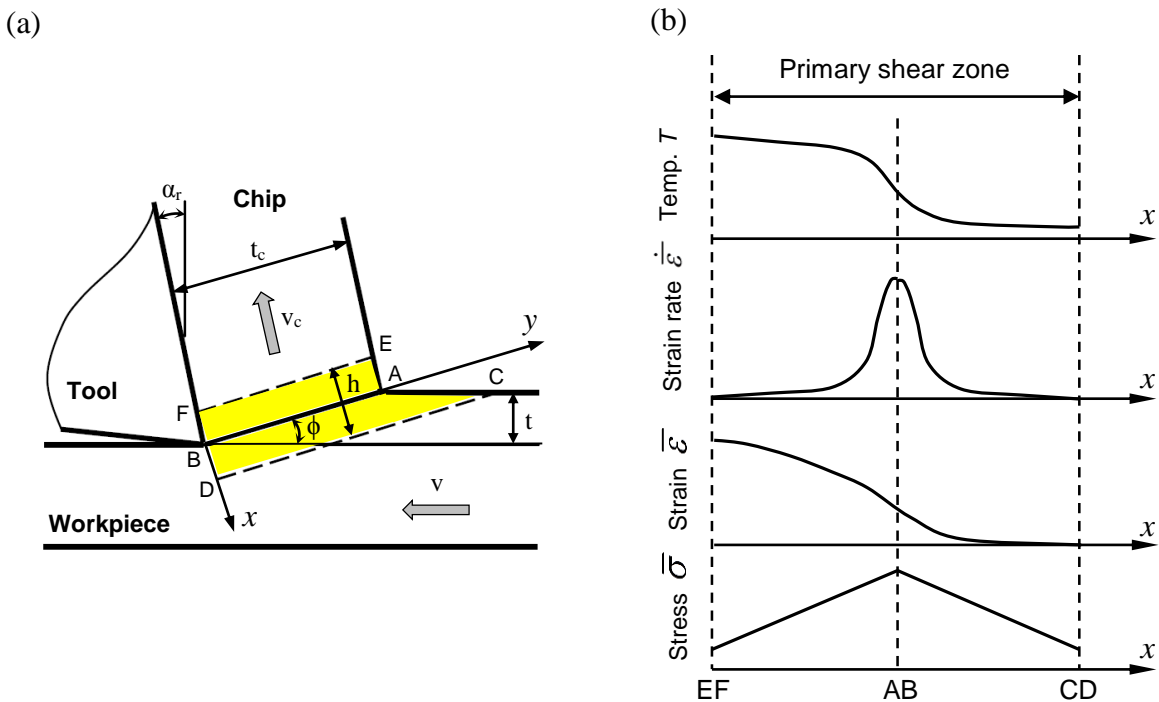


Fig. 6.3: (a) parallel-sided shear zone model [33] and (b) typical distributions of flow stress, strain, strain rate, and temperature from the Distributed Primary Zone Deformation (DPZD) model [90].

### 6.2.1.2 The material constitutive equation

The material identification process resulted in the calibration of several constitutive models applicable to metal cutting. Based on the evaluation criteria for constitutive law formulation established by Shi and Attia [91], the calibrated models were then evaluated on several levels: (i) statistical analysis of the goodness of fit of the constitutive data, (ii) accuracy of FE predictions of the cutting force, and (iii) closer conformity to the evolution of flow stress during thermomechanical processing of  $\alpha/\beta$  Ti-alloys.

The highest goodness of fit for the constitutive data was achieved for the Johnson-Cook (JC) and Voce-Johnson-Cook (V-JC) material models described in Eq. 6.1 and Eq. 6.2, respectively. More accurate predictions of the cutting force ( $F_c$ ) were attained, however, with the V-JC law. During thermomechanical processing below the beta transus,  $\alpha/\beta$  Ti-alloys can exhibit flow softening at a critical strain above which the material becomes insensitive to hardening [74, 81]. This phenomenon is termed strain softening. The behavior of flow stress as modeled by the JC and V-JC models is contrasted in Fig. 6.4 for the Ti-alloys under study. The flow stress is normalized with respect to the room temperature yield stress of Alloy 1. The JC law exhibits a monotonic increase in flow stress with increasing strain at all temperatures (Fig. 6.4a). The V-JC law restricts this behavior, and beyond a certain level of strain the material ceases to harden (Fig. 6.4b). Thus, the V-JC law offers a more accurate interpretation of flow stress behavior for Ti-alloys than the widely used JC equation.

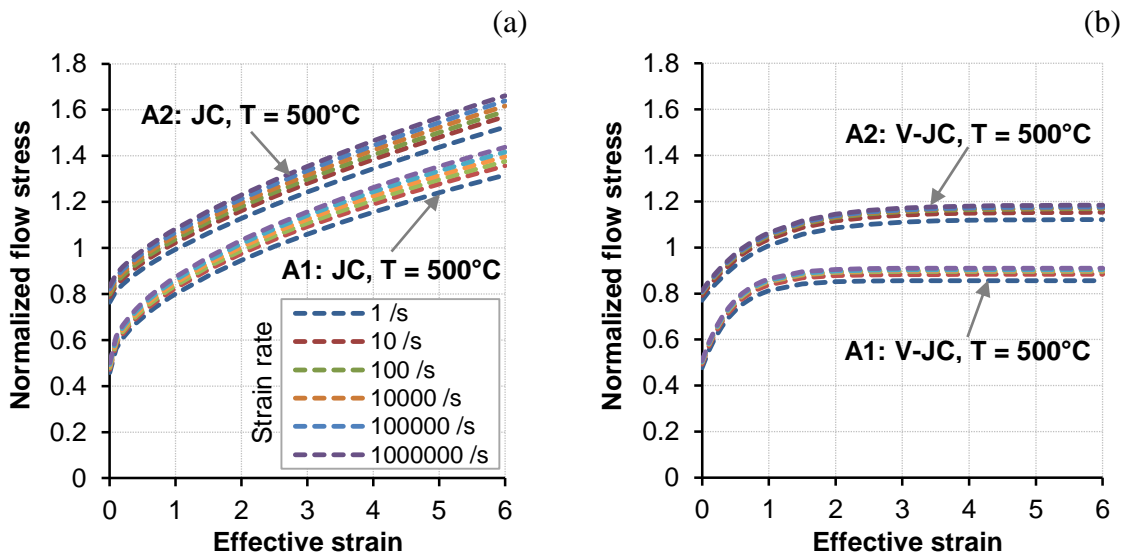


Fig. 6.4: flow stress behavior for both Ti-alloys at  $T = 500^\circ\text{C}$  as a function of effective strain and strain rate, as described by: (a) the JC model and (b) the V-JC model.

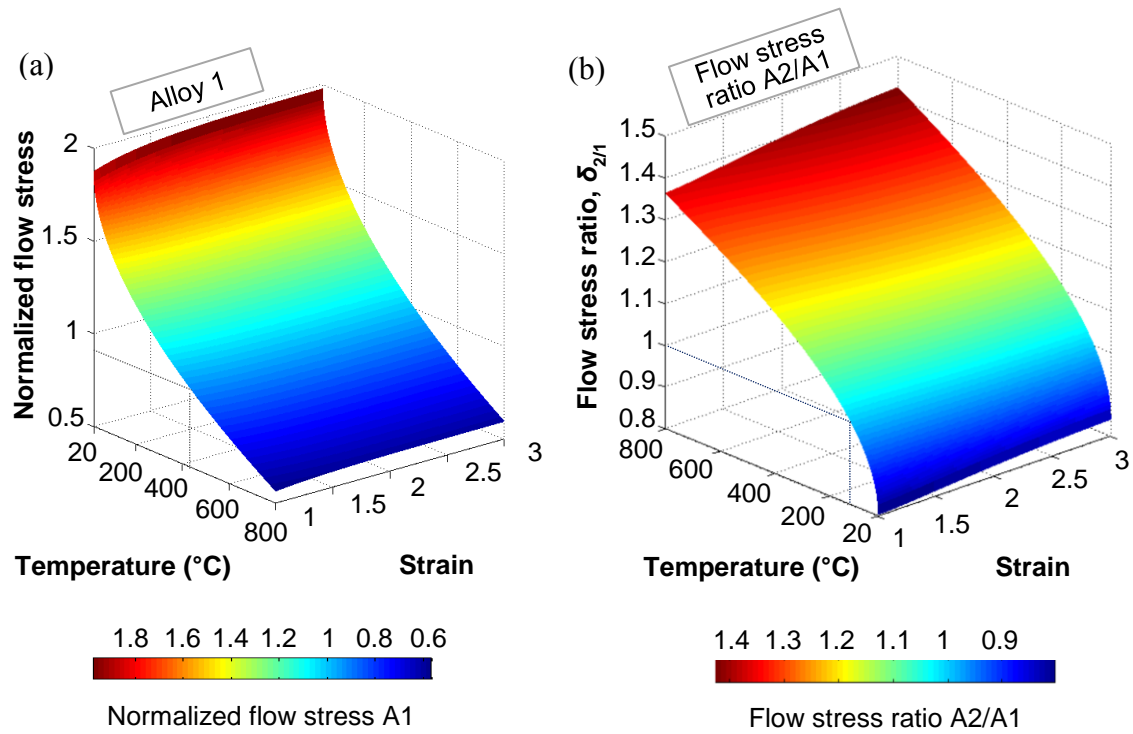


Fig. 6.5: variation with temperature and effective plastic strain of (a) Alloy 1 flow stress, and (b) flow stress ratio of Alloy 2 to Alloy 1, as described by the Voce-Johnson-Cook (V-JC) model, and for a fixed strain rate of  $10^3 \text{ s}^{-1}$ .

Modified versions of the JC equation that can account for a more severe reduction in flow stress due to strain softening were recently developed [74, 81]. These models, however, incorporate up to 5 additional material constants, which make them extremely difficult to calibrate and evaluate using the methods and criteria adopted in this work. The large number of parameters involved in the calibration can lead to non-unique solutions for a particular material. A more detailed discussion regarding the disadvantages of these models is provided in Chapter 7. Based on the above analysis, the V-JC constitutive model was selected and implemented in the FE model for both Ti-alloys.

The flow stress behavior of the Ti-alloys as described by the V-JC model for a fixed strain rate  $\dot{\epsilon} = 10^3 \text{ s}^{-1}$  is depicted in Fig. 6.5. More precisely, Fig. 6.5a shows the variation in flow stress with temperature and effective plastic strain for Alloy 1, and Fig. 6.5b shows the variation in the ratio  $\delta_{2/1} = \bar{\sigma}_2 / \bar{\sigma}_1$  of the flow stress of Alloy 2 to that of Alloy 1 at similar conditions. In Fig. 6.5a, the flow stress is normalized against the room temperature yield stress of Alloy 1. By examining the two figures, it can be seen that Alloy 1 is highly

sensitive to thermal softening and to a much larger extent than Alloy 2. As the temperature exceeds around 420°C (Fig. 6.5a), the flow stress of Alloy 1 drops by around 50%. Beyond a temperature of about 120°C (Fig. 6.5b), Alloy 1 undergoes thermal softening at a higher rate than Alloy 2. Beyond this point, the flow stress ratio  $\delta_{2/1}$  exceeds unity. In addition, at an effective strain  $\bar{\epsilon} > 1$ , Alloy 2 is more sensitive to strain hardening than Alloy 1. It should be noted that according to the V-JC model, the greater part of strain hardening for both Ti-alloys takes place within the range  $0 < \bar{\epsilon} < 1$ , as is evident in Fig. 6.4b.

The above findings indicate that at similar cutting conditions, Alloy 2 is expected to generate larger machining forces and higher cutting temperatures than Alloy 1, leading to more rapid tool deterioration.

### 6.2.1.3 Tribological tool and workpiece interaction

It is common to use a shear friction model with a constant friction coefficient at the tool/chip interface to simulate the cutting of Ti-alloys [73, 82, 93]. This is a reasonable assumption due to the adhesion of workpiece material to the tool and the continuous shearing of the formed TiC layer [126, 127]. Nevertheless, an in-depth numerical investigation of the effect of friction models on force and residual stress predictions was carried out for the Ti-alloys under study. The objective was to identify the model that offers the best overall agreement between predicted and experimentally measured machining forces and RS. It was found that hybrid friction models, which provide a closer representation of the real tool/chip interaction, produce more accurate predictions.

Zorev's sticking-sliding friction model was selected due to improved predictions with respect to the thrust force and residual stresses, and due to its dependency on the normal pressure, which is an important parameter that governs tribological interactions at the tool/chip interface [65]. Zorev's friction model is given by:

$$\begin{aligned} \tau_f &= \mu \sigma_n & \text{in the sliding region, where } & \mu \sigma_n < k_s, \text{ and} & & (6.3) \\ \tau_f &= k_s & \text{in the sticking region, where } & \mu \sigma_n \geq k_s, \end{aligned}$$

where  $\tau_f$  and  $\sigma_n$  are the friction shear stress and normal stress acting on the tool rake face, respectively,  $\mu$  is the sliding friction coefficient at the tool/chip interface, and  $k_s$  is the local shear flow stress of the deforming material.

As a first step, the average Coulomb friction coefficient for the investigated range of cutting parameters was estimated from the experimentally measured cutting and thrust forces. An iterative procedure was then implemented using Zorev's friction model, wherein the experimentally estimated Coulomb friction coefficient was used as a starting point. This initial value was then varied slightly until the best agreement between experimental data and FE predictions was obtained. As a result, a sliding friction coefficient  $\mu = 0.55$  was selected. In addition to cutting forces, which are commonly used to fine tune the value of the friction coefficient, RS were included in the iterative process to achieve an acceptable level of overall accuracy. The influence of the friction coefficient on the predicted forces and RS is mapped in the flow diagram presented in Fig. 6.1 that also illustrates the iterative procedure.

The friction models that were studied include: (i) shear friction with a fixed coefficient at two levels,  $m = 0.6$  and  $0.9$ , (ii) Zorev's sticking-sliding model with  $\mu = 0.55$  in the sliding region, (iii) a hybrid friction model with  $m = 0.9$  and  $\mu = 0.55$  in the sticking and sliding regions, respectively, and (iv) several variations of the hybrid model introduced by Sima et al. [74], which divides the contact region at the tool/chip interface into 3 friction regions: a sticking region with  $m = 1$ , a shear friction region with a fixed coefficient  $m < 1$ , and a sliding region with a fixed coefficient  $\mu$ . The regions are located at the hone radius (curved cutting edge), within the uncut chip thickness (straight cutting edge), and beyond the uncut chip thickness, respectively.

Numerous cutting simulation cases were run at the conditions constituting the corners of the orthogonal cutting matrix for Alloy 1,  $(t_1, v_1)$  and  $(t_3, v_3)$ , for the above friction models. Simulation conditions in the figures displaying FEM results are identified as follows:

|     |       |            |          |        |
|-----|-------|------------|----------|--------|
| 1   | 2     | 3          | 4        | 5      |
| A2/ | V-JC/ | Zorev 0.55 | (10000): | t3, v3 |

where (1) gives the alloy type; (2) indicates the constitutive law; (3) designates the tool/chip interface friction model followed by the friction coefficient value; (4) indicates the number of elements used to mesh the workpiece; and (5) denotes the cutting parameters  $(t_i, v_i)$ .

As shown in Fig. 6.6, Zorev's model was found to eliminate the large discrepancy in the prediction of the thrust force, a common problem in FE simulations [128]. In addition, Zorev's model offered more accurate residual stress predictions as shown in Fig. 6.7. This is especially true at low cutting speed conditions  $(t_i, v_1)$ .

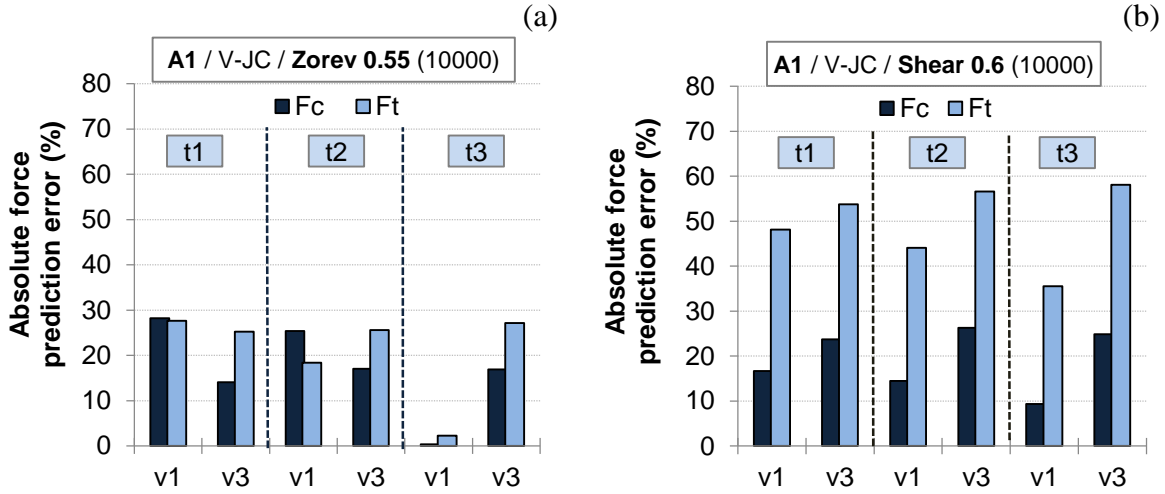


Fig. 6.6: Alloy 1: comparison of force prediction errors over the full range of conditions ( $t_i$ ,  $v_i$ ) obtained with: (a) Zorev's friction model ( $\mu = 0.55$ ) and (b) constant shear friction ( $m = 0.6$ ).

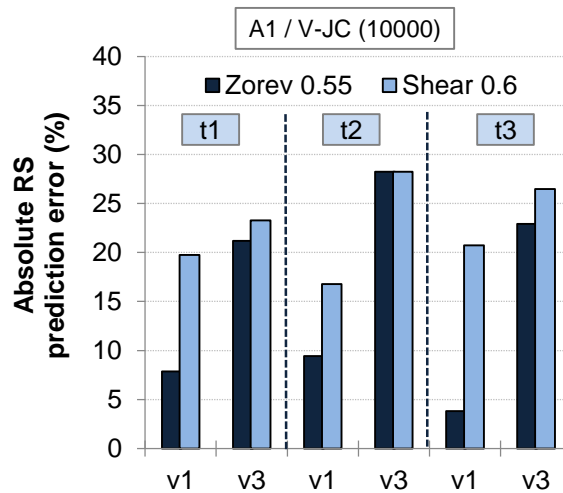


Fig. 6.7: Alloy 1: comparison of RS prediction errors over the full range of conditions ( $t_i$ ,  $v_i$ ) obtained with Zorev's friction model ( $\mu = 0.55$ ) and constant shear friction ( $m = 0.6$ ).

In order to accelerate the attainment of steady-state machining conditions during the FE simulations, a large heat transfer coefficient  $h_c = 10^6 \text{ kW/m}^2 \text{ }^\circ\text{C}$  was adopted, and perfect contact was assumed at the tool/chip interface. The FE model was, therefore, not only optimized for accuracy, but also for computational efficiency. The reduction in simulation time from several days to only 24-36 hours is an important attribute that makes the model a more practical investigative tool of added value to industry.

#### *6.2.1.4 Geometrical aspects*

The effect of workpiece thickness on predicted residual stress profiles was evaluated. Several cutting simulations were performed with fixed cutting parameters, but with varying workpiece thickness from 0.3 to 2 mm. It was found that thickness has a small influence on the superficial residual stress. However, it has a large effect on the predicted residual stress profiles, most probably due to the altered temperature distribution in the near-surface layers. The effect on RS distribution was found to be minimal beyond a thickness of 1 mm. Furthermore, the influence of tool stroke or cutting length on the convergence of surface residual stresses was investigated for several values between 2 and 8 mm. It was observed that within the investigated range of parameters, and for the adopted model assumptions and idealizations, a tool stroke exceeding 2 mm could attain steady-state cutting and achieve convergence of surface residual stresses.

#### *6.2.1.5 Tool and workpiece mesh density and distribution*

A mesh grading strategy was implemented that maintained a dense mesh in the vicinity of the cutting zone and in the newly generated workpiece surface. For the accuracy of predictions, it was important to implement a mesh distribution that can account for sharp stress, strain, and temperature gradients in the primary shear zone, the forming chip, and the machined surface. The latter was especially important for residual stress predictions. One of DEFORM's main strengths is its capability to continually monitor mesh distortion and to perform uninterrupted automatic remeshing according to user set criteria. Consequently, a meshing strategy was implemented with the following guidelines:

- Placing at least 10 elements within the uncut chip thickness, which dictates the minimum admissible number of elements in the workpiece.
- Maintaining a high mesh density in the shear zone, the forming chip, and the machined surface through the use of suitably positioned mesh windows coupled with automatic remeshing.
- Applying a graded mesh to the tool that models its geometry with high fidelity and preserves a high mesh density at the tool tip and in the tool/workpiece contact regions.
- Selecting remeshing criteria that preserve the integrity of the mesh during the simulation.

A convergence analysis was carried out to examine the effect of mesh density on FE predictions. The analysis showed that while its effect on machining forces was small, element size had a significant influence on residual stress predictions. For the investigated cutting conditions, compressive residual stresses (RS) were largely underpredicted for element sizes above 15  $\mu\text{m}$ . In addition, the residual stress distributions predicted with low mesh densities were almost linear, which is never the case in reality. Excessively large elements cannot account for sharp stress, strain and temperature gradients in the near-surface layer. This affects the magnitude of predicted RS as well as their distribution. Thus, the workpiece was meshed with a minimum of 10,000 elements resulting in an element size of 4-8  $\mu\text{m}$  in the primary shear zone, the forming chip, and the workpiece surface.

## 6.2.2 Model description

### 6.2.2.1 Geometry, kinematics, and boundary conditions

As a result of the model optimization described in the previous section, a workpiece length of 4 mm and thickness of 1 mm were adopted. To model a sharp cutting edge, an edge radius of 10  $\mu\text{m}$  was employed. This was based on a measurement performed on a metallographic tool section perpendicular to the cutting edge with an optical microscope at high magnification. The FE model setup and boundary conditions are shown in Fig. 6.8.

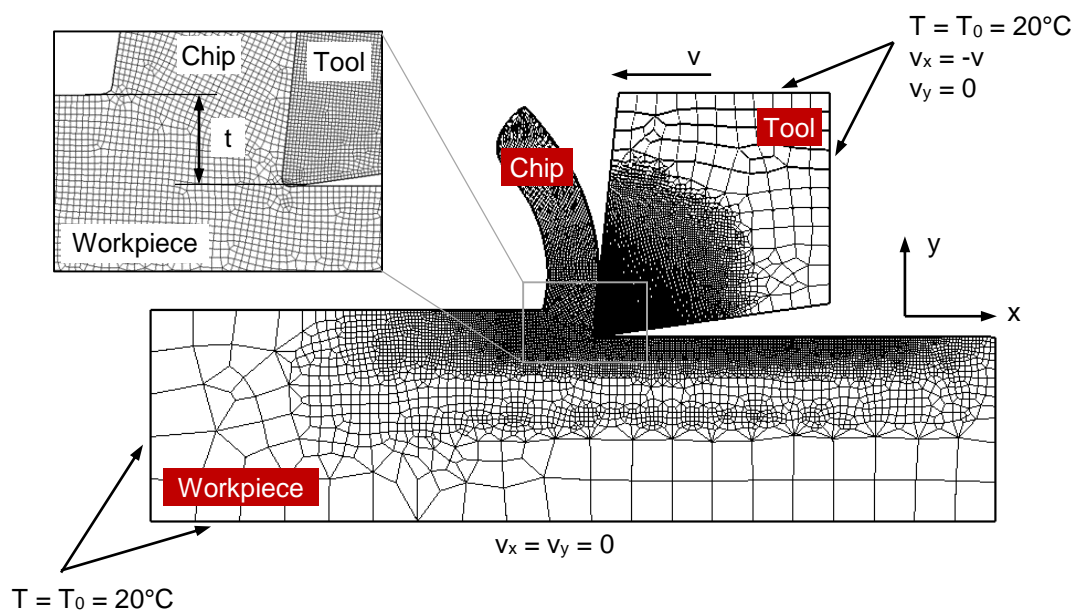


Fig. 6.8: FE model setup and boundary conditions.

During the FE simulation, the tool moves relative to the fixed workpiece at the desired uncut chip thickness ( $t$ ) and with the required cutting speed ( $v$ ). Velocities  $v_x = v_y = 0$  are imparted to the nodes in the bottom edge of the workpiece, sufficiently distant from the cutting zone, to fix them in space. On the other hand, velocities  $v_x = -v$  and  $v_y = 0$  are assigned to the tool as shown. The workpiece and tool edges furthest away from the cutting zone are retained at ambient temperature  $T_0 = 20^\circ\text{C}$ . Heat transfer with the environment is enabled for the edges that are closer to the cutting zone. Having reached its stroke of 2.5 mm, the tool is retracted, and the workpiece is allowed to cool down to room temperature, mainly by conduction with the material bulk and by convection with the surrounding environment.

#### 6.2.2.2 *Material modeling*

To predict residual stresses, the workpiece material is modeled as an elasto-plastic body to allow the recovery of elastic strains and the formation of deformation gradients that lead to incompatibilities between the surface and underlying layers. The tool, however, is modeled as a rigid body. Temperature dependent physical and thermal properties of the material supplied by the industrial partner are assigned to the workpiece in the FE simulations. The thermophysical properties of Kennametal grade K68 uncoated carbide tools are assigned to the tool. The Voce-Johnson-Cook (V-JC) material constitutive law calibrated as per the procedure described in section 6.2.1.1 is adopted for both alloys.

### **6.3 FE model validation and analysis of results**

In this section the accuracy of FE model predictions involving continuous non-segmental chip formation is assessed. The FE model was validated against experimentally measured forces, temperatures, and RS for both Ti-alloys over the full range of investigated parameters ( $t_i, v_i$ ).

#### **6.3.1 Machining forces**

A comparison between experimentally acquired (Exp) and numerically predicted (FEM) machining forces for both Ti-alloys is given in Fig. 6.9. Good agreement exists between experimental and predicted forces. The FE predictions reflect the substantial increase in force with increasing uncut chip thickness. Although the experimental cutting force exhibited a small increase with rising speed, predictions suggest a small reduction in cutting force. This discrepancy could be due to the assumed non-segmental chip morphology.

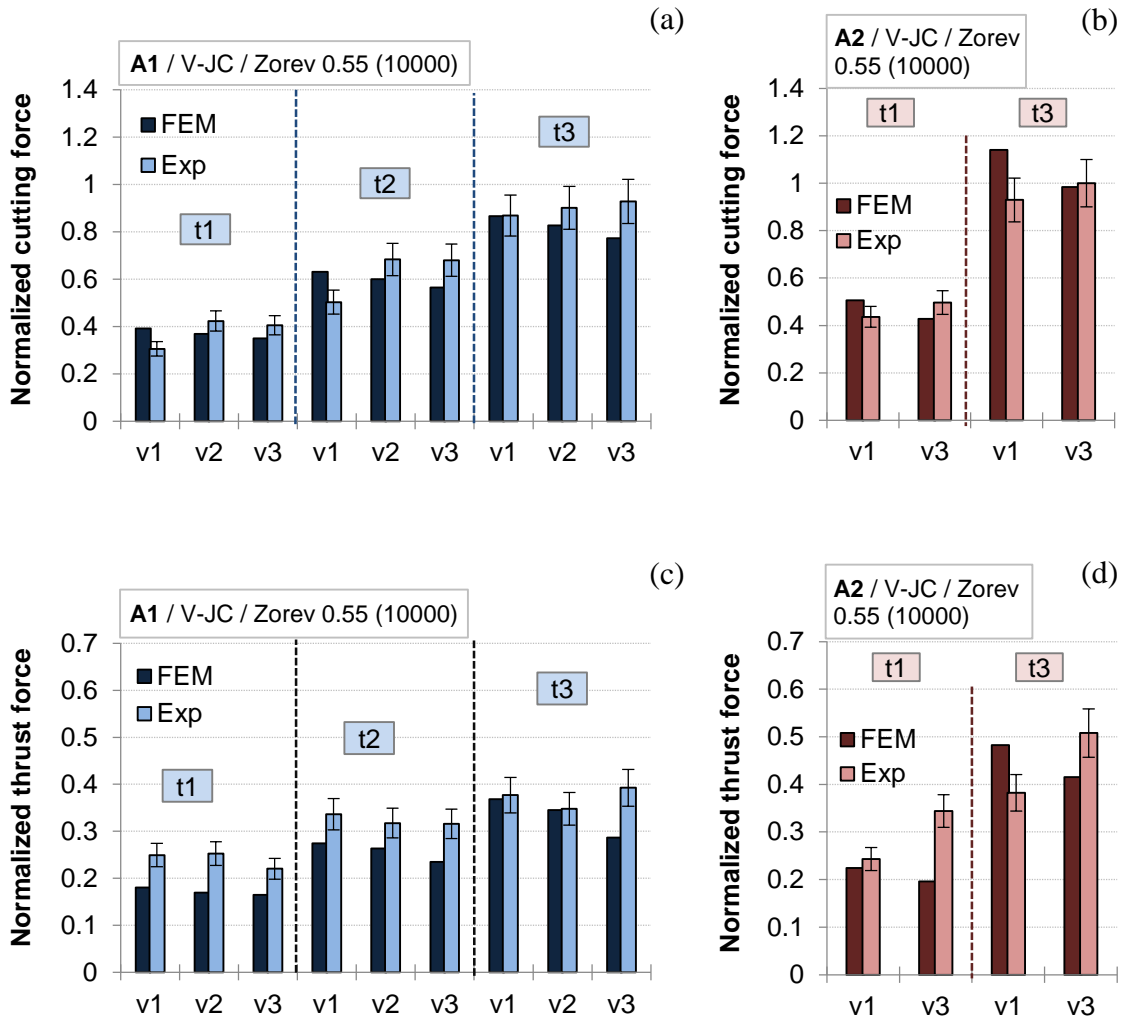


Fig. 6.9: comparison between FE predictions and experimentally acquired: (a, b) cutting force ( $F_c$ ) for Alloy 1 and Alloy 2, respectively, and (c, d) thrust force ( $F_t$ ).

An estimate of force prediction errors is shown in Fig. 6.10 for both Ti-alloys. Over the finish turning regime under study, cutting force predictions were mostly accurate to within  $\pm 15\%$  as shown in Fig. 6.10(a, b), except for conditions  $(A_1, (t_1, v_1))$ ,  $(A_1, (t_2, v_1))$ , and  $(A_2, (t_3, v_1))$  where the average error was around 25%. For Alloy 1, the thrust force was underpredicted by up to  $\approx 30\%$  as shown in Fig. 6.10c, except for condition  $(A_1, (t_1, v_2))$  that neared 35%. The thrust force prediction error was within  $\pm 30\%$  for Alloy 2 as shown in Fig. 6.10d, except for condition  $(A_2, (t_1, v_3))$  that approached 45%. It should be noted that in FE simulations it is common to have errors exceeding 50% in thrust force predictions [128].

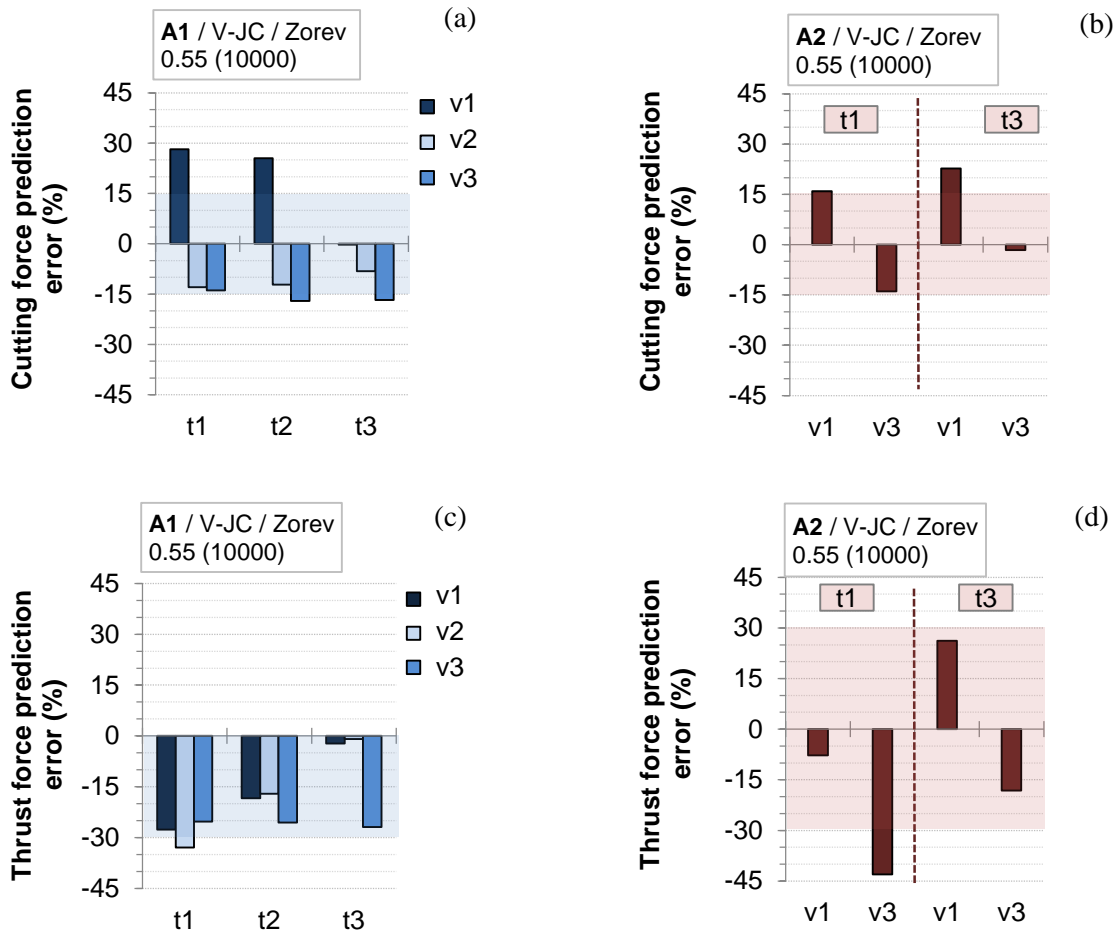


Fig. 6.10: percentage errors in FE predictions of (a, b) cutting force ( $F_c$ ) and (c, d) thrust force ( $F_t$ ).

### 6.3.2 Cutting zone temperatures

Using an IR camera, it was not possible to obtain a clear vision of the cutting tool or the workpiece surface after engagement. This was due to the continuously winding nature of the chip that concealed the cutting zone (Fig. 3.11). Thus, the peak temperature measured in the free surface of the chip at several instances during cutting was compared to the predicted temperature at the same position. The range of temperatures predicted by the FE model and measured by the IR camera for several values of emissivity is given in Table 6-1.

Temperature readings acquired from the infrared images depend on the value of emissivity. When the value  $e = 0.3$  calibrated for unmachined Alloy 1 specimens was used for the chip, the temperatures in the chip were underpredicted by around 30%. The free surface of a typical chip obtained during orthogonal cutting is shown in Fig. 4.1. Increased roughness and obscurity of the surface are factors that are known to increase the emissivity.

Table 6-1: Alloy 1: IR measurements for various emissivity values and FE predictions of the maximum temperature in the chip's free surface over the investigated cutting conditions.

| <b>Emissivity</b> | <b>IR temperature range (°C)</b> | <b>FEM temperature range (°C)</b> |
|-------------------|----------------------------------|-----------------------------------|
| 0.3               | 572 - 755                        | 395 – 560                         |
| 0.4               | 472 - 623                        |                                   |
| 0.5               | 423 - 535                        |                                   |

The chip would therefore be expected to have a higher emissivity than the workpiece. With  $e = 0.4$ , the underprediction of chip surface temperature is reduced from around 30% to 15%. In the absence of experimental measurements of chip emissivity at high temperatures, a value of  $e = 0.4$  is adopted. Furthermore, no phase transformation products were observed in the near-surface layer of machined Alloy 1 specimens, even for the harshest condition ( $t_3, v_3$ ). This confirms that the temperature in the near-surface layer did not exceed the beta transus ( $970 \pm 50^\circ\text{C}$ ) of the Ti-6Al-4V alloy as predicted by the FE model.

#### 6.3.2.1 Effect of cutting parameters on temperature distribution

Through dimensional analysis, Shaw [1] established that for a given tool-workpiece-environment combination,

$$\bar{\theta}_T \propto v^{0.5} t^{0.3}, \quad (6.4)$$

where  $\bar{\theta}_T$  is the mean tool face temperature. The mean tool face temperature predicted by the FE model for Alloy 1 was found to follow a relationship that is in close agreement with Shaw, given by:

$$\bar{\theta}_T \propto v^{0.46} t^{0.25} \quad (6.5)$$

This relationship was obtained by studying the dependence of the average predicted temperature at the tool/chip interface ( $T_{\text{int}}$ ) on the cutting speed ( $v$ ) and uncut chip thickness ( $t$ ) over the range of investigated cutting conditions ( $t_i, v_i$ ) as shown in Fig. 6.11. The effect of speed on temperature predictions at high uncut chip thickness conditions ( $A_1, (t_3, v_i)$ ) is illustrated in Fig. 6.12. Specifically, Fig. 6.12a shows the temperature distribution at the tool/chip interface beyond the tool tip O and along the  $x$ -axis delineating the rake face. The temperature field in the tool, the workpiece surface, and the chip is shown in Fig. 6.12b.

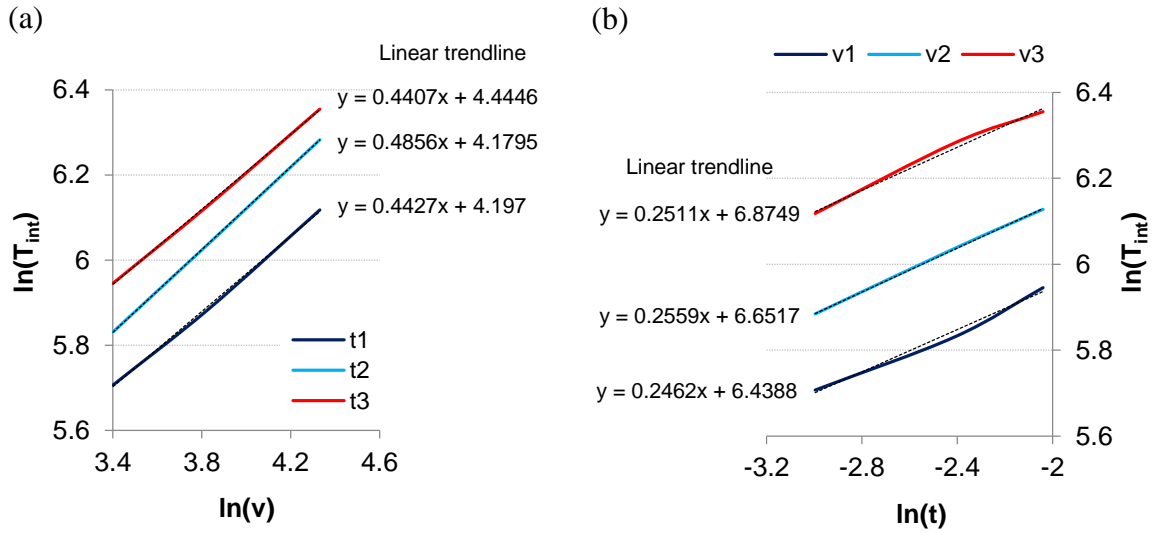


Fig. 6.11: Alloy 1: the dependence of the average predicted temperature at the tool/chip interface,  $T_{int}$ , on: (a) the cutting speed,  $v$ , and (b) the uncut chip thickness,  $t$ .

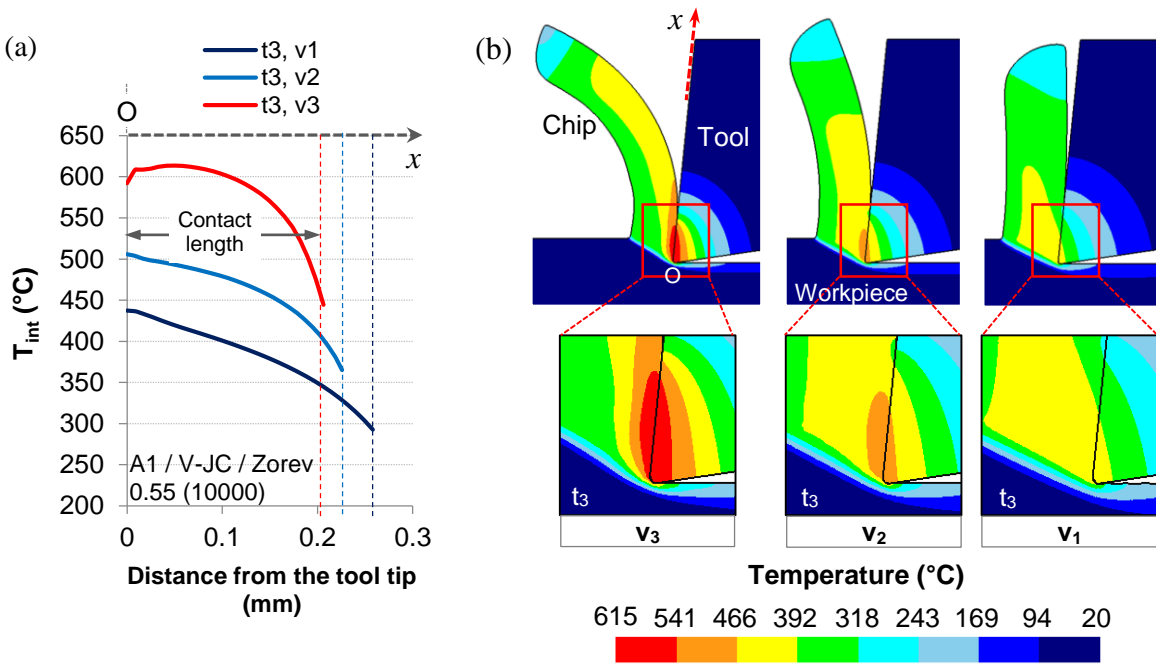


Fig. 6.12: Alloy 1: effect of cutting speed on temperature predictions at high uncut chip thickness conditions ( $t_3, v_i$ ): (a) temperature distribution at the tool/chip interface and (b) temperature field in the tool, workpiece surface, and the chip.

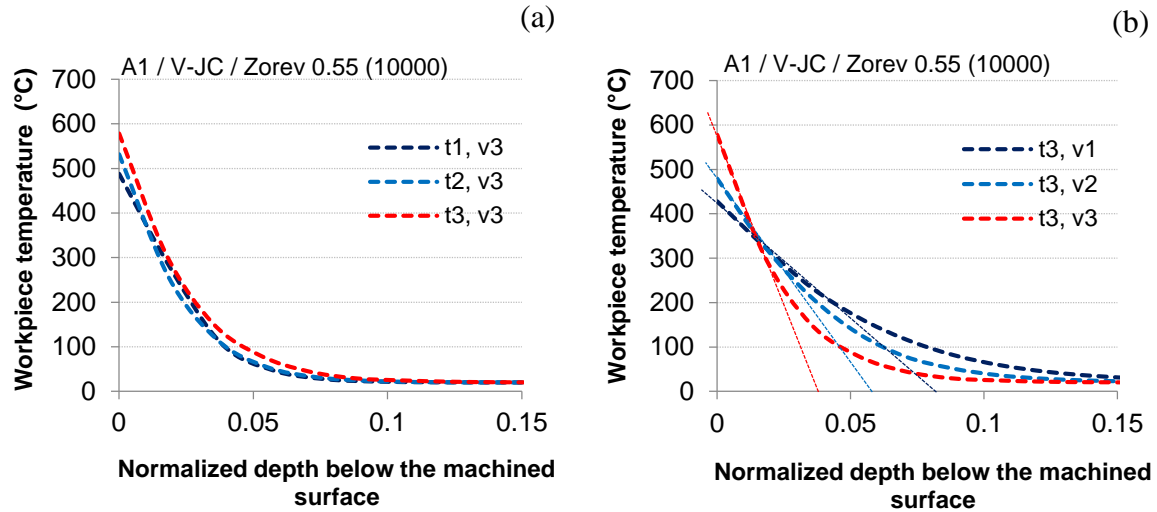


Fig. 6.13: Alloy 1: predicted temperature distribution in the workpiece surface after a simulated cutting length of 2.5 mm, and under the effect of: (a) uncut chip thickness,  $t$ , at conditions ( $t_i, v_3$ ) and (b) cutting speed,  $v$ , at conditions ( $t_3, v_i$ ).

Increasing the cutting speed by 150% ( $v_1$ - $v_3$ ) promoted an increase in tool tip temperature of around 150°C (Fig. 6.12a) combined with a higher extent of chip curl (Fig. 6.12b). Thus, the contact length was reduced, and thermomechanical loads were further concentrated at the tool tip. This in turn contributed to a larger increase in cutting zone temperature. It is evident from Fig. 6.11 and Fig. 6.12, as expected, that the temperature at the tool/chip interface and in the shear zones is predominantly controlled by the cutting speed. In consequence, cutting speed exerts a higher influence than uncut chip thickness on the temperature distribution in the workpiece surface as illustrated in Fig. 6.13. This can have an important bearing on residual stresses (RS).

### 6.3.3 Residual stresses

A comparison between FE predictions (FEM) and experimental measurements (Exp) is presented in Fig. 6.14. Experimental and predicted surface RS are generally in good agreement. FE predictions reflect the experimentally determined trends of diminished compressive RS with increasing cutting speed and enhanced compressive RS with increasing uncut chip thickness. Residual stress prediction errors for Alloy 1 are shown in Fig. 6.15. At conditions of low and intermediate speed ( $v_1$  and  $v_2$ ), the prediction error is within  $\pm 10\%$ . At high speed ( $v_3$ ), compressive RS are underpredicted by around 25% on average.

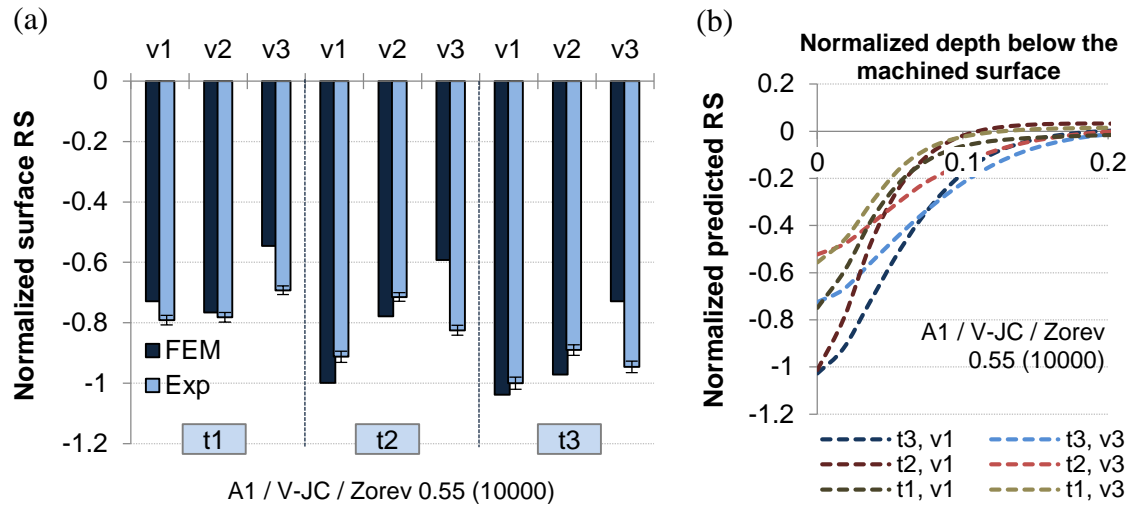


Fig. 6.14: Alloy 1: (a) comparison between FE predictions and experimental measurements of RS and (b) effect of cutting parameters ( $t_i$ ,  $v_i$ ) on predicted residual stress profiles.

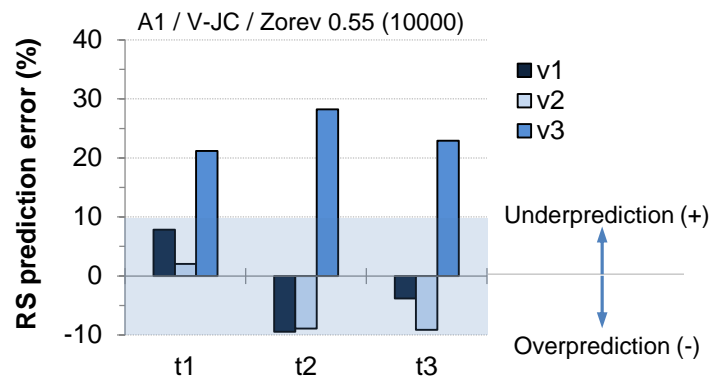


Fig. 6.15: Alloy 1: FE residual stress prediction errors over the range of investigated cutting conditions ( $t_i$ ,  $v_i$ ) for dry orthogonal cutting.

It is believed that to improve the accuracy of predictions at high cutting speed, chip segmentation should be accounted for in the FE model. In high speed machining of Ti-64 at  $v = 320$  m/min, it was shown that chip segmentation can lead to a drop in predicted surface temperatures and an associated increase in compressive RS [54].

### 6.3.3.1 Effect of cutting parameters on residual stresses

Using the FE model, an attempt was made to predict the sub-surface distribution of RS, which was not measured by XRD. The effect of cutting parameters on the residual stress profiles is shown in Fig. 6.14b. The upward shift with increasing cutting speed indicates a state of diminished compressive RS. The downward shift with increasing uncut chip

thickness reveals more compressive superficial and sub-surface RS. As shown in Fig. 6.13b, with increasing speed, sharper temperature gradients are developed coupled with more elevated surface temperatures. Due to the Ti-alloy's low thermal conductivity, the added heat energy is confined in a shallower sub-surface layer. This causes RS to be very sensitive to surface temperature. As elaborated in section 5.2.2, tensile RS are generated by high intensity thermal loads due to non-uniform thermal expansion. Thus, cutting conditions involving high speed, large hone radii, and flank wear that promote elevated surface temperatures can shift RS from a compressive to a tensile state by promoting the dominance of thermally induced deformation (Fig. 5.13).

To investigate further, FE simulations were performed of high speed machining. The range of cutting speeds was extended to 274 m/min. In addition, the effect of honed cutting edges on RS was studied for hone radii of up to 0.080 mm. This numerical investigation was conducted after having acquired a high confidence level in the accuracy of FE predictions through the validation process. As a result, the optimized model parameters were maintained.

The effect of cutting speed on predicted surface RS up to the high speed range is shown in Fig. 6.16a for conditions  $(A_1, (t_3, v_i))$ . Furthermore, the effect of hone radius on surface RS for conditions  $(A_1, (t_3, v_3, r_i))$ , where  $r$  represents the hone radius, is shown in Fig. 6.16b. Residual stresses were adjusted for chip segmentation at high cutting speeds. It is later established in Chapter 7 that compressive RS are underpredicted by around 25% when chip segmentation is neglected at high speeds. The experimental measurements of RS at lower speeds are included for the purpose of validation. The ratio of the von Mises effective stress to the flow stress of the Ti-alloy is also shown. This ratio is estimated based on the instantaneous values of temperature, effective strain, and effective strain rate corresponding to the peak effective stress encountered by the surface elements at the center of the cutting path. A value of unity denotes the onset of plastic deformation. The stress ratios resulting from conditions where the mechanically induced stresses are largely dominant are in the range of 1 to 1.25. This is representative of cutting with moderate speeds and sharp edges, as per the conditions investigated experimentally. On the other hand, stress ratios associated with high cutting speeds and honed edges that encourage thermally induced deformation are in the range of 1.25 to 1.90. This is indicative of the occurrence of thermal softening in the surface material. Variations in RS and stress ratios are plotted against the predicted peak

temperature in the machined surface for every cutting condition. FE modeling provides a valuable tool to examine the distribution of state variables that cannot be directly measured. The temperature and stress distributions along the workpiece surface under the effect of high cutting speeds and honed cutting edges are shown in Fig. 6.17. These distributions were conveniently captured at a tool position of 1.6 mm within the cutting path. They reveal the state of the machined surface in front of the cutting tool, during contact, and behind the cutting tool. A position locator depicts the position of the tool tip, which coincides with sharp stress and temperature peaks.

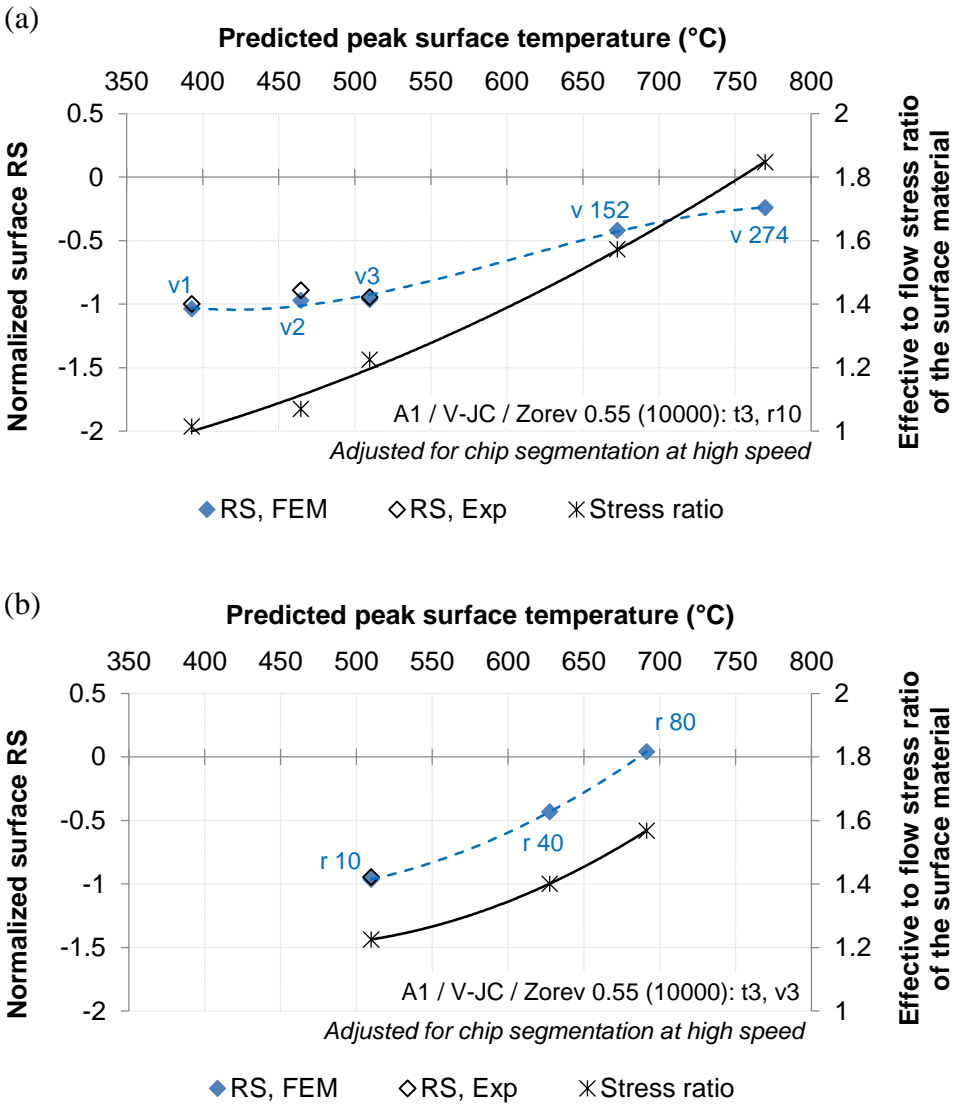


Fig. 6.16: Alloy 1: effect of (a) cutting speed,  $v$ , and (b) hone radius,  $r$ , on residual stresses, peak temperature, and the ratio of effective stress to flow stress in the machined surface.

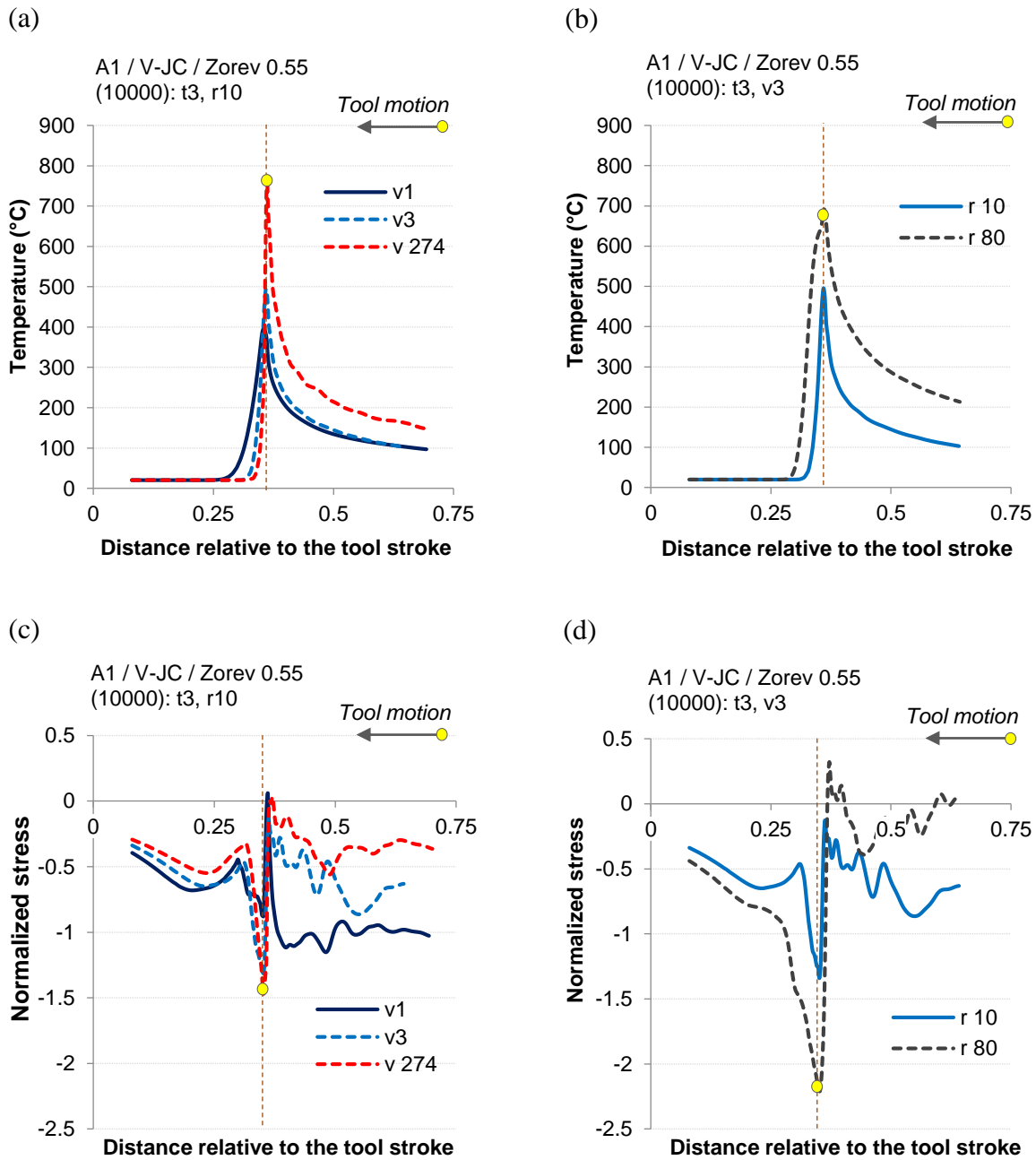


Fig. 6.17: Alloy 1: the effect of cutting speed ( $v$ ) and hone radius ( $r$ ) on the predicted (a, b) temperature distribution and (c, d) stress distribution along the machined surface at a tool position of 1.6 mm within the cutting path for conditions (A<sub>1</sub>, (t<sub>3</sub>, v<sub>i</sub>)) and (A<sub>1</sub>, (t<sub>3</sub>, v<sub>3</sub>, r<sub>i</sub>)).

As evident in Fig. 6.16, high speed machining results in a sharp reduction in compressive RS, reaching around 60% at  $v = 274$  m/min. Honed cutting edges have a similar effect. Moreover, increasing the hone radius to 0.080 mm shifted RS from the compressive to the tensile region. The above behavior is explained with reference to Fig. 6.17. It is clear

that unconventionally high speeds and large hone radii lead to a significant temperature rise in the machined surface during cutting (Fig. 6.17(a, b)). The added intensity of the thermal load causes more severe expansion in the surface material. Therefore, larger compressive stresses are generated due to restraints by the underlying layers. Thus, the compressive stress level during contact shifts downwards (Fig. 6.17(c, d)). A more severe shift is triggered by the edge hone due to its contribution to larger mechanical loads. Behind the tool tip, the surface that has already initiated rapid cooling is almost representative of the final residual stress state. Due to the added contribution of thermal loading, the compressive RS in the machined surface are diminished. These stresses shift upward towards the tensile region with increasing speed (Fig. 6.17c) and into the tensile region with increasing hone radius (Fig. 6.17d) as the balance is shifted towards thermally induced plastic deformation.

With increasing uncut chip thickness, a substantial increase in machining forces takes place (Fig. 6.9) compared with a limited surface temperature rise (Fig. 6.13a). The influence of uncut chip thickness on the predicted effective stress field is shown in Fig. 6.18. With increasing uncut chip thickness, the effective stress in the primary shear zone and in the machined surface increases gradually. The size and penetration depth of the stress field also increases, indicating a wider and more deeply penetrating elasto-plastic deformation zone.

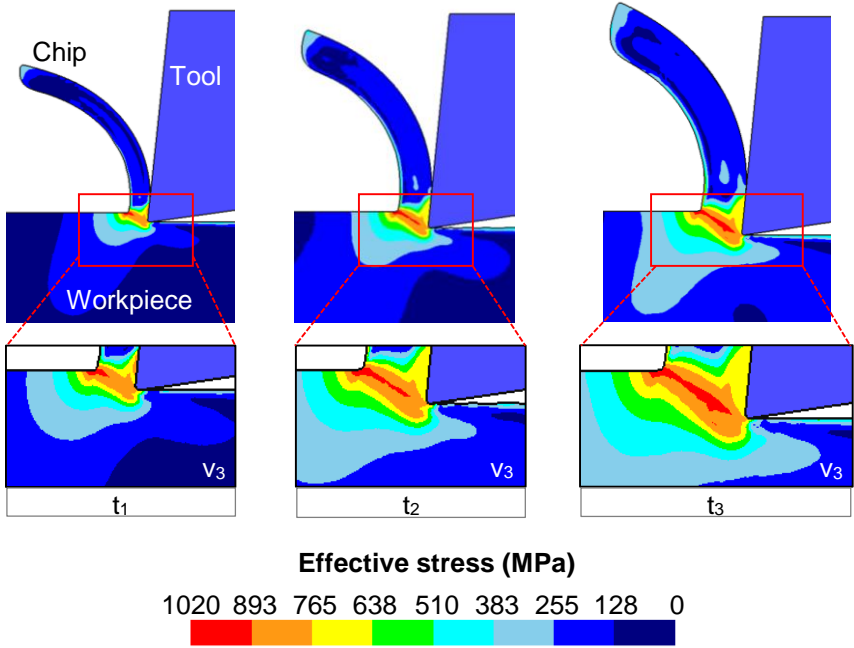


Fig. 6.18: Alloy 1: the influence of uncut chip thickness on the predicted effective stress field in the cutting zone and in the machined surface.

Thus, strains of larger magnitude and penetration depth are produced by more dominant mechanical loads. The superficial stress distribution at a tool position of 1.6 mm within its stroke is shown in Fig. 6.19 for cutting conditions  $(A_1, (t_i, v_1))$ . A comparison is made between the stress distributions for low and high uncut chip thickness,  $t_1$  and  $t_3$ , respectively. At  $t_3$ , a larger extent of plastic unloading in tension takes place behind the tool tip. This indicates an increase in the dominance of the tensile phase of the loading cycle. In other words, a larger extent of plastic deformation in tension is produced in the machined surface. The final outcome is enhanced compressive stresses. This is reflected in the downward shift of the stress profile behind the tool.

Consequently, larger feed rates within the finish turning regime shift the balance further towards mechanically induced plastic deformation. This is due to the relatively small influence of uncut chip thickness on the average temperature in the cutting zone and in the machined surface. The result is an increasingly compressive overall state. A critical uncut chip thickness level may exist, however, above which the compressive portion of the mechanical loading cycle becomes more dominant, and thermal stresses begin to rise. At this point, the trend may be reversed, and RS may become less compressive with increasing uncut chip thickness.

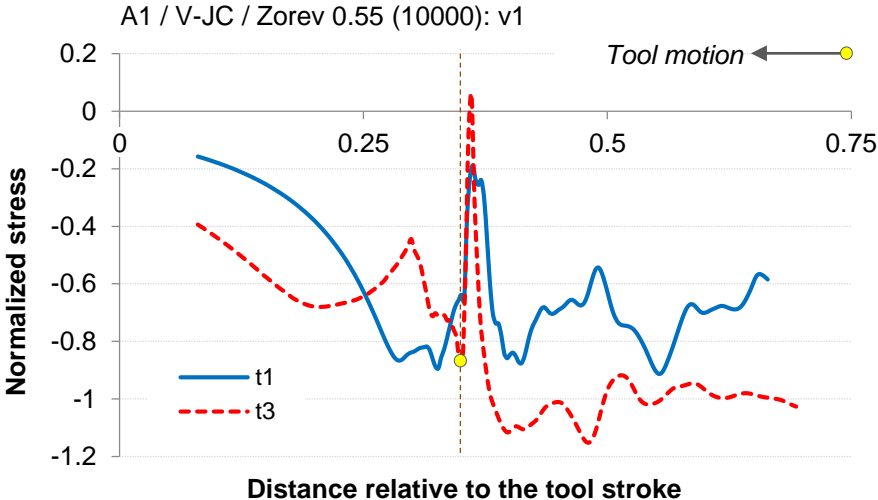


Fig. 6.19: Alloy 1: effect of uncut chip thickness on the predicted stress distribution along the machined surface at a tool position of 1.6 mm within the cutting path for conditions  $(A_1, (v_1, t_i))$ .

### 6.3.3.2 *The effect of flank wear on residual stress formation*

Regarding Alloy 2, a large discrepancy between predicted (FEM) and experimental (Exp) RS was obtained at high uncut chip thickness  $t_3$  (Fig. 6.20a). As elaborated previously in section 4.3.3.2, Alloy 2 did not exhibit a similar trend to Alloy 1 of enhanced compressive RS with increasing uncut chip thickness. Little change in RS was observed at low cutting speed  $v_1$ , while at high speed  $v_3$ , compressive RS were reduced. The FE model, however, predicted a substantial rise in compressive RS with increasing uncut chip thickness similar to Alloy 1. This is reflected by the downward shift of the residual stress profiles between conditions  $(t_1, v_1)$  and  $(t_3, v_1)$  in Fig. 6.20b.

To explain this discrepancy in residual stress predictions, the cutting tools were examined for wear at high uncut chip thickness conditions. The flank wear generated by Alloy 2 was around 1.5 times larger than Alloy 1 as shown in Fig. 4.6. Flank wear (VB) was primarily measured with a tool analyzer, and the cutting edge was examined in the unpolished state. For the purpose of this discussion, wear measured by this method is referred to as gross flank wear. To obtain a more precise measurement, a metallurgical microscope was used to examine the cutting edge in the metallographic state (involving sectioning, mounting and polishing) at high magnification for the condition  $(t_3, v_3)$  combining high uncut chip thickness and high cutting speed. Fig. 6.21 shows a metallographic section of a carbide tool used in dry orthogonal cutting of Alloy 1 at this condition in the unpolished state (Fig. 6.21a) and after polishing with SiC paper (Fig. 6.21b). It was concluded that for the small amount of wear encountered during finish cutting, which is in the order of 20 to 50  $\mu\text{m}$ , the real flank wear can be overestimated by a factor of around 3 for an unpolished edge. This could be due to the adhered workpiece material on the cutting edge, which was removed during polishing of the tool section. This is a common problem for Ti-alloys and tungsten carbide tools. Researchers have used various methods to remove adhered material that masks the worn surfaces, such as immersion in HF acid solution prior to the wear measurement [129].

A sensitivity analysis was performed for Alloy 2 through which the effect of several key factors on predicted RS was examined. These factors include the constitutive law, tool/chip interface friction, and flank wear. Residual stress predictions were found to be mostly sensitive to flank wear, which was introduced into the FE model by changing the cutting edge from its previously sharp state to a pre-worn state (Fig. 6.22).

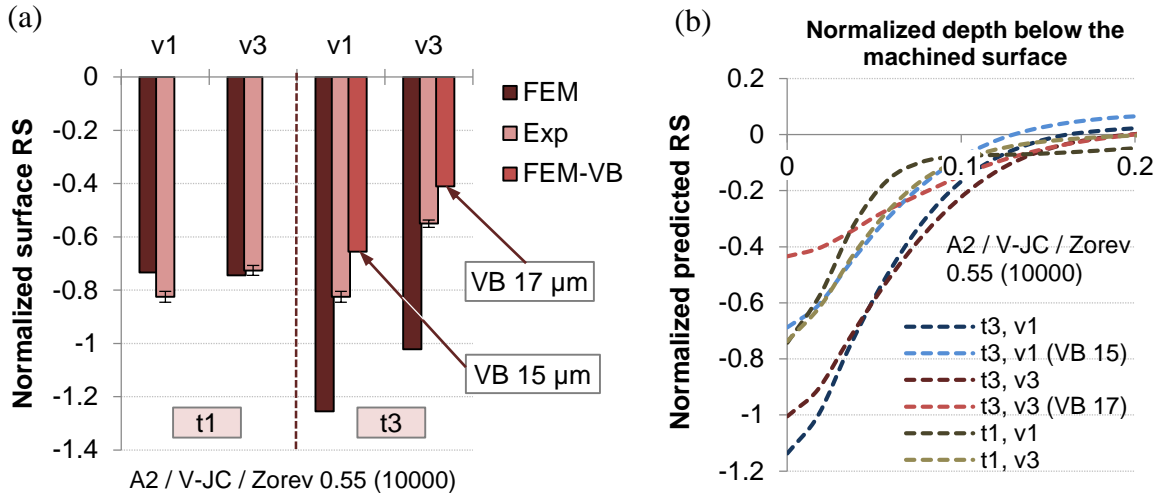


Fig. 6.20: Alloy 2: (a) comparison between FE predictions and experimental measurements of RS and (b) effect of cutting parameters on predicted RS profiles, incorporating the effect of flank wear.

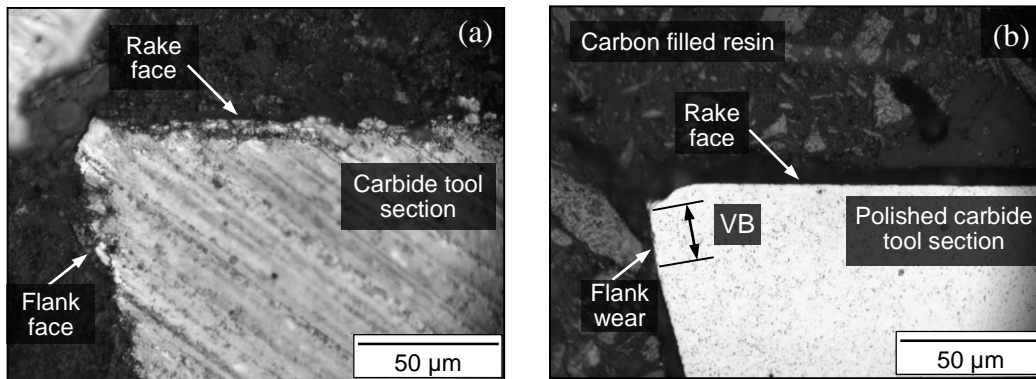


Fig. 6.21: metallographic section of a carbide tool used in dry orthogonal cutting of Alloy 1 at condition (t<sub>3</sub>, v<sub>3</sub>): (a) prior to polishing and (b) in the polished state.

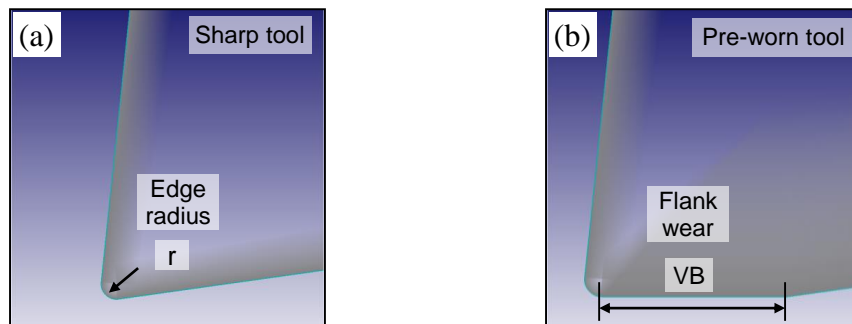


Fig. 6.22: (a) sharp tool with edge radius  $r = 10 \mu\text{m}$  adopted in FE simulations for Alloy 1; (b) pre-worn tool with flank wear (VB) used in FE simulations for Alloy 2 at high uncut chip thickness.

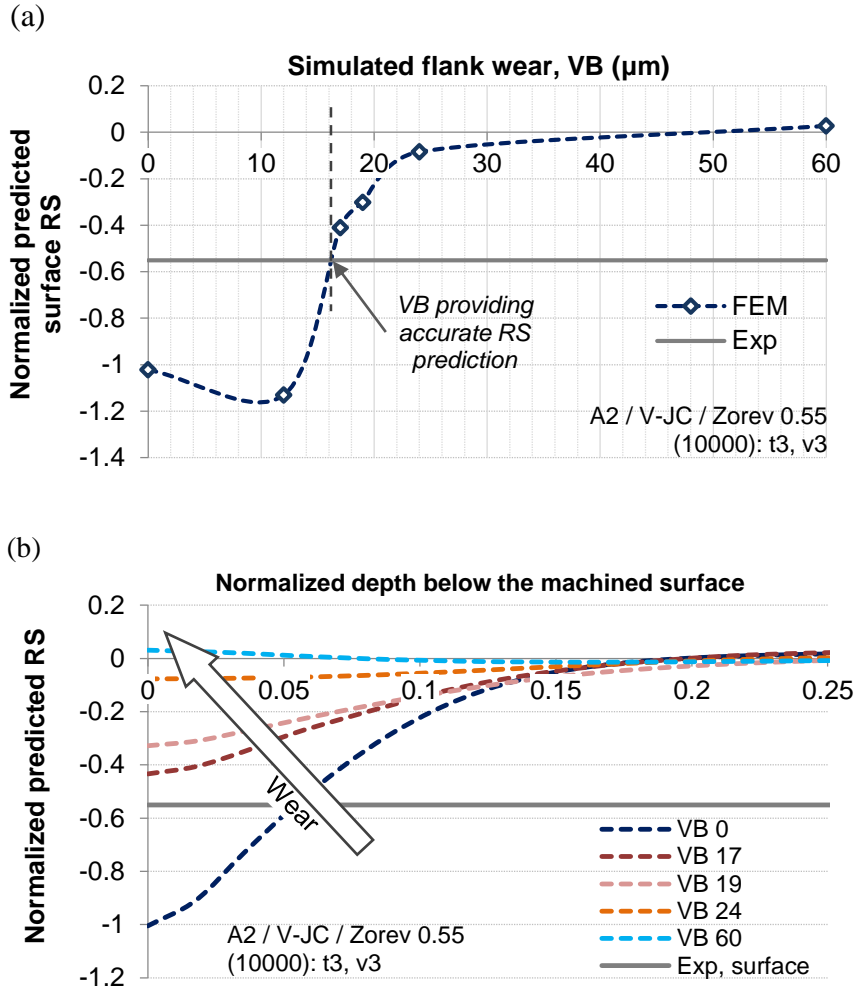


Fig. 6.23: Alloy 2: effect of flank wear (VB) on FE predictions of (a) surface RS and (b) residual stress distribution in the sub-surface layers at condition (t<sub>3</sub>, v<sub>3</sub>).

The wear was varied between 0.25 and 0.5 of the average flank wear  $VB = 47 \mu\text{m}$  for condition (t<sub>3</sub>, v<sub>3</sub>). The case of maximum flank wear ( $VB_{\text{max}} = 60 \mu\text{m}$ ) was also investigated. Residual stresses were found to be highly sensitive to flank wear, as evidenced in Fig. 6.23. The effect of the modeled wear land on predicted surface RS (FEM) is shown in Fig. 6.23a in comparison with the measured result (Exp). It was observed that flank wear  $VB \leq 12 \mu\text{m}$  has a small effect on residual stress predictions. Above this value, however, a steep reduction in compressive RS occurs. This is accompanied by a rapid upward shift of the residual stress profile towards the tensile region (Fig. 6.23b). As shown in Fig. 6.23a, the wear land that provides an accurate prediction of RS ( $\approx 16 \mu\text{m}$ ) amounts to around one third of the gross flank wear ( $47 \mu\text{m}$ ) for this condition. This is in agreement with the relationship established

experimentally between the gross flank wear detected in the unpolished state (Fig. 6.21a) and the real flank wear measured for a polished cutting edge (Fig. 6.21b). If the gross flank wear measured for Alloy 2 for the conditions  $(t_3, v_1)$  and  $(t_3, v_3)$ , amounting to 40 and 47  $\mu\text{m}$ , respectively, is reduced by a factor of around 3, the residual stress prediction error drops significantly as shown in Fig. 6.20a. RS predicted for a pre-worn tool are denoted by “FEM-VB”. The above discussion confirms that RS are highly sensitive to flank wear. For accurate residual stress predictions, flank wear exceeding 12  $\mu\text{m}$  should be included in the FE model. At low uncut chip thickness where flank wear is negligible, prediction errors are lower than 10%. At high uncut chip thickness, by integrating flank wear into the model, the prediction error is reduced to around 25%. As a result, the developed FE model can accurately capture the behavior of RS in Ti-alloys.

To analyse the mechanism by which flank wear influences RS, the impact of wear on the intensity of thermal and mechanical loads was assessed separately. The temperature fields in the cutting zone, and the temperature distribution below the machined surface for the condition  $(A_2, (t_3, v_3))$  are shown in Fig. 6.24. The results for three cutting edge conditions are compared: (i) wear free edge with  $\text{VB} = 0$ , (ii) pre-worn edge with  $\text{VB} = 17 \mu\text{m}$ , and (iii) pre-worn edge with  $\text{VB} = 60 \mu\text{m}$ .

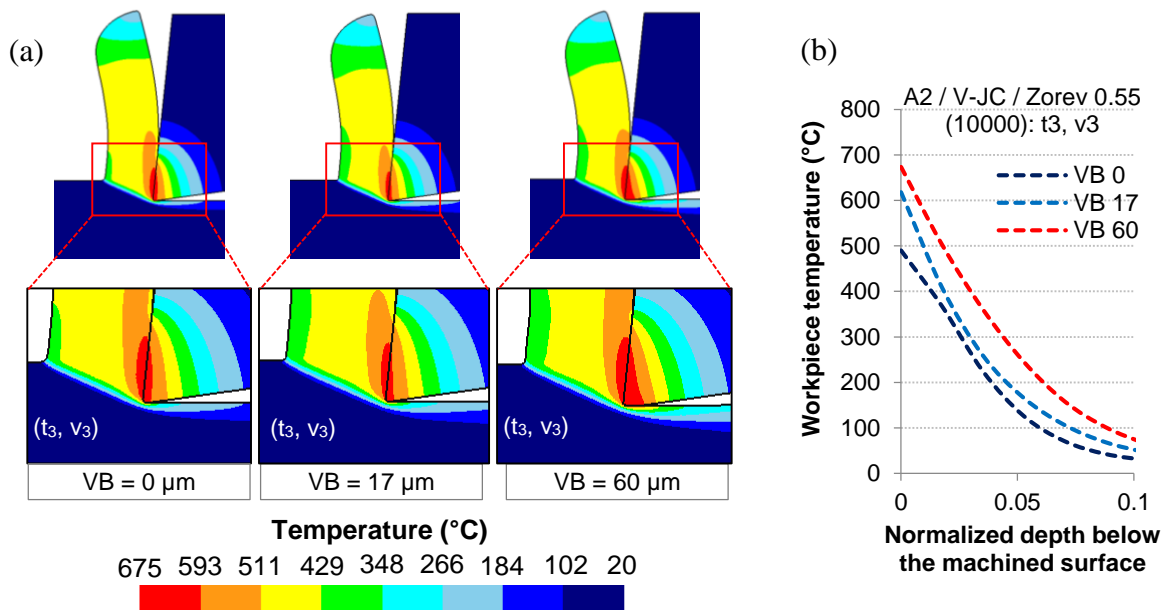


Fig. 6.24: Alloy 2: effect of flank wear (VB) at condition  $(t_3, v_3)$  on: (a) the temperature field in the cutting zone and (b) the temperature distribution beneath the machined surface.

With increasing wear, the high temperature region (600 to 675°C) expands from the tool/chip interface to the tool/workpiece interface (Fig. 6.24a). This is accompanied with a significant temperature rise in the machined surface (Fig. 6.24b). Due to the larger contact area and increased friction, the tertiary shear zone becomes an important heat source. With  $V_B = 60 \mu\text{m}$ , the interface temperature at the flank wear land assumes an almost uniform distribution ranging from around 650 to 675°C. This corresponds to a temperature rise of around 40% with respect to the wear free edge. However, a small increase in the cutting force ( $\approx 8\%$ ) is observed. With increasing wear, the thermal contribution to plastic deformation increases abruptly causing a rapid upward shift in residual stress profiles as shown in Fig. 6.23b. At a certain point, the thermal effect becomes dominant, and residual stresses shift from compressive to tensile, as in the case of  $V_B = 60 \mu\text{m}$ .

#### **6.3.4 Interpretation of the dissimilar behavior of the Ti-alloys under study**

The FE model was used to interpret the dissimilar behavior of the two alloys, Ti-6Al-4V (Alloy 1) and Ti-6Al-2Sn-4Zr-6Mo (Alloy 2), under analysis. As previously elaborated in Chapter 4, Alloy 2 generated higher machining forces and produced larger flank wear in the carbide tools than Alloy 1. This was true for both oblique cutting and orthogonal cutting processes. Alloy 2 was found to have superior bulk hardness (by  $\approx 20\%$ ) to Alloy 1 at ambient temperature and in the absence of deformation. The experimental findings confirm the results of the material identification process, which revealed that Alloy 2 undergoes thermal softening at a lower rate and is more sensitive to strain hardening (Fig. 6.5).

Except during orthogonal cutting at high uncut chip thickness due to the previously discussed effect of wear, Alloy 2 exhibited higher magnitudes of surface compressive RS. In order to explain the mechanism by which this occurs, a comparison is made of the predicted temperature and stress fields for both alloys at identical cutting conditions ( $t_1, v_i$ ) as shown in Fig. 6.25. Higher temperatures are produced in the primary shear zone, at the tool/chip interface, and in the tool tip for Alloy 2, together with wider and more deeply penetrating stress fields. Stresses of higher magnitude are generated in the primary shear zone and the secondary shear zone compared to Alloy 1. This reflects the characteristic flow stress behavior of the alloys described by the Voce-Johnson-Cook (V-JC) constitutive law. The larger mechanical loads and more elevated tool temperatures generated when machining Alloy 2 explain the higher wear rate in the carbide tools for this material.

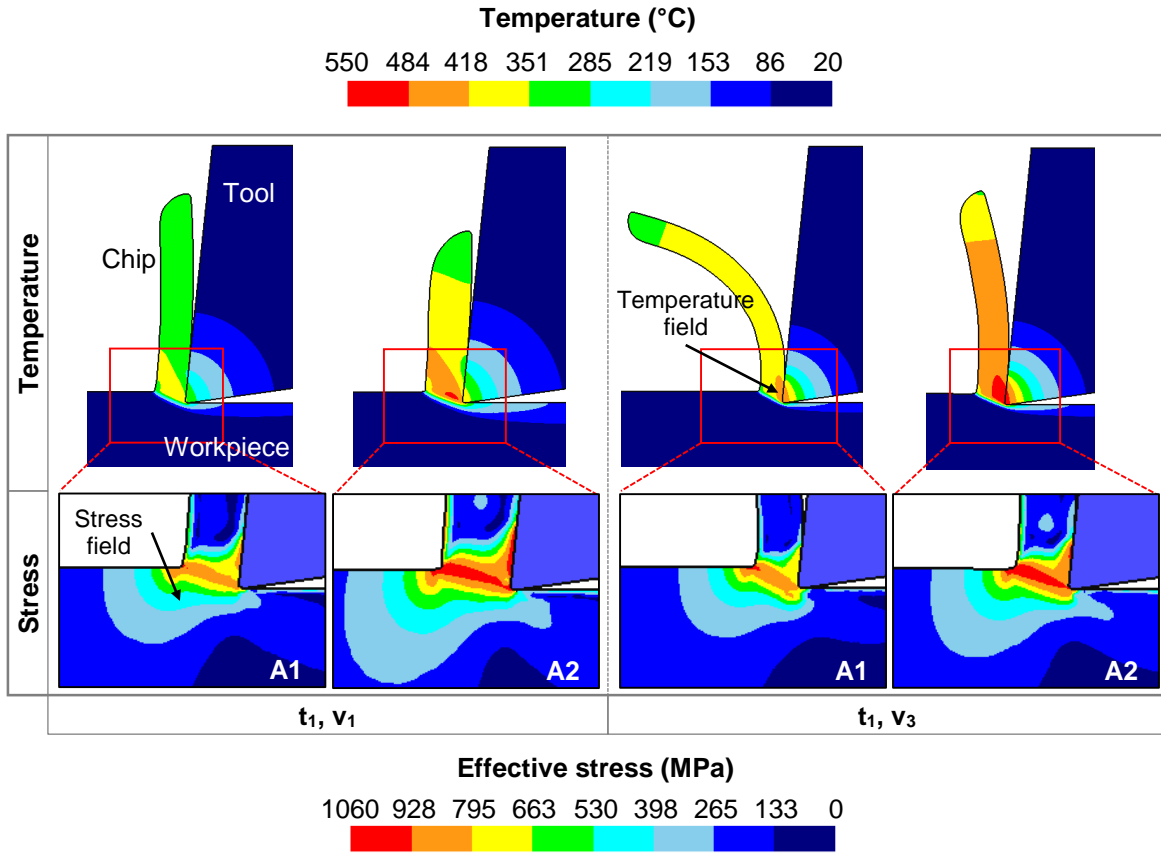


Fig. 6.25: comparison between Alloy 1 and Alloy 2 of predicted temperature and effective stress fields in the cutting zone for cutting conditions  $(t_1, v_i)$ .

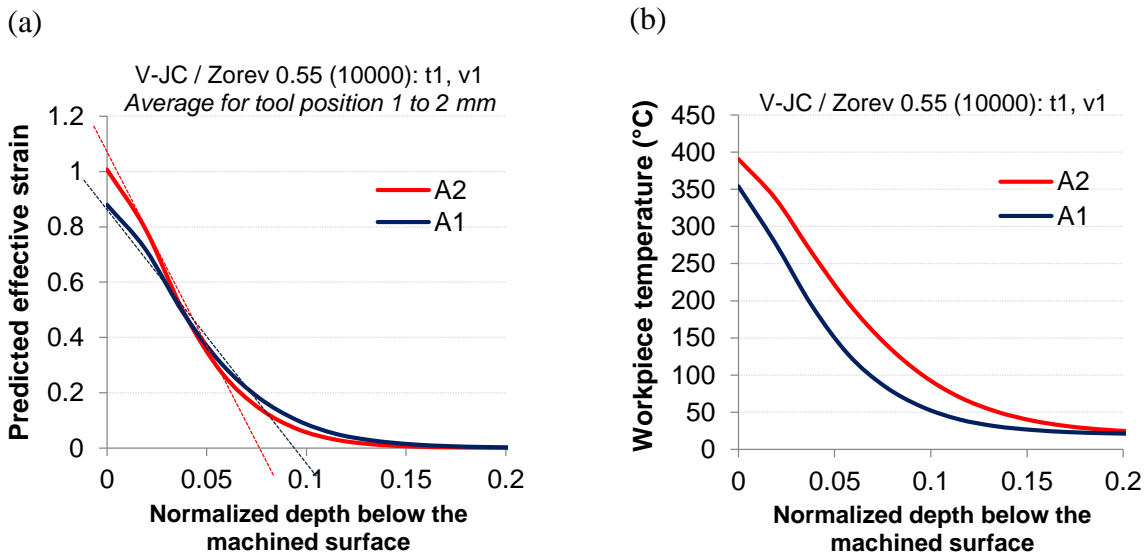


Fig. 6.26: comparison of FE predictions between Alloy 1 and Alloy 2 at cutting condition  $(t_1, v_1)$  of: (a) effective strain distribution and (b) temperature distribution below the machined surface.

To analyse the effect of the thermomechanical loading on RS, the predicted effective strain distributions (Fig. 6.26a) and temperature distributions (Fig. 6.26b) in the machined surface were compared for condition  $(t_1, v_1)$ . A larger strain gradient is formed in the near-surface layer of Alloy 2 although it is subjected to slightly higher temperatures during cutting. Since it undergoes thermal softening to a much lesser degree, plastic deformation during cutting could be restricted to a shallower layer. Once the load is removed and elastic deformation in the underlying material is relieved, the shallower plastically deformed layer is subjected to more stringent constrictions by the bulk material, thereby exhibiting a state of larger compressive residual stresses. Furthermore, the lower sensitivity to thermal softening of Alloy 2 makes it less susceptible to thermally induced plastic deformation. Therefore, it is less prone to thermally induced tensile RS, and plastic deformation is more predominantly controlled by mechanical loads. Consequently, the resulting RS are more compressive.

# CHAPTER 7    CHIP SEGMENTATION IN Ti-6Al-4V AND ITS EFFECT ON FE PREDICTIONS

## 7.1 Introduction

The machining of Ti-alloys is characterized by the formation of segmental chips that result in a cyclic variation of forces with considerable amplitude variations. The resulting vibration limits the material removal rate, promotes accelerated tool wear, and could have a negative influence on the surface integrity of the machined part [130, 131]. It is, therefore, crucial to achieve an understanding of the criteria that promote segmental chip formation, and more importantly its effect on aspects of surface integrity that are not readily detectable such as machining-induced residual stresses.

In this work, the term *non-segmental* chip is used to describe the continuous non-cyclic steady-state chip, which forms the basis of orthogonal cutting mechanics. The term *segmental* chip is used to designate the continuous cyclic *sawtooth* chip that is commonly produced when machining Ti-alloys. In the FE model presented in Chapter 6, chip morphology was assumed to be of the non-segmental nature. It was suggested, however, that the accuracy of residual stress predictions at high cutting speed could be improved by the modeling of segmental chip formation. In this chapter, the relevance of segmental chip morphology to the prediction of machining-induced residual stresses is investigated. Segmental chip formation is introduced into the FE model through the use of the Cockroft & Latham damage criterion, and a comparison is made between the experimentally measured and the predicted chip geometry, machining forces, and residual stresses. The FE model is then used to analyze the influence of chip segmentation on residual stresses.

## 7.2 Characterization of chip segmentation for Ti-6Al-4V

In order to characterize segmental chip formation for Ti-6Al-4V, the chips obtained during orthogonal cutting were metallographically prepared and examined at high magnification. In addition to the bimodal Ti-6Al-4V alloy machined within the conventional range of cutting speed (20 to 90 m/min) and which is the main focus of this research, a mill-annealed alloy of the same nominal composition was machined at unconventionally high speed  $v = 350$  m/min.

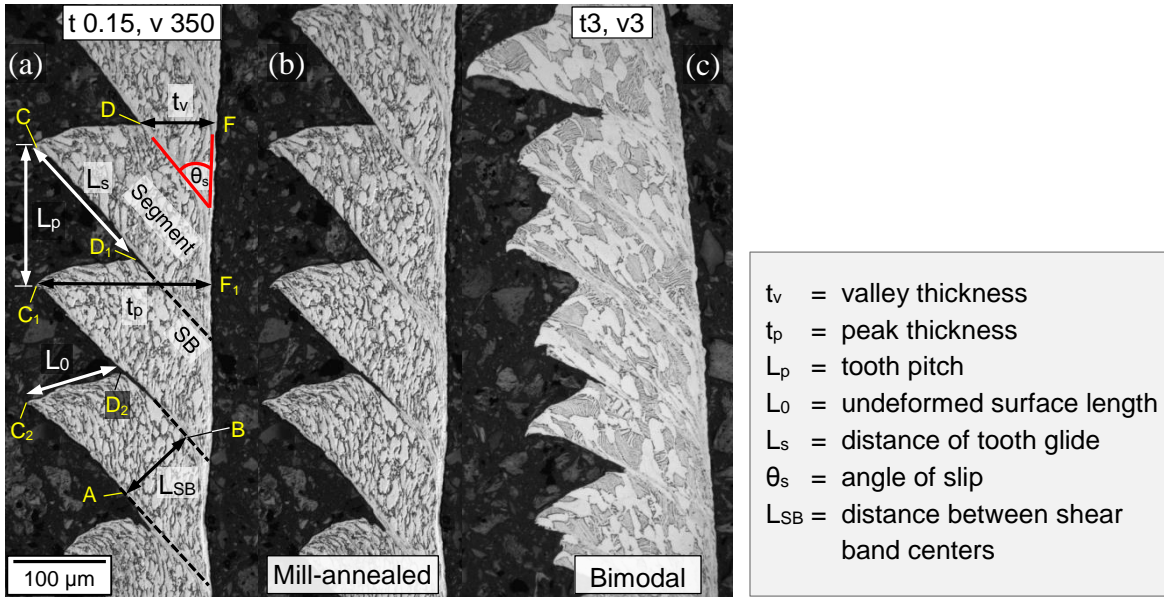


Fig. 7.1: (a, b) metallographically prepared chip of mill-annealed Ti-6Al-4V orthogonally machined with  $(t, v) = (0.15 \text{ mm/rev}, 350 \text{ m/min})$ , with (a) showing typical geometrical features of segmental chips; (c) chip specimen of bimodal Ti-6Al-4V (Alloy 1) obtained at conditions  $(t_3, v_3)$ .

Fig. 7.1 compares the chip morphology of the mill-annealed alloy obtained at condition  $(t, v) = (0.15 \text{ mm/rev}, 350 \text{ m/min})$  to that of the bimodal alloy machined at condition  $(t_3, v_3)$ , where  $v_3$  represents relatively high speed within the conventional range. The main geometrical features of a typical segmented chip are also presented.

As shown in Fig. 7.1a, the chip can be described by average values of the following geometrical features: (1) the minimum or valley thickness,  $t_v$ , given by line DF, (2) the peak thickness,  $t_p$ , denoted by  $C_1F_1$ , (3) the undeformed surface length,  $L_0$ , given by  $C_2D_2$ , (4) the tooth pitch,  $L_p$ , given by  $CC_1$ , (5) the distance between slip zones or shear band centres,  $L_{SB}$ , stretching from A to B, (6) the distance of forward tooth glide or slip,  $L_s$ , denoted by  $CD_1$ , and (7) the angle of slip  $\theta_s$ .

The chip of the mill-annealed alloy machined at 350 m/min (Fig. 7.1b) exhibits equally spaced periodic shear bands. These constitute areas of severe strain localization leading to severe grain distortion. The shear bands are separated by segments of relatively low strain. A region of severely deformed microstructure similar to the shear bands is observed in the secondary shear zone. The chip of the bimodal alloy (Alloy 1) machined at a lower conventional speed (Fig. 7.1c) has less uniform geometry. Strain localization within the shear bands is less severe. The elongation of primary alpha grains in the direction of shear

within the segments indicates a more uniformly distributed deformation in comparison with the mill-annealed alloy. Shear banding is mostly constrained in a smaller region adjacent to the secondary shear zone and does not always extend through the chip. The above comparison brings into perspective the influence of cutting speed on segmental chip formation and the effect of microstructure for a particular nominal alloy composition.

Within the conventional finish-turning regime under investigation (Table 4-2), FE predictions for the bimodal alloy (section 6.3.2) revealed that the nominal shear zone temperature does not exceed 320°C even at the harshest conditions of high uncut chip thickness and high cutting speed ( $t_3$ ,  $v_3$ ). This temperature is much lower than the beta-transus of Ti-6Al-4V ( $970 \pm 50^\circ\text{C}$ ) [117]. This indicates that phase transformations within the shear bands, which constitute evidence of the existence of adiabatic shear [132], are highly unlikely to occur at conventional finish turning conditions. In contrast, the shear bands produced at 350 m/min in the mill-annealed alloy can be subjected to temperatures in excess of 1000°C, leading to non-diffusional phase transformations [133]. At such speeds, the contribution of plastic instability to segmental chip formation increases significantly, and temperature has a far more dominant role.

Furthermore, the irregularity in chip geometry exhibited by the bimodal alloy (Fig. 7.1c) can be attributed to microstructural inhomogeneity and varying deformation behavior between the constituent phases. This irregularity is known to diminish with increasing cutting speed [130], as in the case of the mill-annealed alloy (Fig. 7.1b).

In conclusion, at conventional cutting speeds, and in the presence of irregular chip morphology, the driving mechanism for chip segmentation is unlikely to be adiabatic shear. Segmental chip formation at these conditions is more likely to occur through the periodic fracture mechanism, whereby ductile fracture due to void coalescence and growth initiates within the primary shear zone [79].

From this point onwards, the discussion will focus on the chip morphology of the bimodal Ti-6Al-4V (Alloy 1) machined at conventional cutting speeds. High magnification metallographic images of chips obtained for Alloy 1 over the full range of orthogonal cutting parameter combinations ( $t_i$ ,  $v_i$ ) are shown in Fig. 7.2. Furthermore, the effect of cutting parameters on peak thickness and tooth pitch is shown in Fig. 7.3a and Fig. 7.3b, respectively. Experimental results are normalized with respect to the peak thickness of the chip obtained

for cutting condition  $(t_3, v_1)$ , resulting in the largest compressive RS. To identify the onset of segmentation for Alloy 1, the formation of sawtooth chips and the extent of strain localization were monitored in conjunction with the chip load, defined as the product of the uncut chip thickness  $t$  and the cutting speed  $v$ , such that: chip load =  $(t \times v) \text{ m}^2/\text{min}$ . The resulting chip load for the investigated parameter combinations  $(t_i, v_i)$  is presented in Fig. 7.3c.

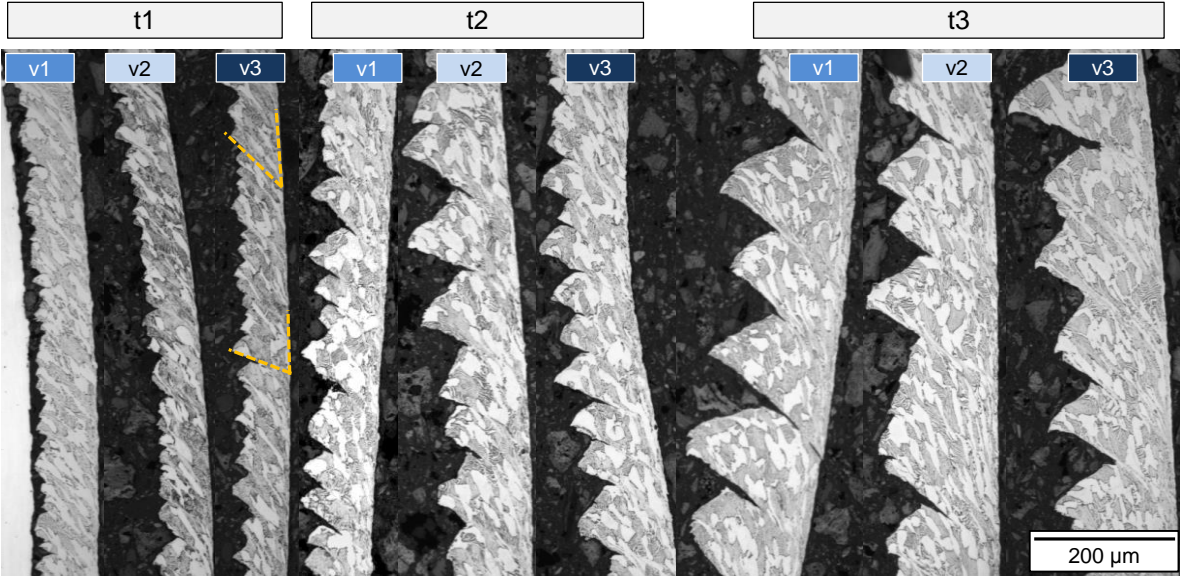


Fig. 7.2: metallographic chip sections produced during orthogonal cutting of bimodal Ti-6Al-4V (Alloy 1) over the full range of investigated cutting parameter combinations  $(t_i, v_i)$ .

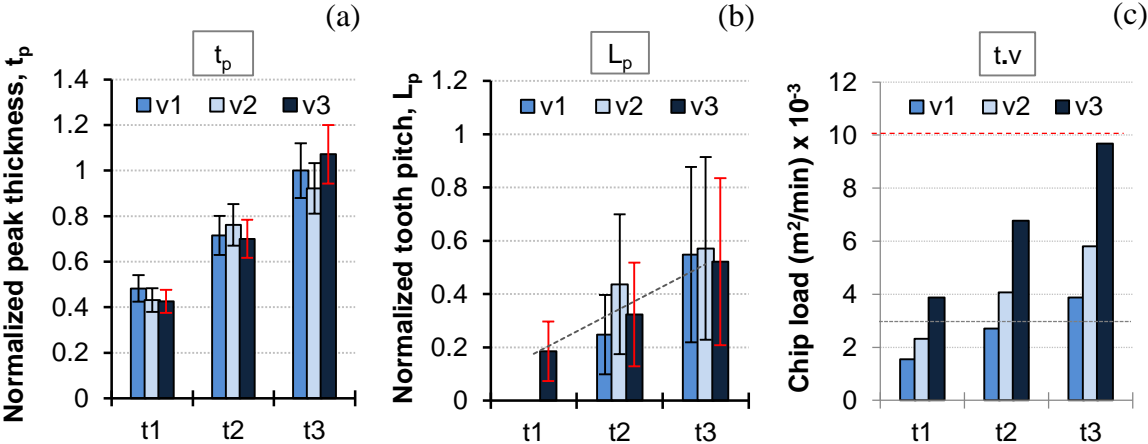


Fig. 7.3: variation in (a) peak thickness, (b) tooth pitch, and (c) chip load with cutting parameters during dry orthogonal cutting of Alloy 1. The bars represent variations about the average value.

In the following sections, the influence of cutting parameters, chip load, and microstructural inhomogeneity on chip morphology is discussed with reference to Fig. 7.2 and Fig. 7.3.

#### *7.2.1.1 Effect of cutting parameters*

At low uncut chip thickness  $t_1$ , and for low and intermediate cutting speeds ( $v_1$  and  $v_2$ ), the chips produced were non-segmental in nature. Estimates of the tooth pitch at these conditions were, therefore, not possible. At condition ( $t_1, v_3$ ) involving low uncut chip thickness and high speed, however, sharp aperiodic sawteeth began to form, together with variations in the angle of slip. Sawtooth formation involved a larger angle of slip. In other words, the shear angle diminished with the appearance of sawteeth.

Increasing the uncut chip thickness produced considerable growth in the average peak thickness  $t_p$  and tooth pitch  $L_p$  as quantified in Fig. 7.3(a, b). The average tooth pitch  $L_p$  is directly proportional to the uncut chip thickness. For a fixed cutting speed, a larger tooth pitch indicates a lower segmentation frequency [130]. Therefore, segmentation frequency is inversely proportional to the uncut chip thickness. At intermediate uncut chip thickness  $t_2$ , no intense shear banding was identifiable between the sawtooth segments for all cutting speeds. This is further evidence that within the investigated range of cutting parameters, periodic fracture is the dominant mechanism as opposed to adiabatic shear.

In general, the influence of cutting speed on chip morphology within the conventional range under study is small compared to that of the uncut chip thickness. The highest cutting speed  $v_3$ , however, improves the periodicity of sawtooth formation and promotes a higher degree of geometrical homogeneity. No clear trend for the effect of cutting speed on the peak thickness  $t_p$  could be identified (Fig. 7.3a). As shown in Fig. 7.3b, the tooth pitch  $L_p$  exhibits similar behavior with increasing speed at intermediary and high uncut chip thickness levels. At high uncut chip thickness  $t_3$ , however, the effect of cutting speed on  $L_p$  is modest compared to intermediary uncut chip thickness  $t_2$ . At  $t_2$ , increasing the cutting speed from  $v_1$  to  $v_2$  caused an increase in the tooth pitch  $L_p$  and the associated distance between the slip zones  $L_{SB}$  as evidenced in Fig. 7.2. A further increase in speed from  $v_2$  to  $v_3$ , however, had the opposite effect. The tooth pitch was reduced, and slip zones became closer. At condition ( $t_3, v_3$ ) involving high uncut chip thickness and high cutting speed, more severe grain distortion is observed between the segments within recurring shear bands (Fig. 7.2).

In order to explain the aforementioned changes in chip morphology with increasing cutting speed, its effect on the experimentally measured cutting force  $F_c$  is examined in conjunction with the predicted temperature distributions along the shear plane. Fig. 7.4 shows the temperature distributions along the shear plane predicted by the FE model for cutting conditions  $(t_2, v_i)$  and  $(t_3, v_i)$ . The region of interest is that of localized strain rate in close proximity to the tool tip denoted by OA and delineated by a steep strain rate gradient. This region is prone to localized thermal softening that can potentially lead to plastic instability at elevated temperatures [131, 134].

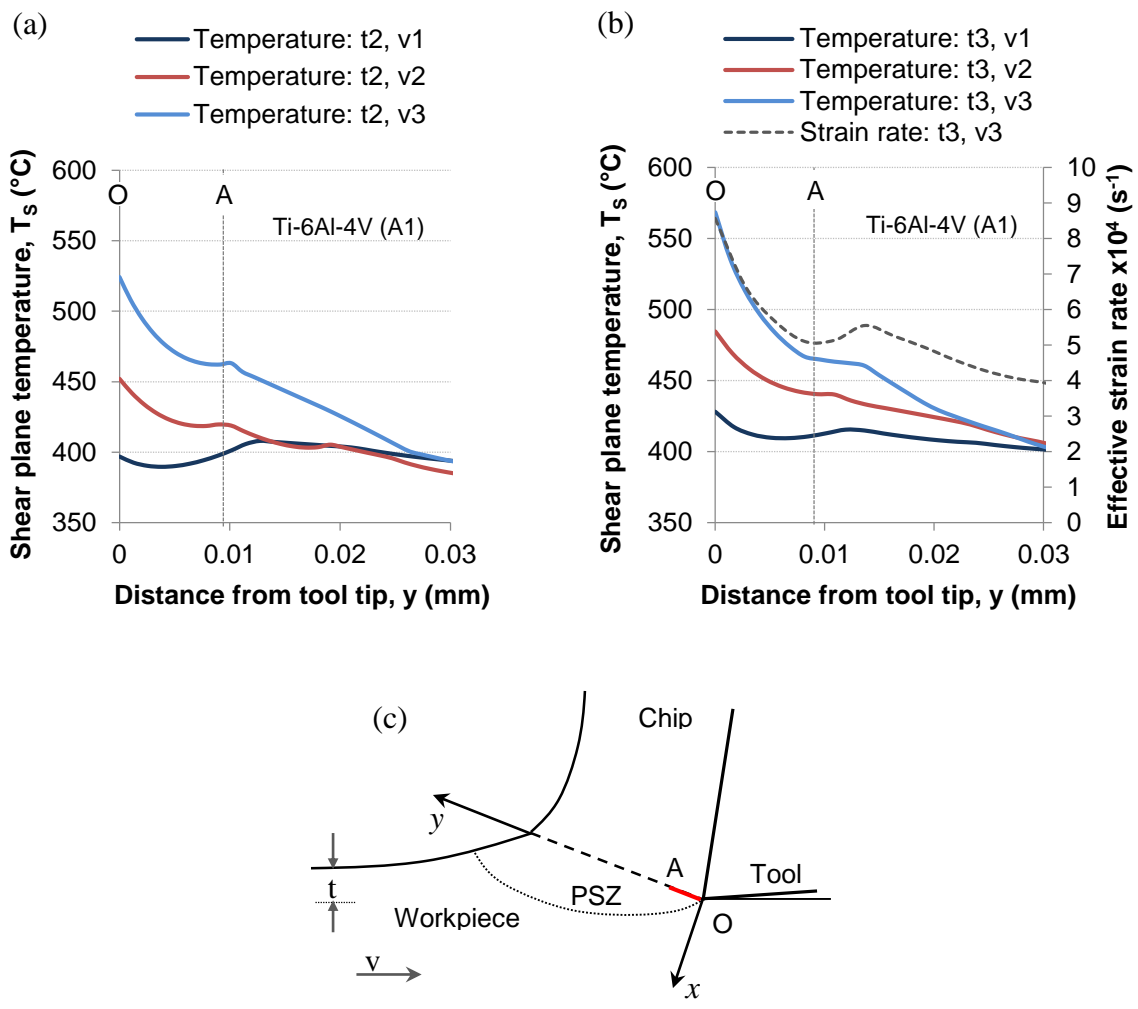


Fig. 7.4: Alloy 1: FE predictions of the effect of cutting speed on localized temperature distribution along the shear plane in close proximity to the tool tip at conditions (a)  $(t_2, v_i)$  and (b)  $(t_3, v_i)$ . The region of interest is delineated by a steep strain rate gradient and denoted by OA in (c).

As reported previously (section 4.3.3.1), the cutting force  $F_c$  sustained by Alloy 1 at intermediate uncut chip thickness  $t_2$  increases by around 35% when the cutting speed is increased from  $v_1$  to  $v_2$ . This behavior indicates a net strain rate hardening of the material with increasing speed. As a result, the length of forward tooth glide increases, while the slip zones become further apart (Fig. 7.2). As the cutting speed is further increased from  $v_2$  to  $v_3$  at uncut chip thickness  $t_2$ , there is very little change in the cutting force  $F_c$ . This indicates that the increment in thermal softening counterbalances the strain rate hardening associated with increasing speed. In addition, the localized temperature rise in the shear plane at  $v_3$  (Fig. 7.4a) promotes a larger extent of shear concentration between the segments. The overall result is smaller tooth pitch and reduced tooth glide (Fig. 7.2).

At high uncut chip thickness conditions ( $t_3, v_i$ ), the influence of speed on the cutting force is minimal. The effect of strain rate hardening is compensated by that of thermal softening. It is evident by comparing Fig. 7.4a and Fig. 7.4b that more elevated temperatures are attained in close proximity to the tool tip compared to conditions ( $t_2, v_i$ ). At cutting condition ( $t_3, v_3$ ), the deformation-induced temperature rise is at its highest. This promotes more localized thermal softening and leads to the appearance of shear bands with relatively severe strain localization that were not observed at the other cutting conditions (Fig. 7.2).

#### *7.2.1.2 Effect of chip load*

With reference to Fig. 7.3c, within the investigated range of cutting parameters, sawtooth chips began to appear at a chip load of around  $0.003 \text{ m}^2/\text{min}$  corresponding to cutting condition ( $t_2, v_1$ ). Recurring shear bands with severe strain localization only became visible, however, at a chip load of about  $0.010 \text{ m}^2/\text{min}$  at condition ( $t_3, v_3$ ). This value is considerably higher than the critical chip load of  $0.004 \text{ m}^2/\text{min}$  identified by Bayoumi and Xie [133] for the onset of plastic instability in Ti-6Al-4V. This is a further indication that although strain localization was evidently more severe at high feed rate and cutting speed conditions, plastic instability due to adiabatic shear is not the sole acting mechanism and is unlikely to be the root cause for segmental chip formation.

#### *7.2.1.3 Effect of microstructural inhomogeneity*

As evidenced in Fig. 7.2, chip geometry is generally inhomogeneous for the investigated finish turning regime. Although the periodicity of segmentation was improved at high cutting speed  $v_3$ , variations in peak thickness  $t_p$  and tooth pitch  $L_p$  within  $\pm 12\%$  and

$\pm 60\%$ , respectively, were observed for a fixed cutting condition. These variations, shown as error bars in Fig. 7.3(a, b), indicate that the microstructural inhomogeneity of the bimodal Ti-6Al-4V alloy has a major impact on chip formation.

#### 7.2.1.4 *The mechanism governing chip segmentation*

Based on the characterization of chip segmentation in Ti-6Al-4V, it is concluded that the root cause of segmental chip formation in Ti-alloys, as opposed to being purely thermal, is the localized strain imposed by the cutting process leading to periodic fracture. The extent of strain localization is influenced by several factors: cutting parameters, tool geometry, the microstructure of the workpiece material, and the associated thermophysical properties. Strain localization can be further intensified by deformation-induced thermal gradients arising at high cutting speeds and leading to the occurrence of adiabatic shear that may well be a precursor to fracture. Adiabatic shear does not negate the occurrence of fracture.

### 7.3 FE modeling of segmental chip formation

In order to model chip segmentation in Ti-alloys, the Cockroft & Latham (C-L) ductile fracture criterion was integrated into the FE model. The criterion relates material failure to the principal stress in tension and the accumulated plastic strain. It is given by:

$$\int_0^{\bar{\epsilon}_f} \sigma^* d\bar{\epsilon} = C_f \quad (7.1)$$

where  $\sigma^*$ ,  $\bar{\epsilon}$ , and  $\bar{\epsilon}_f$  are the maximum principal stress in tension, the effective strain, and the effective strain at failure, respectively, and  $C_f$  is the critical damage at failure. The criterion is phenomenological. It states that when the “damage” given by the integrand in Eq. 7.1 reaches the critical value  $C_f$ , the deforming material fails by ductile fracture. It also implies that both shear strain and tensile stresses contribute to ductile fracture. The Voce-Johnson-Cook (V-JC) constitutive law was adopted in this work. As elaborated in section 6.2.1.2, the V-JC model offered a more accurate representation of the flow stress behavior of Ti-alloys than the widely used Johnson-Cook (JC) model and more accurate predictions.

Prior to implementing the ductile fracture criterion in the FE model, however, an attempt was made to simulate segmental chip formation using the strain softening approach for the Ti-6Al-4V alloy under study. This approach postulates that chip segmentation in Ti-alloys occurs solely as a result of strain softening due to dynamic recrystallization (DRX).

The JC law modified by Calamaz et al. [81] was applied. It is referred to as the C-JC constitutive law and is given by:

$$\sigma_f = \left( A + B\bar{\varepsilon}^n \left( \frac{1}{\exp(\bar{\varepsilon}^a)} \right) \right) \left( 1 + C \ln \left( \frac{\dot{\bar{\varepsilon}}}{\dot{\bar{\varepsilon}}_0} \right) \right) \times \left( 1 - \left( \frac{T - T_r}{T_m - T_r} \right)^m \right) \left( D + (1 - D) \tanh \left( \frac{1}{(\bar{\varepsilon} + S)^c} \right) \right) \quad (7.2)$$

with

$$D = 1 - \left( \frac{T}{T_m} \right)^d, \quad (7.3)$$

$$S = \left( \frac{T}{T_m} \right)^b, \quad (7.4)$$

where  $\sigma_f$ ,  $\bar{\varepsilon}$ ,  $\dot{\bar{\varepsilon}}$ ,  $\dot{\bar{\varepsilon}}_0$  and are the flow stress, effective strain, effective strain rate and reference effective strain rate, respectively;  $T$ ,  $T_r$ , and  $T_m$  are the instantaneous, room and melt temperature, respectively;  $A$ ,  $B$ ,  $n$ ,  $C$ , and  $m$  are the parameters of the JC law; and  $a$ ,  $b$ ,  $c$  and  $d$  are the additional parameters of the C-JC law.

The parameters of the JC equation were determined previously through the proprietary NRC methodology described in section 6.2.1.1, combining orthogonal cutting tests with analytical and FE modeling. Several combinations of the 4 additional parameters ( $a$ ,  $b$ ,  $c$ , and  $d$ ) were then selected that retain identical flow stress behavior to the JC equation at low strain levels  $\leq 0.3$ . The resulting flow stress-strain curves for 2 such combinations and for several strain rate levels are shown in Fig. 7.5(a, b) in comparison with the JC and V-JC models. The associated chip morphology and strain distributions for the high uncut chip thickness and high speed condition ( $t_3$ ,  $v_3$ ) are shown in Fig. 7.5(c, d) in contrast with the experimentally obtained chip. None of the implemented conditions could produce segmental chips that were comparable to those obtained experimentally. The segmentation was mild, and the chips were almost wavy in nature. Moreover, the sensitivity of the predicted chip geometry to the additional parameters of the C-JC model was low. The strain softening approach is, therefore, not sufficient to model segmental chip formation for the bimodal Ti-6Al-4V microstructure and the range of cutting parameters under investigation.

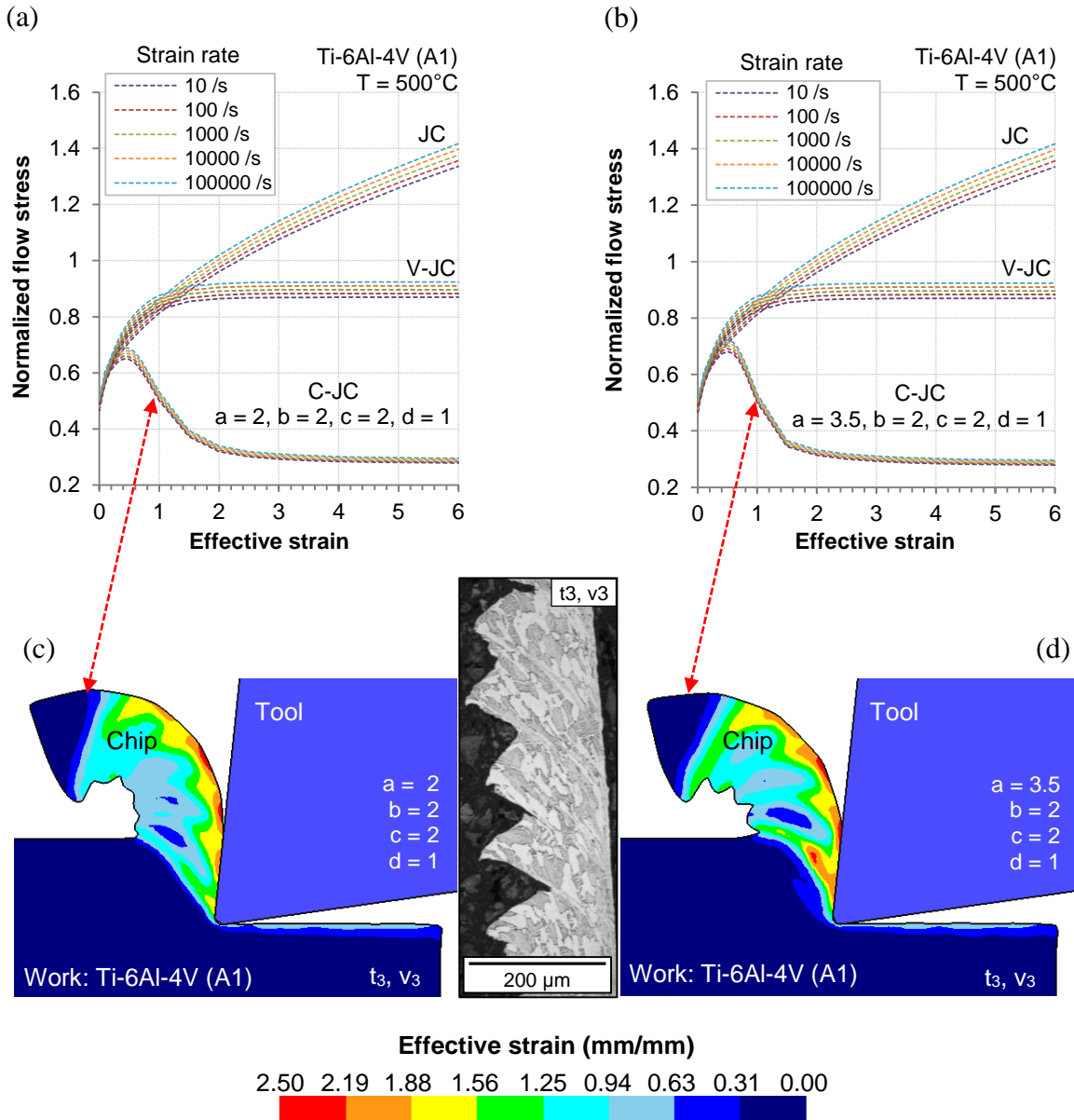


Fig. 7.5: Alloy 1; (a, b) flow stress-strain curves for 2 combinations of the C-JC model parameters, in comparison with JC and V-JC curves; the corresponding chip morphology and strain distribution is shown in (c, d) for condition (t<sub>3</sub>, v<sub>3</sub>) in contrast with the experimental result.

Moreover, the determination of the additional parameters required for the strain softening approach is based on an inverse methodology that relies on the comparison of FE predictions with experimental results [74]. Firstly, the sensitivity of the flow curves to each of the additional parameters is analyzed. Several combinations of the additional parameters are then selected that maintain similar flow stress behavior at low strain to that described by the JC law. FE element simulations are then performed for each of the selected parameter

combinations. The predicted chip geometry and machining forces are compared with experimental results. Finally, the parameter combinations producing the closest agreement between experimental and predicted results are identified and adopted for the Ti-alloy under investigation. Such a procedure can be very lengthy. It is also difficult to converge to a unique solution for a given material due to the large number of parameters involved.

### 7.3.1 Implementation of the ductile fracture criterion

A flowchart integrating the ductile fracture criterion into the FE model and depicting its interactions with other model components is shown in Fig. 7.6. In DEFORM™, the accumulated damage value  $C_t$  at time  $t$  is expressed in terms of the effective strain rate and the time increment. Thus, Eq. 7.1 is rewritten as:

$$\int_0^t \sigma * \dot{\epsilon} dt = C_t \quad (7.5)$$

With this approach, the integration limit becomes the time to failure instead of the effective plastic strain at failure. The critical damage at failure  $C_f$  is assigned by the user. At the end of every time step, the damage value for every element is accumulated as follows:

$$C_t = C_{t-1} + (\text{maximum tensile principal stress}) \times (\text{effective strain rate}) \times dt \quad (7.6)$$

where  $C_t$  is the accumulated damage value at time  $t$ , and  $C_{t-1}$  is the damage value at the previous step at time  $t-1$ . At the end of each step, the value of  $C_t$  is compared to the critical damage value  $C_f$  for every element in the mesh, and as soon as  $C_t \geq C_f$  for a certain number of elements specified by the user (usually 3-5 elements), these elements are deleted from the mesh. It should be noted that only positive damage arising from tensile principal stresses is accumulated. If the principal stress is negative (compressive), then  $C_t = C_{t-1}$ . The DEFORM™ finite element code contains subroutines that perform element deletion in several steps. Firstly, elements having satisfied the damage criterion are deleted from the mesh. This is followed by extraction and smoothing of the workpiece border. The smoothing operation diminishes the volume loss in the workpiece caused by element deletion. It also aids the convergence of the FEM solver. Finally, the workpiece is re-meshed, and the corrected properties are assigned to the newly generated mesh by interpolation [70].

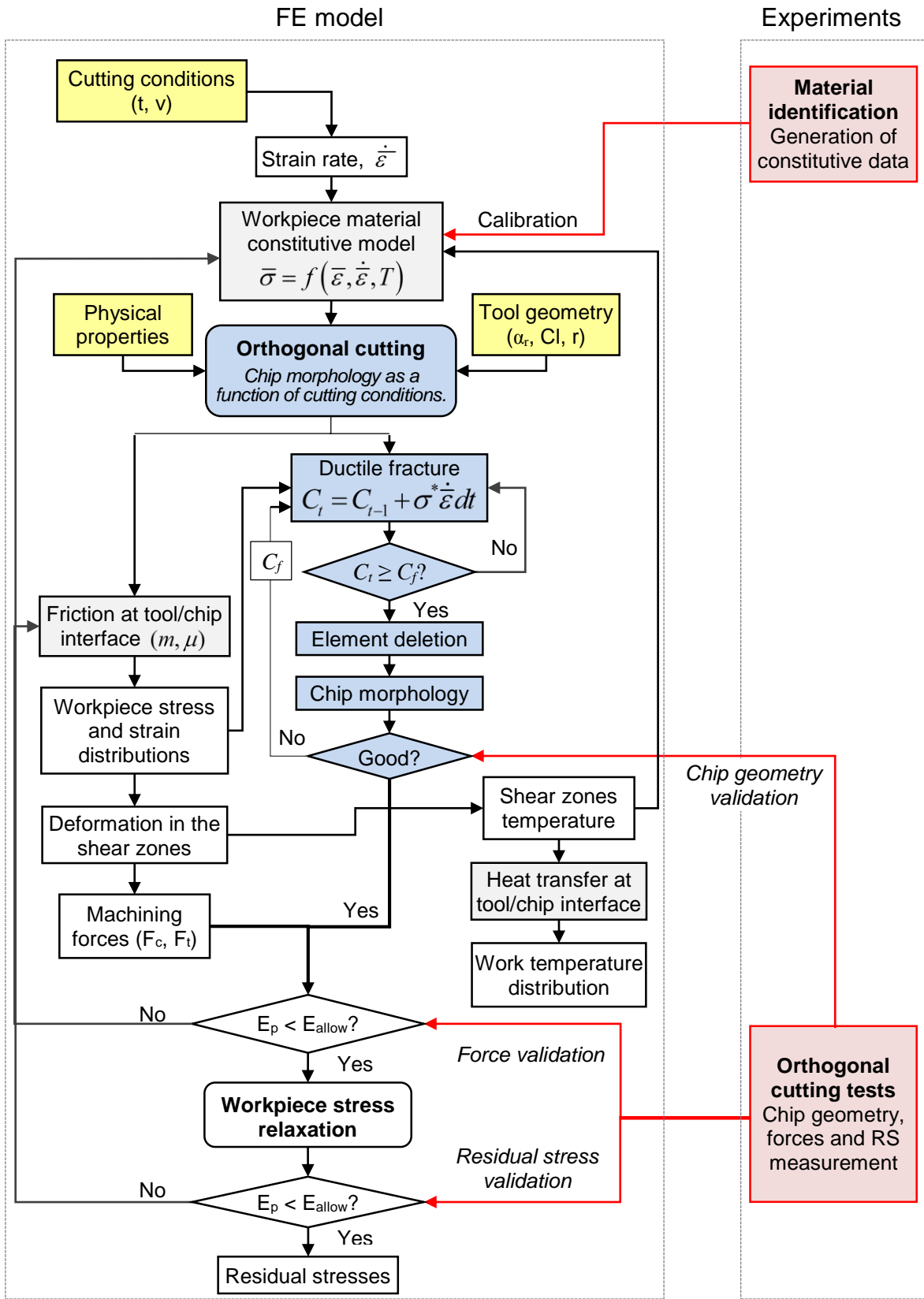


Fig. 7.6: flow diagram of the FE simulation including the effect of chip morphology.

By this approach, the predicted chip morphology is a function of cutting parameters and tool geometry. Its impact on the prediction of forces, temperatures and machining-induced residual stresses (RS) is now considered. The build-up of damage, the crack initiation site, and the direction of crack propagation in the shear zone are driven by the magnitude and direction of the principal tensile stress, as well as the level of accumulated plastic strain in the deforming material.

In addition to the contribution of the above factors, the onset of fracture is essentially controlled by the critical damage at failure  $C_f$ . For accurate FE predictions, this value should be suitably determined. As a measure of the tensile energy per unit volume (Eq. 7.1), it can be determined by estimating the area under the stress-strain curve from a uniaxial tensile test. Such tests, however, are performed at very low strain and strain rate levels compared to those encountered during machining. Material subjected to localized deformation within shear bands can easily undergo plastic strain levels exceeding 2 at strain rates as high as  $10^5 \text{ s}^{-1}$ . Thus, it is highly probable that the critical damage at failure obtained in this manner does not reflect the real behavior of the material. The critical damage at failure adjusted for high strain and strain rate levels can be up to one order of magnitude higher than that determined by a uniaxial tensile test [92].

Consequently, an iterative procedure to determine  $C_f$  was adopted in this work based on FE predictions. After several iterations, a value was selected that gives the closest agreement between FE predictions and experimental results. The selection of  $C_f$  was based on the overall accuracy of predicted machining forces, RS, and chip geometry. The iterative approach was performed for a fixed cutting condition ( $t_3, v_3$ ), combining the highest uncut chip thickness and cutting speed levels in the investigated range of parameters. The critical damage at failure  $C_f$  was varied from 100 to 150 MPa. At  $C_f = 150 \text{ MPa}$ , sawtooth chips ceased to form halfway through the tool stroke. Beyond this point, the results were similar to those obtained without the use of a ductile fracture criterion. At  $C_f = 100 \text{ MPa}$ , the crack propagated all through the chip, which became fragmented or discontinuous. As no such chips were observed experimentally, the admissible range of  $C_f$  is  $100 < C_f < 150 \text{ MPa}$ . Its effect on the predicted cutting force  $F_c$ , thrust force  $F_t$ , and RS is depicted in Fig. 7.7. More precisely, Fig. 7.7a compares the predicted (FEM) and experimental (Exp) results for various values of  $C_f$  within the admissible range, and Fig. 7.7b shows its effect on the absolute

prediction errors. A marked improvement in FE element predictions is obtained when segmental chip formation is incorporated into the model. At  $C_f = 120$  MPa, very good agreement exists between predicted and experimental results (Fig. 7.7a). The absolute error in force and residual stress predictions for  $C_f = 120$  MPa is below 5% (Fig. 7.7b).

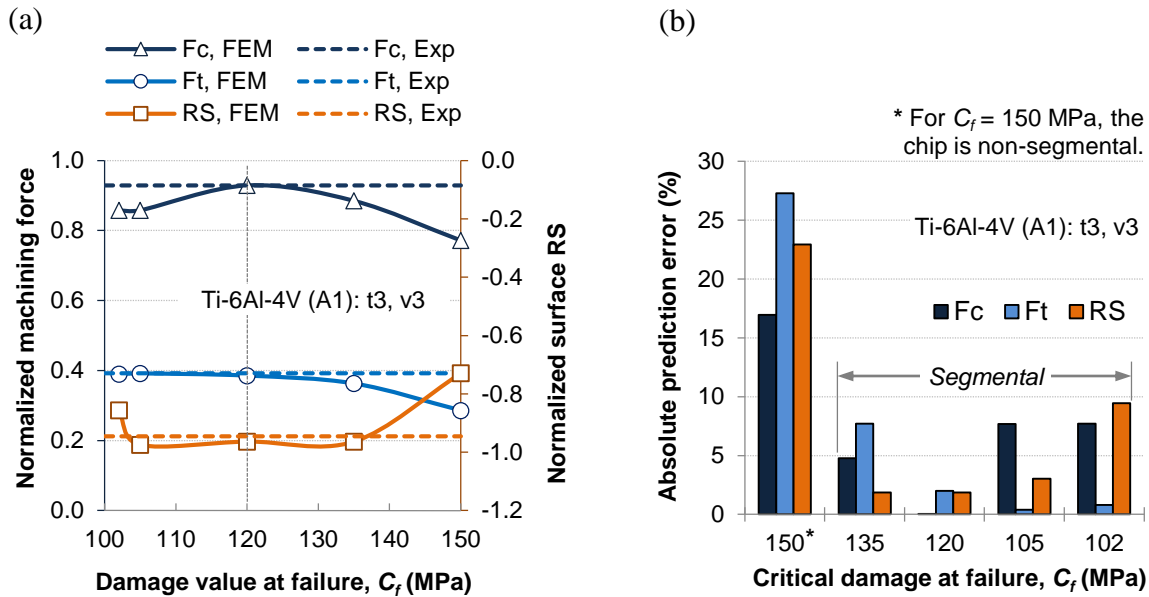


Fig. 7.7: effect of the critical damage at failure  $C_f$  on the predicted cutting force  $F_c$ , thrust force  $F_t$  and residual stresses (RS), with (a) comparing predicted (FEM) and experimental (Exp) results, and (b) showing the influence of  $C_f$  on FE prediction errors.

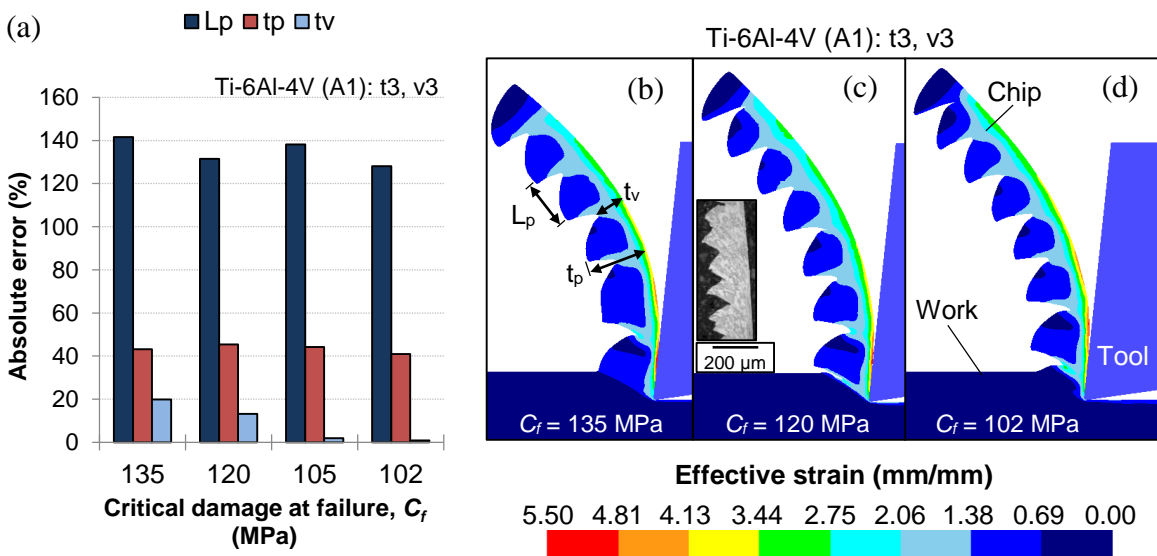


Fig. 7.8: Alloy 1: effect of the critical damage at failure  $C_f$  on (a) chip geometry prediction errors and (b) chip morphology and strain distribution, for the cutting condition ( $t_3$ ,  $v_3$ ).

The effect of the critical damage at failure  $C_f$  on the predicted chip geometry is shown in Fig. 7.8 for the cutting condition ( $t_3, v_3$ ). The variation in chip geometry prediction errors with  $C_f$  within the admissible range is shown in Fig. 7.8a. The estimated error values are presented in Table 7-1. The valley thickness ( $t_v$ ), peak thickness ( $t_p$ ), and tooth pitch ( $L_p$ ) were overpredicted by the FE model. Although the valley thickness  $t_v$  was more sensitive to  $C_f$  than the other parameters, the impact of  $C_f$  on chip geometry was generally limited. A continuous decrease in valley thickness  $t_v$  was observed with decreasing  $C_f$ . The tooth pitch  $L_p$  exhibited a similar trend, except at 105 MPa. In general, as the value of  $C_f$  diminished, the distance between shear centres decreased slightly, and segmentation took place at marginally higher frequency. The peak thickness was relatively insensitive to changes in  $C_f$ .

The impact of  $C_f$  on the morphology and strain distribution within the simulated chip is depicted in Fig. 7.8(b-d) in comparison with the experimentally obtained chip. The examined cases reveal regions of concentrated strain between the segments and a severely strained layer at the back of the chip arising from deformation within the secondary shear zone. Relatively lower, but uniformly distributed strain also exists within the segments, as is the case experimentally. The simulated chip, however, exhibits higher homogeneity and more periodic behavior than its experimental counterpart.

Based on the overall accuracy of FE element predictions of machining forces, residual stresses, and chip geometry (Fig. 7.7 and Fig. 7.8), a fixed value of  $C_f = 120$  MPa was selected for the Ti-6Al-4V alloy and the cutting conditions under investigation. This value was adopted for high cutting speed conditions ( $t_i, v_3$ ) to study the effect of segmental chip morphology on machining-induced residual stresses.

Table 7-1: chip geometry prediction error as a function of the critical damage at failure  $C_f$  for Ti-6Al-4V (Alloy 1) and cutting condition ( $t_3, v_3$ ).

| Critical damage value, $C_f$ (MPa) | FE prediction error (%) |                       |                    |
|------------------------------------|-------------------------|-----------------------|--------------------|
|                                    | Valley thickness, $t_v$ | Peak thickness, $t_p$ | Tooth pitch, $L_p$ |
| 135                                | 20                      | 43                    | 142                |
| <b>120</b>                         | <b>13</b>               | <b>45</b>             | <b>131</b>         |
| 105                                | 2                       | 44                    | 138                |
| 102                                | 1                       | 41                    | 128                |

## 7.4 Effect of chip segmentation on FE predictions

The effect of chip segmentation on FE predictions of machining forces at high cutting speed conditions ( $t_i, v_3$ ) is shown in Fig. 7.9. Previous predictions made with non-segmental chip morphology are denoted by “FEM”. Those implementing the Cockcroft & Latham criterion with  $C_f = 120$  MPa resulting in segmental chips are denoted by “FEM,  $C_f$  120”. Experimental values of average steady-state machining forces are represented by “Exp”.

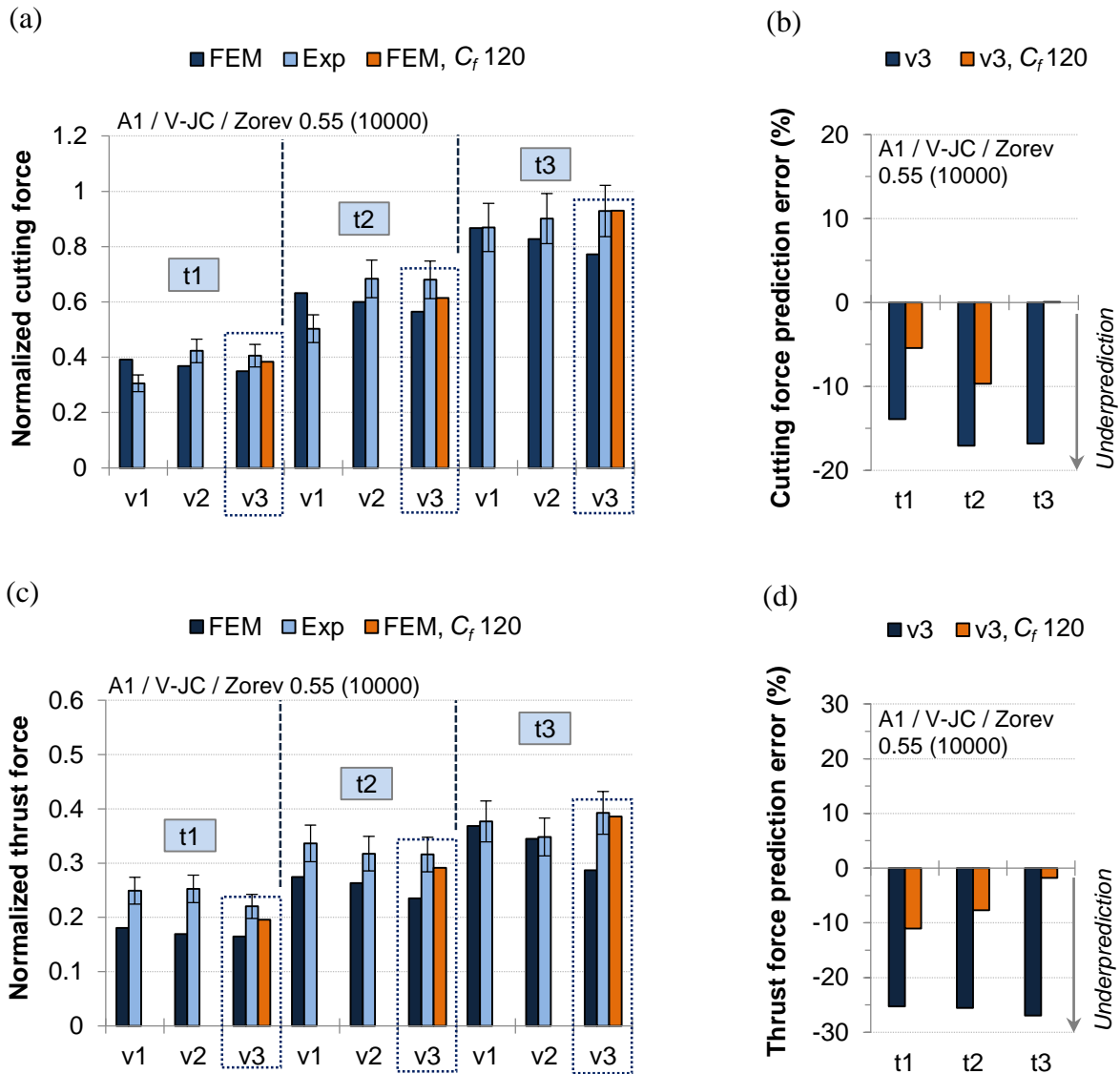


Fig. 7.9: effect of chip segmentation on force predictions at high speed conditions ( $t_i, v_3$ ), contrasting trends and prediction errors for (a, b) the cutting force and (c, d) the thrust force.

As shown in Fig. 7.9a, when chip segmentation is considered at high cutting speed  $v_3$ , predicted cutting forces are in closer agreement with experimental results. For a non-segmental chip, the FE model predicts a reverse trend of declining cutting force with increasing speed compared to the experimental results. This inaccuracy is diminished by the introduction of the ductile fracture criterion. The prediction error in cutting force is reduced to within  $\pm 10\%$  for high speed conditions as shown in Fig. 7.9b. A similar improvement was observed for the thrust force (Fig. 7.9(c, d)).

The exclusion of chip segmentation produced a larger drop in compressive RS at high speed compared to the measured values (Fig. 7.10a). This exaggerated decline in compressive RS at high speed  $v_3$  coincides with the erroneous reduction in machining forces elaborated in Fig. 7.9. Upon implementation of the ductile fracture criterion, the underprediction of compressive RS was diminished, and the accuracy of residual stress predictions was improved significantly (Fig. 7.10b). Furthermore, the prediction error for RS over the full range of investigated cutting conditions was reduced to within  $\pm 10\%$ . The attribution of the discrepancy in RS prediction at high cutting speed to the exclusion of chip segmentation from the FE model was, therefore, verified. At cutting speeds  $v \geq (0.85 \times v_3)$ , chip segmentation should be considered in the FE model for accurate prediction of machining-induced RS.

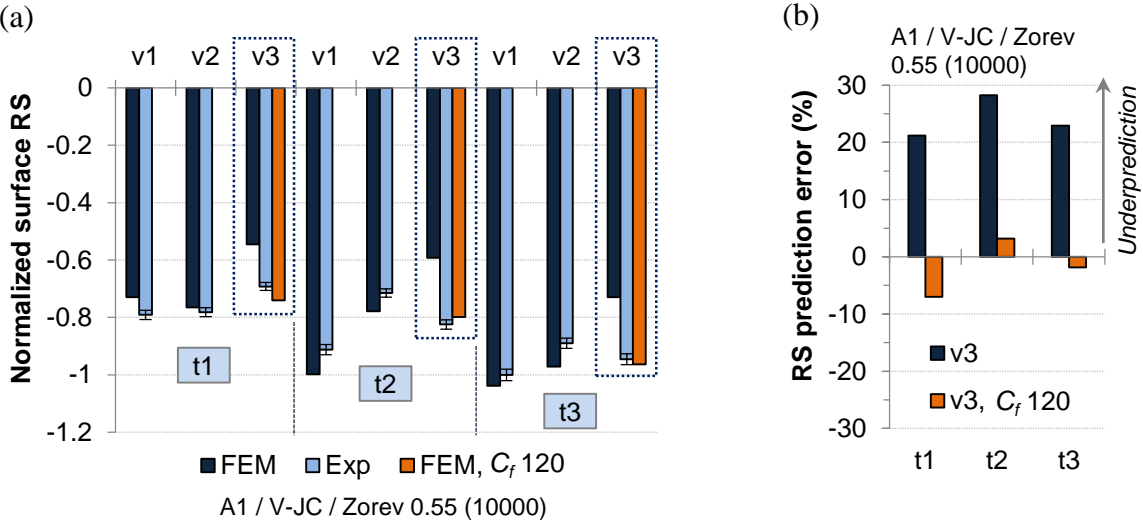


Fig. 7.10: effect of chip segmentation on RS predictions at high speed  $v_3$ , contrasting (a) trends and (b) prediction accuracy. The resulting error range for the investigated cutting regime is given in (c).

## 7.5 Mechanism governing the effect of segmentation on RS predictions

At high cutting speed  $v_3$  within the investigated conventional range (20 to 90 m/min), both machining forces and compressive RS are underpredicted when non-segmental chip morphology is assumed, and larger prediction errors are obtained (Fig. 7.9 and Fig. 7.10). Chip segmentation promotes an increase in the predicted machining forces and compressive RS relative to the non-segmental chip, thereby diminishing the prediction errors. This suggests that the effect is of a mechanical nature. The influence of chip segmentation on the predicted temperature and residual stress distribution in the sub-surface for condition  $(t_3, v_3)$  is shown in Fig. 7.11. Segmentation was found to have a negligible effect on temperature distribution (Fig. 7.11a), whereas both the magnitude and the gradient of compressive RS were increased (Fig. 7.11b). This shows that the effect of chip segmentation on machining-induced RS at high speed within the conventional range is predominantly mechanical. For the purpose of validation, the measured surface residual stress value is shown in Fig. 7.11b.

During high speed machining of Ti-6Al-4V at  $v = 320$  m/min, it was shown that chip segmentation leads to a reduction in the predicted workpiece surface temperature compared to a non-segmental chip [54]. As elevated temperatures are known to shift RS towards the tensile state, the reduction in temperature associated with chip segmentation at very high speeds leads to larger predicted compressive RS. Thus, at unconventionally high speeds, the effect of chip segmentation on machining-induced RS is predominantly thermal.

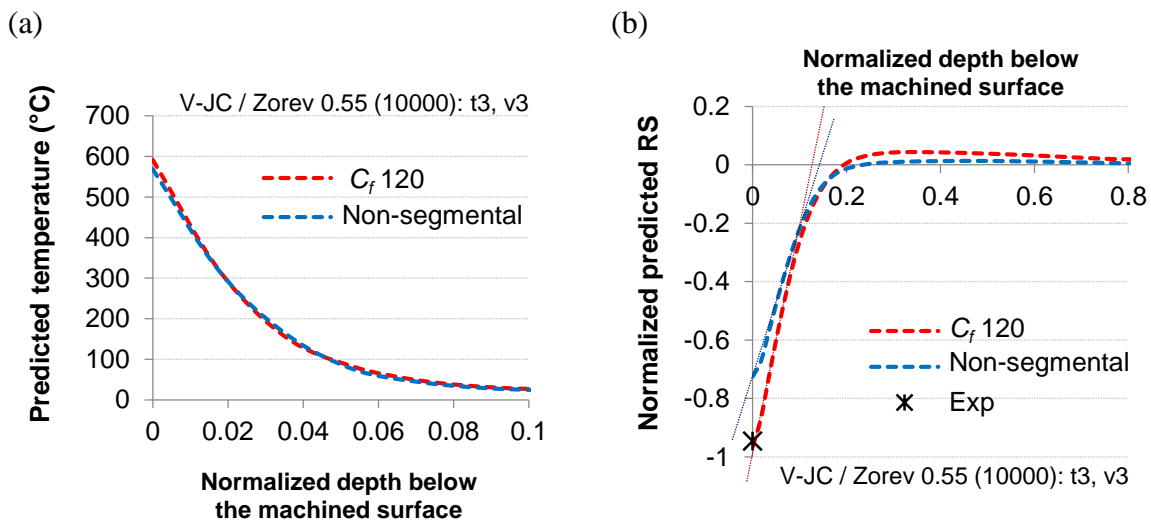


Fig. 7.11: predicted (a) temperature and (b) residual stress distributions below the machined surface for Ti-6Al-4V (Alloy 1) at condition  $(t_3, v_3)$  for non-segmental and segmental chip morphologies.

Fig. 7.12a shows the distribution of effective strain along the machined surface within the steady-state region in the direction of the tool path. The machined surface associated with a segmental chip appears to have sustained a larger degree of plastic deformation. The strain distribution below the surface at the point of contact with the tool tip is depicted in Fig. 7.12b. It was obtained at a tool stroke of 2.5 mm corresponding to the end of the cutting path. Chip segmentation produced a marked increase in the magnitude and gradient of effective strain, while the depth of the plastically deformed layer remained practically unchanged. Increased plastic deformation relative to the bulk of the material and a sharper deformation gradient are conditions that promote residual stresses of higher magnitudes.

Fig. 7.13 shows the evolution of stresses in the workpiece at the condition  $(t_3, v_3)$  in relation to the crack initiation and propagation sequence. The stress behavior (a-d) and the corresponding progression of fracture (e-h) are examined at identical simulation time steps. The crack initiation site for the bimodal Ti-alloy under study is located at the free surface adjacent to the primary shear zone ( Fig. 7.13e). This is true at all uncut chip thickness levels within the investigated range of cutting parameters. The crack initiates at point C and then propagates towards the tool tip O parallel to the direction of shear. This is in agreement with the periodic fracture theory of segmental chip formation [135-137].

As the chip glides against the fractured surface, the material behind the tool tip in the machined surface is subjected to higher loads as shown in Fig. 7.13c. A gradual increase in effective stress takes place following the onset of fracture. Upon the emergence of a newly forming segment ( Fig. 7.13d), the stresses are released and approach their initial levels. Due to the cyclic nature of the process, the surface material undergoes a repetitive loading cycle as machining progresses accompanying the formation of every segment. Simultaneously, the compressive region ahead of the cutting tool gradually shrinks in size and becomes more concentrated in the vicinity of the tool tip until the emergence of a new segment as shown in Fig. 7.13(a-d). For condition  $(t_3, v_3)$ , the effective stress in the machined surface ranged from around 600 to 750 MPa. For a non-segmental chip at the same condition, a lower nominal value of around 550 MPa was estimated that was almost constant. Consequently, while the temperature distribution in the workpiece surface remains almost the same relative to a non-segmental chip (Fig. 7.11a), the material sustains larger mechanical loads of a cyclic nature leading to more severe plastic deformation with sharper gradients.

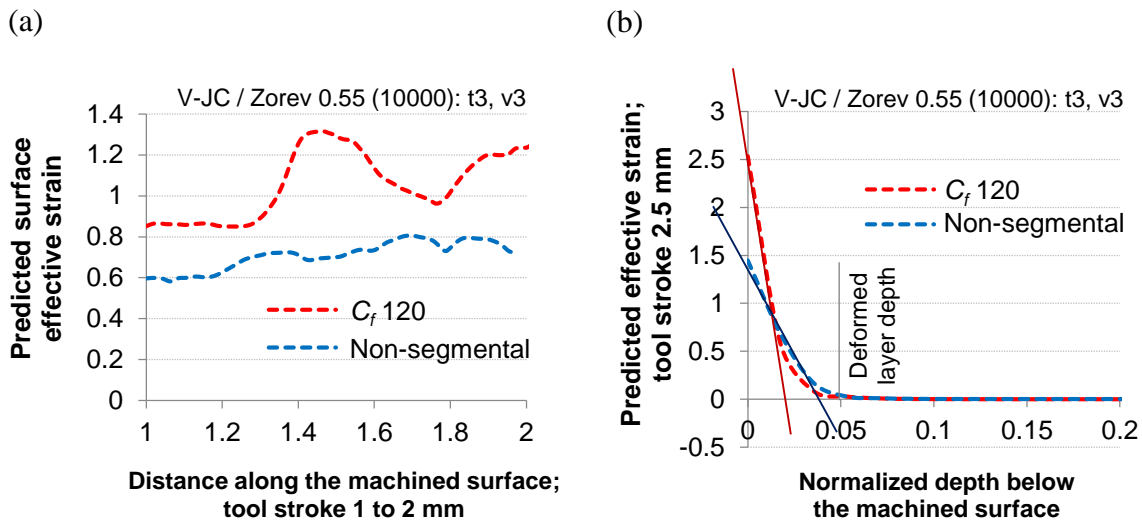


Fig. 7.12: predicted strain distribution (a) along the workpiece surface within the steady-state region and (b) below the machined surface for segmental and non-segmental chip morphology.

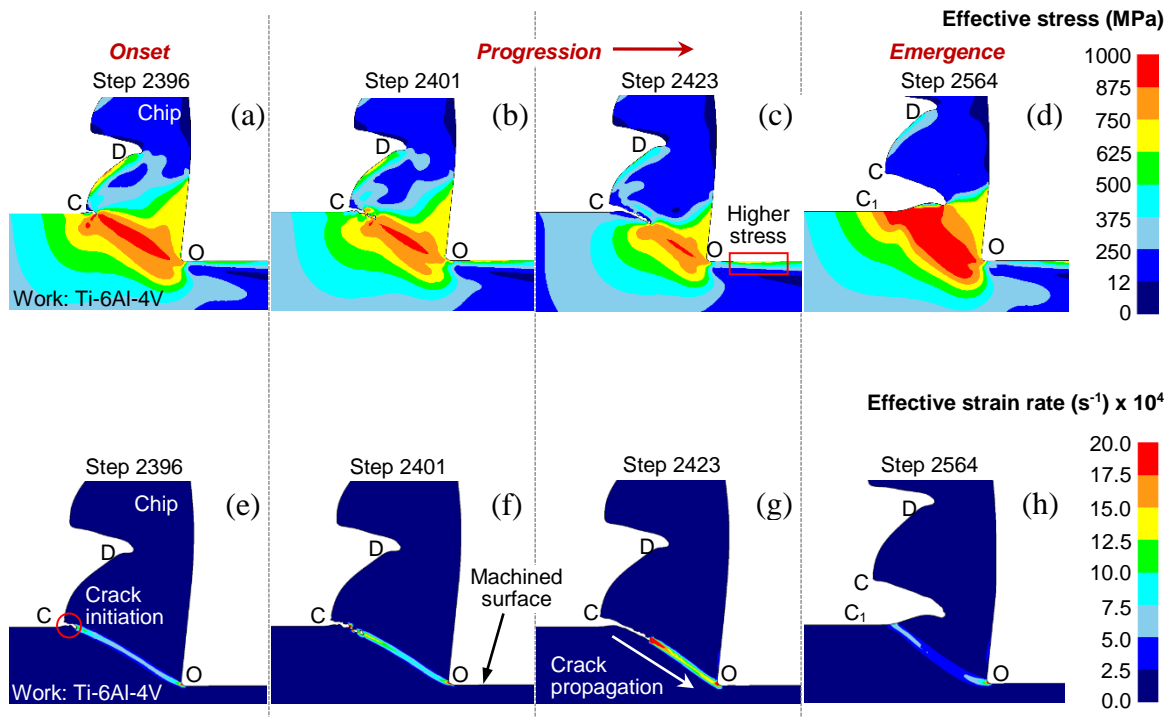


Fig. 7.13: FE predictions of (a-d) stress evolution in the workpiece and (e-h) the corresponding crack initiation and propagation sequence at condition  $(t_3, v_3)$  for Ti-6Al-4V (Alloy 1).

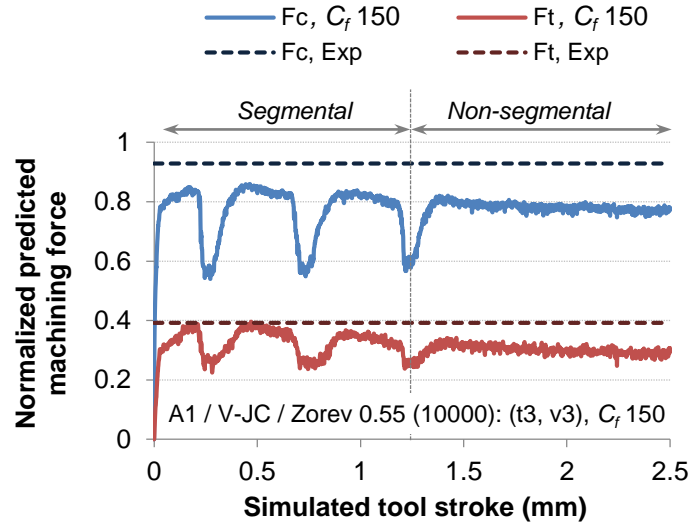


Fig. 7.14: predicted cutting ( $F_c$ ) and thrust ( $F_t$ ) force signals for Ti-6Al-4V (Alloy 1) at cutting condition  $(t_3, v_3)$ , and for a critical damage at failure  $C_f = 150$  MPa.

Fig. 7.14 shows the predicted force signals at condition  $(t_3, v_3)$  for a critical damage value  $C_f = 150$  MPa. Two distinct chip morphologies were observed for this condition. Initially, the chip was segmental in nature, resulting in cyclic force variation. Around halfway through the tool stroke, however, deformation became more uniform, and segmentation ceased to occur. In the absence of segmentation, the steady-state signal settled at a value below the peak of the previously cyclic signal. The ratio of the peak cyclic force to the steady-state non-cyclic force was around 1.10 and 1.31 for the cutting ( $F_c$ ) and thrust ( $F_t$ ) force components, respectively. This agrees with experimental results reported by Sun et al. [130].

For a periodic saw toothed chip, the segmentation frequency  $f_c$  can be estimated as the ratio of the cutting speed ( $v$ ) to the undeformed length ( $L_0$ ) depicted in Fig. 7.1 [130]:

$$f_c = \frac{v}{L_0} \quad (7.7)$$

Based on the experimental measurements of chip geometry, the segmentation frequencies for conditions  $(t_3, v_1)$  and  $(t_3, v_3)$  were found to be around 5,650 and 14,100 Hz, respectively, amounting to an increase of around 150%. The ratio of frequencies at the above conditions was almost identical to that of the cutting speeds. Thus, at high cutting speeds, elements in the machined surface are subjected to higher frequency loads of larger amplitude as illustrated in Fig. 7.13 and Fig. 7.14. This promotes more severe superficial and sub-surface

deformation as elaborated in Fig. 7.12. Consequently, compressive RS of higher magnitude are induced in the machined surface.

In conclusion, the assumption of non-segmental chip morphology at high cutting speed leads to the underprediction of compressive RS. When chip segmentation is modeled, larger compressive RS are predicted, and prediction errors are reduced. The mechanism by which this occurs is dictated by the cutting speed. Within the conventional range of speeds, chip segmentation increases the mechanical contribution to plastic deformation, which results in larger compressive RS. At unconventionally high speeds, the thermal contribution is diminished, thereby achieving the same result.

## CHAPTER 8 CONCLUSIONS AND RECOMMENDATIONS

### 8.1 Experimental investigation

An extensive experimental investigation was conducted for two aerospace grade Ti-alloys, Ti-64 (Alloy 1) and Ti-6246 (Alloy 2), in the finish turning regime. The effect of depth of cut ( $doc$ ), cutting speed ( $v$ ), feed rate ( $f$ ), and tool corner radius ( $R$ ) on surface integrity was investigated including residual stresses (RS), surface roughness, and the near-surface microstructure (NSM). Experiments were performed under wet conditions with the use of forced lubrication. In the following, cutting parameter combinations are represented by  $(doc_i, v_i, f_i, R_i)$ , where  $i = 1$  to 3 denotes the parameter levels in order of increasing magnitude. The following conclusions were drawn:

1. **State of RS and dominant parameters:** Over the investigated finish turning regime, RS are compressive in nature for both Ti-alloys. Cutting speed  $v$ , feed rate  $f$ , and corner radius  $R$  have significant effects on RS. The magnitude of compressive RS is controlled by interactions between these three parameters. It is verified by statistical analysis that  $doc$  does not have a statistically significant effect on RS. The uttermost compressive residual stress state is attained, however, at conditions of high depth of cut, high speed, high feed, and small corner radius  $(doc_2, v_2, f_3, R_1)$  for both Ti-alloys.
2. **Compressive RS in Ti-64:** In general, larger compressive RS are generated at conditions with opposing levels of feed rate and corner radius,  $(doc_i, v_i, f_1, R_3)$  and  $(doc_i, v_i, f_3, R_1)$ . At high feed rate, compressive RS are substantially enhanced by increasing the cutting speed. Conditions of high speed, high feed, and small corner radius  $(doc_i, v_2, f_3, R_1)$  promote compressive RS of higher magnitudes.
3. **Compressive RS in Ti-6246:** Larger compressive RS are generated at conditions of high feed rate and small corner radius  $(doc_i, v_i, f_3, R_1)$ . Compressive RS induced in Ti-6246 exceed Ti-64 levels by around 45% on average.
4. **Accuracy and benefits of the empirical models:** The developed empirical models are of good value to industry as they provide fast and accurate predictions of RS with errors in the range of  $\pm 70$  MPa. In addition, they successfully reflect the trends and mutual interactions between cutting parameters with respect to RS. Consequently, the models can serve as guidelines during product development and manufacturing.

5. **State of surface finish and dominant parameters:** For the investigated range of cutting parameters surface roughness is within the acceptable limits for aero-engine applications. Nevertheless, feed rate has the most significant detrimental effect on surface finish. Increasing the feed rate by 150% produces an average increase of around 100% in the Ra value for both Ti-alloys.
6. **Conflict between RS and surface finish:** A conflict exists between RS and surface roughness in that the enhanced compressive RS obtained at higher levels of feed are at the expense of surface finish. Based on guidelines developed in this work, optimal cutting parameters can be selected with respect to RS and surface roughness. For applications where surface finish is highly critical, it is recommended to machine Ti-64 at conditions of low feed and large corner radius ( $doc_i, v_i, f_1, R_3$ ) and Ti-6246 at conditions of low feed and small corner radius ( $doc_i, v_i, f_1, R_1$ ). Such conditions promote moderately compressive RS and enhanced surface quality.
7. **Near-surface microstructure (NSM):** For the investigated finish turning regime, machining parameters do not have a visible effect on microstructure. Machining does not cause significant work hardening of the sub-surface material. Surfaces are free from machining artefacts such as cracks, tears, and redeposited materials. No grain distortion or white layer formation is observed.
8. **Parameter range for high surface integrity:** As a result of the extensive experimental investigation and the comprehensive analysis of surface integrity, a suitable range of cutting parameters is identified for finish turning of aerospace grade Ti-alloys that promotes compressive RS and enhanced surface quality. The machining of Ti-alloys can be further optimized based on these findings.

## 8.2 FE modeling

A thermomechanically coupled 2D FE model of the orthogonal cutting process was constructed in DEFORM™. As a preliminary step towards model development, a numerical study was performed on the relative contribution of thermal loads, mechanical loads, and phase transformations to the resultant stress state in commercially available materials. The FE model was optimized for residual stress predictions in Ti-alloys and validated against experimental measurements over a wide range of cutting conditions. It was then used as a

virtual machining medium to gain insight into the effect of cutting parameters, tool edge preparation, flank wear, and chip segmentation on residual stress formation. This was achieved by examining the evolution of state variables at a level that was extremely difficult to achieve experimentally. In the following, cutting parameter combinations are represented by  $(t_i, v_i)$ , where  $i = 1$  to 3 denotes the levels of uncut chip thickness ( $t$ ) and cutting speed ( $v$ ) in order of increasing magnitude. The following conclusions were drawn:

9. **FE model accuracy and computational efficiency:** Through precise characterization of flow stress behavior, high fidelity modeling of the cutting edge, and the simulation of chip segmentation at relatively high speeds, residual stress prediction errors for Ti-64 are limited to  $\pm 10\%$  over the entire range of cutting parameters. By adopting suitable geometries, efficient remeshing strategies, optimized boundary conditions, and efficient time steps, the computational time is reduced from several days to 24-36 hours. Thus, the model constitutes an investigative tool of good benefit to the aerospace industry.
10. **Voce-Johnson-Cook (V-JC) flow stress model:** The V-JC constitutive law more accurately captures the flow stress behavior of Ti-alloys at high strains than the widely adopted Johnson-Cook (JC) model. By inhibiting the monotonic strain hardening behavior that is a characteristic of the JC model, the V-JC law leads to a higher prediction accuracy. As it maintains an identical number of material parameters (5), calibration can be performed with a high degree of certainty through advanced material identification procedures based on machining tests.
11. **Effect of chip segmentation on RS (Ti-64):** Within the conventional range of speeds, the mechanism by which chip segmentation influences residual stress generation is of a mechanical nature. The machined surface behind the tool undergoes a repetitive loading cycle beginning with the formation of every segment, during which it withstands larger loads than those sustained with an assumedly non-segmental chip. At high speed, the machined surface is subjected to higher frequency loads of larger amplitude. This promotes more severe deformation with sharper gradients. Compressive RS are, therefore, enhanced by an enlarged mechanical contribution to plastic deformation.
12. **Residual stress evolution during cutting (Ti-64):** A deeper understanding of the evolution of RS during cutting can be obtained by separating the thermally and mechanically induced residual stress components. The resulting thermomechanically generated stress state is

dependent on the imbalance between the thermal and mechanical components, which is influenced by cutting conditions. Cutting with moderate speeds and sharp tools shifts the imbalance towards mechanically generated stresses (compressive), whereas high speeds and large edge radii shift the imbalance towards thermally induced stresses (tensile).

13. **Effect of flank wear (Ti-6246):** Residual stresses are highly sensitive to flank wear that can completely alter their behavior and reverse existing trends. Wear in excess of 12  $\mu\text{m}$  should not be overlooked. The significant temperature rise with increasing wear rapidly diminishes compressive RS as thermal stresses predominate over the contribution of mechanical loads. Progressive flank wear can eventually shift RS from a compressive to a tensile state.
14. **Recommendations for the machining of Ti-alloys:** Compressive RS can be generated in Ti-alloys by limiting the contribution of thermal stresses. The onset of plastic deformation under predominantly thermal loading conditions depends on the initial yield stress of the alloy and its sensitivity to thermal softening. An early onset of plastic deformation favors tensile RS. Machining with minimal tool wear, sufficiently small hone radii, and moderate speeds promotes compressive RS. Larger levels of feed (uncut chip thickness) can enhance compressive RS as they shift the imbalance further towards mechanically generated stresses. It is also possible to further increase the magnitude of compressive RS by machining at higher speeds due to their sizeable contribution to both mechanically induced and thermally generated stresses. This is, however, highly dependent on the use of appropriate modes of cooling/lubrication for the selected range of speeds.

In conclusion, the fundamental understanding gained from this work as highlighted in items 1-14 provides important contributions to the knowledge base in the field of machining-induced RS. Prior to this work, limited information was available on RS in Ti-alloys, especially during the critical finishing operation at cutting conditions relevant to the aerospace industry. A comprehensive analysis of RS and surface integrity led to the identification of a favorable parameter range that promotes compressive RS and high surface integrity, highly essential attributes for part longevity. Important guidelines were established for the optimal selection of cutting parameters to achieve a desirable combination of RS and surface roughness that were lacking in the open literature. Empirical models were developed

that offer reasonable predictions of RS during finish turning of Ti-alloys, which were previously only available for milling operations. Modern techniques for material characterization and improved practices were adopted in the development of more efficient and more accurate FE models optimized for residual stress prediction, which constitute a valuable resource to industry. The limitations of state variable distribution measurements were overcome through the use of the developed FE models to gain additional knowledge of the contribution of material properties and cutting parameters to the shift in the balance between mechanically and thermally induced plastic deformation. A clearer understanding of the relative significance of thermal and mechanical loads to residual stress formation was obtained. The nature of the effect of chip segmentation on residual stress generation at relatively high conventional speeds was determined, which was previously only known for high speed machining conditions. The adopted methodology that combined experimental investigation and FEM led to a thorough characterization of machining-induced RS in Ti-alloys. In consequence, the work was successful in satisfying the specific and terminal objectives of the research.

### **8.3 Recommendations for future work**

Further to the experimental findings and the knowledge gained from the FE modeling, and based on industrial requirements and developing trends, it is recommended to extend the research to address the following area(s):

1. Development of a 3D finite element model of the cutting process to predict residual stresses in aerospace grade Ti-alloys, Ti-64 and Ti-6246. The proposed objective is to develop a computationally efficient model that can address typical conditions used in production. The model can be validated using the vast amount of experimental data obtained from the oblique cutting experiments performed in this research.
2. Additional experimental investigation of the effects of tool wear, tool coatings, and workpiece heat treatment on machining-induced RS in Ti-alloys, to be supported by empirical and FE modeling, and to include the effect of various progressive wear modes arising from a combination of chemical and abrasive wear mechanisms.
3. The experimental investigation and FE modeling of combined laser-assisted machining (LAM) and cryogenic cooling on RS in Ti-alloys. Of the many benefits of LAM is the

reduction in machining forces, which combined with cryogenic cooling of the cutting tool can permit higher material removal rates with improved tool life. The effect of such a hybrid process on RS is not known. It is proposed to evaluate RS induced under the above conditions, together with the effects of hybrid machining on cutting performance (productivity and cost) and surface integrity of the machined part. Due to the elevated temperatures and high cooling rates inherent in the process, special consideration should be given to the microstructure evolution of the workpiece material and its effect on residual stress formation. Phase transformation models can be incorporated into FE models to optimize the process for desirable surface microstructures.

4. The investigation through experiments and FE modeling of the combined effect of chip segmentation and tool wear on RS in Ti-alloys at higher material removal rates. Chip segmentation becomes of special significance at higher cutting speeds that promote accelerated wear. Shear localization is more severe with larger feed rates and high cutting speeds. The proposed objective is to characterize the behavior of RS under the above conditions in relation to cutting performance and important aspects of surface integrity, surface roughness, and microstructure.

## REFERENCES

1. Shaw, M.C., *Metal Cutting Principles 2E* C2005: Oxford University Press, Incorporated.
2. Brinksmeier, E., et al., *Residual Stresses - Measurement and Causes in Machining Processes*. CIRP Annals - Manufacturing Technology, 1982. **31**(2): p. 491-510.
3. Withers, P. and H. Bhadeshia, *Residual stress. Part 2—Nature and origins*. Materials Science and Technology, 2001. **17**(4): p. 366-375.
4. McEvily, A.J. and J. Kasivitanuay, *Metal Failures : Mechanisms, Analysis, Prevention (2nd Edition)*2013, Somerset, NJ, USA: Wiley.
5. Grandt, A.F., *Fundamentals of Structural Integrity: Damage Tolerant Design and Evaluation*2004: John Wiley and Sons, inc.
6. Withers, P. and H. Bhadeshia, *Residual stress. Part 1—measurement techniques*. Materials Science and Technology, 2001. **17**(4): p. 355-365.
7. Prevey, P.S., *X-ray diffraction residual stress techniques*. ASM International, ASM Handbook., 1986. **10**: p. 380-392.
8. Wu, D.W. and Y. Matsumoto, *The Effect of Hardness on Residual Stresses in Orthogonal Machining of AISI 4340 Steel*. Journal of Engineering for Industry, 1990. **112**(3): p. 245-252.
9. Zhang, L. and M. Mahdi, *Applied mechanics in grinding—IV. The mechanism of grinding induced phase transformation*. International Journal of Machine Tools and Manufacture, 1995. **35**(10): p. 1397-1409.
10. Vansevenant, E. and J. Peters, *An Improved Mathematical Model to Predict Residual Stresses in Surface Plunge Grinding*. CIRP Annals - Manufacturing Technology, 1987. **36**(1): p. 413-416.
11. Mishra, A. and T. Prasad, *Residual stresses due to a moving heat source*. International Journal of Mechanical Sciences, 1985. **27**(9): p. 571-581.
12. Mahdi, M. and L.C. Zhang, *Residual stresses in ground components caused by coupled thermal and mechanical plastic deformation*. Journal of Materials Processing Technology, 1999. **95**(1-3): p. 238-245.
13. Mahdi, M. and L. Zhang, *Applied mechanics in grinding. Part 7: residual stresses induced by the full coupling of mechanical deformation, thermal deformation and phase transformation*. International Journal of Machine Tools and Manufacture, 1999. **39**(8): p. 1285-1298.
14. Mahdi, M. and L. Zhang, *Applied mechanics in grinding—VI. Residual stresses and surface hardening by coupled thermo-plasticity and phase transformation*. International Journal of Machine Tools and Manufacture, 1998. **38**(10-11): p. 1289-1304.
15. Mahdi, M. and L. Zhang, *Applied mechanics in grinding—V. Thermal residual stresses*. International Journal of Machine Tools and Manufacture, 1997. **37**(5): p. 619-633.
16. Chen, X., W.B. Rowe, and D.F. McCormack, *Analysis of the transitional temperature for tensile residual stress in grinding*. Journal of Materials Processing Technology, 2000. **107**(1-3): p. 216-221.

17. Mahdi, M. and L. Zhang, *A theoretical investigation on the mechanically induced residual stresses due to surface grinding*. Progress of Cutting and Grinding, 1996. **3**: p. 484-487.
18. Lin, Z.-C., Y.-Y. Lin, and C.R. Liu, *Effect of thermal load and mechanical load on the residual stress of a machined workpiece*. International Journal of Mechanical Sciences, 1991. **33**(4): p. 263-278.
19. Liu, C.R. and M.M. Barash, *Variables Governing Patterns of Mechanical Residual Stress in a Machined Surface*. Journal of Manufacturing Science and Engineering, 1982. **104**(3): p. 257-264.
20. Liu, C.R. and M.M. Barash, *The Mechanical State of the Sublayer of a Surface Generated by Chip-Removal Process—Part 1: Cutting With a Sharp Tool*. Journal of Manufacturing Science and Engineering, 1976. **98**(4): p. 1192-1199.
21. Liu, C.R. and M.M. Barash, *The Mechanical State of the Sublayer of a Surface Generated by Chip-Removal Process—Part 2: Cutting With a Tool With Flank Wear*. Journal of Manufacturing Science and Engineering, 1976. **98**(4): p. 1202-1208.
22. Okushima, K. and Y. Kakino, *The residual stress produced by metal cutting*, Ft. Belvoir: Defense Technical Information Center.
23. Smallman, R.E. and R.J. Bishop, *Modern Physical Metallurgy and Materials Engineering - Science, Process, Applications (6th Edition)*, 1999, Elsevier.
24. Cullity, B.D., *Elements of x-ray diffraction* 1978, Reading, Mass.: Addison-Wesley Pub. Co.
25. Mittal, S. and C.R. Liu, *Method of modeling residual stresses in superfinish hard turning*. Wear, 1998. **218**(1): p. 21-33.
26. Fuh, K.-H. and C.-F. Wu, *Residual-stress model for the milling of aluminum alloy (2014-T6)*. Journal of Materials Processing Technology, 1995. **51**(1-4): p. 87-105.
27. El-Khabeery, M.M. and M. Fattough, *Residual stress distribution caused by milling*. International Journal of Machine Tools and Manufacture, 1989. **29**(3): p. 391-401.
28. Sridhar, B.R., et al., *Effect of machining parameters and heat treatment on the residual stress distribution in titanium alloy IMI-834*. Journal of Materials Processing Technology, 2003. **139**: p. 628-34.
29. El-Axir, M.H., *A method of modeling residual stress distribution in turning for different materials*. International Journal of Machine Tools and Manufacture, 2002. **42**(9): p. 1055-1063.
30. Liang, S.Y. and J.C. Su, *Residual Stress Modeling in Orthogonal Machining*. CIRP Annals - Manufacturing Technology, 2007. **56**(1): p. 65-68.
31. Ulutan, D., B. Erdem Alaca, and I. Lazoglu, *Analytical modelling of residual stresses in machining*. Journal of Materials Processing Technology, 2007. **183**(1): p. 77-87.
32. Lazoglu, I., et al., *An enhanced analytical model for residual stress prediction in machining*. CIRP Annals - Manufacturing Technology, 2008. **57**(1): p. 81-84.
33. Oxley, P.L.B., *The mechanics of machining : an analytical approach to assessing machinability*. Ellis Horwood series in mechanical engineering 1989, Chichester [England]; New York: E. Horwood ; Halsted Press.
34. Waldorf, D.J., *A simplified model for ploughing forces in turning*. Journal of Manufacturing Processes, 2006. **8**(2): p. 76-82.
35. Altintas, Y., *Manufacturing automation : metal cutting mechanics, machine tool vibrations, and CNC design* 2000, New York: Cambridge University Press.
36. Jaeger, J. *Moving sources of heat and the temperature at sliding contacts*. 1942.

37. Komanduri, R. and Z.B. Hou, *Thermal modeling of the metal cutting process Part I - temperature rise distribution due to shear plane heat source*. International Journal of Mechanical Sciences, 2000. **42**(9): p. 1715-1752.
38. Komanduri, R. and Z. Hou, *Thermal modeling of the metal cutting process—Part II: temperature rise distribution due to frictional heat source at the tool–chip interface*. International Journal of Mechanical Sciences, 2001. **43**(1): p. 57-88.
39. Lazoglu, I. and Y. Altintas, *Prediction of tool and chip temperature in continuous and interrupted machining*. International Journal of Machine Tools and Manufacture, 2002. **42**(9): p. 1011-1022.
40. McDowell, D.L., *An approximate algorithm for elastic-plastic two-dimensional rolling/sliding contact*. Wear, 1997. **211**(2): p. 237-246.
41. Grzesik, W., *Modelling and Simulation of Machining Processes and Operations*, in *Advanced Machining Processes of Metallic Materials* 2008, Elsevier: Amsterdam. p. 49-67.
42. Maranhão, C. and J. Paulo Davim, *Finite element modelling of machining of AISI 316 steel: Numerical simulation and experimental validation*. Simulation Modelling Practice and Theory, 2010. **18**(2): p. 139-156.
43. Guo, Y.B., S. Anurag, and I.S. Jawahir, *A novel hybrid predictive model and validation of unique hook-shaped residual stress profiles in hard turning*. CIRP Annals - Manufacturing Technology, 2009. **58**(1): p. 81-84.
44. Anurag, S., Guo, Y. B., Liu, Z. Q., *A new finite element approach without chip formation to predict residual stress profile parameters in metal cutting*. Proceedings of the ASME 2009 International Manufacturing Science and Engineering Conference MSEC2009, 2009(MSEC2009-84236).
45. Salio, M., T. Berruti, and G. De Poli, *Prediction of residual stress distribution after turning in turbine disks*. International Journal of Mechanical Sciences, 2006. **48**(9): p. 976-984.
46. Chen, L., et al., *Effects of Edge Preparation and Feed when Hard Turning a Hot Work Die Steel with Polycrystalline Cubic Boron Nitride Tools*. CIRP Annals - Manufacturing Technology, 2006. **55**(1): p. 89-92.
47. Hua, J., D. Umbrello, and R. Shivpuri, *Investigation of cutting conditions and cutting edge preparations for enhanced compressive subsurface residual stress in the hard turning of bearing steel*. Journal of Materials Processing Technology, 2006. **171**(2): p. 180-187.
48. Ee, K.C., O.W. Dillon Jr, and I.S. Jawahir, *Finite element modeling of residual stresses in machining induced by cutting using a tool with finite edge radius*. International Journal of Mechanical Sciences, 2005. **47**(10): p. 1611-1628.
49. Sasahara, H., T. Obikawa, and T. Shirakashi, *Prediction model of surface residual stress within a machined surface by combining two orthogonal plane models*. International Journal of Machine Tools and Manufacture, 2004. **44**(7-8): p. 815-822.
50. Marusich, T. and E. Askari. *Modeling residual stress and workpiece quality in machined surfaces*. 2001.
51. Nasr, M.N.A., E.G. Ng, and M.A. Elbestawi, *Modelling the effects of tool-edge radius on residual stresses when orthogonal cutting AISI 316L*. International Journal of Machine Tools & Manufacture, 2007. **47**(2): p. 401-11.

52. Outeiro, J.C., D. Umbrello, and R. M'Saoubi, *Experimental and numerical modelling of the residual stresses induced in orthogonal cutting of AISI 316L steel*. International Journal of Machine Tools and Manufacture, 2006. **46**(14): p. 1786-1794.
53. Shet, C. and X. Deng, *Residual stresses and strains in orthogonal metal cutting*. International Journal of Machine Tools and Manufacture, 2003. **43**(6): p. 573-587.
54. Chen, L., T.I. El-Wardany, and W.C. Harris, *Modelling the Effects of Flank Wear Land and Chip Formation on Residual Stresses*. CIRP Annals - Manufacturing Technology, 2004. **53**(1): p. 95-98.
55. Outeiro, J.C., et al., *Analysis of residual stresses induced by dry turning of difficult-to-machine materials*. CIRP Annals - Manufacturing Technology, 2008. **57**(1): p. 77-80.
56. Valiorgue, F., et al., *A new approach for the modelling of residual stresses induced by turning of 316L*. Journal of Materials Processing Technology, 2007. **191**(1-3): p. 270-273.
57. Nasr, M.N.A., E.G. Ng, and M.A. Elbestawi, *Effects of Strain Hardening and Initial Yield Strength on Machining-Induced Residual Stresses*. Transactions of the ASME. Journal of Engineering Materials and Technology, 2007. **129**(4): p. 567-79.
58. Umbrello, D., R. M'Saoubi, and J.C. Outeiro, *The influence of Johnson-Cook material constants on finite element simulation of machining of AISI 316L steel*. International Journal of Machine Tools and Manufacture, 2007. **47**(3-4): p. 462-470.
59. Li, J.L., L.L. Jing, and M. Chen, *An FEM study on residual stresses induced by high-speed end-milling of hardened steel SKD11*. Journal of Materials Processing Technology, 2009. **209**(9): p. 4515-4520.
60. Rohde, J. and A. Jeppsson, *Literature review of heat treatment simulations with respect to phase transformation, residual stresses and distortion*. Scandinavian Journal of Metallurgy, 2000. **29**(2): p. 47-62.
61. *DEFORM Integrated 2D-3D Version 10.2 User's Manual*, 2011, Columbus, Ohio: Scientific Forming Technologies Corporation (SFTC).
62. Ng, E.-G. and D.K. Aspinwall, *Modelling of hard part machining*. Journal of Materials Processing Technology, 2002. **127**(2): p. 222-229.
63. Özel, T., *The influence of friction models on finite element simulations of machining*. International Journal of Machine Tools and Manufacture, 2006. **46**(5): p. 518-530.
64. Attia, M.H. and L. Kops, *Thermal Consideration of the Design of Multilayer Coated Tools for High Speed Machining*, in *ASME International Mechanical Engineering Congress and Exposition 2004*: Anaheim, California, USA. p. 803-813.
65. Shi, B. and H. Attia, *Modeling the thermal and tribological processes at the tool-chip interface in machining*. Machining Science and Technology, 2009. **13**(2): p. 210-226.
66. Shi, B., H. Attia, and T. Wang, *Simulation of the Machining Process, Considering the Thermal Constriction Resistance of Multi-layer Coated Tools*, in *8th CIRP International Workshop on Modeling of Machining Operations 2005*, pp. 551-558: Chemnitz, Germany.
67. Thiele, J., et al., *Effect of cutting-edge geometry and workpiece hardness on surface residual stresses in finish hard turning of AISI 52100 steel*. Journal of Manufacturing Science and Engineering, 2000. **122**: p. 642.
68. Özel, T. and D. Ulutan, *Prediction of machining induced residual stresses in turning of titanium and nickel based alloys with experiments and finite element simulations*. CIRP Annals - Manufacturing Technology, 2012. **61**(1): p. 547-550.

69. Hua, J., et al., *Effect of feed rate, workpiece hardness and cutting edge on subsurface residual stress in the hard turning of bearing steel using chamfer + hone cutting edge geometry*. Materials Science and Engineering A, 2005. **394**(1-2): p. 238-248.
70. Ceretti, E., M. Lucchi, and T. Altan, *FEM simulation of orthogonal cutting: serrated chip formation*. Journal of Materials Processing Technology, 1999. **95**(1-3): p. 17-26.
71. Zhang, Y.C., et al., *Chip formation in orthogonal cutting considering interface limiting shear stress and damage evolution based on fracture energy approach*. Finite Elements in Analysis and Design, 2011. **47**(7): p. 850-863.
72. Ye, G.G., et al., *Modeling periodic adiabatic shear band evolution during high speed machining Ti-6Al-4V alloy*. International Journal of Plasticity, 2013. **40**(0): p. 39-55.
73. Umbrello, D., *Finite element simulation of conventional and high speed machining of Ti6Al4V alloy*. Journal of Materials Processing Technology, 2008. **196**(1-3): p. 79-87.
74. Sima, M. and T. Özel, *Modified material constitutive models for serrated chip formation simulations and experimental validation in machining of titanium alloy Ti-6Al-4V*. International Journal of Machine Tools and Manufacture, 2010. **50**(11): p. 943-960.
75. Özel, T., et al., *Investigations on the effects of multi-layered coated inserts in machining Ti-6Al-4V alloy with experiments and finite element simulations*. CIRP Annals - Manufacturing Technology, 2010. **59**(1): p. 77-82.
76. Molinari, A., X. Soldani, and M.H. Miguélez, *Adiabatic shear banding and scaling laws in chip formation with application to cutting of Ti-6Al-4V*. Journal of the Mechanics and Physics of Solids, 2013. **61**(11): p. 2331-2359.
77. Miguélez, M.H., X. Soldani, and A. Molinari, *Analysis of adiabatic shear banding in orthogonal cutting of Ti alloy*. International Journal of Mechanical Sciences, 2013. **75**(0): p. 212-222.
78. Liu, R., et al., *An enhanced constitutive material model for machining of Ti-6Al-4V alloy*. Journal of Materials Processing Technology, 2013. **213**(12): p. 2238-2246.
79. Hua, J. and R. Shivpuri, *Prediction of chip morphology and segmentation during the machining of titanium alloys*. Journal of Materials Processing Technology, 2004. **150**(1-2): p. 124-133.
80. Chen, G., et al., *Finite element simulation of high-speed machining of titanium alloy (Ti-6Al-4V) based on ductile failure model*. The International Journal of Advanced Manufacturing Technology, 2011. **56**(9-12): p. 1027-1038.
81. Calamaz, M., D. Coupard, and F. Girot, *A new material model for 2D numerical simulation of serrated chip formation when machining titanium alloy Ti-6Al-4V*. International Journal of Machine Tools and Manufacture, 2008. **48**(3-4): p. 275-288.
82. Alvarez, R., R. Domingo, and M.A. Sebastian, *Investigation of Ti6Al4V Orthogonal Cutting Numerical Simulations using Different Material Models*. AIP Conference Proceedings, 2010. **1252**(1): p. 787-794.
83. Umbrello, D., et al., *Hardness-based flow stress for numerical simulation of hard machining AISI H13 tool steel*. Journal of Materials Processing Technology, 2008. **199**(1-3): p. 64-73.
84. Umbrello, D., et al., *Modeling Of White And Dark Layer Formation In Hard Machining Of AISI 52100 Bearing Steel*. Machining Science and Technology: An International Journal, 2010. **14**(1): p. 128 - 147.

85. Umbrello, D., J. Hua, and R. Shivpuri, *Hardness-based flow stress and fracture models for numerical simulation of hard machining AISI 52100 bearing steel*. Materials Science and Engineering A, 2004. **374**(1-2): p. 90-100.
86. Umbrello, D. and L. Filice, *Improving surface integrity in orthogonal machining of hardened AISI 52100 steel by modeling white and dark layers formation*. CIRP Annals - Manufacturing Technology, 2009. **58**(1): p. 73-76.
87. Umbrello, D., et al., *A numerical model incorporating the microstructure alteration for predicting residual stresses in hard machining of AISI 52100 steel*. CIRP Annals - Manufacturing Technology, 2010.
88. Nasr, M.N.A., E.G. Ng, and M.A. Elbestawi, *A modified time-efficient FE approach for predicting machining-induced residual stresses*. Finite Elements in Analysis and Design, 2008. **44**(4): p. 149-161.
89. Shi, B., H. Attia, and N. Tounsi, *Identification of Material Constitutive Laws for Machining-Part II: Generation of the Constitutive Data and Validation of the Constitutive Law*. ASME Transactions, Journal of Manufacturing Science and Engineering., 2010. **132**, **051009**.
90. Shi, B., H. Attia, and N. Tounsi, *Identification of Material Constitutive Laws for Machining-Part I: An analytical model describing the stress, strain, strain rate and temperature fields in the primary shear zone in orthogonal metal cutting*. ASME Transactions, Journal of Manufacturing Science and Engineering., 2010. **132**, **051008**.
91. Shi, B. and H. Attia, *Evaluation criteria of the constitutive law formulation for the metal-cutting process*. Proceedings of the Institution of Mechanical Engineers, Journal of Engineering Manufacture, 2010. **Vol. 224 Part B**.
92. Bejjani, R., *Machinability and Modeling of Cutting Mechanism for Titanium Metal Matrix Composites*, Department of Mechanical Engineering., 2012, Polytechnique Montreal.
93. Abboud, E., et al., *Finite Element-based Modeling of Machining-induced Residual Stresses in Ti-6Al-4V under Finish Turning Conditions*. Procedia CIRP, 2013. **8**(0): p. 63-68.
94. Ramesh, A. and S.N. Melkote, *Modeling of white layer formation under thermally dominant conditions in orthogonal machining of hardened AISI 52100 steel*. International Journal of Machine Tools and Manufacture, 2008. **48**(3-4): p. 402-414.
95. Koistinen, D.P. and R.E. Marburger, *A general equation prescribing the extent of the austenite-martensite transformation in pure iron-carbon alloys and plain carbon steels*. Acta Metallurgica, 1959. **7**(1): p. 59-60.
96. Valiorgue, F., et al., *3D modeling of residual stresses induced in finish turning of an AISI304L stainless steel*. International Journal of Machine Tools and Manufacture, 2012. **53**(1): p. 77-90.
97. Arunachalam, R.M., M.A. Mannan, and A.C. Spowage, *Residual stress and surface roughness when facing age hardened Inconel 718 with CBN and ceramic cutting tools*. International Journal of Machine Tools and Manufacture, 2004. **44**(9): p. 879-87.
98. Pawade, R.S., S.S. Joshi, and P.K. Brahmkar, *Effect of machining parameters and cutting edge geometry on surface integrity of high-speed turned Inconel 718*. International Journal of Machine Tools and Manufacture, 2008. **48**(1): p. 15-28.

99. Sharman, A.R.C., J.I. Hughes, and K. Ridgway, *An analysis of the residual stresses generated in Inconel 718(TM) when turning*. Journal of Materials Processing Technology, 2006. **173**(3): p. 359-367.
100. Mantle, A.L. and D.K. Aspinwall. *Surface integrity of a high speed milled gamma titanium aluminide*. 2001. Elsevier Ltd.
101. Mantle, A.L. and D.K. Aspinwall, *Surface integrity and fatigue life of turned gamma titanium aluminide*. Journal of Materials Processing Technology, 1997. **72**(Compendex): p. 413-420.
102. Che-Haron, C.H. and A. Jawaid, *The effect of machining on surface integrity of titanium alloy Ti-6% Al-4% v*. Journal of Materials Processing Technology, 2005. **166**(2): p. 188-192.
103. Che-Haron, C.H., *Tool life and surface integrity in turning titanium alloy*. Journal of Materials Processing Technology, 2001. **118**(1-3): p. 231-237.
104. Ginting, A. and M. Nouari, *Surface integrity of dry machined titanium alloys*. International Journal of Machine Tools and Manufacture, 2009. **49**(3-4): p. 325-332.
105. Dahlman, P., F. Gunnberg, and M. Jacobson, *The influence of rake angle, cutting feed and cutting depth on residual stresses in hard turning*. Journal of Materials Processing Technology, 2004. **147**(2): p. 181-184.
106. Javidi, A., U. Rieger, and W. Eichseder, *The effect of machining on the surface integrity and fatigue life*. International Journal of Fatigue, 2008. **30**(10-11): p. 2050-2055.
107. Outeiro, J.C., et al., *Machining residual stresses in AISI 316L steel and their correlation with the cutting parameters*. Machining Science and Technology, 2002. **6**(2): p. 251-270.
108. Capello, E., *Residual stresses in turning: Part I: Influence of process parameters*. Journal of Materials Processing Technology, 2005. **160**(2): p. 221-228.
109. Li, W., et al., *Residual stresses in face finish turning of high strength nickel-based superalloy*. Journal of Materials Processing Technology, 2009. **209**(10): p. 4896-4902.
110. Liu, M., J.-i. Takagi, and A. Tsukuda, *Effect of tool nose radius and tool wear on residual stress distribution in hard turning of bearing steel*. Journal of Materials Processing Technology, 2004. **150**(3): p. 234-241.
111. Capello, E., *Residual stresses in turning: Part II. Influence of the machined material*. Journal of Materials Processing Technology, 2006. **172**(3): p. 319-326.
112. Pineault, J., Chalhoub, H., *Residual stress measurements on Pratt & Whitney RT S-35642 titanium alloy coupons using x-ray diffraction techniques*, 2013, performed by Proto Manufacturing Ltd., Oldcastle, Ontario, owned by Pratt & Whitney Canada, Toronto.
113. Davim, J.P., *Machining: fundamentals and recent advances*2008: Springer.
114. Taylor, B.N. and C.E. Kuyatt, *NIST Technical Note 1297*. Guidelines for evaluating and expressing the uncertainty of NIST measurement results, NIST, Gaithersburg, MD, 1994: p. 24.
115. Boothroyd, G., *Fundamentals of metal machining*1965: Edward Arnold.
116. Donachie, M.J., *Titanium a technical guide*, 2000, Materials Park, OH: ASM International.
117. Chandler, H., *Heat treater's guide : practices and procedures for nonferrous alloys*1996, Materials Park, OH: ASM International.

118. Fan, Y., et al., *Effect of phase transformations on laser forming of Ti-6Al-4V alloy*. Journal of Applied Physics, 2005. **98**(1): p. 013518-013518-10.
119. Denis, S., et al., *Stress-phase-transformation interactions - basic principles, modelling, and calculation of internal stresses*. Materials Science and Technology, 1985. **1**(10): p. 805-814.
120. Ramesh, A., et al., *Analysis of white layers formed in hard turning of AISI 52100 steel*. Materials Science and Engineering, 2005. **390**: p. 88-97.
121. Porter, D.A. and K.E. Easterling, *Phase transformations in metals and alloys* 1992, London; New York: Chapman & Hall.
122. Zorev, N.N. *Interrelationship between shear processes occurring along tool face and on shear plane in metal cutting*. in *Proceedings of the International Production Engineering Research Conference, Sep 9-12 1963*. 1963. New York, NY, United States: American Society of Mechanical Engineers (ASME).
123. Shi, B., et al., *Numerical and experimental investigation of laser-assisted machining of Inconel 718*. Machining Science and Technology, 2008. **12**(4): p. 498-513.
124. Velásquez, J.D.P., et al., *Sub-surface and surface analysis of high speed machined Ti-6Al-4V alloy*. Materials Science and Engineering: A, 2010. **527**(10-11): p. 2572-2578.
125. Movahhedy, M.R., Y. Altintas, and M.S. Gadala, *Numerical analysis of metal cutting with chamfered and blunt tools*. Journal of Manufacturing Science and Engineering, 2002. **124**(2): p. 178.
126. Min, W. and Z. Youzhen, *Diffusion wear in milling titanium alloys*. Materials Science and Technology, 1988. **4**(6): p. 548-553.
127. Hartung, P.D., B.M. Kramer, and B.F. von Turkovich, *Tool Wear in Titanium Machining*. CIRP Annals - Manufacturing Technology, 1982. **31**(1): p. 75-80.
128. Shi, B. and H. Attia, *Current Status and Future Direction in the Numerical Modeling and Simulation of Machining Processes: A Critical Literature Review*. Machining Science and Technology, 2010. **14**(2): p. 149-188.
129. Dearnley, P.A. and A.N. Grearson, *Evaluation of principal wear mechanisms of cemented carbides and ceramics used for machining titanium alloy IMI 318*. Materials Science and Technology, 1986. **2**(1): p. 47-58.
130. Sun, S., M. Brandt, and M.S. Dargusch, *Characteristics of cutting forces and chip formation in machining of titanium alloys*. International Journal of Machine Tools and Manufacture, 2009. **49**(7-8): p. 561-568.
131. Komanduri, R., *Some clarifications on the mechanics of chip formation when machining titanium alloys*. Wear, 1982. **76**(1): p. 15-34.
132. Rogers, H.C., *Adiabatic plastic deformation*. Annual Review of Materials Science, 1979. **9**(1): p. 283-311.
133. Bayoumi, A.E. and J.Q. Xie, *Some metallurgical aspects of chip formation in cutting Ti-6wt.%Al-4wt.%V alloy*. Materials Science and Engineering: A, 1995. **190**(1-2): p. 173-180.
134. Recht, R.F., *Catastrophic thermoplastic shear*. J. Appl. Mech., 1964. **86**: p. 189.
135. Vyas, A. and M.C. Shaw, *Mechanics of Saw-Tooth Chip Formation in Metal Cutting*. Journal of Manufacturing Science and Engineering, 1999. **121**(2): p. 163-172.
136. Shaw, M.C. and A. Vyas, *Chip Formation in the Machining of Hardened Steel*. CIRP Annals - Manufacturing Technology, 1993. **42**(1): p. 29-33.

137. Nakayama, K., M. Arai, and T. Kanda, *Machining Characteristics of Hard Materials*. CIRP Annals - Manufacturing Technology, 1988. **37**(1): p. 89-92.

## APPENDIX A

Table A-1: cutting matrices for oblique turning of Ti-6Al-4V (Alloy 1) and Ti-6Al-2Sn-4Zr-6Mo (Alloy 2). Alloy 2 test conditions are shaded. The parameters  $doc$ ,  $v$ ,  $f$ , and  $R$  represent the depth of cut, cutting speed, feed rate and tool corner radius, respectively.

| Test #, Alloy 1 | Cutting parameters |       |       |       | Test #, Alloy 2 |
|-----------------|--------------------|-------|-------|-------|-----------------|
|                 | $doc$              | $v$   | $f$   | $R$   |                 |
| A1-01           | $doc_1$            | $v_1$ | $f_1$ | $R_1$ | A2-01           |
| A1-02           | $doc_1$            | $v_1$ | $f_1$ | $R_2$ |                 |
| A1-03           | $doc_1$            | $v_1$ | $f_1$ | $R_3$ | A2-02           |
| A1-04           | $doc_1$            | $v_1$ | $f_2$ | $R_1$ | A2-03           |
| A1-05           | $doc_1$            | $v_1$ | $f_2$ | $R_2$ |                 |
| A1-06           | $doc_1$            | $v_1$ | $f_2$ | $R_3$ | A2-04           |
| A1-07           | $doc_1$            | $v_1$ | $f_3$ | $R_1$ | A2-05           |
| A1-08           | $doc_1$            | $v_1$ | $f_3$ | $R_2$ |                 |
| A1-09           | $doc_1$            | $v_1$ | $f_3$ | $R_3$ | A2-06           |
| A1-10           | $doc_1$            | $v_2$ | $f_1$ | $R_1$ | A2-07           |
| A1-11           | $doc_1$            | $v_2$ | $f_1$ | $R_2$ |                 |
| A1-12           | $doc_1$            | $v_2$ | $f_1$ | $R_3$ | A2-08           |
| A1-13           | $doc_1$            | $v_2$ | $f_2$ | $R_1$ | A2-09           |
| A1-14           | $doc_1$            | $v_2$ | $f_2$ | $R_2$ |                 |
| A1-15           | $doc_1$            | $v_2$ | $f_2$ | $R_3$ | A2-10           |
| A1-16           | $doc_1$            | $v_2$ | $f_3$ | $R_1$ | A2-11           |
| A1-17           | $doc_1$            | $v_2$ | $f_3$ | $R_2$ |                 |
| A1-18           | $doc_1$            | $v_2$ | $f_3$ | $R_3$ | A2-12           |
| A1-19           | $doc_2$            | $v_1$ | $f_1$ | $R_1$ | A2-13           |
| A1-20           | $doc_2$            | $v_1$ | $f_1$ | $R_2$ | A2-14           |
| A1-21           | $doc_2$            | $v_1$ | $f_1$ | $R_3$ | A2-15           |
| A1-22           | $doc_2$            | $v_1$ | $f_2$ | $R_1$ |                 |
| A1-23           | $doc_2$            | $v_1$ | $f_2$ | $R_2$ |                 |
| A1-24           | $doc_2$            | $v_1$ | $f_2$ | $R_3$ |                 |
| A1-25           | $doc_2$            | $v_1$ | $f_3$ | $R_1$ | A2-16           |
| A1-26           | $doc_2$            | $v_1$ | $f_3$ | $R_2$ | A2-17           |
| A1-27           | $doc_2$            | $v_1$ | $f_3$ | $R_3$ | A2-18           |
| A1-28           | $doc_2$            | $v_2$ | $f_1$ | $R_1$ | A2-19           |
| A1-29           | $doc_2$            | $v_2$ | $f_1$ | $R_2$ | A2-20           |
| A1-30           | $doc_2$            | $v_2$ | $f_1$ | $R_3$ | A2-21           |
| A1-31           | $doc_2$            | $v_2$ | $f_2$ | $R_1$ |                 |
| A1-32           | $doc_2$            | $v_2$ | $f_2$ | $R_2$ |                 |
| A1-33           | $doc_2$            | $v_2$ | $f_2$ | $R_3$ |                 |
| A1-34           | $doc_2$            | $v_2$ | $f_3$ | $R_1$ | A2-22           |
| A1-35           | $doc_2$            | $v_2$ | $f_3$ | $R_2$ | A2-23           |
| A1-36           | $doc_2$            | $v_2$ | $f_3$ | $R_3$ | A2-24           |

## APPENDIX B

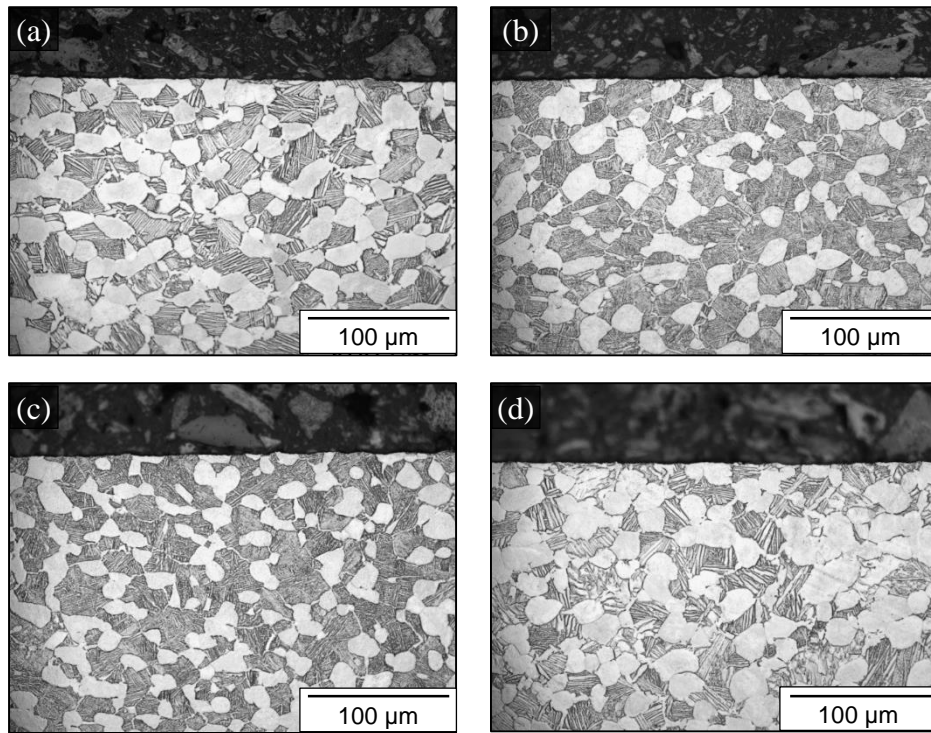


Fig. B.1: near-surface microstructure of longitudinally turned Ti-6Al-4V (Alloy 1) at  $\times 500$  magnification etched with Kroll's reagent. Specimens are oriented parallel to the direction of feed, and were machined at the following cutting conditions:

(a)  $(doc_1, f_1, v_2, R_3)$ ; (b)  $(doc_2, f_1, v_2, R_3)$ ; (c)  $(doc_1, f_3, v_2, R_3)$ ; (d)  $(doc_2, f_3, v_2, R_3)$ .

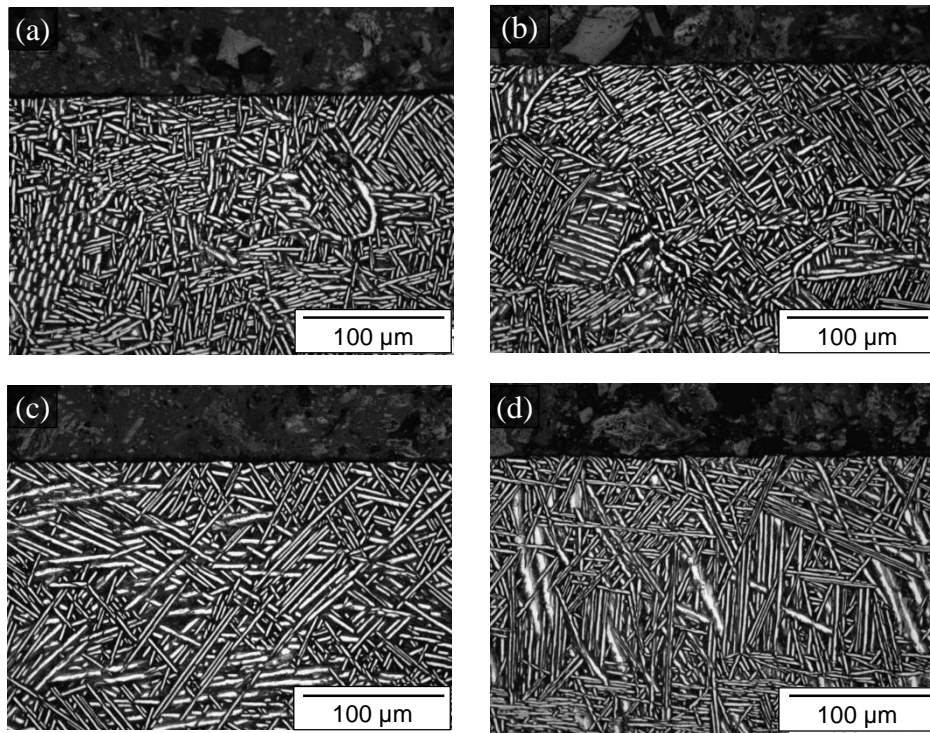


Fig. B.2: near-surface microstructure of longitudinally turned Ti-6Al-2Sn-4Zr-6Mo (Alloy 2) at  $\times 500$  magnification etched with Kroll's reagent. Specimens are oriented parallel to the direction of feed, and were machined at the following cutting conditions:

(a) ( $doc_1, f_1, v_2, R_3$ ); (b) ( $doc_2, f_1, v_2, R_3$ ); (c) ( $doc_1, f_3, v_2, R_3$ ); (d) ( $doc_2, f_3, v_2, R_3$ ).